ANALYTICAL AND COMPUTATIONAL MODELING OF TEMPERATURE DEPENDENT MATERIAL PROPERTIES, RESIDUAL STRESS, AND TORSIONAL BEHAVIOR FOR COLD-FORMED STEEL MEMBERS

by

Yu Xia

A dissertation submitted in partial fulfillment of
the requirements for the degree of

Doctor of Philosophy
(Civil and Environmental Engineering)

at the

UNIVERSITY OF WISCONSIN–MADISON

2022

Date of final oral examination: 07/26/2022

The dissertation is approved by the following members of the Final Oral Committee:

Hannah B. Blum, Assistant Professor, Civil and Environmental Engineering

Benjamin W. Schafer, Professor, Civil and Systems Engineering (Johns Hopkins University)

Pavana Prabhakar, Assistant Professor, Mechanical Engineering

Bu Wang, Assistant Professor, Civil and Environmental Engineering

THESIS AUTHORSHIP ATTRIBUTION

This thesis contains materials published or submitted for publication, based on the work presented in this thesis, for which I am the main author or co-author.

Journal Articles

Xia, Yu, Ding, Chu, Li, Zhanjie , Schafer, Benjamin W., and Blum, Hannah B. “Numerical modeling of stress-strain relationships for advanced high strength steels.” *Journal of Constructional Steel Research*, 182 (2021): 106687. https://doi.org/10.1016/j.jcsr.2021.106687

Xia, Yu, Yan, Xia, Gernay, Thomas, and Blum, Hannah B. "Elevated temperature and post-fire stress-strain modeling of advanced high-strength cold-formed steel alloys." *Journal of Constructional Steel Research* 190 (2022): 107116. https://doi.org/10.1016/j.jcsr.2021.107116

Submitted Journal Article

Xia, Yu and Blum, Hannah B. "Material properties of advanced high-strength cold-formed steel alloys under subzero temperatures." Manuscript submitted in 2022, under review.

Conference Papers

Xia, Yu, Li, Zhanjie, Schafer, Benjamin W., and Blum, Hannah B. (2019). Material

property characterization of advanced high strength cold-formed steel. Advances in Engineering Materials, Structures and Systems: Innovations, Mechanics and Applications (pp. 1083-1088). CRC Press.

Xia, Yu and Blum, Hannah B. (2020) Geometric imperfection measurements of cold-formed steel members using a portable non-contact 3D laser scanner. Structural Stability Research Council 2020 Annual Stability Conference, Atlanta, Georgia, 2020, 1-15

Xia, Yu, Sudhiwana, Tanapat, and Blum, Hannah B. (2020) Material properties of cold-formed steel under subzero temperatures. CFSRC Colloquium, 2020, 1–7. http://jhir.library.jhu.edu/handle/1774.2/63254

Xia, Yu, Yan, Xia, Gernay, Thomas, and Blum, Hannah B. (2020) Modeling of stress-strain relationship of advanced high-strength cold-formed steel at elevated temperature. CFSRC Colloquium, 2020, 1–9.
http://jhir.library.jhu.edu/handle/1774.2/63167

Xia, Yu, Li, Zhanjie, Schafer, Benjamin W., and Blum, Hannah B. "Experimental study on residual stresses of dual phase high-strength cold-formed steel angles." ce/papers 4, no. 2-4 (2021): 387-392.
https://doi.org/10.1002/cepa.1307

Xia, Yu, Yan, Xia, Gernay, Thomas, and Blum, Hannah B. "Experimental and numerical study of the behavior of HSLA and DP cold-formed high-strength steels at elevated temperature." ce/papers 4, no. 2-4 (2021): 1264-1271.

https://doi.org/10.1002/cepa.1420

Xia, Yu, Glauz, Robert S., Schafer, Benjamin W., Seek, Michael, and Blum, Hannah B. (2022) Cold-formed steel strength predictions for torsion. Structural Stability Research Council 2022 Annual Stability Conference, Denver, Colorado, 2022, 1-16

ACKNOWLEDGMENTS

I would like to thank my advisor Prof. Hannah Blum for her strong support and guidance on my research, studying, and teaching during the past four years. Prof. Blum provides me with helpful suggestions when I was stuck on my research or had any worry or anxiety. She illustrates respect for the relationship between her and her students, not only myself but also anyone in our group. The past four years are the most fulfilling and interesting time of my studenthood. Thanks very much, Prof. Blum!

Also, I would like to thank many people that provide me with much help on my research. I would like to thank Prof. Benjamin Schafer for his super helpful advice on almost all my research projects and the opportunities for me to know advanced high-strength steel (AHSS). I would like to thank Prof. Zhanjie Li, Dr. Chu Ding, and Mr. Damir Akchurin for their advice and help on the AHSS project. I would like to thank Prof. Thomas Gernay and Dr. Xia Yan for their advice and help on the fire modeling project. I would like to thank Mr. Robert Glauz and Prof. Michael Seek for their knowledge and wisdom in helping me better understand the world of torsion. I would like to thank Mr. Jacob Zeuske for his help with all my experimental studies.

I would also like to thank my research group mates and my friends for having a great four-year together. For Ed, Hyeyoung, and Max, it's great to know them, work with them, and learn from them in Blum's group during the past years. For Qitong and Zheng, it's my pleasure to know the folks, and I will always remember the supports they provided and the time we spent together.

Finally, I would like to thank my parents. No word can express my appreciation. They always support me and trust me without any condition. They provide me

with everything they can. It has been three years since we reunited last time. And finally, I can see them soon, and hopefully, they will be proud of me, just like how I feel proud of them.

CONTENTS

LIST OF TABLES

LIST OF FIGURES

ABSTRACT

Thin-walled cold-formed steel (CFS) members have been widely used in the construction industry because of their unique advantages. A new family of CFS known as advanced high-strength steel (AHSS) has been developed with unprecedented combinations of strength and ductility. An extensive study of the material properties and member structural performance of AHSS is presented. The study consists of five different parts. The first three parts introduce the material properties of AHSS under different temperature scenarios including ambient, elevated temperatures, and subzero temperatures. Each of the three parts contains the experimental stress-strain curves and key material properties, as well as the developments of the constitutive relation modeling and the predictive equations for the parameters required by the proposed constitutive models. The fourth part introduces the residual stress distribution of press-braked AHSS members. An experimental study using the sectioning method is conducted for the residual stress measurement and a numerical study using a validated finite element model is presented to provide extra residual stress data through the steel sheet thickness. The fifth part introduces the torsional behaviors of CFS members. It contains two parametric studies using validated models. The first parametric study contains the predictive equations of bimoment capacity for members under torsional loads. The second parametric study contains the controlling interaction equations between moment and bimoment for members under combined bending-torsion with different bracing and loading conditions. The study shows the uniqueness of AHSS material and structural behaviors compared with conventional steel and provides useful data and information for potential AHSS applications in the construction industry in the future.

Chapter 1

Introduction

1.1 Motivation

Thin-walled cold-formed steel (CFS) members formed from coils of mild steel have been widely used in the structural and construction industries in the United States and globally since the 1940s. In general, CFS members have unique advantages, including nestable sections for compact packaging and shipping, lightweight and consequently high strength-to-weight ratios, and high recyclability [1].

Owing to material science advances at the microstructural level over the past two decades, advanced high-strength steel (AHSS) has been developed. AHSS are steels with unique microstructures utilizing complex deformation and phase transformation processes to achieve unprecedented combinations of strength and ductility. The design and manufacture of AHSS require circumspect selections of chemical compositions and precisely controlled heating and cooling processes.

Subsequently, AHSS exhibit a multiphase microstructure containing one or more phases different from ferrite, pearlite, or cementite. Rather, these phases, for example, include martensite, bainite, austenite, and/or retained austenite that are sufficient in quantities to produce unique mechanical properties.

AHSS includes new grades of sheet steel with yield strength up to 1250 MPa, ultimate strength up to 1900 MPa, and tensile elongation upwards of 20% to 30%. In addition, different from conventional steels, the terminology AHSS is classified by its metallurgical designation, rather than the steel grades. As a result, AHSS can have a wider range of grades (e.g., with ultimate strength as low as 440 MPa and yield strength as low as 210 MPa) than the conventional high strength steels, which require a yield strength higher than 460 MPa [2].

AHSS has been maturely developed and applied in the automobile industry for its excellence in stiffness, crash performance and formability [3]. The civil construction industry requires different design constraints than the automobile industry, therefore research needs to be carried out on the application of AHSS members as load-bearing components in structural framing for civil construction. For any attempt to characterize the structural performance of AHSS members, accurate understandings of the natural material properties, the effects of the forming processes, and member-level structural behaviors under typical loading conditions are essential.

1.2 Scope and objectives

This study is designed to thoroughly understand the material behavior at different temperature scenarios, the residual stresses, and the member structural behavior under torsional loads for cold-formed steel, particularly the AHSS.

The research on the AHSS material behavior at different temperature scenarios consists of three parts. The first part considers the ambient temperature scenario as the most common case, the second part considers the elevated temperature scenario simulating the steel under fire, and the third part considers the subzero temperature scenario for potential application in high latitude regions with cold climate. Each part focuses on providing the experimental stress-strain database and the accurate modeling of the constitutive relationship for AHSS at different temperatures. To achieve these objectives, a series of tensile coupon tests on specimens with a wide range of strengths and elongations made from dual phase steel, martensitic steel, high-strength low-alloy steel, and conventional mild steel alloys were conducted. Based on the test results including stress-strain curves and key material properties extracted from the stress-strain curves, comparisons between the experimental stress-strain data and the fits using existing models are analyzed. The causes for the unsatisfactory fit accuracy using existing models are discussed and the development of an updated model designed for both AHSS and other CFS showing similar stress-strain behavior is presented.

The residual stress research focuses on providing the residual stress magnitude and distribution for the press-braked lipped angle AHSS sections. To achieve this objective, four lipped angle sections cut from two press-braked dual phase

members were cut using the sectioning method. The strains at selected locations including corners, flat regions of legs, and lips for both inner and outer surfaces were measured during the whole sectioning process. Residual stresses on both surfaces and corresponding membrane and flexural residual stresses were calculated from these measured strains.

The torsion research focuses on developing the bimoment strength prediction for CFS members only under torsional loads and the moment-bimoment interaction equations for CFS members under combined bending-torsion. To achieve these objectives, a group of simulation models was designed and developed for different loading scenarios after being validated with existing experimental results [4]. Effects from different steel grades, cross-section geometries, member lengths, loading directions, and eccentricities were studied in the simulation. Based on the simulation data, a parametric study to develop a simple uniform equation to calculate the member bimoment strength under torsion alone is provided. Besides, another detailed parametric study to develop the interaction equations for CFS under combined bending-torsion is given.

Additionally, a numerical study focusing on determining the stiffnesses of purlin bracing in metal building system is presented as supplementary for AHSS member structural behavior. To achieve this objective, a finite element model was developed to simulate the reality condition of a Zee purlin truncation laterally supported by a pair of bolted channel bracing. AHSS stress-strain curve was adopted in the material property definition. Both the lateral linear stiffness and rotational stiffness along purlin longitudinal direction provided by purlin bracing for purlins with

different web depths were calculated and given using different loading conditions.

1.3 Dissertation Layout

This dissertation consists of seven chapters besides the introduction and the conclusion. For Ch. 2 to 6, each chapter summarizing one aspect of the overall project. Ch. 2 and 3 are published journal articles [5], [6]. Ch. 4 is a journal article manuscript that has been submitted. Ch. 5 and 6 summarize the ongoing work that will be implemented into journal articles in the near future, and a large portion of these two chapters are from conference proceedings [7], [8]. The following is a brief summary of the content provided in each chapter of this dissertation. It should be noted that there is no overall literature review chapter as relevant information is presented within each individual chapter.

Chapter 2 contains details on the test setup, procedures, and results for the tensile coupon test on AHSS specimens at ambient. Besides, detailed analysis on the characteristics of the AHSS stress-strain curves is conducted and the development of a two-stage plus linear model are proposed. The prediction for the required parameters in the proposed model is provided.

Chapter 3 contains details on the developments of an updated two-stage plus linear model and an updated bilinear plus linear model based on different stress hardening processes for different steel using different test methods (e.g., steady-state method and residual method). Besides, the predictive equations for the required parameters of the proposed models are given as functions of test temperature.

Chapter 4 contains details on the test setup, procedures, and results for the tensile coupon test on AHSS specimens at subzero temperatures down to -60°C. Besides, predictions for material properties are given and a comparison for the effects on important material properties under subzero temperatures between the steel specimens in this study and different steel specimens from literature with a wide range of thicknesses, grades, and steel types are included.

Chapter 5 contains details on the residual stress measurement using sectioning method for lipped angle specimens with different corner radii cut from dual phase steel members. Besides, a numerical simulation aiming reproducing the steel member manufacturing process is presented and validated by the test data. The through-thickness residual stress distribution at selected locations is given by the validated model.

Chapter 6 contains details on the developments of bimoment strength prediction for CFS members under torsional loads and moment-bimoment interaction equations for CFS members under the combined bending-torsion.

Chapter 7 contains a summary of the project, conclusions, and recommendations for future work.

The appendix introduces a numerical method to determine the stiffness of purlin bracing for metal building system following the reality engineering practice.

Chapter 2

Numerical modeling of stress-strain relationships for advanced high strength steels

Xia, Yu, Ding, Chu, Li, Zhanjie , Schafer, Benjamin W., and Blum, Hannah B. "Numerical modeling of stress-strain relationships for advanced high strength steels." *Journal of Constructional Steel Research*, 182 (2021): 106687. https://doi.org/10.1016/j.jcsr.2021.106687

The main body of Chapter 2 is from this published journal article. Some extra useful relevant information that is not included in the journal article is presented in the Addendum of this chapter.

Abstract

As a result of altered chemical composition, multiphase microstructures, and other micromechanical changes, advanced high-strength steel (AHSS) has three to five times the strength of conventional mild steels. Developed for automotive applications, AHSS has a high potential for application in cold-formed steel construction. However, the material properties must be properly understood and quantified for application to structural design with economic efficiency. A series of tensile coupon tests were carried out to determine typical AHSS material properties. Existing stress-strain models, designed for steels with gradual strain hardening, were studied and recalibrated to the AHSS test data. No existing method provided an accurate fit for all cases. An updated two-stage plus linear stress-strain model, based on the Ramberg-Osgood expression, was developed. The predictive equations for the parameters required by the new model were provided based on the statistical analysis of AHSS test data. In addition, from the discussion of the new model, a novel proof stress was recommended to represent the yield strength of AHSS. The energy was used to compare the AHSS experimental stress-strain curves with conventional steel stress-strain models to examine the rationality of the proposed proof stress as the yield strength in design.

2.1 Introduction

AHSS includes various families of steel, including Dual Phase (DP), Complex Phase (CP), Ferritic-Bainitic (FB), Martensitic (MS), Transformation-Induced Plasticity

(TRIP), and more. Different families of AHSS are made with specifically selected chemical composition and manufacturing processes, which result in unique material properties. Among various AHSS families, DP and MS currently have the lowest manufacturing cost and therefore are advised to be firstly studied for structural engineering applications as they have the lowest cost barrier to entry. DP steels comprise a ferritic matrix that encompasses a hard martensite second phase and a higher percentage composition of the hard martensite second phase generally demonstrates higher steel strength. DP steels are produced by a controlled cooling process from the initial two-phase ferrite plus austenite phase to transform some austenite to ferrite before transforming the remaining austenite to martensite. DP steels typically have a high degree of ductility and may have a lower cost and higher availability than other AHSS. MS steels comprise a martensitic matrix containing ferrite and bainite and generally have the highest strengths. MS steels are produced from the austenite phase to transform most of the austenite to martensite. The chemical composition of MS steels also includes carbon, manganese, silicon, and/or other elements to increase steel hardenability and strengths. MS steels typically have somewhat lowered ultimate elongations at fracture [2].

In this chapter, a series of tensile coupon tests on specimens made from two different families of AHSS (DP and MS) is presented. The tests were conducted per ASTM E8 [9], and additional procedures and techniques recommended by Huang and Young [10] were also adopted. A numerical model of the stress-strain relationship for AHSS is proposed. Existing models on steels with gradual yielding, including conventional CFS and stainless steel, are discussed. Numerical studies

show that existing models discussed in this paper do not accurately fit AHSS σ-ε curves from the tests conducted herein. Therefore, this paper proposes an updated two-stage plus linear stress-strain model for AHSS. The excellent fit between the proposed model and the AHSS test σ-ε curves are achieved. For scenarios when the full σ-ε curve is unavailable, predictive equations for the parameters in the proposed model are also proposed based on a statistical analysis of the AHSS test data. From the discussion on the proposed model, the possibility of adopting a new proof stress level to represent yield strength is also raised. A discussion of the proposed proof stress is carried out by comparing the energy dissipation between the AHSS test curves and conventional stress-strain models.

2.2 Existing stress-strain models

Accurate modeling of the constitutive relationship for metallic materials is essential in advanced structural design and numerical analysis. Different from conventional mild steels with a clear yield point and yield plateau, the σ-ε relationship for sheet steel are generally more rounded with an increased yield strength, an increased ultimate strength, and a decreased proportional limit. To depict the non-linear σ-ε relationship for CFS, various models have been proposed. Among these models, the Ramberg-Osgood (R-O) model [11] is widely recognized and extensively used, not only for CFS but also for other metals with similar stress-strain behaviors including stainless steel and aluminum. The universal form of the R-O model is shown in Eq. 2.1:

$$\varepsilon = \frac{\sigma}{E} + p\left(\frac{\sigma}{\sigma_p}\right)^n \quad \text{for } 0 \leqslant \sigma \leqslant \sigma_u \tag{2.1}$$

where σ denotes stress and ε denotes strain, E is elastic modulus, σ_p is the proof stress which corresponds to a plastic strain of p, and n is the exponential coefficient which determines the degree of curvature for the stress-strain model.

For $p = 0.002$, Fig. 2.1 shows the effect of hardening parameter n on the σ-ε curve. When $n < 1$, the σ-ε curve is concave; when $n = 1$, the σ-ε curve is a straight line between the origin and the ultimate point, which is the end of the model; and when $n > 1$, the σ-ε curve is convex. For the convex case (i.e. $n > 1$), as n increases, the degree of curve convexity becomes less sensitive to the increment of n; and when n approaches positive infinity, the curve is comprised of two straight lines. Thus, $n = 1$ is elastic and $n \to +\infty$ is elastic-perfectly-plastic. The σ-ε curve will pass through the origin and the 0.2% proof stress $\sigma_{0.2}$, regardless of the value of n. The R-O model is only able to depict the constitutive relationship when it is monotonically increasing. The R-O model is unable to depict the strain softening process after the ultimate point. These two constraints apply to all updated models originating from the R-O model. The most commonly used evolution of Eq. 2.1 was proposed by Hill [12], where $p = 0.002$ was used as shown in Eq. 2.2.

$$\varepsilon = \frac{\sigma}{E} + 0.002\left(\frac{\sigma}{\sigma_{0.2}}\right)^n \quad \text{for } 0 \leqslant \sigma \leqslant \sigma_u \tag{2.2}$$

Previous studies [13]–[15] have shown that Eq. 2.2 is able to provide accurate approximations of experimental σ-ε curves at relatively lower stress levels (e.g.

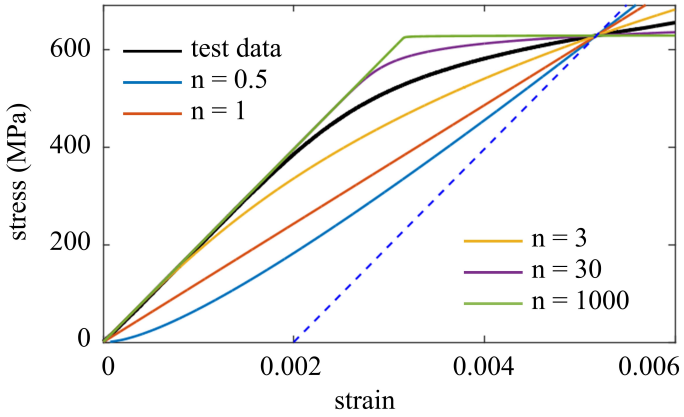

Figure 2.1: Different scenarios of Ramberg-Osgood expression using different n.

up to 0.2% proof stress), and is inaccurate at higher stress regions for CFS sheets. Therefore, the original one-stage R-O model is not able to accurately depict the entire σ-ε behavior of steel up to ultimate. As such, researchers have made updates to the original R-O model. Among all these updates, the central idea is to divide the curve into several stages and model them separately.

A two-stage model R-O was first proposed by Mirambell and Real [13]. They conducted a series of tensile coupon tests of cold-formed stainless steel Type 304/304L and proposed Eq. 2.2 for stress up to $\sigma_{0.2}$ and a new Eq. 2.3 for stress between $\sigma_{0.2}$ and ultimate strength σ_u:

$$\varepsilon = \frac{\sigma - \sigma_{0.2}}{E_{0.2}} + \varepsilon_{pu}\left(\frac{\sigma - \sigma_{0.2}}{\sigma_u - \sigma_{0.2}}\right)^m + \varepsilon_{0.2} \quad \text{for } \sigma_{0.2} \leqslant \sigma \leqslant \sigma_u \tag{2.3}$$

where $E_{0.2}$ is the tangent modulus at $\sigma_{0.2}$, ε_{pu} is the total plastic strain of ultimate point, $\varepsilon_{0.2}$ is the total strain corresponds to $\sigma_{0.2}$, and m is the exponential coefficient determining the degree of curvature of the σ-ε curve between the 0.2% offset and the ultimate.

Rasmussen [14] independently proposed an approximate expression of Eq. 2.3 for austenitic, duplex, and ferritic stainless steel alloy as shown in Eq. 2.4 by neglecting the difference between the ultimate strain ε_u and the plastic strain of the ultimate point ε_{pu} ($\varepsilon_{pu} \approx \varepsilon_u$) because stainless steels are generally ductile.

$$\varepsilon = \frac{\sigma - \sigma_{0.2}}{E_{0.2}} + \varepsilon_u \left(\frac{\sigma - \sigma_{0.2}}{\sigma_u - \sigma_{0.2}} \right)^m + \varepsilon_{0.2} \quad \text{for } \sigma_{0.2} \leqslant \sigma \leqslant \sigma_u \tag{2.4}$$

Rasmussen also proposed an expression of $E_{0.2}$ as shown in Eq. 2.5 and 2.6. To calculate the slope of the curve at $\sigma_{0.2}$, $E_{0.2}$ and m in Eq. 2.4 are unknown before they are calculated, therefore instead of Eq. 2.4, Eq. 2.2 is used as the strain expression in Eq. 2.5 and 2.6.

$$\frac{1}{E_{0.2}} = \frac{\partial \varepsilon(\sigma)}{\partial \sigma}|_{\sigma=\sigma_{0.2}} = \frac{1 + 0.002n\frac{\sigma^{n-1}}{\sigma_{0.2}^n}E}{E}|_{\sigma=\sigma_{0.2}} = \frac{1 + 0.002n\frac{E}{\sigma_{0.2}}}{E} \tag{2.5}$$

$$E_{0.2} = \frac{E}{1 + 0.002n\frac{E}{\sigma_{0.2}}} \tag{2.6}$$

Gardner and Nethercot [15] studied the material properties of Grade 1.4301 stainless steel and updated Eq. 2.3 so that the model passes through the ultimate point. For mathematical consistency, the second stage expression is updated as shown in Eq. 2.7 for $\sigma_{0.2} \leqslant \sigma \leqslant \sigma_u$.

$$\varepsilon = \frac{\sigma - \sigma_{0.2}}{E_{0.2}} + \left(\varepsilon_u - \varepsilon_{0.2} - \frac{\sigma_u - \sigma_{0.2}}{E_{0.2}} \right) \left(\frac{\sigma - \sigma_{0.2}}{\sigma_u - \sigma_{0.2}} \right)^m + \varepsilon_{0.2} \tag{2.7}$$

Additionally, Gardner further updated the second stage expression by forcing

the expression to pass through $\sigma_{0.2}$ and the 1% proof stress $\sigma_{1.0}$ as shown in Eq. 2.8 to expand the applicability of the model to include compression stress-strain behavior, where σ_u is generally unavailable.

$$\varepsilon = \frac{\sigma - \sigma_{0.2}}{E_{0.2}} + \left(0.008 - \frac{\sigma_{1.0} - \sigma_{0.2}}{E_{0.2}}\right)\left(\frac{\sigma - \sigma_{0.2}}{\sigma_{1.0} - \sigma_{0.2}}\right)^m + \varepsilon_{0.2} \quad \text{for } \sigma_{0.2} \leqslant \sigma \leqslant \sigma_u \quad (2.8)$$

Inspired by the work of Gardner and Nethercot [15], Li and Young [16] proposed a two-stage stress-strain model (as shown in Eq. 2.9 for $0 \leqslant \sigma \leqslant \sigma_{0.2T}$ and Eq. 2.10 for $\sigma_{0.2T} < \sigma \leqslant \sigma_{uT}$, where the subscript T indicates the material property at temperature T °C) designed for cold-formed high strength steel at both ambient and elevated temperature, and a series of predictive equations for the parameters required by the model were provided. The proposed two-stage model was verified by the accurate fits with experimental stress-strain curves at both ambient and elevated temperatures up to 1000°C of two series of cold-formed high-strength steels with nominal yield strengths of 700 MPa and 900 MPa at ambient.

$$\varepsilon = \left(\frac{\sigma}{E_T}\right) + 0.002\left(\frac{\sigma}{\sigma_{0.2T}}\right)^n \quad (2.9)$$

$$\varepsilon = \left(\frac{\sigma - \sigma_{0.2T}}{E_{0.2T}}\right) + \left(\varepsilon_{uT} - \varepsilon_{0.2T} - \frac{\sigma_{uT} - \sigma_{0.2T}}{E_{0.2T}}\right)\left(\frac{\sigma - \sigma_{0.2T}}{\sigma_{uT} - \sigma_{0.2T}}\right)^m + \varepsilon_{0.2T} \quad (2.10)$$

Besides two-stage models, multiple-stage models were also proposed to further

improve curve fit accuracy. Hradil et al [17] updated Mirambell's two-stage model [13] and proposed a generalized multiple-stage stress-strain model which was flexible to accommodate any amount of measured or recommended parameters. In their paper, a three-stage model was used as an example of the multiple-stage model. Stress-strain data from the origin to the ultimate was split into three stages by $\sigma_{0.2}$ and $\sigma_{1.0}$. The first stage expression is given in Eq. 2.2, the second stage expression is given in Eq. 2.11, and the third stage expression is given in Eq. 2.12. The definitions of some new parameters, including ${\varepsilon_{0.2}}^{\star}$, ${\varepsilon_{1.0}}^{\star}$, n_2, and n_3, are introduced in the original source [17]. A set of explicit equations as the inversion of Eq. 2.2, 2.11, and 2.12 were also provided.

$$\varepsilon = \frac{\sigma - \sigma_{0.2}}{E_{0.2}} + {\varepsilon_{0.2}}^{\star}\left(\frac{\sigma - \sigma_{0.2}}{\sigma_{1.0} - \sigma_{0.2}}\right)^{n_2} + 0.002 + \frac{\sigma_{0.2}}{E} \quad \text{for } \sigma_{0.2} \leqslant \sigma \leqslant \sigma_{1.0} \tag{2.11}$$

$$\varepsilon = \frac{\sigma - \sigma_{1.0}}{E_{1.0}} + {\varepsilon_{1.0}}^{\star}\left(\frac{\sigma - \sigma_{1.0}}{\sigma_{u} - \sigma_{1.0}}\right)^{n_3} + 0.01 + \frac{\sigma_{1.0}}{E} \quad \text{for } \sigma_{1.0} < \sigma \leqslant \sigma_{u} \tag{2.12}$$

Quach [18] further updated the model for stainless steel from the works of Olsson [19] and Gardner [20], and came up with a new three-stage model. The first stage expression is given by Eq. 2.2. The second stage ranges from $\sigma_{0.2}$ to 2.0% proof stress $\sigma_{2.0}$ and the expression is given by Eq. 2.13.

$$\varepsilon = \frac{\sigma - \sigma_{0.2}}{E_{0.2}} + \left(0.008 + (\sigma_{1.0} - \sigma_{0.2})\left(\frac{1}{E} - \frac{1}{E_{0.2}}\right)\right)\left(\frac{\sigma - \sigma_{0.2}}{\sigma_{1.0} - \sigma_{0.2}}\right)^{m} + \varepsilon_{0.2} \quad (2.13)$$

A similar expression of the second stage was also adopted in [20] and [21]. The third stage ranges from $\sigma_{2.0}$ to σ_u. The third stage expression is based on a linear relationship between true stress σ^t and engineering strain ε, ($\sigma^t = a + b\varepsilon$) and is given by Eq. 2.14:

$$\varepsilon = \frac{\sigma - a}{b - \sigma} \quad \text{for } \sigma_{2.0} < \sigma \leqslant \sigma_u \quad (2.14)$$

where parameters a and b are calculated by Eq. 2.15 and 2.16 using material properties including $\varepsilon_{2.0}$ (the strain of 2.0% proof stress), ε_u (total strain corresponds to σ_u), and σ_u.

$$a = \sigma_{2.0}(1 + \varepsilon_{2.0}) - b\varepsilon_{2.0} \quad (2.15)$$

$$b = \frac{\sigma_u(1 + \varepsilon_u) - \sigma_{2.0}(1 + \varepsilon_{2.0})}{\varepsilon_u - \varepsilon_{2.0}} \quad (2.16)$$

Besides the two-stage and multi-stage models based on the R-O expression, some updated models as transformations of the R-O expression or as combinations of the R-O expression and other equations have been proposed. MacDonald [22] came up with a uniform expression for modeling the full range σ-ε relationship of cold-formed stainless steel as shown in Eq. 2.17.

$$\varepsilon = \frac{\sigma}{E} + 0.002\left(\frac{\sigma}{\sigma_{0.2}}\right)^{i+j\left(\frac{\sigma}{\sigma_{0.2}}\right)^{k}} \quad \text{for } 0 \leqslant \sigma \leqslant \sigma_u \tag{2.17}$$

The idea of this model is to amplify the value of n in Eq. 2.2 for the larger strain region, particularly after $\sigma_{0.2}$. The numerical coefficients i, j, and k were obtained by error minimization on the test data. These coefficients were calculated as numbers between 2.5 to 6.0 and were found to be related to the steel sheet thickness.

Olsson [19] conducted research with a focus on plasticity models for stainless steel alloys and proposed a two-stage model depicting the relationship between the true stress $\sigma^t = \sigma(1+\varepsilon)$ and engineering strain ε. Eq. 2.2 is used as the first stage expression when $0 \leqslant \sigma \leqslant \sigma_{\varepsilon=0.02}$, where $\sigma_{\varepsilon=0.02}$ is the stress corresponding to $\varepsilon = 0.02$. The second stage is depicted as a line when $\sigma_{\varepsilon=0.02} < \sigma \leqslant \sigma_u$.

Abdella [23] proposed an approximate inversion of Eq. 2.2 and Eq. 2.7 for stainless steel alloys as shown in Eq. 2.18 for $0 \leqslant \varepsilon_n < 1$ and 2.19 for $1 < \varepsilon_n \leqslant \varepsilon_{nu}$ respectively:

$$\sigma_n = \frac{r\varepsilon_n}{1 + (r-1)\varepsilon_n^p} \tag{2.18}$$

$$\sigma_n = 1 + \frac{r_{0.2}(\varepsilon_n - 1)}{1 + (r^\star - 1)\left(\frac{\varepsilon_n - 1}{\varepsilon_{nu} - 1}\right)^{p^\star}} \tag{2.19}$$

where σ_n is the stress normalized by $\sigma_{0.2}$, ε_n is the strain normalized by $\varepsilon_{0.2}$. All other parameters are clearly defined in [23]. The proposed explicit expressions were verified by fitting the σ-ε curve database from [14].

Ma et al. [24] conducted a series of material properties experiments on cold-formed high-strength steel with nominal yield strength up to 1100 MPa and proposed a new constitutive model based on the original R-O expression (i.e. Eq. 2.2). The strain, as the output of the model, is explicitly depicted as expressions of plastic strain, ε_{pl}, as shown in Eq. 2.20:

$$\varepsilon = \varepsilon_p + \frac{\sigma}{E} = \varepsilon_p + \left(\frac{\sigma_{0.2}}{E}\right)\left(\frac{\varepsilon_p}{0.002}\right)^{\left(\frac{1}{n_0 + K\varepsilon_p^m}\right)} \tag{2.20}$$

where K is determined per arithmetic consistency at the ultimate point as defined in [24].

Besides the stress-strain model itself, accurate prediction of the parameters required by the model is also essential. Gardner and Yun [25] collected σ-ε curves of CFS sheets with nominal yield strengths ranging from 235 MPa to 1100 MPa from over 700 experiments. They reviewed the predictive equations for the key parameters of the two-stage CFS stress-strain model (e.g. model proposed by Mirambell and Real [13], Eq. 2.2 and 2.3) from existing literature and then developed a series of equations for these parameters based on the literature review and the statistical study on the collected experimental database. The accuracy of the predictive equations was verified by comparison between the stress-strain model using parameters predicted by the proposed equations and parameters captured from the experimental database. Further discussion regarding the suitability of existing predictive parameters with the AHSS database is presented in Section 2.5.1.

2.3 Tensile coupon testing

2.3.1 Test specimens

A total of 43 coupons were cut from 6 steel sheets by waterjet at UW-Madison TEAMLab and H&H Precision Wire in Newport, PA. The AHSS sheets including dual phase steel (DP) and martensitic steel (MS) with five different grades were studied. A piece of high-strength low-alloy steel (HSLA) (a type of conventional high-strength steel) sheet was also studied in this paper. The chemical composition of the tested steels is shown in Table 2.1. Note for DP-340, DP-700, and MS sheets, the composition is typical only, because the exact chemical composition is proprietary. Nominal yield strengths range from 340 MPa to 1200 MPa and nominal ultimate strength range from 590 MPa to 1500 MPa. Nominal dimensions of the coupon are per ASTM E8 [9] as shown in Fig. 2.2. Each steel sheet was labeled by its steel family and nominal yield strength in MPa, i.e.: DP-340, DP-580, DP-700, HSLA-700, MS-1030, and MS-1200. The coupons were labeled by the steel sheet label, the cutting direction, and an index number. For example, HSLA-700L01 stands for coupon #1 cut along the *longitudinal* (coiling) direction of sheet HSLA-700. Other direction labels included "T" for *transverse* direction and "D" for *diagonal* (45°) direction along the sheet. Table 2.2 summarizes the nominal properties and test matrix. Actual width b and thickness t for each coupon were measured before the test using a caliper and micrometer as reported in Table 2.3. HSLA-700 and DP-700 were coated with galvanized zinc and the actual thicknesses of these coupons were measured after removal of the coating by 1-molar HCl solution, after which the

Table 2.1: Chemical composition of AHSS.

steel	DP-340	DP-580	DP-700	HSLA-700	MS-1030	MS-1200
C (max %)	0.12	0.167	0.17	0.104	0.16	0.28
Si (max %)	0.4	1.413	0.4	0.012	0.4	0.4
Mn (max %)	1.6	2	1.7	2.32	1.8	1.3
P (max %)	0.025	0.01	0.02	0.013	0.02	0.02
S (max %)	0.01	0.002	0.01	0.004	0.01	0.01
Al (%)	$\geqslant$ 0.015	0.047	$\geqslant$ 0.01	0.031	0.015	0.015
Nb+Ti (max %)	0.1	0.006	0.15	-	0.1	0.1
Cr+Mo (max %)	1	0.043	1	0.606	1	1
V (max %)	0.2	0.005	-	0.001	-	-
B (max %)	0.005	0.0003	0.005	0.0001	0.005	0.01
Cu (max %)	0.2	0.02	0.2	0.02	0.2	0.2
Ni (%)	-	0.01	-	0.01	-	-
Sn (%)	-	0.008	-	0.002	-	-
N (%)	-	0.004	-	0.005	-	-
Cb (%)	-	0.003	-	0.002	-	-
Sb (%)	-	-	-	0.001	-	-
Ca (%)	-	-	-	0.001	-	-

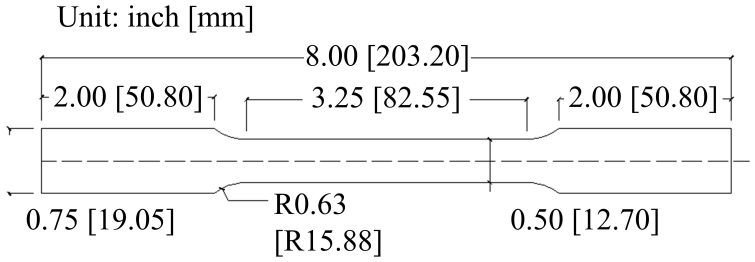

Figure 2.2: Nominal dimensional tensile coupon test specimen.

thickness of the coupons was reduced by 0.04 mm on average. The other steel sheets were uncoated.

2.3.2 Test procedures

A MTS Criterion Model 43 loading system with a maximum capacity of 50 kN was used for the tensile tests. An extensometer with a 25.4 mm gauge length was

Table 2.2: Nominal coupon properties and test matrix.

steel	t (mm)	σ_y (MPa)	σ_u (MPa)	test matrix
DP-340	1.4	340	590	L:2, T:2, D:1
DP-580	1.8	580	980	L:5, T:4, D:0
DP-700	1.4	700	980	L:2, T:2, D:2
HSLA-700	0.6	700	980	L:5, T:3, D:0
MS-1030	1.0	1030	1300	L:4, T:2, D:2
MS-1200	1.0	1200	1500	L:3, T:2, D:2

attached to the coupon center to measure strain. Before the test, the measured width b and thickness t of the coupon were input into the test control program, so that the real-time relationship between engineering stress (applied load divided by the initial cross-sectional area of the reduced parallel section) and strain (extensometer reading) was available during the test. A previous study [26] has indicated some loading rate σ-ε sensitivity. During the test, two different loading rates conforming to ASTM requirements [9] were used: initially, the loading rate was 0.2 mm/min until the stress achieved the nominal yield strength; the loading rate was then increased to 0.6 mm/min until fracture. Similar to the recommendation in [10], a slower loading rate before achieving the nominal yield strength was utilized to guarantee sufficient data in determining the elastic modulus. Consistent with Huang's recommendation [10], each test was manually paused twice. When the test was paused, the stress would decrease until stable and the duration for each pause was three minutes. For each test, the first pause was at the nominal yield strength and the second pause was at the nominal ultimate strength, as shown in Figure 2.3(a). Pausing near the yield strength (0.2% proof stress) and ultimate strength for 100 s to allow the stress relaxation to take place is recommended by [10]. Before testing, only the nominal values of yield and ultimate strengths are

known, therefore the nominal values were utilized for the generation of static drops. The static drop is used to estimate any stress amplification from the loading rate and to calculate the static stress.

2.3.3 Test results

For each test, the primary result is the dynamic σ-ε curve. Following the steps as depicted in Fig. 2.3, the static stress for each applicable data point is calculated by subtracting the stress amplification from its dynamic stress using the two static drops generated during the test, where $\Delta\sigma_x$ is the stress amplification of location x. When x is between the proportional limit and the left end of the first static drop, $\Delta\sigma_x$ is calculated by Eq. 2.21; when x is between the right end of the first static drop and the left end of the second static drop, $\Delta\sigma_x$ is calculated by Eq. 2.22; when x is after the right end of the second static drop, $\Delta\sigma_x$ is calculated by Eq. 2.23.

$$\Delta\sigma_x = \frac{\varepsilon_x \Delta\sigma_1}{\varepsilon_1} \tag{2.21}$$

$$\Delta\sigma_x = \frac{(\Delta\sigma_2 - \Delta\sigma_1) \times (\varepsilon_x - \varepsilon_1)}{\varepsilon_2 - \varepsilon_1} + \Delta\sigma_1 \tag{2.22}$$

$$\Delta\sigma_x = \Delta\sigma_2 \tag{2.23}$$

When the loading is paused to generate the static drops, the strain increases slightly; when the loading is resumed, the stress rapidly increases from the valley of static drop and continues along the original dynamic path. These processes

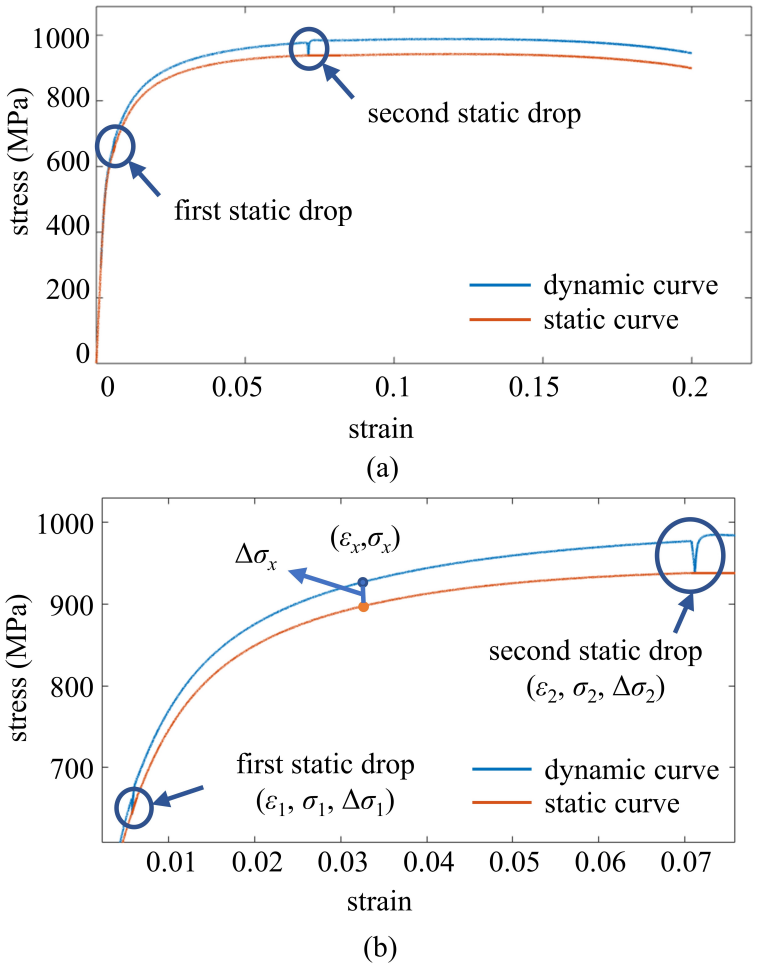

Figure 2.3: (a) Comparison between dynamic and static σ-ε curve; (b) (zoom-in view) conversion from dynamic stress to static stress.

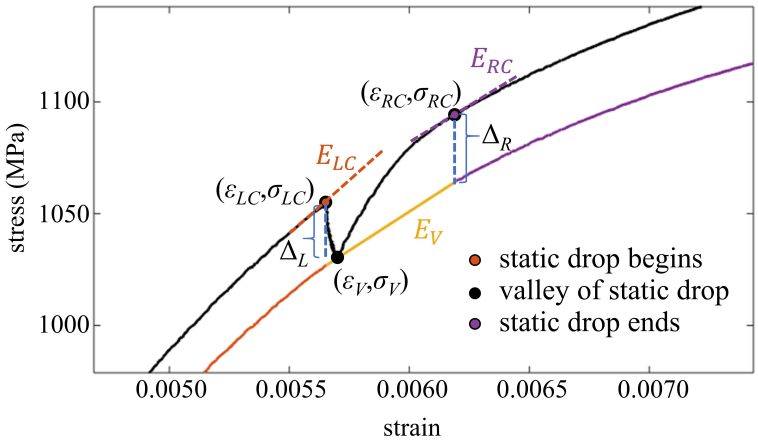

Figure 2.4: V shape dynamic stress-strain relationship at static drops.

generated a V shape dynamic stress-strain relationship as shown in Fig. 2.4.

A linear relationship is proposed and recommended to define the static stress-strain relationship for data within the V shape. First, the points where static drop begins and ends, as well as the valley of the V shape of static drop are found manually. The linear relationship is assumed to pass through the valley and its slope is E_V as calculated by Eq. 2.24:

$$E_V = \tan \frac{\arctan E_{LC} + \arctan E_{RC}}{2} \tag{2.24}$$

where E_{LC} is the slope at the beginning (left) of the static drop and it is defined as the slope of linear regression for the ten data points before, E_{RC} is the slope at the end (right) of the static drop and it is defined as the slope of linear regression for the ten data points after.

The stress amplification at the beginning of the static drop, Δ_L, is calculated by Eq. 2.25, and the stress amplification at the end of the static drop, Δ_R, is calculated

by Eq. 2.26:

$$\Delta_L = \sigma_{LC} - [E_V(\varepsilon_{LC} - \varepsilon_V) + \sigma_V] \tag{2.25}$$

$$\Delta_R = \sigma_{RC} - [E_V(\varepsilon_{RC} - \varepsilon_V) + \sigma_V] \tag{2.26}$$

where ε_{LC} and σ_{LC} are the strain and stress of static drop beginning, ε_{RC} and σ_{RC} are the strain and stress of static drop end, ε_V and σ_V are the strain and stress of static drop valley.

Note that for the first static drop, the loading rate was 0.2 mm/min until the pause, and changed to 0.6 mm/min when the loading resumed. Therefore, the difference between Δ_L and Δ_R of the first static drop might indicate the difference in stress amplification resulting from different loading rates. A faster loading rate will result in a slightly larger dynamic stress amplification (and hence a slightly larger static drop), but regardless of the loading rate, the static drop will always reach the same level.

A summary of a representative static σ-ε curve for each steel is shown in Fig. 2.5. To ensure each data point on the σ-ε curve has the same weight, the experimental curve was represented by a generalized curve. Sadowski et al. [27] used a two-stage seventh-order polynomial to represent the experimental curve. However, their polynomial model used strain as the model input and stress as the model output, which is the inverse of the R-O expression, and although the coefficient of variance between the polynomial and the experimental σ-ε curve was larger

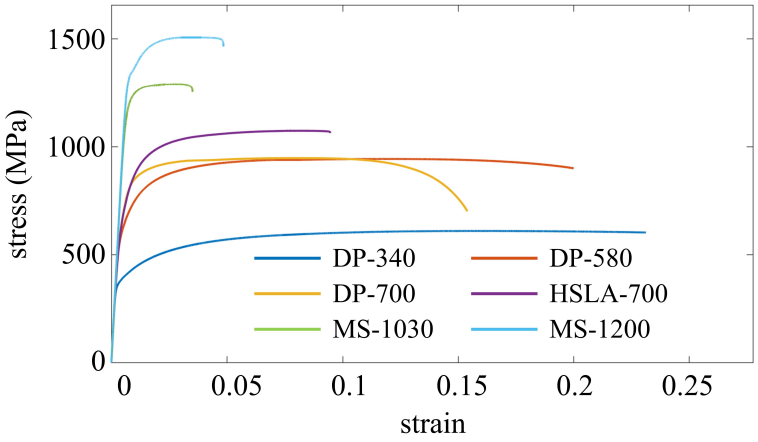

Figure 2.5: Representative static σ-ε curve for each steel.

than 0.96, some local differences were significant. To avoid these two issues, the experimental σ-ε curve was constructed by linear interpolation along the stress axis with a uniform stress increment of 0.1 MPa.

Material properties including elastic modulus E, 0.2% proof stress $\sigma_{0.2}$, strain at 0.2% proof stress $\varepsilon_{0.2}$, ultimate strength σ_u, ultimate strain ε_u, fracture stress σ_f, and fracture strain ε_f were extracted from the static σ-ε curves and are given in Table 2.3.

For E, the slope of the linear regression of all data points between stresses of 20% and 45% of the nominal yield strength was used [10]. The 0.2% offset point was determined as the point with a plastic strain of 0.002. The ultimate point was determined as the point with the largest static stress. The ratio of $\sigma_u/\sigma_{0.2}$, which is an indicator of curve non-linearity, varies from 1.1 to 1.7. AHSS with lower nominal yield strength tends to have a larger $\sigma_u/\sigma_{0.2}$. The fracture strain was obtained as the strain prior to a considerable reduction of engineering stress from the real-time stress-strain relationship due to fracture of the specimen [10]. In addition, two

Table 2.3: Properties of AHSS coupon specimens.

series	t	b	E	$\varepsilon_{0.2}$	$\sigma_{0.2}$	ε_u	σ_u	ε_f	σ_f
	mm	mm	GPa	%	MPa	%	MPa	%	MPa
DP-340L01	1.382	12.76	215	0.38	378	15.2	608	22.1	601
DP-340L02	1.373	12.74	208	0.36	338	13.7	575	17.4	550
DP-340T01	1.378	12.74	213	0.37	357	10.8	598	11.9	581
DP-340T02	1.381	12.74	219	0.36	360	14.6	603	22.1	580
DP-340D01	1.390	12.75	203	0.38	365	14.2	595	16.4	580
DP-580L01	1.819	13.10	193	0.52	622	11.7	958	13.0	957
DP-580L03	1.818	13.03	197	0.52	626	11.8	945	20.0	902
DP-580L04	1.816	13.12	188	0.53	625	11.8	945	19.8	872
DP-580L13	1.810	12.96	191	0.53	636	9.1	954	16.2	907
DP-580L23	1.803	12.90	197	0.52	638	12.4	970	22.9	841
DP-580T01	1.817	13.07	198	0.52	634	10.2	953	12.4	940
DP-580T02	1.812	13.02	207	0.51	643	9.9	952	11.3	940
DP-580T03	1.802	13.04	209	0.51	640	9.2	962	11.3	922
DP-580T06	1.794	13.07	207	0.51	645	9.7	970	11.2	947
DP-700L01	1.399	12.63	208	0.55	725	7.5	950	16.4	654
DP-700L02	1.394	12.73	216	0.53	717	7.8	952	14.7	705
DP-700T01	1.422	12.61	223	0.50	659	6.7	951	13.7	812
DP-700T02	1.422	12.63	217	0.50	648	6.0	947	13.8	802
DP-700D01	1.410	12.72	227	0.50	681	5.8	937	9.4	826
DP-700D02	1.416	12.73	206	0.54	696	6.0	945	15.8	634
HSLA-700L02	0.620	12.25	175	0.62	732	7.8	1037	8.3	1032
HSLA-700L03	0.629	12.61	176	0.59	677	7.7	993	8.1	986
HSLA-700L04	0.626	12.60	219	0.52	709	5.1	1022	5.4	1014
HSLA-700L08	0.630	12.53	216	0.52	698	6.6	1004	7.7	980
HSLA-700L16	0.628	12.63	191	0.57	714	7.8	1072	9.5	1061
HSLA-700T02	0.619	12.60	199	0.54	677	6.8	1009	7.0	1007
HSLA-700T03	0.623	12.60	183	0.56	656	7.2	982	7.5	981
HSLA-700T11	0.616	12.63	198	0.55	689	7.8	1045	8.7	1035
MS-1030L01	1.000	12.73	225	0.77	1286	3.0	1380	5.6	978
MS-1030L02	1.006	12.73	214	0.77	1223	2.1	1306	3.1	1284
MS-1030L03	0.999	12.74	219	0.75	1199	2.6	1288	3.3	1252
MS-1030L04	1.002	12.73	216	0.76	1206	3.1	1304	3.4	1288
MS-1030T01	1.008	12.73	215	0.75	1173	2.6	1316	3.0	1291
MS-1030T02	1.007	12.77	226	0.72	1174	2.2	1326	2.4	1313
MS-1030D01	1.010	12.73	214	0.75	1185	2.1	1317	2.1	1307
MS-1030D02	1.011	12.73	211	0.76	1175	2.3	1313	6.9	844
MS-1200L01	1.008	12.80	205	0.84	1311	2.9	1490	6.5	1140
MS-1200L02	0.995	12.73	219	0.80	1322	2.9	1505	4.6	1462
MS-1200L03	0.997	12.76	199	0.85	1292	3.6	1490	3.9	1455
MS-1200T01	1.008	12.76	234	0.77	1324	3.4	1519	4.0	1491
MS-1200T02	1.004	12.78	216	0.79	1280	3.3	1471	3.9	1433
MS-1200D01	1.003	12.81	220	0.81	1337	3.8	1534	7.0	1230
MS-1200D02	1.008	12.79	215	0.80	1282	2.4	1460	5.7	1158

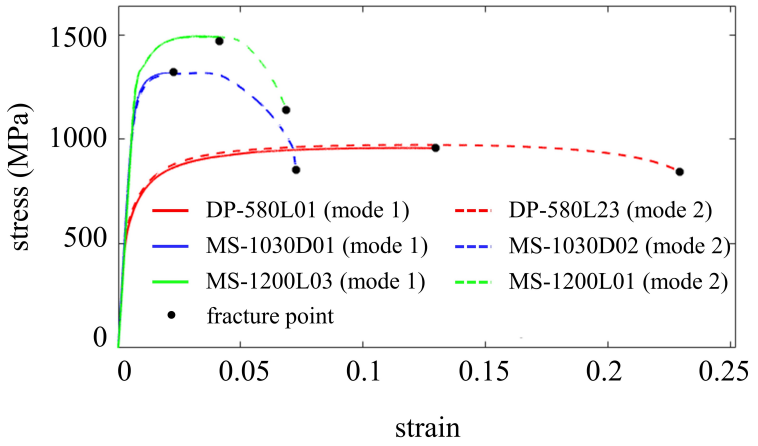

Figure 2.6: Different strain hardening modes for DP-580, MS-1030 and MS-1200.

different fracture modes are observed among the experimental AHSS σ-ε curves and some examples are shown in Fig. 2.6. The first mode (mode 1) has a sudden fracture and the second mode (mode 2) has a gradual strain softening process. Different fracture modes affect the fracture point. In addition, there are generally no obvious effects of cutting directions on the material properties.

2.4 Updated two-stage plus linear stress-strain model

In this section, existing two-stage and multiple-stage stress-strain models discussed as in Section 2.2 were used to fit the AHSS σ-ε curves from experiments as described in Section 2.3.3. Although some of the researchers provided predictive equations for essential parameters of their stress-strain model, the equations were derived from particular steel databases, which are different from AHSS in types, grades, and stress-strain behaviors. Therefore, to achieve an optimal fit, the predictive expressions were not adopted in this section; rather, the required parameters of these

models were fit from the AHSS experimental results. The optimal fit was achieved by maximizing the coefficient of determination (R^2) between the experimental curve and the numerical model, as shown in Eq. 2.27:

$$R^2 = 1 - \frac{SS_{res}}{SS_{tot}} = 1 - \frac{\sum_i (\varepsilon_i - \varepsilon(\sigma_i))^2}{\sum_i (\varepsilon_i - \overline{\varepsilon}_i)^2} \tag{2.27}$$

where σ_i and ε_i are the stress and strain of data point i of the experimental curve; $\varepsilon(\sigma_i)$ is the model strain corresponding to σ_i; $\overline{\varepsilon}_i$ is the average of experimental strains.

Noticeably, for R-O models, the R^2 is calculated by the difference of strain, rather than stress. Therefore, for higher strain ranges (e.g. the third stage of the three-stage model), R^2 could be small (i.e. poor fit between the test curve and the model), even if the difference between the test curve and the model is not obvious visually.

2.4.1 Optimal fit between AHSS stress-strain curves and existing models

The optimal fit between experimental and existing models, using DP-700L02 as an example, is shown in Fig. 2.7. Models proposed by Mirambell [13] (Fig. 2.7(a)) and Rasmussen [14] (Fig. 2.7(b)) provide accurate fit for the first stage; while the strain model prediction is lower than experimental strain at the beginning of the second stage (starting from 0.2% proof stress). Additionally, neither of these two models mathematically passes through the ultimate point, the difference in the ultimate strain between the model prediction and the test data is obvious. The

percentage difference for Mirambell's model ranges from 6.5% to 23.7% and for Rasmussen's model ranges from 12.4% to 47.4%. The inaccuracy of strain prediction in the high-stress range is large when applying Rasmussen's model, because the AHSS being studied in particular the MS, is less ductile than the stainless steel discussed in [14], and the approximation of using ultimate strain as the plastic strain of the ultimate point leads to an obvious inaccuracy.

Gardner's works [15] [20] provide three formats of the updated second stage model (Eq. 2.7, Eq. 2.8, and Eq. 2.13). As shown in Fig. 2.7(c), Eq. 2.7 mathematically ensures the model passes through the ultimate point, while similar to the case of Mirambell's model, the strain is underestimated at the beginning of the second stage. Eq. 2.8 provides excellent fit accuracy between 0.2% proof stress and 1.0% proof stress, while the fit after 1.0% proof stress is less accurate, particularly in the high-stress range.

The model proposed by Quach [18] (Fig. 2.7(d)) gives excellent fit for the first two stages, while the third stage by using Eq. 2.14 provides less accurate fit. Also, Quach's model requires three more parameters ($\sigma_{1.0}$, $\sigma_{2.0}$ and $\varepsilon_{2.0}$) than Mirambell's and Rasmussen's model, which might limit the feasibility of the model. Hradil's three-stage model [17] (Fig. 2.7(e)) provides excellent fit accuracy for MS-1030 and MS-1200 along the full stress range. For DP and HSLA, the first two stages are excellently fitted, while the fit for the beginning of the third stage (Eq. 2.12) is less accurate, particularly for DP-340. Also, Hradil's model requires more parameters ($\sigma_{1.0}$ and an extra exponential coefficient for the third stage) than others' two-stage models. The accuracy of the fit can be increased if the number of model stages

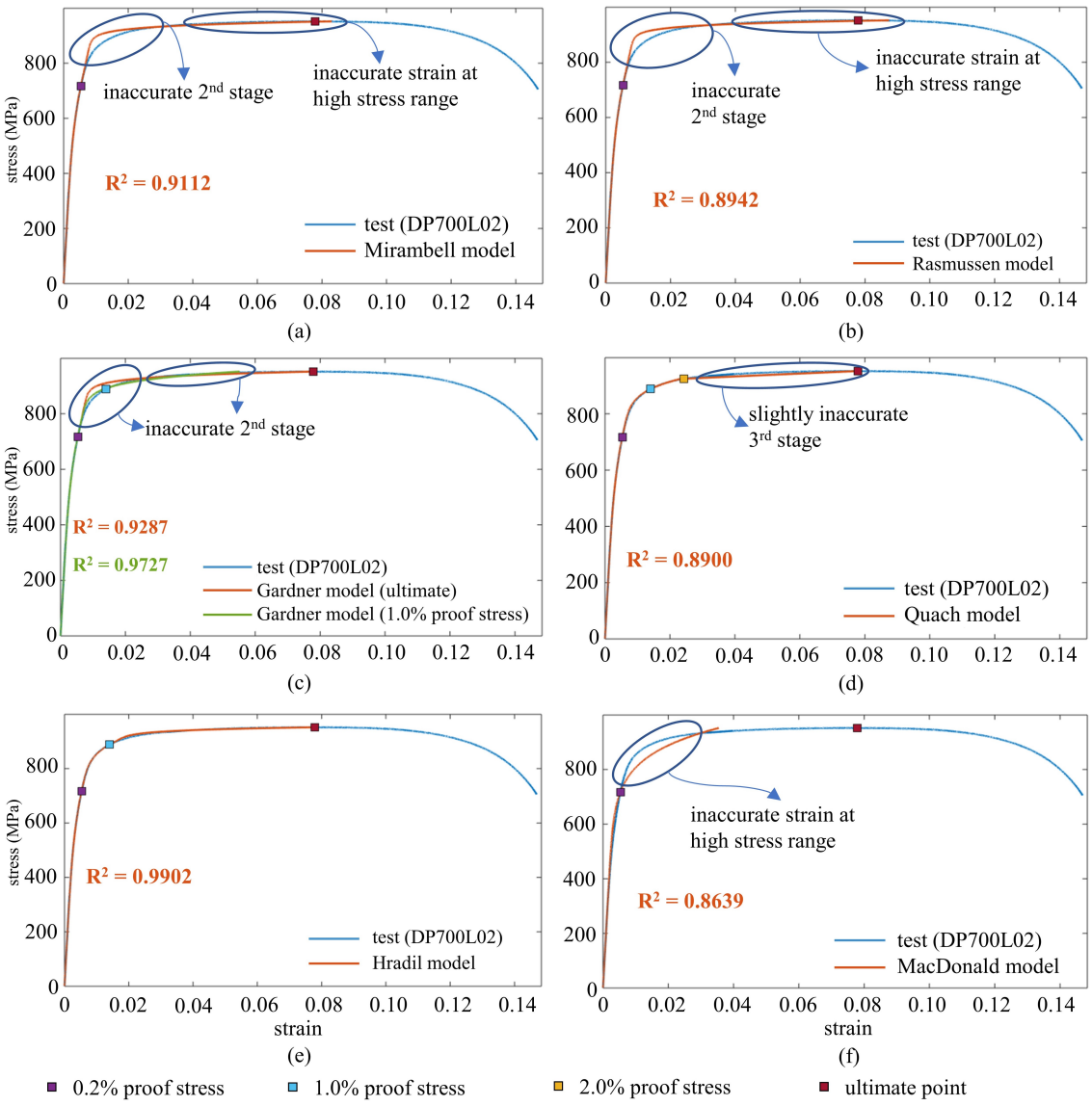

Figure 2.7: Examples of fit between AHSS σ-ε curves and existing models.

increases, however, an increased number of extra parameters are also required (at least two extra parameters for each extra stage).

MacDonald's one-stage model with variable exponential coefficients [22] (Fig. 2.7(f)) provides an excellent fit up to $\sigma_{0.2}$, while the fit is less accurate for the higher stress range. More importantly, the model is particularly sensitive to the three parameters i, j, and K, and no accurate predictive equations are available for these parameters. Therefore, the model is only applicable when the full experimental stress-strain data is available.

2.4.2 Updated stress-strain model

Based on the discussion above, the existing models might not be able to provide an accurate fit for the AHSS stress-strain database, particularly for DP and HSLA steels. Although the existing models can accurately fit the AHSS test stress-strain curves up to around 0.2% proof stress for most cases, different levels of inaccuracies are commonly observed thereafter. Although the post-yield inaccuracies might not result in significant differences for many structural design and analysis cases, some other important scenarios can be sensitive to these inaccuracies. These scenarios include numerical simulations of steel forming, blast crushing, collapse, etc., where the relationship between local strain and engineering strain is crucial [28]. Therefore, a new model describing the stress-strain behavior of AHSS as shown in Fig. 2.8 is proposed. The proposed model is updated from Gardner's two-stage model (Eq. 2.2 and Eq. 2.7), which passes through the origin, 0.2% proof stress, and ends at the ultimate point. The expressions for the first stage and the second stage of the

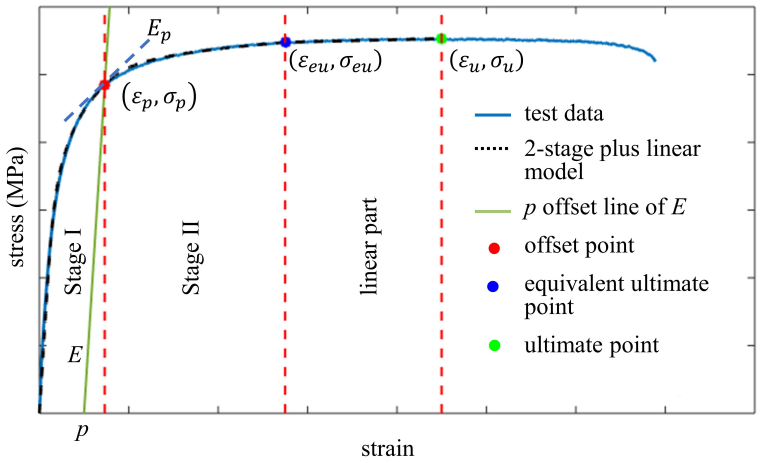

Figure 2.8: Schematic diagram for the proposed two-stage plus linear model.

proposed stress-strain model are shown in Eq. 2.28:

$$\varepsilon = \begin{cases} \frac{\sigma}{E} + p\left(\frac{\sigma}{\sigma_p}\right)^n & \text{for } 0 \leqslant \sigma \leqslant \sigma_p \\ \frac{\sigma-\sigma_p}{E_p} + \left(\varepsilon_{eu} - \varepsilon_p - \frac{\sigma_{eu}-\sigma_p}{E_p}\right)\left(\frac{\sigma-\sigma_p}{\sigma_{eu}-\sigma_p}\right)^m + \varepsilon_p & \text{for } \sigma_p < \sigma \leqslant \sigma_{eu} \end{cases} \tag{2.28}$$

where ε_p and σ_p are the strain and stress of p offset (with a plastic strain of p); E_p is the tangent modulus at σ_p as calculated by Eq. 2.29; ε_{eu} and σ_{eu} are the strain and stress of the equivalent ultimate point.

$$\frac{1}{E_p} = \frac{\partial \varepsilon(\sigma)}{\partial \sigma}|_{\sigma=\sigma_p} = \frac{1 + pn\frac{\sigma^{n-1}}{\sigma_p^n}E}{E}|_{\sigma=\sigma_p} = \frac{1 + pn\frac{E}{\sigma_p}}{E} \Rightarrow E_p = \frac{E}{1 + pn\frac{E}{\sigma_p}} \tag{2.29}$$

Two major updates are made for the newly proposed model. The first update is to change the demarcation point (referred to as *offset point* hereinafter) between the

first and the second stage from 0.2% proof stress to a reassigned proof stress p. The second update is to change the end of the second stage from the ultimate point to *the equivalent ultimate point*.

The equivalent ultimate point is defined as the point with stress equals to 99% of the ultimate strength at the strain hardening stage. The first stage of the proposed model is adopted from the origin to the offset point and the second stage is adopted from the offset point to the equivalent ultimate point. The σ-ε relationship from the equivalent ultimate point to the ultimate point is described as a line.

For the first update, from the discussion in Section 2.4.1, the existing two-stage models are not able to provide an accurate fit at the beginning of the second stage. The inaccuracy is caused by the inaccurate calculation of tangent modulus $E_{0.2}$ at $\sigma_{0.2}$, and $E_{0.2}$ is required in the second-stage expression (e.g. Eq. 2.7). $E_{0.2}$ is calculated by using the first stage expression (Eq. 2.2) because the second stage equation (Eq. 2.7) is unknown before the determination of $E_{0.2}$. This compromise is only accurate when the transition between the first and the second stage is smooth. From the experimental σ-ε relationship (e.g. Fig. 2.5), DP and HSLA steels curves are highly non-linear when the plastic strain is smaller than 0.005; MS steels curves are largely non-linear when the plastic strain is smaller than 0.002, while the nonlinearity tends to be small and stable when the plastic strain approaches 0.005. Therefore, to provide an accurate tangent modulus at the offset point, a larger plastic strain p is needed, particularly for the DP and HSLA steels. The proof stress offset p from 0.002 to 0.020 at an increment of 0.001 were iterated for each experimental σ-ε curve to find the optimal fit with the optimal p by using the error minimization

method. From the result shown in Fig. 2.9, it is found that the optimal p for DP and HSLA steels is larger than 0.005, while for MS steels it is less than 0.005. In addition, for each experimental σ-ε curve, the optimal p has a positive correlation with increasing $\sigma_u/\sigma_{0.2}$. A predictive equation is proposed for the optimal p as shown in Eq. 2.30 (the black dashed line in Fig. 2.9), so that p can be predicted for AHSS of different grades when $\sigma_u/\sigma_{0.2}$ is known.

$$p = \frac{4}{150}\left(\frac{\sigma_u}{\sigma_{0.2}} - 1\right) \tag{2.30}$$

While the data presented in Fig. 2.9 shows a clear trend between the optimal proof stress offset p and the $\sigma_u/\sigma_{0.2}$ ratio, there is a visible scatter in the data. For each steel, a total of five to nine coupons were tested. Due to inherent variability in the samples, the optimal p found using error minimization might not be the only feasible value of the proof stress offset. Therefore, a range of p values within the scatter for each material was considered and tested for fit accuracy by determining the R^2 for all specimens. The range of p values for each material that fit all specimens with an R^2 greater or equal to 0.995 was determined and is shown as the error bars in Fig. 2.9. The recommended values of the proof stress offset p for each material were chosen to reflect the trend of decreasing proof stress offset with increasing nominal strength from the range of applicable offset values and are given in Table 2.4.

The second update is inspired by the characteristic of the AHSS σ-ε curve. Compared with other steels with rounded σ-ε curve, AHSS σ-ε curves have a long strain hardening process with almost no stress increase before the ultimate point.

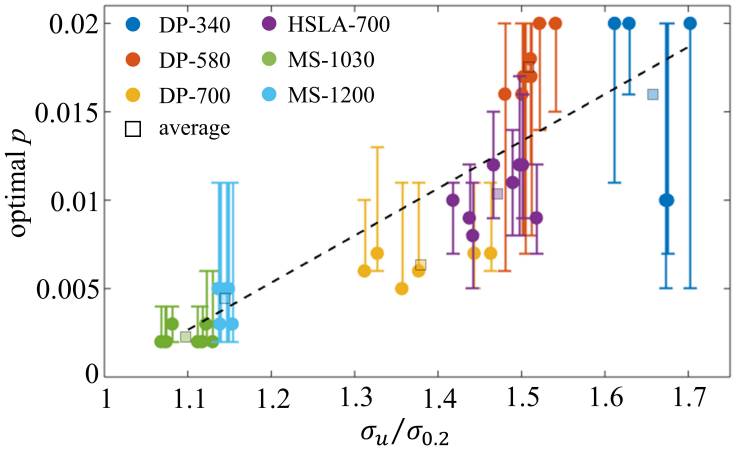

Figure 2.9: The relationship between $\sigma_u/\sigma_{0.2}$ and the optimal p.

For example, from σ_{eu} to σ_u, the average strain increases are 46% for DP-340, 70% for DP-580, 91% for DP-700, 54% for HSLA-700, 68% for MS-1030, and 47% for MS-1200. For existing two-stage models as discussed in Section 2.2, the slope change rate for the second stage model is determined by the second derivative of the σ-ε relationship as shown in Eq. 2.31, where all parameters are material properties except for m.

$$\frac{\partial^2 \varepsilon(\sigma)}{\partial \sigma^2} = \frac{(\varepsilon_u - \varepsilon_{0.2} - \frac{\sigma_u - \sigma_{0.2}}{E_{0.2}})m(m-1)}{(\sigma_u - \sigma_{0.2})^m}(\sigma - \sigma_{0.2})^{m-2} \tag{2.31}$$

From the discussion on Fig. 2.1, for test curves with a long horizontal tail portion before the ultimate point (e.g. case $n = 1000$), m will be dramatically increased for Fig. 2.1 to fit this tail. As a result, the increment of m will lower the model strain output and thus sacrifice the model fit accuracy at the beginning of the second stage. Therefore, to further improve the model accuracy, the long strain hardening tail portion with minimal stress increase before the ultimate point is excluded from

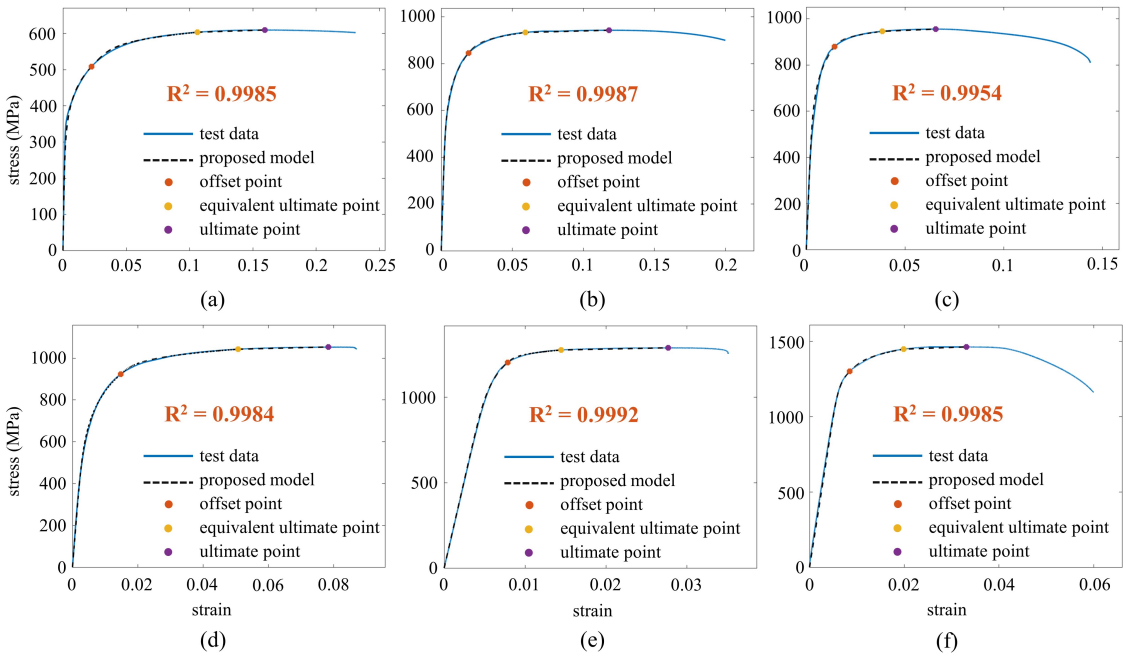

Figure 2.10: Representative examples of the optimal fit with the experimental σ-ε curves using the proposed two-stage plus linear model for (a) DP-340; (b) DP-580; (c) DP-700; (d) HSLA-700; (e) MS-1030; (f) MS-1200.

the second stage model. The long horizontal tail portion is modeled with adequate accuracy and simplicity as a linear relationship between the equivalent ultimate point and the ultimate point.

Representative examples of the optimal fit with test data using the proposed two-stage plus linear model for each steel are shown in Fig. 2.10. A summary of the average values of strain and stress at the offset point and the equivalent ultimate point as well as n and m determining the optimal fit for each material is shown in Table 2.4.

Table 2.4: Offset point, equivalent ultimate point and exponential coefficients for AHSS and HSLA steel.

sheet	DP-340	DP-580	DP-700	HSLA-700	MS-1030	MS-1200
p (%)	2.0	1.5	1.0	1.0	0.2	0.2
ε_p (%)	2.2	1.9	1.4	1.5	0.8	0.8
σ_p (MPa)	493.6	853.7	882.4	914.7	1202.6	1307.0
σ_u/σ_p	1.2	1.1	1.1	1.1	1.1	1.1
ε_{eu} (%)	9.4	6.3	3.5	4.6	1.5	2.2
σ_{eu} (MPa)	589.9	946.9	937.4	1010.2	1305.4	1480.5
n	6.2	7.0	7.6	6.2	8.7	15.0
m	4.2	3.2	2.6	3.2	3.2	3.2

2.5 Predictive equations for model parameters

The σ-ε relationship for the updated model requires seven material property parameters (E, σ_p, ε_p, σ_{eu}, ε_{eu}, σ_u, and ε_u) and two non-property parameters (n and m). By definition, ε_p and σ_{eu} can be calculated by expressions $\varepsilon_p = \sigma_p/E + p$ and $\sigma_{eu} = 0.99\sigma_u$. Therefore, seven parameters are needed to build the proposed model. Some of the required parameters are not always provided in design code or from a steel manufacturer, and some are not always available from experiments in some cases. To enable the usability of the proposed model for these cases, the recommendations for these key parameters are provided.

2.5.1 Predictive equations for model parameters from literature

Among the unknown parameters, some are commonly required by existing stress-strain models, which include elastic modulus, ultimate strength, and ultimate strain. Therefore, predictive equations of these parameters were used to fit the test results of AHSS and HSLA steel. Gardner and Yun [25] adopted the Mirambell and Real

model [13] and developed predictive equations and numerical values for required model parameters after conducting a statistical study on the CFS database. Fig. 2.11 shows two examples of different situations (cases 1, 2, and 3 from [25]) for the Mirambell and Real model [13] built by parameters from test results and the predictive equations developed in [25]. The first example on conventional CFS, shown in Fig 2.11(a), is from a tensile test on 3.0 mm thick G450 specimen [29]. When using all parameters from the test (case 1), the 2-stage model [13] can provide an accurate fit with the experimental curve. When using E, $\sigma_{0.2}$, and σ_u from the test, while using the rest parameters predicted by the proposed equations (case 2) to build the 2-stage model, the fit is generally accurate except at the high-stress range approaching σ_u. When only $\sigma_{0.2}$ is available from the test and all other required parameters are calculated by the proposed equations (case 3) to build the 2-stage model, the model fit is inaccurate after passing through $\sigma_{0.2}$. The second example (Fig 2.11(b)) shows an experimental σ-ε curve from the AHSS database (DP580-L01). For case 1, as discussed in Section 2.4.1, the 2-stage model built by parameters from the test can fit well for the first stage, while the beginning of the second stage is not accurately fitted. For case 2 and case 3, the first stage is well fitted, while the fit for the second stage is inaccurate. Similar to this example, the situations of different cases for DP-340, DP-580, DP-700, and HSLA-700 are similar. For MS steels, although the fits for case 2 and case 3 are still not accurate, the inaccuracy is slightly smaller than that of DP or HSLA steel.

From Gardner and Yun's paper [25], the fit range for exponential coefficients n and m are different from the range of the proposed model. For the conventional

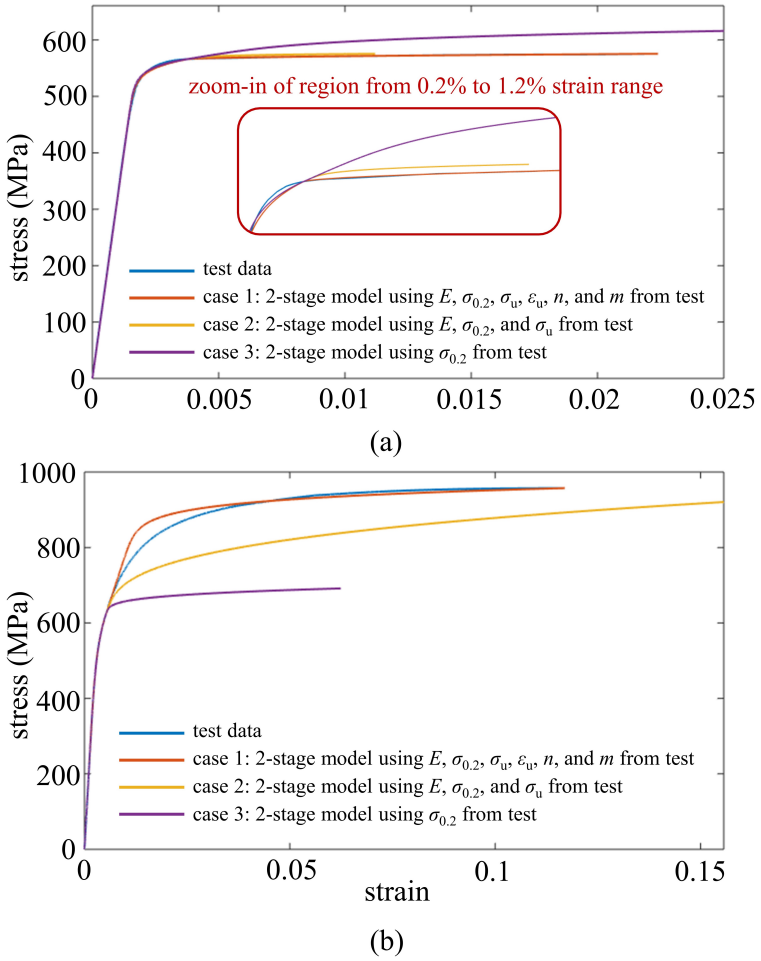

Figure 2.11: Examples of comparisons between stress-strain model [13] constructed by parameters from test and predicted parameters [25] for (a) conventional CFS (G450 steel from [29]) and (b) AHSS (DP-580L01).

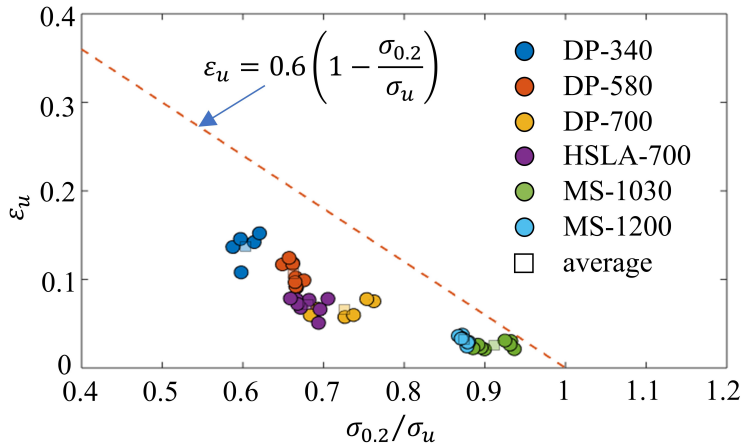

Figure 2.12: Comparison of ε_u between prediction [25] and AHSS test data.

2-stage model, n determines the curvature from the origin to $\sigma_{0.2}$, and m determines the curvature from $\sigma_{0.2}$ to σ_u. For the proposed 2-stage plus linear model, n determines the curvature from the origin to σ_p, and m determines the curvature from σ_p to σ_{eu}. Therefore, the predictive equations for n and m of existing two-stage models are not applicable for n and m of the proposed model. The average E of the tested AHSS sheets, as discussed in Section 2.3.3, is 208.0 GPa with a coefficient of variance of 0.065. Gardner and Yun's paper [25] and the AISI-S100 standard for cold-formed steel [30] recommends 203 GPa for E, which is only 2% lower than the test results. Therefore, $E = 203$ GPa is recommended for AHSS in this paper when the test result is unavailable. A linear relationship between ε_u and $\sigma_{0.2}/\sigma_u$ is proposed for both hot-rolled steel and CFS sheets, and its fit with AHSS results is shown in Fig. 2.12 [25]. From the figure, the predicted ε_u is 34% to 261% higher than the results from the tests.

For σ_u, the relationship between $\sigma_u/\sigma_{0.2}$ and $\sigma_{0.2}$ with three different expressions

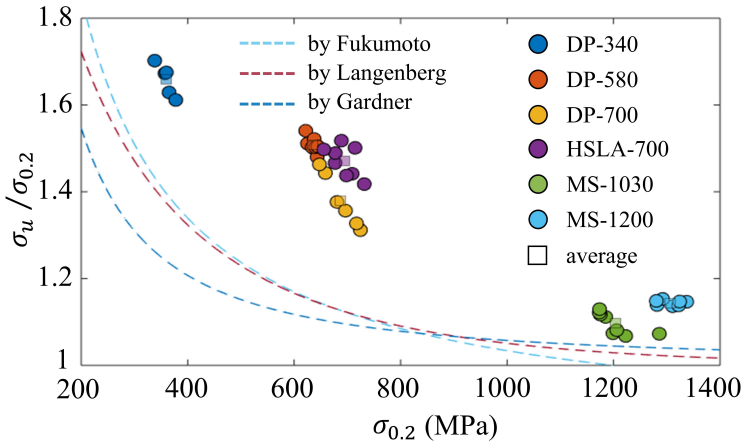

Figure 2.13: Comparison of $\sigma_u/\sigma_{0.2}$ between prediction ([25] [31] [32]) and AHSS test data.

proposed by Fukumoto [31] (Eq. 2.32), Langenberg [32] (Eq. 2.33), and Gardner [25] (Eq. 2.34) were compared.

$$\sigma_u/\sigma_{0.2} = 0.83 + 203.8/\sigma_{0.2} \tag{2.32}$$

$$\sigma_u/\sigma_{0.2} = [1 - 0.72e^{-0.0027\sigma_{0.2}}]^{-1} \tag{2.33}$$

$$\sigma_u/\sigma_{0.2} = 1 + (130/\sigma_{0.2})^{1.4} \tag{2.34}$$

The fit with AHSS and HSLA steel curves is shown in Fig. 2.13. It was found the predicted $\sigma_u/\sigma_{0.2}$ is largely conservative compared with tests results. Predicted σ_u can be calculated by the product of $\sigma_u/\sigma_{0.2}$ and $\sigma_{0.2}$. The ultimate strength σ_u calculated by Eq. 2.32 and Eq. 2.33 is up to 26% less than the test results, while 28% less when using Eq. 2.34.

From the discussion above, the predictive equations from literature might not able to reasonably predict ε_u and σ_u of the AHSS database. Therefore, predictive equations for key parameters, excluding E, required by the proposed two-stage plus linear model need to be provided.

2.5.2 Expressions for material-property parameters

The predictive equations for material-property parameters required by the proposed two-stage plus linear model are provided based on a known 0.2% proof stress $\sigma_{0.2}$, which is typically available from a low strain level test or directly provided by the steel manufacturer. The relationship between σ_p and $\sigma_{0.2}$ is plotted in Fig. 2.14. Test data for different steels are plotted as circles with different colors; additionally, the average of each steel is plotted as a square with the corresponding color. The plot suggests a strong linear relationship between σ_p and $\sigma_{0.2}$ and therefore a linear expression in MPa as shown in Eq. 2.35 is fitted to describe the relationship.

$$\sigma_p = \begin{cases} 1.23 \times \sigma_{0.2} + 60 & \text{for DP and HSLA} \\ \sigma_{0.2} & \text{for MS} \end{cases} \tag{2.35}$$

Two trendlines with $\pm 5\%$ variance are added to the plot and most of the test data is between the trendlines, which indicates a good accuracy of the expression. The maximum error between the predictive σ_p by Eq. 2.35 and the test data is 6.1%. It is recommended to use $p = 0.002$ for MS steels, therefore $\sigma_p = \sigma_{0.2}$.

The relationship between σ_u and σ_p extracted from test data is plotted in Fig. 2.15. The plot indicates a strong linear relationship between the two parameters

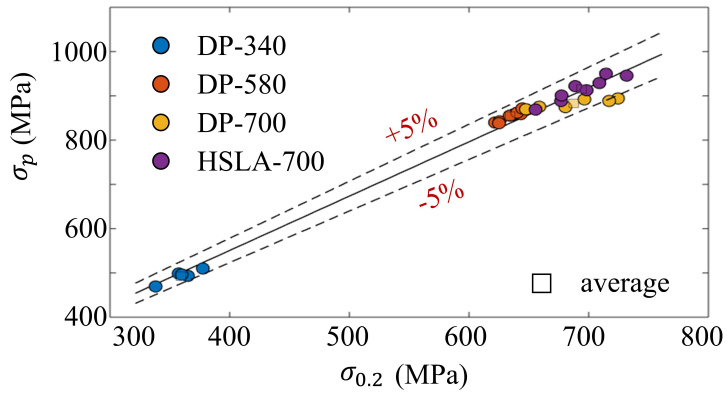

Figure 2.14: Predictive expression for selected proof stress σ_p for AHSS when measured 0.2% proof stress $\sigma_{0.2}$ is available.

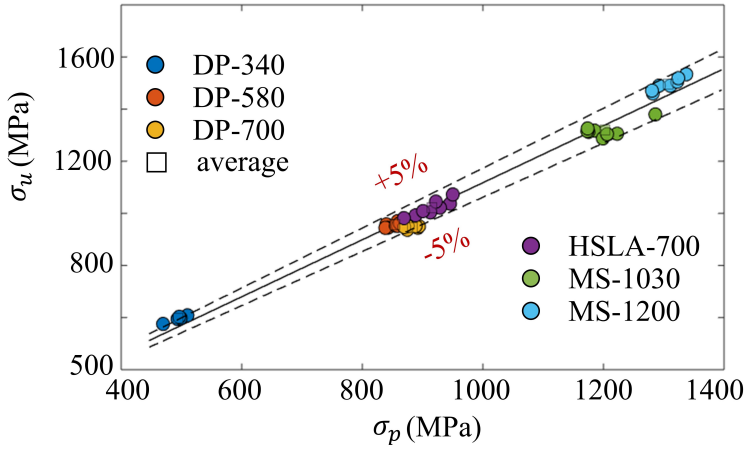

Figure 2.15: Predictive expression for ultimate strength σ_u.

and a linear expression in MPa is fitted to the test data as shown in Eq. 2.36.

$$\sigma_u = 1.09 \times \sigma_p + 24 \tag{2.36}$$

Most test data is within the two trendlines with ±5% variance for Eq. 2.36. For the case that σ_p is not available directly, σ_p is calculated by Eq. 2.35 firstly and then σ_u is calculated by Eq. 2.36. In this case, the difference of σ_u between the predicted

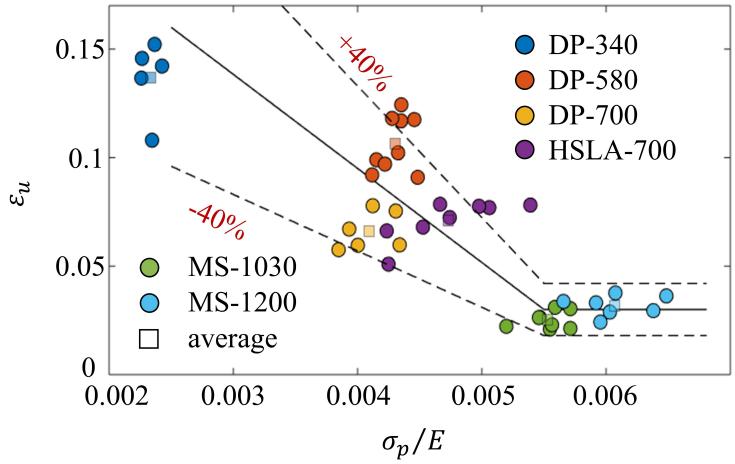

Figure 2.16: Predictive expression for ultimate strain ε_u.

value and experimental data is less than 5% except for DP-700; the difference for DP-700 is less than 10%.

The relationship between ε_u and σ_p/E is plotted in Fig. 2.16. As discussed in Section 2.3.3 and Section 2.4, even for the same type of steel with same cutting direction, ε_u may vary significantly because of the stress plateau near the ultimate point. Therefore, the relationship between ε_u and σ_p/E is not as clear as the two aforementioned stress expressions, while still sufficiently visible. For the four sheets of steel with nominal yield strength less than 1000 MPa, the ultimate strain decreases when σ_p/E increases; for MS-1030 and MS-1200, the ultimate strain is generally stable. Therefore, a two-part predictive expression as shown in Eq. 2.37 is fitted to the data.

$$\varepsilon_u = \begin{cases} -\frac{130}{3} \times \frac{\sigma_p}{E} + \frac{161}{600} & \text{for DP and HSLA} \\ 0.03 & \text{for MS} \end{cases} \tag{2.37}$$

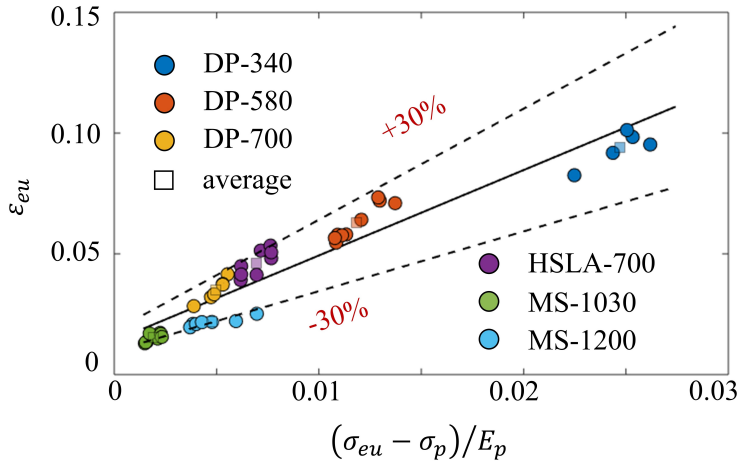

Figure 2.17: Predictive expression for strain of the equivalent ultimate point ε_{eu}.

To include the relatively large variance of the ultimate strain, two trendlines with $\pm$ 40% variance are plotted and most test data is between these two trendlines. This large difference tolerance is also commonly used for the predictive expression for ultimate strain of stainless steel [14] and conventional CFS [25] [33]. The difference between the predictive expression and the average of the test data is less than 20%.

The relationship between ε_{eu} and $(\sigma_{eu} - \sigma_p)/E_p$ is plotted in Fig. 2.17. E_p is the tangent modulus at σ_p and it is calculated by Eq. 2.29. A linear relationship is found and the line of best fit is closely approximated by Eq. 2.38.

$$\varepsilon_{eu} = 3.54 \times \frac{\sigma_{eu} - \sigma_p}{E_p} + 0.014 \tag{2.38}$$

Two trendlines with $\pm$ 30% variance with Eq. 2.38 are added to the plot in Fig. 2.17 and most of the test data lies between the trendlines. Similar to the case of ultimate strain, the difference between the predictive expression and the corresponding average value of strains of equivalent ultimate points from the

experiment for each steel is less than 20%.

2.5.3 Recommendation for exponential coefficients n and m

As discussed in Section 2.2 (Fig. 2.1), the non-material property exponential coefficients n and m determine the degree of curvature for the first and second stage of the model, respectively, as described by Eq. 2.28. The values for n and m shown in Table 2.4 are determined by error minimization. A summary of n for each test is shown in Fig. 2.18. Based on the observation of σ-ε curves for different types of steels (e.g. Fig. 2.5), the degree of curvature for the first stage, n, generally increases when the yield strength of steel increases. For example, the curve transition from the end of the linear elastic region to the selected offset point for DP-340 is relatively gradual, while for the two MS sheets of steel is relatively sharp. This observation is supported by the error minimization fitting of n shown in Fig. 2.18 which indicates an overall trend that n increases as the steel strength increases. Due to the obvious scatter in the plot, instead of a continuous expression, a tabular recommendation of n for each steel is proposed as shown by the black solid squares in Fig. 2.18 as the average approximation of the test data.

Similarly, m depicts the degree of the curvature for the second stage of the model from σ_p to σ_{eu}. Therefore, a relationship exists between m and σ_p/σ_u as plotted in Fig. 2.19. A linear relationship is observed and a linear expression given in Eq. 2.39 is fitted to the test data.

$$m = -12.55 \times \frac{\sigma_p}{\sigma_u} + 14.43 \tag{2.39}$$

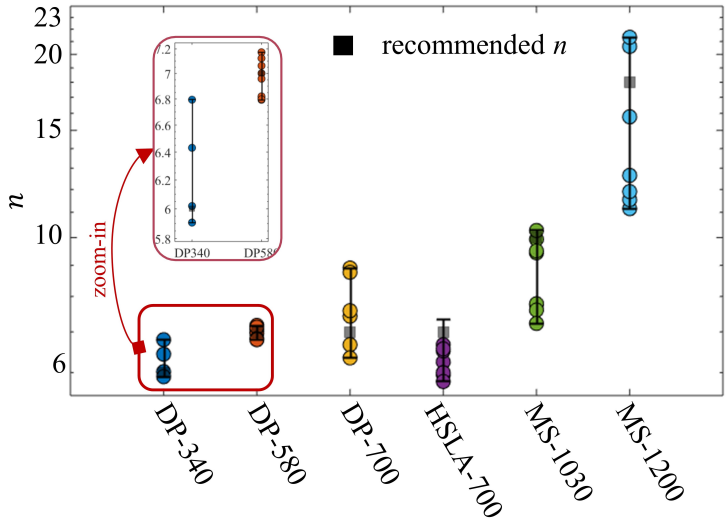

Figure 2.18: Recommendation for first stage exponential coefficient n based on statistics study of experiment results.

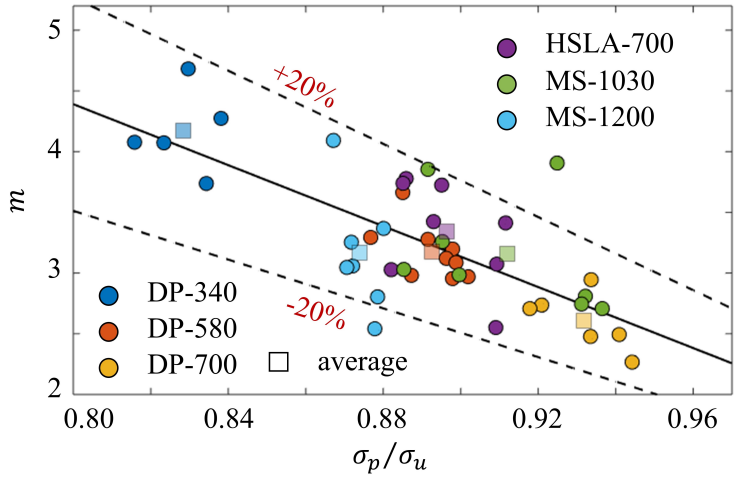

Figure 2.19: Predictive equation for second stage exponential coefficient m.

Most m data is within $\pm$ 20% variance trendlines of Eq. 2.39; while the difference between Eq. 2.39 and the average of the test data given in Table 2.4 is less than 10%.

2.6 Yield strength determination

In conventional CFS numerical modeling, the 0.2% proof stress $\sigma_{0.2}$ is widely considered as yield strength and used as the offset point for existing stress-strain models as described in Section 2.2. From the discussion in Section 2.4, using $\sigma_{0.2}$ as the offset point is not able to accurately fit the AHSS experimental stress-strain database. Instead, using the recommended p proof stress as the offset point is proposed for its excellent fit with the database. Additionally, as shown in Table 2.4, the ratio between σ_u and σ_p is 1.1 for almost all AHSS and HSLA steel; the only exception is DP-340 where its ratio is 1.2. The value of this ratio is close to the ratio of $\sigma_u/\sigma_{0.2}$ for most conventional CFS [25]. Therefore, the applicability of using the recommended p proof stress to represent the yield strength is investigated.

In this section, the energy method was used to verify the rationality of defining the yield strength using the recommended p proof stress. The area under the load-displacement curve from the origin to the fracture point is the dissipated energy during the whole loading process. From the definition of engineering strain and engineering stress, the area under the engineering σ-ε curve is proportional to the dissipated energy, hence it will be called equivalent energy dissipation. If the areas under any two σ-ε curves are equal, the energy dissipations of these two loading processes are equal. The equivalent energy dissipation for each experimental σ-ε curve was calculated by the area under the curve. The equivalent energy dissipation for conventional steel stress-strain models was set equal to that of the experiment, and then the corresponding yield strength σ_y for these models was calculated. The calculated yield strength of each conventional model was compared with

the conventional 0.2% proof stress $\sigma_{0.2}$ and recommended p proof stress σ_p from Table 2.4. Additionally, when adopting $\sigma_y = \sigma_p$ in the conventional models, the differences in the equivalent energy dissipation between conventional models and experimental σ-ε curves were discussed.

The area S_0 under the experimental σ-ε curve from the origin to the fracture point for each specimen is calculated by trapezoidal numerical integration. Two conventional steel stress-strain models, the elastic perfect plastic model (referred to as EPP model hereinafter) and the artificial elastic-plastic model with strain hardening and softening (referred to as AEP model hereinafter) [34], are used in this section. Schematic diagrams of the EPP and AEP models are shown in Fig. 2.20. Most required parameters are determined from the experimental σ-ε curves, including elastic modulus E, ultimate strain ε_u, ultimate strength σ_u, fracture strain ε_f, and fracture stress σ_f. The yield strength σ_y and the yield strain ε_y of both the EPP and AEP models are the unknown material-property parameters to be determined.

The area S_1 under the EPP model is calculated by Eq. 2.40.

$$S_1 = \int_0^{\varepsilon_f} \sigma(\varepsilon) d\varepsilon = \frac{1}{2} \times \frac{\sigma_y}{E} \times \sigma_y + \sigma_y \times (\varepsilon_f - \frac{\sigma_y}{E}) = (\varepsilon_f - \frac{\sigma_y}{2E}) \times \sigma_y \tag{2.40}$$

By assuming an equal energy dissipation between the experimental curve and the EPP model, σ_y is calculated by solving $S_1 = S_0$ as shown in Eq. 2.41.

$$\sigma_y = E\varepsilon_f - \sqrt{(E\varepsilon_f)^2 - 2ES_0} \tag{2.41}$$

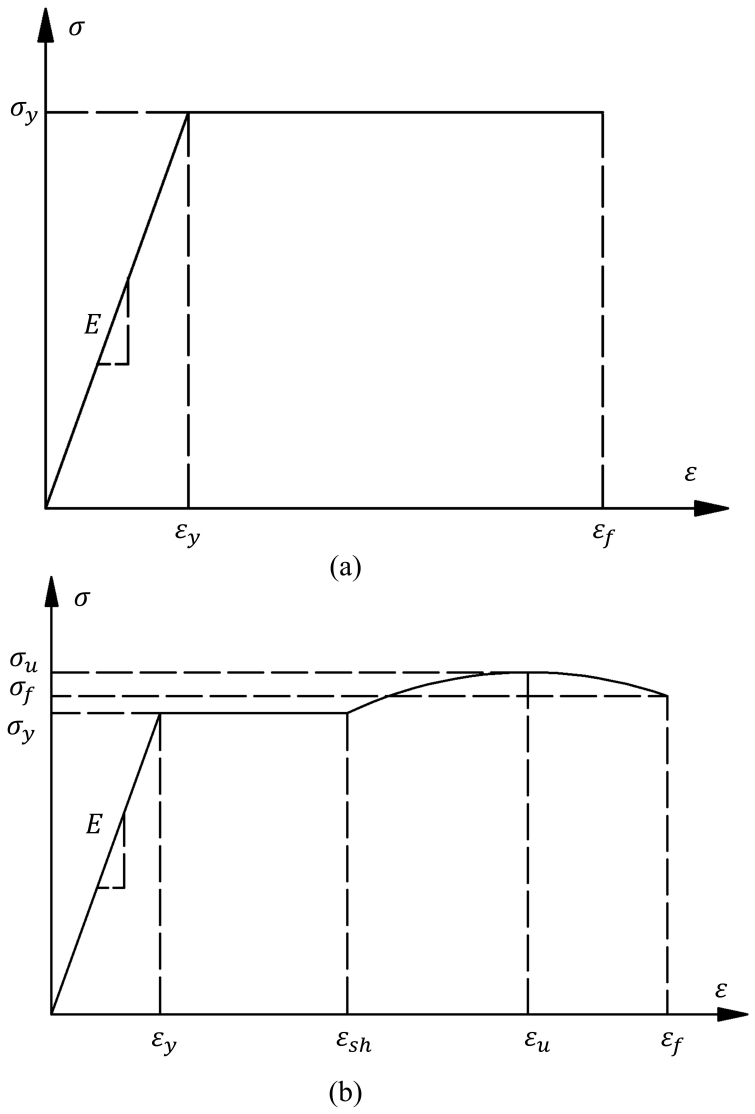

Figure 2.20: The schematic diagram for (a) the EPP model and (b) the AEP model.

The calculated σ_y is located on the experimental σ-ε curve, and its corresponding offset $p_{EPP} = \varepsilon_y - \sigma_y/E$ is calculated. The p_{EPP} values are averaged across each steel and are given in Table 2.5. The calculated p_{EPP} value is significantly larger than the traditional 0.2% and greater than the recommended offset p given in Table 2.4. The average percentage difference $\Delta\sigma_{0.2EEP}$ between the calculated σ_y and $\sigma_{0.2}$ from the test as well as the average percentage difference $\Delta\sigma_{pEEP}$ between the calculated σ_y and the recommended proof stress σ_p from the test as determined in Section 2.4.2 are calculated and shown in Table 2.5. Overall, σ_y from the EPP model is closer to σ_p than $\sigma_{0.2}$ for DP and HSLA steels, while $\sigma_{0.2}$ is adopted as σ_p for MS steels. This shows that the recommended offset proof stress σ_p determined in Section 2.4.2 is a better fit to represent the yield strength for the DP and HSLA steels than the traditional 0.2% proof stress.

For the AEP model, at the position where the yield plateau ends and the non-linear strain hardening starts, ε_{sh}, is not clearly defined quantitatively. In this paper, ε_{sh} was initially determined by the statistical result of $\lambda = \varepsilon_{sh}/\varepsilon_y$ for CFS specimens with a similar σ-ε curve shape as the AEP model from previous studies. From Rogers's report [35], three specimens, 060-G300-SCDR3, 060-G300-SCL2, and 060-G300-SCT3 are applicable and their λ values are 6.70, 6.98, and 9.40 respectively. From Abdel's paper [36], specimens A-9 and B-4 are applicable and their λ values are 3.68 and 7.40 respectively. From Huang's paper [10], specimens AF-R1 and GF-R1 are applicable and their λ values are 2.50 and 4.20 respectively. The average value of λ is 5.84. Based on this data, λ in the AEP model is initially assumed as 6, an approximation of this average.

No mathematical model is specified in the literature for the strain hardening and strain softening regions. In this study, a quadratic model $\sigma(\varepsilon) = a\varepsilon^2 + b\varepsilon + c$ for $\varepsilon_{sh} \leqslant \varepsilon \leqslant \varepsilon_f$ is used. The values of ε_u, σ_u, ε_f, and σ_f from the experimental σ-ε curves are used to build the AEP model, and σ_y is the only unknown parameter to be determined. The coefficients a, b, and c were solved by Eq. 2.42, Eq. 2.43, and Eq. 2.44 which are expressions of σ_y.

$$a = \frac{\varepsilon_{sh}(\sigma_f - \sigma_u) + \varepsilon_u(\sigma_y - \sigma_f) + \varepsilon_f(\sigma_u - \sigma_y)}{(\varepsilon_{sh} - \varepsilon_f)(\varepsilon_u - \varepsilon_{sh})(\varepsilon_f - \varepsilon_u)} \tag{2.42}$$

$$b = -\frac{\varepsilon_{sh}^2(\sigma_f - \sigma_u) + \varepsilon_u^2(\sigma_y - \sigma_f) + \varepsilon_f^2(\sigma_u - \sigma_y)}{(\varepsilon_{sh} - \varepsilon_f)(\varepsilon_u - \varepsilon_{sh})(\varepsilon_f - \varepsilon_u)} \tag{2.43}$$

$$c = -\frac{\varepsilon_{sh}\varepsilon_u\sigma_f(\varepsilon_u - \varepsilon_{sh}) + \varepsilon_{sh}\varepsilon_f\sigma_u(\varepsilon_{sh} - \varepsilon_f) + \varepsilon_u\varepsilon_f\sigma_y(\varepsilon_f - \varepsilon_u)}{(\varepsilon_{sh} - \varepsilon_f)(\varepsilon_u - \varepsilon_{sh})(\varepsilon_f - \varepsilon_u)} \tag{2.44}$$

Noticeably, by combining $\sigma_y = a\varepsilon_{sh}^2 + b\varepsilon_{sh} + c$, $\sigma_u = a\varepsilon_u^2 + b\varepsilon_u + c$, and $\sigma_f = a\varepsilon_f^2 + b\varepsilon_f + c$, three constraints are generated and they are sufficient to solve a, b, and c as a set of unique solutions. By definition, σ_u is the peak of the strain hardening process, and likewise should be the peak of the quadratic model. Therefore, the percentage difference between the peak of the quadratic model and the ultimate strength, δ_{peak}, is calculated, and if it is less than 1%, then the solution is considered valid. After the calculation of a, b, and c as expressions of σ_y, the area S_2 under the AEP model is calculated as an expression of σ_y as shown in Eq. 2.45.

$$S_2 = \int_0^{\varepsilon_f} \sigma(\varepsilon)d\varepsilon = (\lambda - \frac{1}{2})\frac{\sigma_y^2}{E} + \int_{\varepsilon_{sh}}^{\varepsilon_f} a\varepsilon^2 + b\varepsilon + c\,d\varepsilon \tag{2.45}$$

The yield strength σ_y is then calculated by solving $S_0 = S_2$ using the generalized reduced gradient nonlinear algorithm in Excel Solver and δ_{peak} is then checked if it is within the 1% tolerance. Applying the initial λ for DP-340 and DP-580 gives very small δ_{peak}. For DP-700, HSLA-700, MS-1030, and MS-1200, δ_{peak} is larger than 10%. The major cause is, for these cases, a is significantly larger than that of DP-340 and DP-580. The references ([10] [35] [36]) used to calculate the initial λ only covered conventional grade steels, instead of high-strength steels. Good fits were achieved by varying λ and it was determined to use $\lambda = 6$ for DP-340 and DP-580, $\lambda = 4$ for DP-700 and HSLA-700, and $\lambda = 2$ for MS-1030 and MS-1200. The adjusted λ for each steel is inversely correlated to its nominal yield strength.

By using the adjusted λ for the AEP model, σ_y is calculated and then located on the experimental σ-ε curve, and its corresponding offset $p_{AEP} = \varepsilon_y - \sigma_y/E$ is calculated. The p_{AEP} values are averaged across each steel and are shown in Table 2.5. For DP and HSLA steels, p_{AEP} is significantly larger than 0.2%, while it is close to the recommended p given in Table 2.4, and for MS steels, p_{AEP} is slightly larger than the recommended 0.2%. The average percentage difference $\Delta\sigma_{0.2AEP}$ between the calculated σ_y and $\sigma_{0.2}$ as well as the average percentage difference $\Delta\sigma_{pAEP}$ between the calculated σ_y and σ_p (from Table 2.4) are calculated and shown in Table 2.5. The large differences between the σ_y and $\sigma_{0.2}$ indicate the irrationality of using $\sigma_{0.2}$ as yield strength for DP and HSLA steels, while the small difference between σ_y and σ_p shows the potential of using σ_p as the yield strength for AHSS.

Table 2.5: Comparison among AHSS test curves, EPP model, and AEP model.

steel	DP-340	DP-580	DP-700	HSLA-700	MS-1030	MS-1200
p_{EPP} (%)	4.8	3.3	1.5	1.9	0.5	0.8
$\Delta\sigma_{0.2EPP}$ (%)	-35.8	-30.9	-24.4	-28.4	-5.0	-9.0
$\Delta\sigma_{pEPP}$ (%)	-11.9	-7.0	-2.9	-5.7	-5.0	-9.0
ΔS_{EPP} (%)	-11.8	-6.9	-2.9	-5.5	-4.5	-8.4
p_{AEP} (%)	1.8	1.5	1.3	0.8	0.2	0.6
$\Delta\sigma_{0.2AEP}$ (%)	-23.0	-25.9	-26.4	-22.0	-1.0	-3.7
$\Delta\sigma_{pAEP}$ (%)	2.5	-0.2	-2.9	2.7	-1.0	-3.7
ΔS_{AEP} (%)	1.5	-0.0	-1.6	0.9	-0.5	-1.2
λ	6	6	4	4	2	2

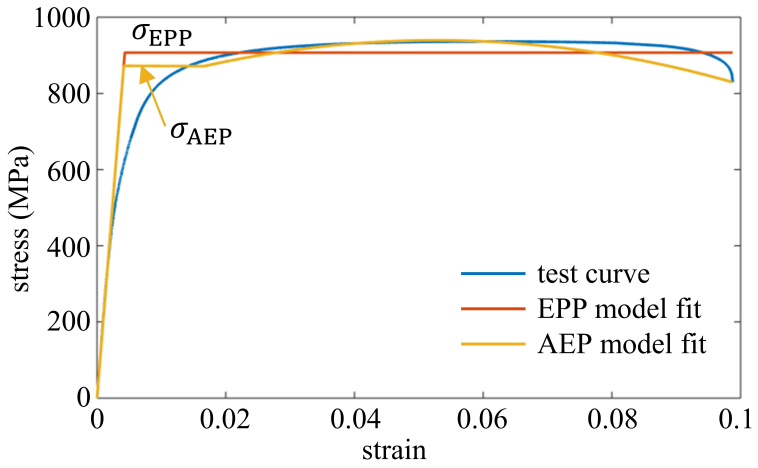

Figure 2.21: EPP and AEP model based on test curve (DP-700D01).

An example of EPP and AEP models determined from an experimental σ-ε curve (DP-700D01) is shown in Fig. 2.21.

In addition, the percentage difference of energy dissipation ΔS_{EPP} between the experimental σ-ε curve and the EPP model when adopting $\sigma_y = \sigma_p$ is calculated and the averages are shown in Table 2.5. It is found that the energy dissipation of the EPP model is smaller than the actual experiment for all steels, and ranges from -1.0% to -13.3%. Similarly, the percentage difference of energy dissipation ΔS_{AEP}

between the experiments and the AEP model when adopting $\sigma_y = \sigma_p$ is calculated, and the averages are shown in Table 2.5. The average difference for each steel is less than 2%, which supports using σ_p as the yield strength in the AEP model. As expected, the AEP model gives a better fit to the data than the EPP model, but both models illustrate the necessity for using the recommended offset as given in Table 2.4 to represent the yield strength in conventional material models.

2.7 Conclusions

Advanced high-strength steels have different material properties compared with conventional steels. A series of tensile coupon tests on DP, HSLA, and MS steels with nominal yield strength from 340 MPa to 1200 MPa were carried out. Essential material properties including elastic modulus, 0.2% proof stress, ultimate strength, and fracture elongation were determined. Coupons were cut from different directions along the sheet rolling direction and no obvious difference in material properties due to cutting directions was observed. Existing stress-strain models for conventional CFS and stainless steels were discussed but they were not found to provide an accurate fit with the AHSS database, especially around the yield region. An updated two-stage plus linear stress-strain model was therefore developed based on the Ramberg-Osgood model. Excellent fits were achieved between the proposed model and the AHSS database. For the required parameters of the proposed model, a series of predictive equations were proposed to model the general stress-strain relationships of AHSS. A discussion on the determination of yield strength was

carried out by comparing the energy dissipation between experimental stress-strain curves and conventional stress-strain models, including the EPP model and the AEP model. The calculated yield strength of the conventional models showed poor fit with conventional 0.2% proof stress for DP and HSLA steels, but excellent consistency when the yield strength was represented by a novel recommended proof stress in the proposed stress-strain model. The stress-strain model and predictive equations presented herein could be utilized to model the constitutive relationship of AHSS in future work including analytical simulations.

Addendum

This section presents some information as supplements of the published journal article (the main body from Abstract to Conclusion for this chapter).

The setup of the loading system is shown in Fig. 2.22 and a close shot of the extensometer and the specimen is shown in Fig. 2.23.

The length of the reduced parallel section as shown in Fig. 2.2 for the tensile coupon is 82.55 mm (3.25 inch), which meets the requirement of [9]. The gauge length of the extensometer is 25.4 mm (1 inch).

The relationship between $\sigma_{0.2}/\sigma_u$ and ε_u for AHSS and HSLA steel is shown in Fig. 2.12. Comparing with the prediction equation [25] derived from a statistical study on conventional CFS, the AHSS and HSLA steel data is substantially deflected. To fit the experimental data in this study using the same form of equation, an update equation and its fit is shown in Fig. 2.24.

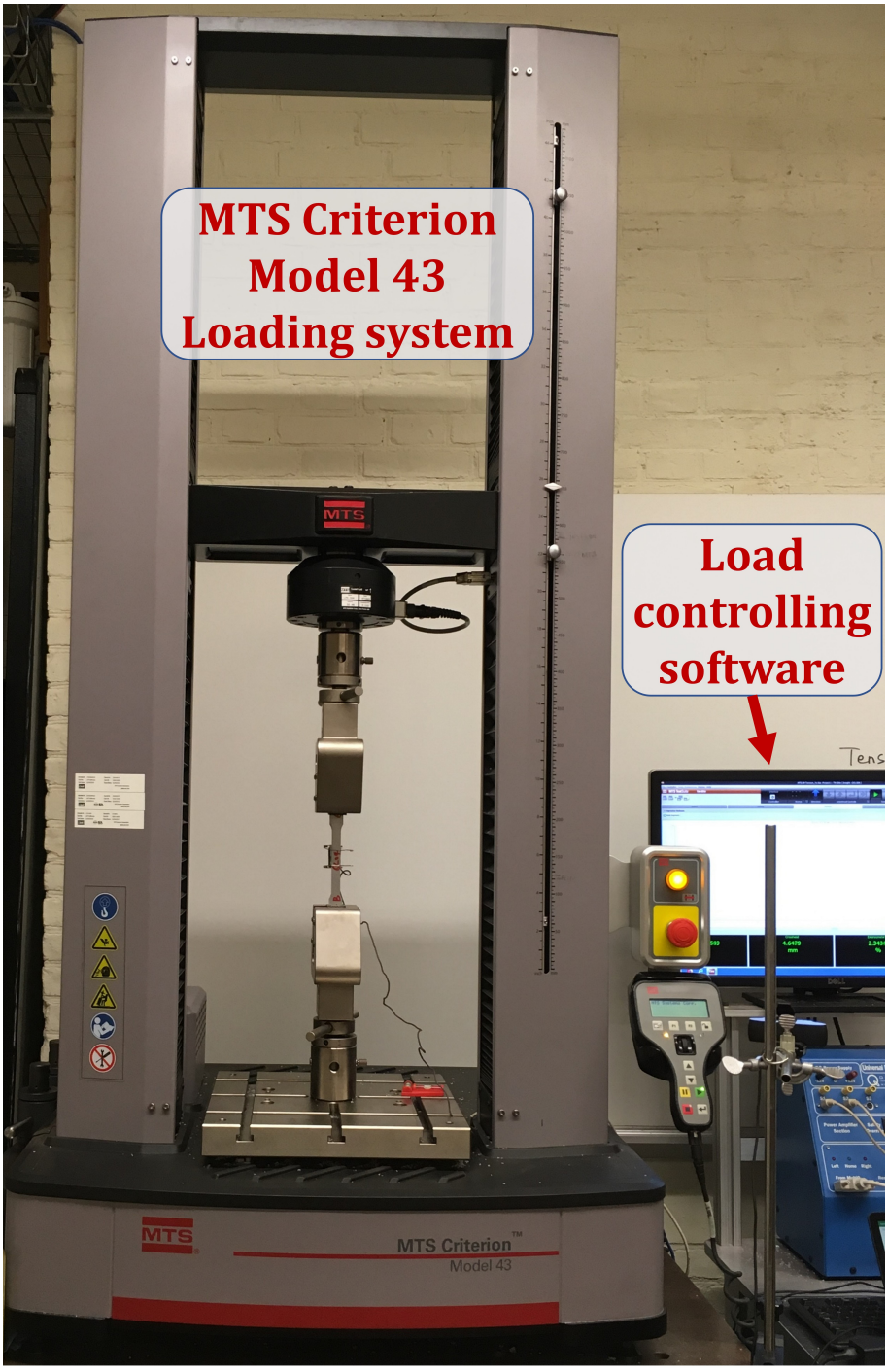

Figure 2.22: Loading system setup for the tensile coupon test as described in Section 2.3.

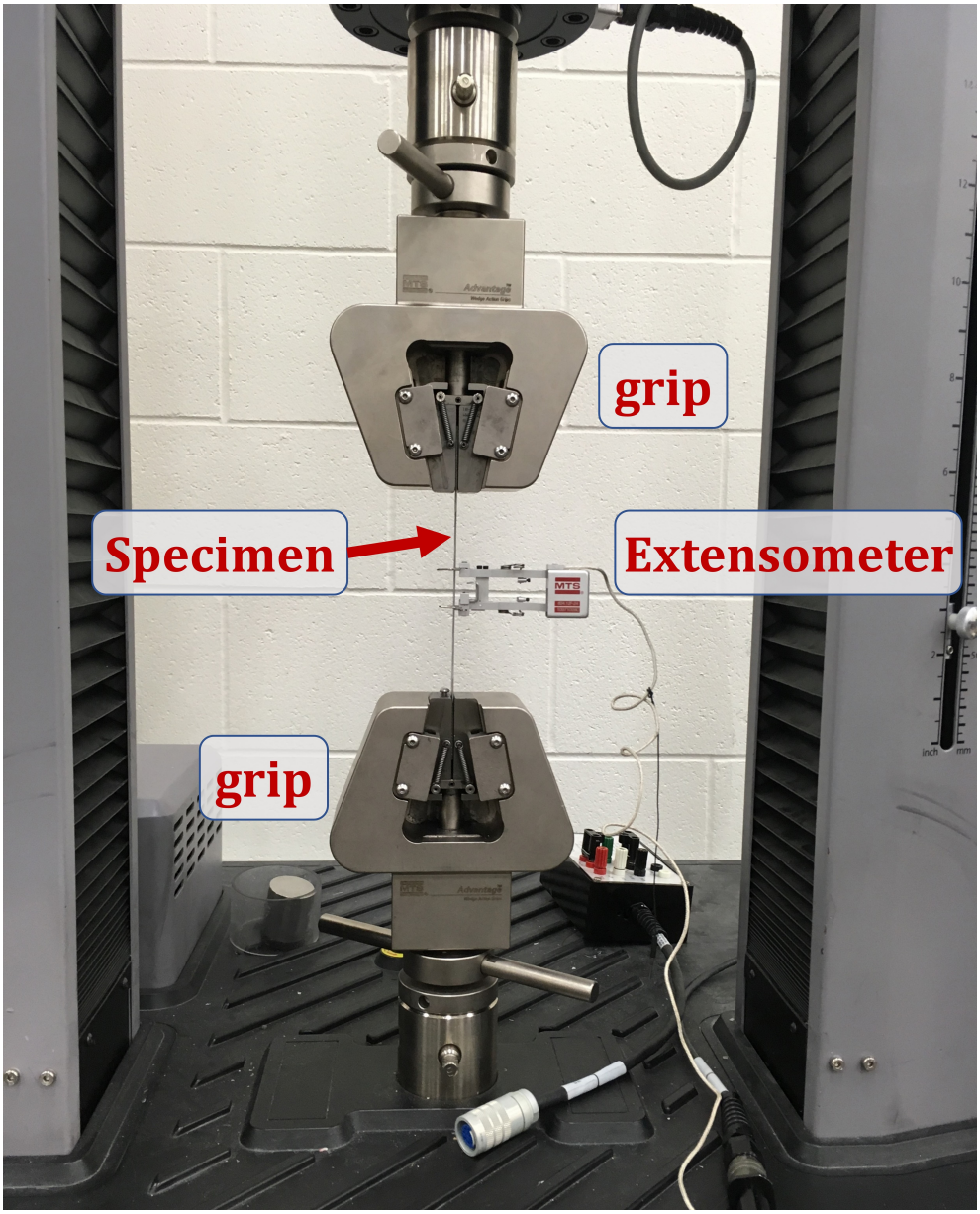

Figure 2.23: Close shot on the specimen for the tensile coupon test as described in Section 2.3.

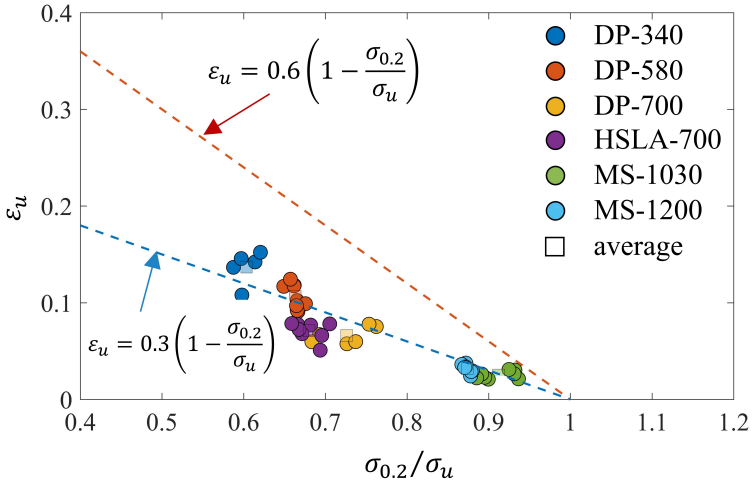

Figure 2.24: Comparison of ε_u between existing prediction [25], updated prediction, and AHSS test data.

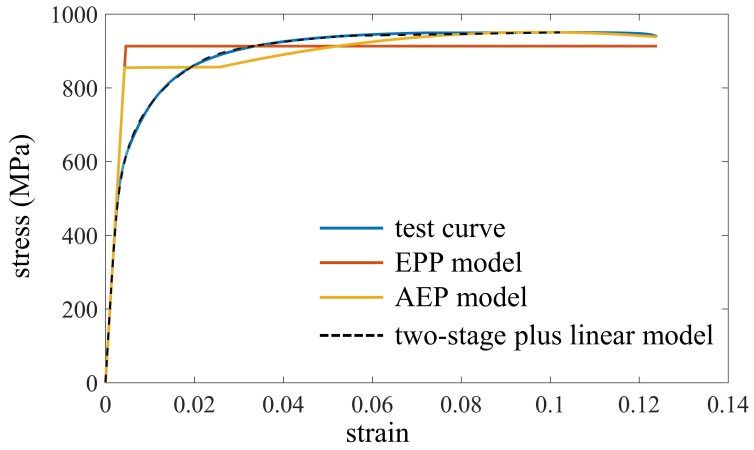

Figure 2.25: Comparison between a representative test curve (DP-580T01), its corresponding EPP and AEP model, and its curve fit using two-stage plus linear model.

Fig. 2.21 illustrates a representative test curve (DP-700D01) with its corresponding EPP and AEP model that has the same energy dissipation from start to specimen fracture. Fig. 2.25 presents an additional example test curve (DP-580T01) with its EPP and AEP model curve as well as the corresponding curve fit using the proposed two-stage plus linear model.

Chapter 3

Elevated temperature and post-fire stress-strain modeling of advanced high-strength cold-formed steel alloys

Xia, Yu, Yan, Xia, Gernay, Thomas, and Blum, Hannah B. "Elevated temperature and post-fire stress-strain modeling of advanced high-strength cold-formed steel alloys." *Journal of Constructional Steel Research* 190 (2022): 107116. https://doi.org/10.1016/j.jcsr.2021.107116

The main body of Chapter 3 is from the above published journal article. Some extra relevant figure and table that are not included in the journal article is presented in the Addendum of this chapter.

The data used as the benchmark for this modeling work is from a series of experiments on the material properties of AHSS at elevated temperatures and after

cooling down as presented in the following published journal articles:

Yan, Xia, Xia, Yu, Blum, Hannah B. and Gernay, Thomas. "Elevated temperature material properties of advanced high strength steel alloys." *Journal of Constructional Steel Research* 174 (2020): 106299.

Yan, Xia, Xia, Yu, Blum, Hannah B. and Gernay, Thomas. "Post-fire mechanical properties of advanced high-strength cold-formed steel alloys." *Thin-Walled Structures* 159 (2021): 107293.

Abstract

Advanced high-strength cold-formed steels (AHSS) have been developed with yield strengths up to 1250 MPa and ultimate strengths up to 1900 MPa. Accurate stress-strain modeling of these new steel alloys is required for the eventual application of AHSS into the building construction industry, including the material behavior of AHSS subjected to elevated temperatures. A series of new constitutive material models are proposed based on the experimental AHSS stress-strain database at elevated temperatures (i.e., steady-state and transient-state test methods) and post-fire scenarios (i.e., residual test method). The stress-strain curves from experiments on two families of AHSS, including dual phase steel with nominal yield strengths of 340 MPa and 700 MPa, and martensitic steel with nominal yield strengths of 1030 MPa and 1200 MPa, reported in a previous study are considered. Existing stress-strain models are investigated and fit to the AHSS database, in addition to the development of new material models. The required input parameters of the

proposed stress-strain models are determined, and their corresponding predictive expressions are proposed. It is shown the stress-strain behaviors of AHSS could be accurately described by the proposed models. The data generated by this research addresses fire safety design and will be essential in supporting the adoption of these next-generation steels in future infrastructure.

3.1 Introduction

Recent advances in steel manufacturing processes have led to materials with significantly enhanced capabilities at a competitive cost. New grades of steel, referred to as Advanced High-Strength Steels (AHSS), have been recently developed. AHSS are steels with unique microstructures utilizing complex deformation and phase transformation processes to achieve unprecedented strength and ductility combinations. The design and manufacture of AHSS require a careful selection of chemical compositions and precisely controlled heating and cooling processes. Subsequently, AHSS exhibit a multiphase microstructure containing one or more phases different from ferrite, pearlite, or cementite. Instead, these phases, for example, include martensite, bainite, austenite, and/or retained austenite that are sufficient in quantities to produce unique mechanical properties [2]. AHSS includes new grades of steels with yield strengths up to 1250 MPa, ultimate strengths up to 1900 MPa, and tensile elongations upwards of 20% to 30% [2]. In addition, different from conventional steels, the terminology AHSS is classified by its metallurgical designation rather than the steel grades. As a result, AHSS can have a broader range of grades

(e.g., with ultimate strength as low as 440 MPa and yield strength as low as 210 MPa) than the conventional high strength steels [2].

Although AHSS has not yet been adopted as a structural material in the construction industry, AHSS has been utilized widely in the automobile industry [2]. However, the past two decades have shown an increase in the use of conventional high-strength structural steel (HSSS) in infrastructure. For example, Beijing National Stadium (2008) and China Central Television Headquarters (2012) in Beijing adopted Q460 steel as the main structural material, 1 Manhattan West (2019) in New York adopted steel with $\sigma_y = 485$ MPa in its perimeter steel moment frame, and Friends Arena (2012) in Stockholm used S460, S690, and S900 steel members for the chords [37]–[39]. These cases show that the quantity and quality demands for high-strength steel as structural material have rapidly developed around the world [37], [40], indicating a promising prospect. Adopting AHSS in the construction industry can provide many unique advantages, notably with cold-formed steel (CFS) structures, which provide efficient, lightweight, and resilient solutions for a range of building applications. Nevertheless, these novel materials' behavior must be understood and characterized under extreme environments that may arise in structural applications, including high temperatures scenarios resulting from fire. In the current design codes [30], [41]–[43], the deterioration of critical mechanical properties, including elastic modulus and yield strength at elevated temperatures, are recommended based on research primarily focused on hot-rolled steels (HRS). Furthermore, the design guidance of the structural steel performance after the cooling down from the elevated temperature is limited, and research on the mechanical

property deterioration of cold-formed high-strength steel subjected to fire loads is extremely limited or non-existent. At ambient, the yield strength and tensile strength of CFS members increase due to the cold-forming process. However, these strength increases quickly deteriorate when the steel is exposed to fire, and this phenomenon is even more severe on high-strength steels [44].

In this study, thorough discussions on the development of the constitutive relationship of AHSS at elevated temperature and after cooling down are carried out. Two dual-phase steel sheets (with nominal yield strengths of 340 MPa and 700 MPa) and two martensitic steel sheets (with nominal yield strengths of 1030 MPa and 1200 MPa) were recently studied experimentally by the authors [45], [46]. The mechanical and geometric characteristics of the AHSS experimental stress-strain curves are summarized. The modeling of the AHSS stress-strain relationship in different fire-related scenarios is discussed to provide accurate descriptions for advanced numerical simulation. Firstly, existing stress-strain models for steel at elevated temperature and after cooling down are reviewed and calibrated to best fit the AHSS experimental stress-strain data, however, it was determined that updated models are necessary to accurately fit the AHSS data. Secondly, based on the characteristics of the AHSS experimental stress-strain curves, two stress-strain models are developed for two different strain hardening behaviors. The fit accuracy for both proposed models is verified with the AHSS data in addition to other steel grades with similar stress-strain behaviors. Thirdly, a discussion on the prediction of model parameters as functions of test temperature is carried out, so that the stress-strain curve can be predicted at any given temperature within

the temperature range. Finally, three examples for applying the proposed models corresponding to three different elevated temperature test methods are presented to help readers better understand the application of the models.

3.2 Review on high temperature studies and existing steel stress-strain models

The behavior of materials exposed to fire is generally characterized using either the steady-state test method or the transient-state test method. For the steady-state test, the specimen is heated to the assigned elevated temperature until the specimen temperature is stabilized and then uniaxially pulled till fracture. The steady-state test's output is directly the stress-strain curve. For the transient-state test, the specimen is loaded to and stabilized at the assigned stress level and then gradually heated until fracture. The transient-state test output is the strain-temperature relationship, which can be transferred to the stress-strain relationship. The steady-state test method is widely employed in existing literature [44], [47]–[58] to investigate the material properties of conventional CFS, stainless steel, and high-strength CFS at elevated temperature, because this test method is easy to implement, and the test result is straightforward. Many researchers also employ the transient-state test method [48]–[50], [52], [55], [59] because it can accurately mimic the actual situation when steel is exposed to fire. However, the transient-state test has several drawbacks. Specifically, it is more complex to conduct and post-process. The generated stress-strain curve typically includes sparse data points and only covers a

relatively small strain range.

The steel post-fire material behavior is commonly simulated by the residual test method. Data has been reported by several authors for CFS [51], [60]–[67]. For the residual test, the specimen is heated to the assigned high temperature until the specimen temperature is stabilized, then cooled down to the ambient temperature, and finally pulled uniaxially until fracture. The residual test method directly outputs the stress-strain curve, and the residual stress-strain curve consists of a large number of data points covering the whole strain range from the origin to the fracture point.

3.2.1 Steady-state tests

From the existing steady-state test results for CFS, most stress-strain curves at elevated temperature show a nonlinear rounded curve shape, where the Ramberg-Osgood (R-O) equation [11], as shown in Eq. 3.1, is the most widely used model to describe the stress-strain relationship:

$$\varepsilon = \frac{\sigma}{E} + p\left(\frac{\sigma}{\sigma_p}\right)^n \quad \text{for } 0 \leqslant \sigma \leqslant \sigma_u \tag{3.1}$$

where σ is stress, which is the model input, E is elastic modulus, p is the predefined plastic strain, σ_p is the proof stress when the plastic strain equals p, and n is the exponential coefficient determining model curvature.

Previous research has made various updates on the original R-O model (Eq. 3.1) to fit the experimental stress-strain curves from studies on different types and grades of CFS for both ambient and elevated temperature cases. The R-O

model updates for CFS at elevated temperatures can be generally classified into two categories.

The first category includes the addition of a β factor. Although some minor differences might exist in the forms adopted by different studies, one representative expression is shown in Eq. 3.2 and is referred to as the *one-stage R-O model* hereinafter:

$$\varepsilon_T = \frac{\sigma_T}{E_T} + \beta(\frac{\sigma_{yT}}{E_T})(\frac{\sigma_T}{\sigma_{yT}})^n \quad \text{for } 0 \leqslant \sigma_T \leqslant \sigma_{uT} \tag{3.2}$$

where β is a numerical parameter, and σ_y is the yield strength. The subscript T for any material property stands for this property at temperature T from the test.

Two different methods were developed in adopting the one-stage R-O model. For the first method, β is fixed as a constant and n is given as a function of T. For example, various β and n were determined in [44], [48], [54]–[56], [68] for a variety of CFS and stainless steel by adopting this method. For the second method, n is fixed, while β varies at different test temperatures, for example, which was adopted in [47].

The second category of updates includes the transformation from the original one-stage R-O model to a two-stage model. This model type will be referred to as the *two-stage R-O model* and is derived from the two-stage R-O models at ambient (e.g., [13]). Chen and Young [50], [52] studied the material properties of cold-rolled EN 1.4462 and EN 1.4301 stainless steels up to 960°C as well as G450 and G550 CFS up to 970°C. They adopted and updated the two-stage models for stainless steel at ambient [13], [14] to describe their experimental stress-strain curves. The

expressions of the two-stage model are shown in Eq. 3.3 for the first stage and Eq. 3.4 for the second stage:

$$\varepsilon_T = \frac{\sigma_T}{E_T} + 0.002(\frac{\sigma_T}{\sigma_{yT}})^n \quad \text{for } 0 \leqslant \sigma_T \leqslant \sigma_{yT} \tag{3.3}$$

$$\varepsilon_T = \frac{\sigma_T - \sigma_{yT}}{E_{yT}} + \varepsilon_{uT}(\frac{\sigma_T - \sigma_{yT}}{\sigma_{uT} - \sigma_{yT}})^m + \varepsilon_{yT} \quad \text{for } \sigma_{yT} < \sigma_T \leqslant \sigma_{uT} \tag{3.4}$$

where n and m are the exponential coefficients for the first and second stage respectively, ε_{uT} is the ultimate strain, σ_{uT} is the ultimate strength, and E_{yT} is the tangential modulus at the yield strength which is calculated by Eq. 3.5 and 3.6.

$$\frac{1}{E_{yT}} = \frac{\partial \varepsilon_T(\sigma_T)}{\partial \sigma_T}|_{\sigma_T=\sigma_{0.2T}} = \frac{1 + 0.002n\frac{\sigma_T^{n-1}}{\sigma_{0.2T}^n}E_T}{E_T}|_{\sigma_T=\sigma_{0.2T}} = \frac{1 + 0.002n\frac{E_T}{\sigma_{0.2T}}}{E_T} \tag{3.5}$$

$$E_{yT} = \frac{E_T}{1 + 0.002n\frac{E_T}{\sigma_{0.2T}}} \tag{3.6}$$

Imran et al. [57] studied the mechanical properties of tensile coupons cut from Grade 350 CFS square hollow section up to 800°C. They used Eq. 3.3 for the first stage and proposed a different expression for the second stage as shown in Eq. 3.7,

$$\varepsilon_T = \frac{\sigma_T - \sigma_{0.2T}}{E_{0.2T}} + \alpha(\frac{\sigma_T - \sigma_{0.2T}}{\sigma_{uT} - \sigma_{0.2T}})^m + \varepsilon_{0.2T} \quad \text{for } \sigma_{0.2T} < \sigma_T \leqslant \sigma_{uT} \tag{3.7}$$

where α is a numerical parameter that is predicted as a linear function of T, n is predicted as piece-wise linear functions of T, and m is given as 3.

Gardner et al. [53] analyzed the performance of stainless steel alloys at elevated temperatures from existing resources and updated the second stage expression based on an updated two-stage R-O model at ambient [20]. The updated expression is shown in Eq. 3.8 for $\sigma_{0.2T} < \sigma_T \leqslant \sigma_{uT}$. The exponential coefficients n and m were given based on T and steel grade.

$$\varepsilon_T = \frac{\sigma_T - \sigma_{0.2T}}{E_{0.2T}} + (0.02 - \varepsilon_{0.2T} - \frac{\sigma_{t2.0T} - \sigma_{0.2T}}{E_{0.2T}})(\frac{\sigma_T - \sigma_{0.2T}}{\sigma_{t2.0T} - \sigma_{0.2T}})^m + \varepsilon_{0.2T} \qquad (3.8)$$

For both one-stage and two-stage R-O models, σ_T is the model input, and ε_T is the model output. Also, the derivatives of the model expressions indicate the model expressions are monotonic-increasing. Therefore, the models can depict the stress-strain relationship up to the ultimate point. The strain-softening after the ultimate point cannot be predicted by R-O models.

In addition to the numerical parameters (e.g. β, p, n, m, etc.), some material-property parameters are also required by these models (e.g. E_T and σ_y of Eq. 3.2). Temperature-dependent predictive equations for the material properties are needed in the stress-strain model to enable transient structural fire analyses. These equations are developed from a statistical analysis of the experimental data. As different material properties of CFS can exhibit different performances depending on the test temperatures, predictive equations are often formulated as piecewise functions. Two different approaches are found in the literature. For the first approach, a

unified equation with several numerical coefficients to be determined is used as the predictive equation for all required material properties. For example, Eq. 3.9 is adopted by [49], [50], [52], Eq. 3.10 is adopted by [48], [55], Eq. 3.11 is adopted by [63], and Eq. 3.12 is adopted by [57]:

$$R_{X_T} = a - \frac{(T-b)^c}{d} \tag{3.9}$$

$$R_{X_T} = a(T-b)^c + d \tag{3.10}$$

$$R_{X_T} = a + \frac{c}{T}(T-d)^b \tag{3.11}$$

$$R_{X_T} = \frac{1}{a + be^{cT}} \tag{3.12}$$

where R_{X_T} is the retention factor for material property X at temperature T, which is defined as the ratio between a parameter X_T at T and this parameter X_0 at ambient, and a, b, c, and d are the numerical coefficients to be calibrated.

The other approach uses a combination of several basic functions (e.g., linear, power, and exponential) to provide the piecewise function of T as the predictive equations for the material-property parameters required by the stress-strain models. For example, the elastic modulus, strengths, and strains of the steels being studied in [44], [54] are predicted by piecewise linear or power functions of T.

3.2.2 Transient-state tests

The transient-state test method was adopted in the following studies. Outinen and Mäkeläinen [59] investigated the material properties of S350GC+Z CFS at

elevated temperature. The strain-temperature relationships were converted to stress-strain curves from ambient to 1000°C. Chen and Young [50], [52] studied the material properties of EN 1.4462 and EN 1.4301 cold-formed stainless steels at elevated temperature up to 760°C as well as G450 CFS at elevated temperature up to 660°C. Huang and Young [49] examined the material properties of a cold-formed lean duplex stainless steel (EN 1.4162) and reported stress-strain curves up to 750°C. However, no stress-strain model designed for the transient-state test results was proposed in the above studies. Chen and Ye [48], [55] studied the material properties of G550 CFS and Q345 CFS up to 550°C. The converted stress-strain relationship was modeled by the one-stage R-O model (Eq. 3.2), where $A = \beta \cdot (\sigma_{yT}/E_T)$ was given as different constants based on different steel types and different test temperature ranges and n was given as polynomials for different T.

3.2.3 Residual tests

Tao et al. [69] analyzed the post-fire behavior of structural and reinforcing steels from eight different studies. The experimental stress-strain curves from these studies show a distinct yield point and yield plateau, followed by the nonlinear strain hardening and softening process. Inspired by Mander's model for steel at ambient [70], a four-stage stress-strain model was proposed to simulate the post-fire constitutive relationship for the investigated steels accurately, and the expressions for the model are given in Eq. 3.13 to Eq. 3.16 respectively:

$$\sigma_T = E_T \varepsilon_T \quad \text{for } 0 \leqslant \varepsilon_T \leqslant \varepsilon_{yT} \tag{3.13}$$

$$\sigma_T = \sigma_{yT} \quad \text{for } \varepsilon_{yT} < \varepsilon_T \leqslant \varepsilon_{shT} \tag{3.14}$$

$$\sigma_T = \sigma_{uT} - (\sigma_{uT} - \sigma_{yT})(\frac{\varepsilon_{uT} - \varepsilon_T}{\varepsilon_{uT} - \varepsilon_{shT}})^{\rho} \quad \text{for } \varepsilon_{shT} < \varepsilon_T \leqslant \varepsilon_{uT} \tag{3.15}$$

$$\sigma_T = \sigma_{uT} \quad \text{for } \varepsilon_{uT} < \varepsilon_T \tag{3.16}$$

where subscript T represents the target temperature for the residual test, ε_{shT} is the strain at the end of the yield plateau and the onset of the nonlinear strain hardening, and ρ is the exponential coefficient determining the nonlinearity of the strain hardening process and it is calculated by Eq. 3.17.

$$\rho = E_{shT}(\frac{\varepsilon_{uT} - \varepsilon_{shT}}{\sigma_{uT} - \sigma_{yT}}) \quad \text{for } \varepsilon_{shT} < \varepsilon_T \leqslant \varepsilon_{uT} \tag{3.17}$$

Gunalan and Mahendran [60] studied the post-fire mechanical properties of G300, G500, and G550 CFS alloys cooling down from up to 800°C. A distinct yield point and yield plateau were observed in both the post-fire and the ambient results. More significant strength deterioration was observed for G500 and G550 than for G300. The experimental stress-strain curves were simulated by the model proposed by Tao et al. [69].

Huang and Young [63] studied the post-fire behaviors of ferritic stainless steel alloys (EN 1.4003) after exposure to high temperatures up to 1000°C. The experimental results show different stress-strain curve shapes after cooling down from various elevated temperature ranges. For the cases with rounded nonlinear stress-

strain curve shape, a two-stage R-O model (Eq. 3.3 and Eq. 3.4) is adopted. For the cases with a distinct yield point followed by yield plateau and nonlinear strain hardening, an updated inverse form of the model proposed by Tao et al. [69] is adopted.

Kesawan and Mahendran [65] studied the post-fire material properties of G350 and G450 CFS alloys. A distinct yield point and yield plateau followed by nonlinear strain hardening and softening process were observed from all postfire tests, regardless of the stress-strain curve shape at ambient. An elastic-perfectly-plastic model is recommended for the modeling of post-fire stress-strain curves.

Li and Young [66] investigated the post-fire material properties of high-strength CFS alloys after exposure to high temperatures up to 1000°C. The test specimens were cut from three hollow sections. From the results, nonlinear rounded stress-strain behaviors are observed for all ambient cases. For G700 specimens, a distinct yield point and yield plateau were observed when T was between 300°C and 1000°C. For G900 specimens, a distinct yield point and yield plateau were observed when T is between 300°C and 600°C, and the nonlinear rounded stress-strain curve was observed when T is between 700°C and 1000°C. No constitutive model was proposed in their study.

Singh and Singh [67] studied the residual mechanical properties of YSt-310 CFS alloys exposed to target temperatures between 300°C to 800°C. The specimens were cut from three hollow sections with different dimensions. At ambient, the stress-strain curves show gradual yielding with a moderate degree of strain hardening. For the high-temperature cases, a distinct yield point and yield plateau followed

by prominent strain hardening were observed. The two-stage R-O model [13] was recommended for the ambient test, while the model proposed by Tao et al. [69] was recommended for the residual tests.

From existing residual tests, some CFS alloys [63], [65]–[67] show nonlinear rounded stress-strain behaviors (referred to as Mode 1 behavior hereinafter) at ambient and after cooling down from relatively lower temperatures but show linear elastic stress-strain behaviors ending at a distinct yield point followed by a yield plateau (referred to as Mode 2 behavior hereinafter) after cooling down from relatively higher temperatures.

Mode 2 behavior is frequently observed in the ambient tensile tests for HRS. Therefore, existing stress-strain models at ambient proposed for HRS might be able to describe Mode 2 residual stress-strain behaviors for CFS. In engineering practice, several multiphase linear models have been widely adopted, for example, the elastic-perfectly-plastic model [71] and the elastic-linearly hardening model [72]. These models require a few parameters, but the model accuracy is sacrificed at various levels depending on the specific model under consideration. These models are feasible for engineering practice because they provide a less accurate but conservative steel behavior simulation. However, for advanced numerical simulation that requires a high accuracy level, these simple linear models may not be sufficient.

Based on the existing ambient tensile tests of HRS, Yun and Gardner [73] collected over 500 stress-strain curves covering nominal yield strengths from 235 MPa to 960 MPa, and proposed a bilinear plus nonlinear hardening model inspired by

Mander's model [70]. The model uses strain as input and stress as model output. The linear elastic portion is modeled as $\sigma(\varepsilon) = E\varepsilon$ up to ε_y and the yield plateau is modeled as $\sigma(\varepsilon) = \sigma_y$ for $\varepsilon_y < \varepsilon \leqslant \varepsilon_{sh}$. For $\varepsilon_{sh} < \varepsilon \leqslant \varepsilon_u$, the nonlinear strain hardening portion is normalized and modeled by Eq. 3.18:

$$\sigma(\varepsilon) = \sigma_y + (\sigma_u - \sigma_y)(K_1\varepsilon_n + \frac{K_2\varepsilon_n}{(1 + K_3\varepsilon_n^{K_4})^{\frac{1}{K_4}}}) \quad \text{for } 0 \leqslant \varepsilon_n \leqslant 1 \tag{3.18}$$

where ε_{sh} is the strain at the end of the yield plateau and the onset of the nonlinear strain hardening, and ε_n is the normalized strain calculated by Eq. 3.19.

$$\varepsilon_n = \frac{\varepsilon - \varepsilon_{sh}}{\varepsilon_u - \varepsilon_{sh}} \quad \text{for } \varepsilon_{sh} \leqslant \varepsilon \leqslant \varepsilon_u \tag{3.19}$$

The model parameters for the residual test are predicted as a function of T based on the statistical study of the experimental data. Two types of predictive equations exist. The first type uses basic functions (e.g. polynomial, power function, etc.) to predict the required parameters, for example, which was adopted in [60], [62], [65]–[67]. The second type uses an unified function of T (e.g. Eq. 3.9 to 3.12) and the numerical coefficients of the function are calibrated for each parameter, for example, which was adopted in [63].

Table 3.1: Nominal properties of AHSS sheets.

Steel	t (mm)	σ_y (MPa)	σ_u (MPa)
DP-340	1.4	340	590
DP-700	1.4	700	980
MS-1030	1.0	1030	1300
MS-1200	1.0	1200	1500
HSLA-700	0.6	700	980

3.3 Experimental stress-strain curves

An experimental study [45], [46] was carried out in the Multi-Hazard Resilient Structures Lab at Johns Hopkins University to understand the stress-strain behaviors and the material properties of AHSS under various elevated temperature scenarios and provide an experimental benchmark for modeling. The study includes both AHSS properties at elevated temperatures (steady-state and transient-state test protocols) and after cooling down (residual test protocol), representing the post-fire scenario.

Specimens for the tensile coupon test were cut from two dual phase steel (DP) sheets and two martensitic steel (MS) sheets. In addition, specimens cut from a high-strength low-alloy steel (HSLA) sheet were also studied for the steady-state tests for comparison purposes. The nominal properties for the AHSS sheets are shown in Table 3.1. The steel sheets were labeled by their steel family and the nominal yield strength. Details of the experimental test series and results are explained in the related published work [45], [46]. Only the resulting stress-strain curves reported in [45], [46] are shown herein as they are necessary to develop the models and derive the modeling parameters.

For steady-state test, DP-340, DP-700, MS-1030, MS-1200, and HSLA-700 were

tested at each elevated temperature, which includes 20°C (ambient), 200°C, 300°C, 400°C, 500°C, 600°C, and 700°C. The experimental stress-strain curves are shown in Fig. 3.1. For all tests, no distinct yield point or yield plateau is observed; instead, the strain hardening process was gradually developed. Overall trends are visible regarding the change in key material properties, including yield and ultimate strengths, total elongation, and overall stress-strain behaviors at various temperatures. In general, the stress-strain curve's shape varies with the test temperature, and one material may show changes in the stress-strain relationship across temperature ranges. It should be noted that some strain hardening regions are very gradual and therefore may appear as a plateau. Overall, the strength decreases as the temperature increases after an initial strength increase at 200°C, except for HSLA.

For the transient-state test, DP-700 and MS-1200 were studied to compare and supplement corresponding steady-state test results. The converted stress-strain curves are shown in Fig. 3.2. Each transient-state test can provide only one data point for each preselected temperature. Due to the limited number of tests, the transient-state test's stress-strain curves comprise limited data points.

For the residual test, the postfire material properties for DP-340, DP-700, MS-1030, and MS-1200 cooling down from up to 700°C were studied. The experimental stress-strain relationships for the residual tests are shown in Fig. 3.3. Both Mode 1 and Mode 2 stress-strain behaviors are observed. For example, for DP-700, the ambient and 200°C cases show Mode 1 behavior, while cases from 300°C to 600°C show Mode 2 behavior; interestingly, the case at 700°C reverts to Mode 1 behavior.

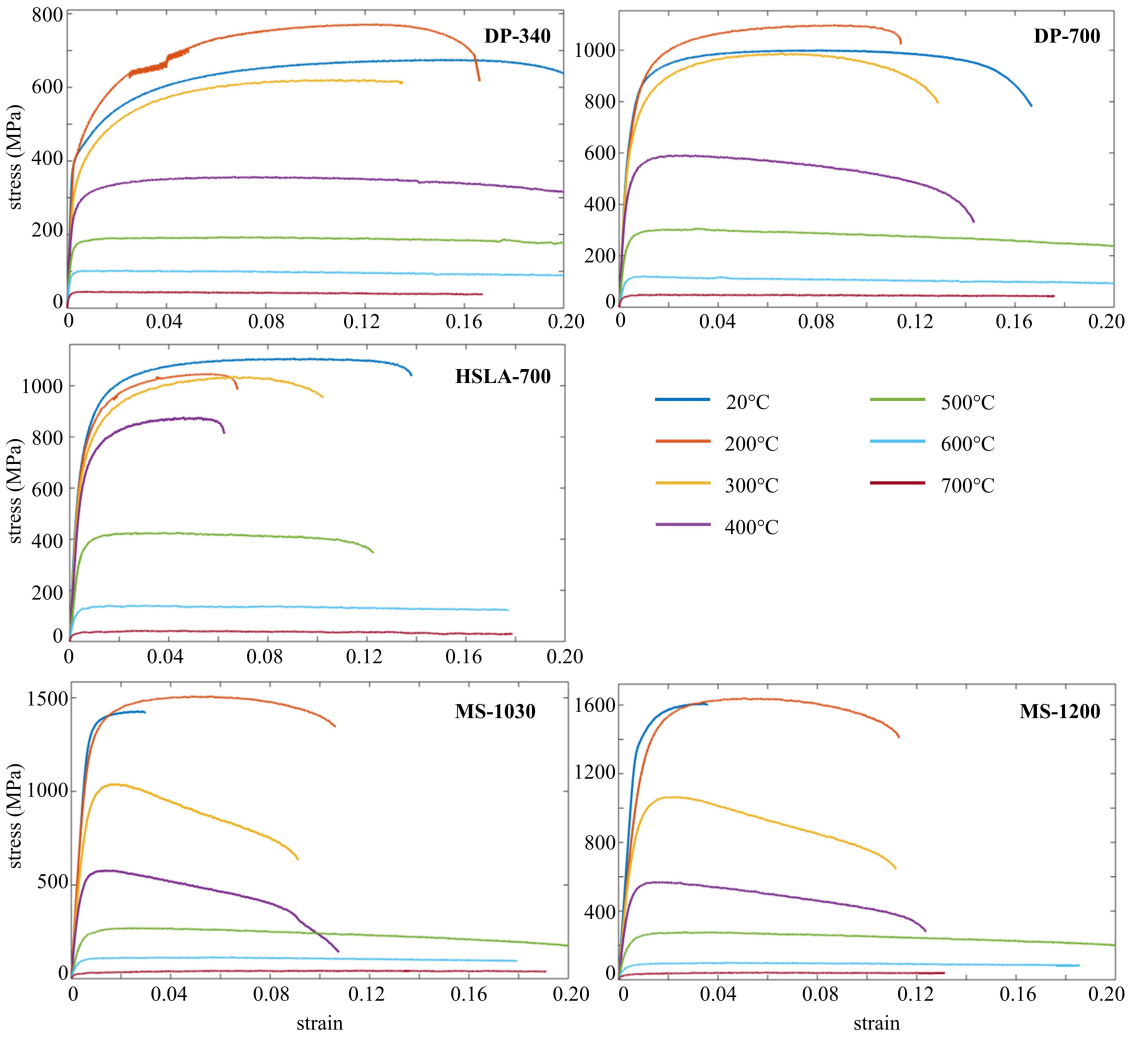

Figure 3.1: Representative stress-strain relationships for steels at elevated temperatures from steady-state tests as reported in [45].

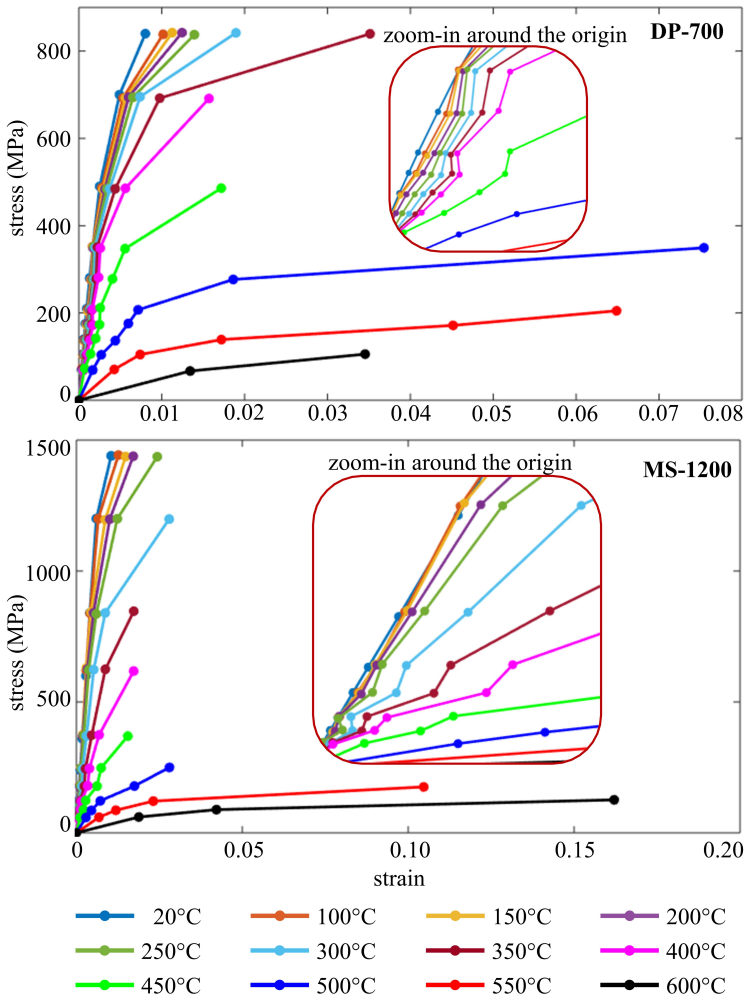

Figure 3.2: Stress-strain relationships for DP-700 and MS-1200 at elevated temperatures from transient-state tests as reported in [45].

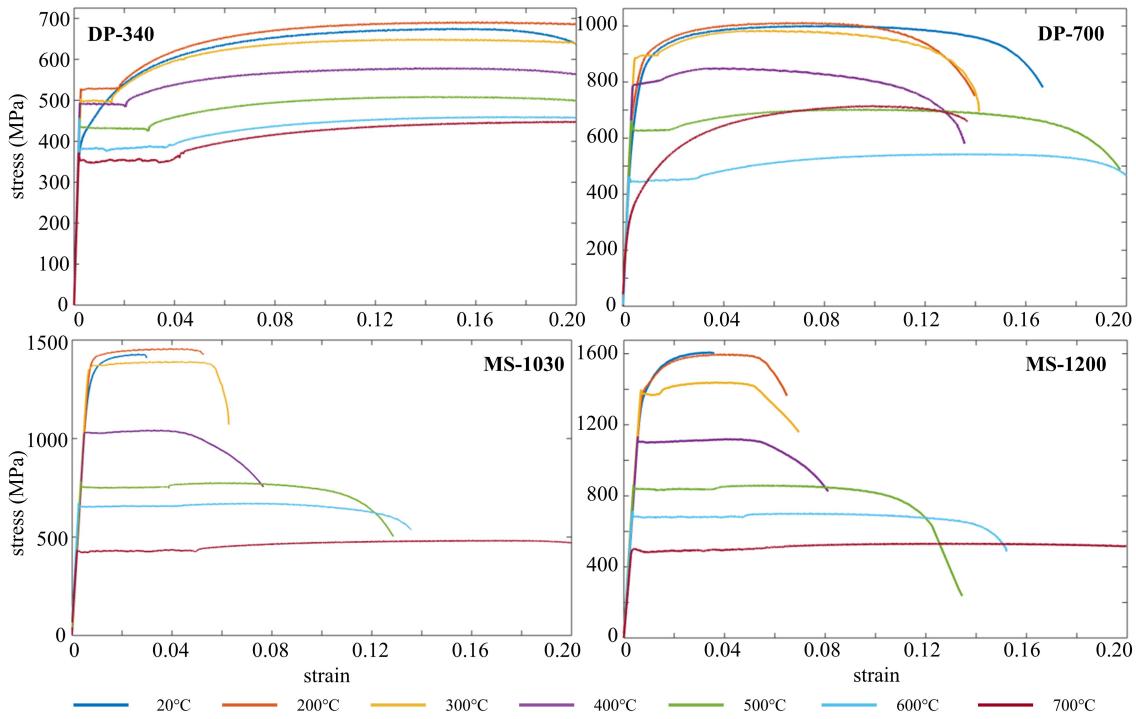

Figure 3.3: Stress-strain relationships from residual tests for steels after cooling down from elevated temperature as reported in [46].

The intense strain hardening process for DP-340 at all test temperatures is observed, which can be evaluated by its high σ_u/σ_y ratio (from 1.17 to 1.26 after cooling down from different test temperatures). All high-temperature tests have a larger elongation at fracture than the case at ambient.

3.4 Optimal fit between AHSS stress-strain curves and existing models

Existing models are adopted to fit the AHSS experimental stress-strain curves. From the discussion on the experimental stress-strain relationships of AHSS at elevated temperature and after cooling down (Section 3.3), two different yielding modes of stress-strain behaviors are observed. R-O models are adopted to fit stress-strain curves with Mode 1 behavior. The four-stage model [69] and the bilinear plus nonlinear hardening model [73] are adopted to fit stress-strain curves with Mode 2 behavior, even if the bilinear plus nonlinear hardening model is not originally designed for high-temperature tests.

The material-property parameters are directly captured from the experimental curves to obtain the mathematically optimal fit between the existing models and the AHSS test data, instead of using predictive equations in the literature. The numerical parameters (e.g., n, m, and K_1 to K_4) are calculated using the error minimization method to search the maximum R^2 by iterating the parameters. Error minimization is a form of mathematical regression analysis aiming for determining the optimal fit for specific data by searching for the parameters with a minimum error of the selected indicator. Common fit error indicator includes R^2, residual sum of squares (RSS), etc. RSS has intrinsic limitations [74], for example, its scale is largely dependent on the data scale. Oppositely, R^2 is a generalized parameter, and it is independent of the data scale, therefore it is appropriate in evaluating model fit for multiple groups of data [25], [75]–[77]. For the stress-input models

(e.g. R-O models), R^2 is calculated by Eq. 3.20; while for the strain-input models (e.g. the four-stage model [69] and the bilinear plus nonlinear hardening model [73]), R^2 is calculated by Eq. 3.21:

$$R^2 = 1 - \frac{SS_{res}}{SS_{tot}} = 1 - \frac{\sum_i (\varepsilon_{Ti} - \varepsilon_T(\sigma_{Ti}))^2}{\sum_i (\varepsilon_{Ti} - \overline{\varepsilon}_{Ti})^2} \tag{3.20}$$

$$R^2 = 1 - \frac{SS_{res}}{SS_{tot}} = 1 - \frac{\sum_i (\sigma_{Ti} - \sigma_T(\varepsilon_{Ti}))^2}{\sum_i (\sigma_{Ti} - \overline{\sigma}_{Ti})^2} \tag{3.21}$$

where σ_{Ti} and ε_{Ti} are the stress and strain of data point i of the experimental curve of temperature T, $\varepsilon_T(\sigma_{Ti})$ is the model strain output calculated by σ_{Ti}, $\sigma_T(\varepsilon_{Ti})$ is the model stress output calculated by ε_{Ti}, $\overline{\varepsilon}_{Ti}$ is the average of the experimental strains, $\overline{\sigma}_{Ti}$ is the average of the experimental stresses.

For the stress-input models, R^2 is calculated from the difference between the test strain and the model strain, not the stress difference. Therefore, for R-O models at a high strain range, R^2 can be small (i.e., poor fit) even if the difference between the test curve and the model is not obvious visually. This illusion's key reason is that the horizontal axis parameter is typically the independent variable, and the vertical axis parameter is typically the dependent variable. While for the R-O models, the inverse situation occurs.

For steady-state tests, the optimal fit using the existing one-stage (DP-700) and two-stage (MS-1200) R-O models are shown in Fig. 3.4 as a sample of results. All R-O models depict the σ-ε relationship between the origin and the ultimate strength. Discrepancies in the shape of the stress-strain curves between existing models and

test data are observed across temperatures. The average R^2 varies from 0.91 to 0.93 for one-stage R-O models and from 0.94 to 0.96 for two-stage R-O models, respectively. From the fit results, the existing one-stage and two-stage R-O models might not accurately predict the AHSS σ-ε behavior from steady-state tests. Similar levels of agreement are found when adopting the existing R-O models on the AHSS σ-ε curves from residual tests with Mode 1 behavior. Therefore, a new constitutive model must be proposed.

The σ-ε curves in transient-state tests are fitted using one-stage R-O models only. The reason is the test curves do not pass through the ultimate point and terminate at a relatively small strain level; thus, some parameters (e.g., ε_u, σ_u, and m) are not applicable for the two-stage models. By comparing the fits using existing one-stage R-O models, Chen and Ye's model [48] can provide accurate fits for both DP-700 and MS-1200 at all test temperatures, and Olawale's model [68] generally provides accurate fits for both AHSS with a few exceptions at various temperatures. Other one-stage R-O models might not fit either DP-700 or MS-1200. Based on the fit results, Chen and Ye's model [48] (Eq. 3.22) is recommended and adopted in this paper for fits of the transient-state results, and the optimal fits are shown in Fig. 3.5.

$$\varepsilon_T = \frac{\sigma_T}{E_T} + 0.002\left(\frac{\sigma_T}{\sigma_{yT}}\right)^n \quad \text{for } 0 \leqslant \sigma_T \leqslant \sigma_{uT} \tag{3.22}$$

The σ-ε curves from residual tests with Mode 2 behavior are fitted using the four-stage model [69] and the bilinear plus nonlinear hardening model [73]. The four-stage model [69] can accurately fit all DP-700 and MS-1200 σ-ε curves, and a few MS-1030 σ-ε curves. However, the fits with all DP-340 σ-ε curves and MS-1030

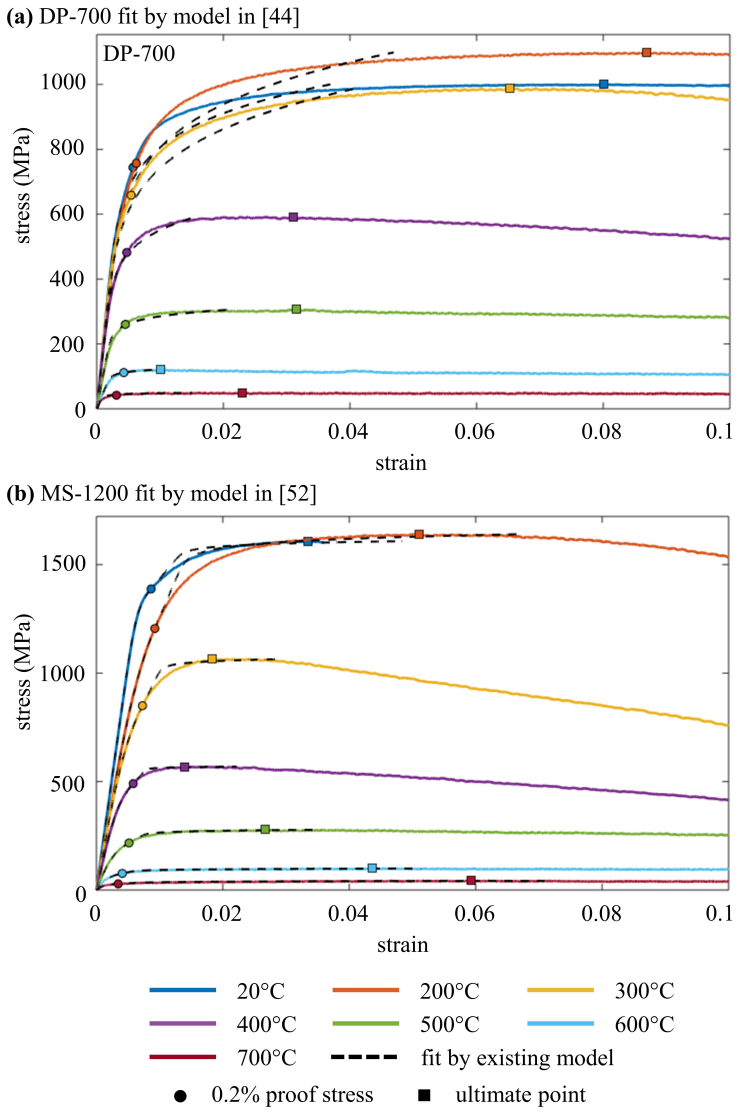

Figure 3.4: Optimal fit examples for (a) DP-700 using representative one-stage R-O model [44] and (b) MS-1200 using representative two-stage model [52].

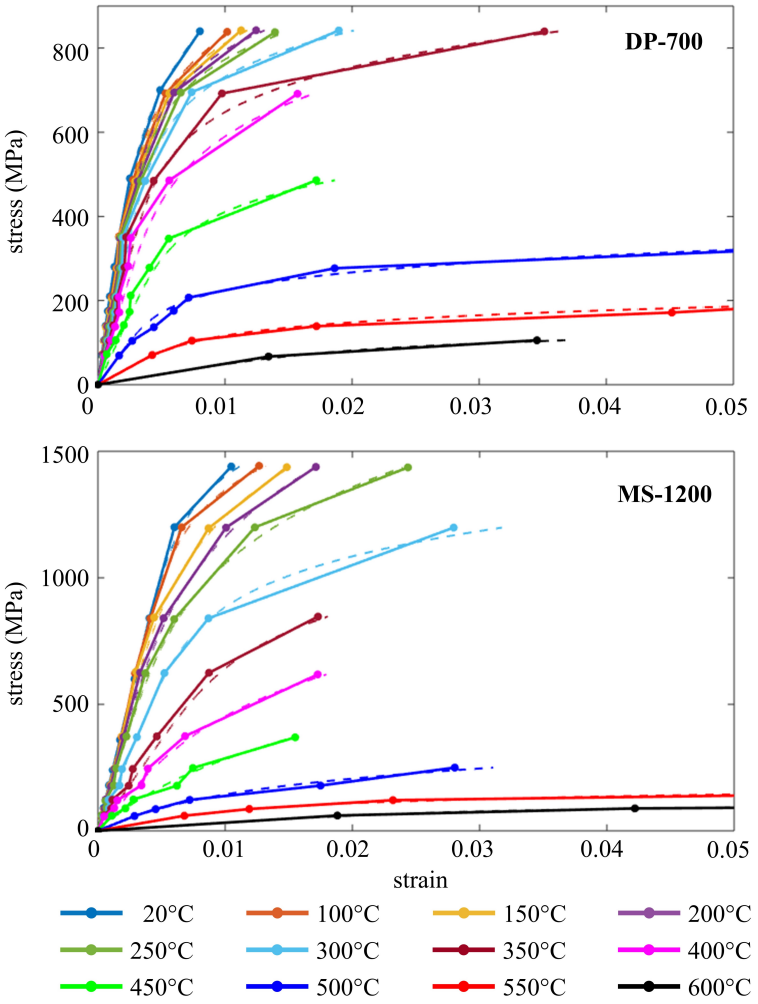

Figure 3.5: Comparison between experimental stress-strain curves (solid lines) from transient-state tests and fit (dashed line) by one-stage R-O model [48] built by parameters from the tests.

σ-ε curves up to 500°C are inaccurate. The average R^2 is 0.76, and the minimum R^2 is 0.69. For the bilinear plus nonlinear hardening model, the four coefficients K_1 to K_4 are recommended as 0.4, 2, 400, and 5 respectively based on the statistical study of the HRS database [73]. The fits are inaccurate by adopting these recommended coefficients for the AHSS residual test data, particularly the MS steel. The average R^2 is 0.71, and the minimum R^2 is 0.32. However, by iterating the four coefficients K_1 to K_4 for each residual test σ-ε curve using the error minimization method, the average R^2 can be as high as 0.99, and the minimum R^2 is 0.97, which significantly increases the fit accuracy. Unfortunately, the calibrated coefficients do not show any clear trend along with temperature change. Therefore it is difficult to provide continuous prediction on these coefficients as a function of T. The improvement indicates the bilinear plus nonlinear hardening model can accurately fit the AHSS residual test σ-ε curves, but the coefficient recommendation must be updated.

3.5 Proposed stress-strain models

The discussion in Section 3.4 revealed that existing models cannot accurately fit the AHSS test curves from the steady-state tests and the residual tests, while one existing one-stage R-O model [48] can fit the AHSS test curves from the transient-state tests. Observed post-yield inaccuracies might have consequences for predictions of structural behavior, for example, in scenarios of blast crushing, collapse, and other cases where the relationship between local strain and engineering strain is crucial [28]. Therefore, in this section, a new model, updated from existing two-stage R-O

models and initially designed for the modeling of AHSS stress-strain relationship at ambient [5], is proposed for the steady-state tests and residual tests with Mode 1 behavior. Besides, an updated model with calibrated numerical coefficients based on the bilinear plus nonlinear hardening model [73] is proposed for the residual tests with Mode 2 behavior.

3.5.1 Updated model for Mode 1 stress-strain behavior

As shown in Fig. 3.6, a two-stage plus linear model is proposed to fit high-temperature tests with Mode 1 behavior. Like other R-O models, the proposed model uses stress at elevated temperature, σ_T, as the model input, and the model output is the corresponding strain prediction, ε_T. The model describes the AHSS stress-strain behavior in high-temperature tests from the origin to the ultimate point. The model consists of two nonlinear stages plus a linear part. The first stage ranges from the origin to the *offset point*, which is defined as the point with a plastic strain, p. Its strain is ε_{pT} and its stress is σ_{pT}. The second stage ranges from the *offset point* to the *equivalent ultimate point*. The *equivalent ultimate point* is defined as the point with a stress equal to 99% of σ_{uT} ($\sigma_{euT} = 0.99\sigma_{uT}$) and a strain of ε_{euT} within the strain hardening region (i.e. $\varepsilon_{euT} < \varepsilon_{uT}$). The final part is proposed as a line between the equivalent ultimate point and the ultimate point. The model expression is given by Eq. 3.23 for $0 \leqslant \sigma_T \leqslant \sigma_{pT}$, Eq. 3.24 for $\sigma_{pT} < \sigma_T \leqslant \sigma_{euT}$, and Eq. 3.25 for $\sigma_{euT} < \sigma_T \leqslant \sigma_{uT}$.

$$\varepsilon_T = \frac{\sigma_T}{E_T} + p\left(\frac{\sigma_T}{\sigma_{pT}}\right)^n \tag{3.23}$$

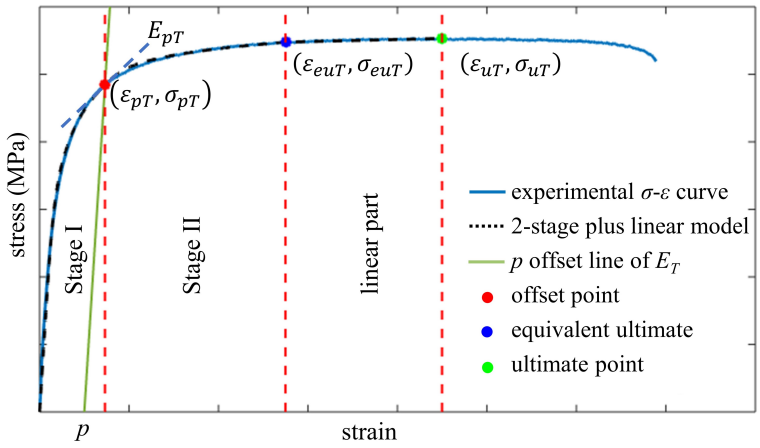

Figure 3.6: Schematic diagram for the proposed two-stage plus linear model.

$$\varepsilon_T = \frac{\sigma_T - \sigma_{pT}}{E_{pT}} + \left(\varepsilon_{euT} - \varepsilon_{pT} - \frac{\sigma_{euT} - \sigma_{pT}}{E_{pT}}\right)\left(\frac{\sigma_T - \sigma_{pT}}{\sigma_{euT} - \sigma_{pT}}\right)^m + \varepsilon_{pT} \tag{3.24}$$

$$\varepsilon_T = \frac{\varepsilon_{uT} - \varepsilon_{euT}}{\sigma_{uT} - \sigma_{euT}} \cdot (\sigma_T - \sigma_{euT}) + \varepsilon_{euT} \tag{3.25}$$

where n and m are the exponential coefficients determining the fit's degree of curvature for the first stage and the second stage respectively, E_{pT} is the tangent modulus at σ_{pT} and it is calculated by Eq. 3.26 and 3.27.

$$\frac{1}{E_{pT}} = \frac{\partial \varepsilon_T(\sigma_T)}{\partial \sigma_T}|_{\sigma_T = \sigma_{pT}} = \frac{1 + pn\frac{\sigma_T^{n-1}}{\sigma_{pT}^n}E_T}{E_T}|_{\sigma_T = \sigma_{pT}} = \frac{1 + pn\frac{E_T}{\sigma_{pT}}}{E_T} \tag{3.26}$$

$$E_{pT} = \frac{E_T}{1 + pn\frac{E_T}{\sigma_{pT}}} \tag{3.27}$$

Table 3.2: Recommendation of p value in percentage for the proposed two-stage plus linear model based on steel strength and test temperature.

Steel	DP-340	DP-700	HSLA-700	MS-1030	MS-1200
$T < 400°C$	2.0%	1.0%	1.0%	0.5%	0.5%
$T \geqslant 400°C$	0.2%	0.2%	0.2%	0.2%	0.2%

Compared with existing two-stage models designed for the high-temperature scenario, the proposed two-stage plus linear model contains three updates. Firstly, the model mathematically passes through the origin $(0, 0)$, the offset point $(\sigma_{pT}, \varepsilon_{pT})$, and the equivalent ultimate point $(\sigma_{euT}, \varepsilon_{euT})$, regardless the specific values of the required parameters of the model. This characteristic guarantees that the model has continuous transitions between every adjacent stage.

Secondly, the plastic strain of the offset point changes from 0.002 to a new value p. The offset point in existing two-stage R-O models was defined as the point with a plastic strain of 0.002. However, this practice does not provide an accurate fit between the model and the AHSS experimental stress-strain curves across all elevated temperatures, because AHSS stress-strain curves show significant nonlinearity. The fit was optimized by varying p from 0.002 to 0.020 at 0.001 increments and iterating n and m to search for the maximum R^2 between the test curve and the model. From the optimization results, the recommendations of p for the various AHSS at different elevated temperature ranges are listed in Table 3.2, where a clear decreasing trend of p with increasing grade strength is observed.

The third update is the change at the end of the second stage from the ultimate point to the equivalent ultimate point, while the remainder of the stress-strain curve (from the equivalent ultimate point to the ultimate point) is described as a line. Compared with other steels with a gradual yielding process (for example, stainless

steel), AHSS σ-ε curves have a relatively long strain hardening process with a small stress increase. For example, when σ_T increases from the equivalent ultimate stress σ_{euT} to the ultimate strength σ_{uT}, where stress only increases 1%, ε_T increases on average 100% for DP-340, 51% for DP-700, 67% for HSLA-700, 52% for MS-1030, and 25% for MS-1200. Including this long, flat strain hardening part in the second stage model distorts the curve with an excessively large exponential coefficient m. Therefore, in the proposed model, the second stage ends at the equivalent ultimate point, and a line represents the remainder of the curve to the ultimate point.

The fit of AHSS σ-ε curves at different temperatures from steady-state tests using the proposed model (Eq. 3.23, 3.24, and 3.25) and the recommended p value (Table 3.2) is shown in Fig. 3.7. The average and minimum R^2 for each AHSS specimen are no less than 0.995 and 0.983, respectively. From the observation of model fit results, the discrepancy between the test data and the stress-input model fit (e.g., R-O models) is negligible when $R^2 \geqslant 0.96$ Compared with the fit of AHSS curves using existing models (Section 3.4), the proposed model significantly increases the fit accuracy.

3.5.2 Updated model for Mode 2 stress-strain behavior

An updated model based on the bilinear plus nonlinear hardening model [73] is proposed for AHSS σ-ε curves from Mode 2 residual tests as shown in Eq. 3.28. The bilinear regions (elastic and yield plateau) are the same as presented in [73]; the expression for the nonlinear hardening is updated.

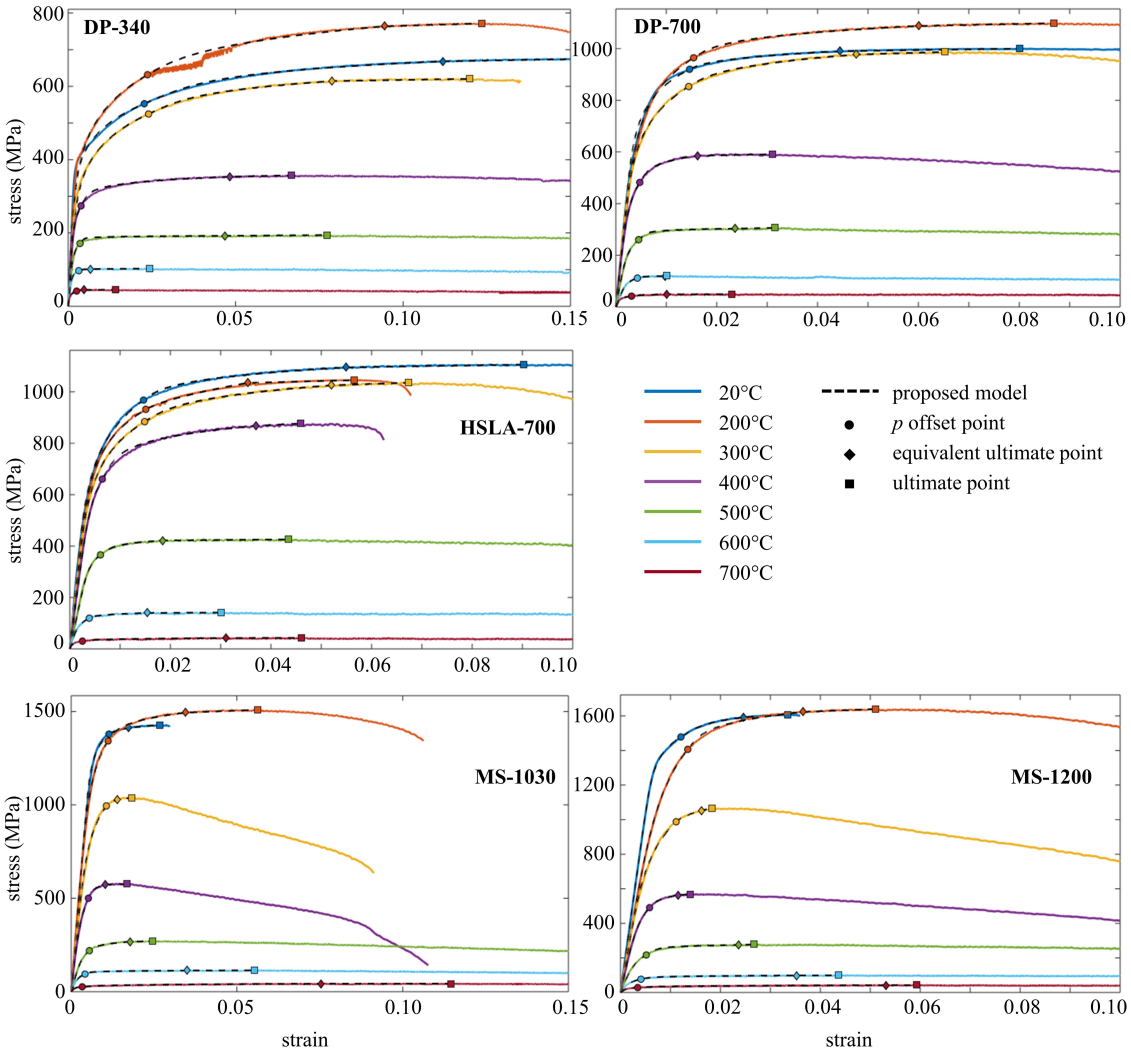

Figure 3.7: Comparison between the stress-strain curves from steady-state tests and fit by the proposed two-stage plus linear model built by test results.

$$\sigma_T = \begin{cases} E_T \varepsilon_T & \text{for } 0 \leqslant \varepsilon_T \leqslant \varepsilon_{yT} \\ \sigma_{yT} & \text{for } \varepsilon_{yT} < \varepsilon_T \leqslant \varepsilon_{shT} \\ \sigma_{yT} + (\sigma_{uT} - \sigma_{yT}) \left[K_1 \varepsilon_{nT} + \frac{K_2 \varepsilon_{nT}}{(1+K_3 \varepsilon_{nT})} \right] & \text{for } 0 \leqslant \varepsilon_{nT} \leqslant 1 \end{cases} \tag{3.28}$$

where ε_{nT} is normalized strain calculated by Eq. 3.29.

$$\varepsilon_{nT} = \frac{\varepsilon_T - \varepsilon_{shT}}{\varepsilon_{uT} - \varepsilon_{shT}} \quad \text{for } \varepsilon_{shT} \leqslant \varepsilon_T \leqslant \varepsilon_{uT} \tag{3.29}$$

The nonlinear hardening part of Eq. 3.28 is a nonlinear interpolation between ε_{yT} and ε_{uT} based on the input strain ε_T. The curve nonlinearity degree is defined by four coefficients (K_1 to K_4) in [73], while it is defined by three coefficients (K_1 to K_3) in the proposed expression by adopting $K_4 = 1$. By iterating K_1 to K_3 using error minimization to search for the maximum average R^2 of the fit between the updated model and the test curves, it is recommended to adopt $K_1 = 0.029$, $K_2 = 4.713$, and $K_3 = 3.855$ for AHSS residual test stress-strain curves with Mode 2 behavior, which provides an average R^2 of 0.983. For Mode 2 behavior cases using the strain-input model (e.g., the bilinear plus nonlinear hardening model), it is found that an excellent agreement is achieved for the curve fit when $R^2 \geqslant 0.95$. The fits between the test curves and the updated model built by the recommended coefficients are shown in Fig. 3.8.

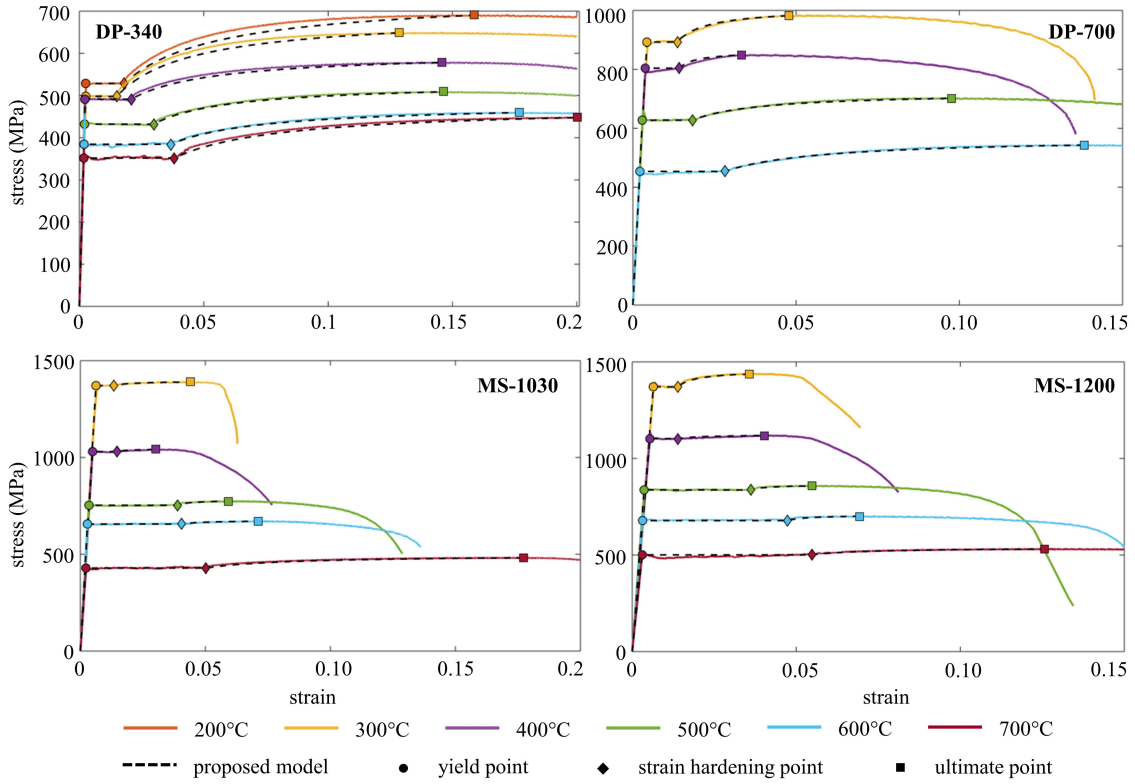

Figure 3.8: Comparison between the sharp mode stress-strain curves from residual tests and fit by the modified three-parameter bilinear plus nonlinear hardening model built by test results and recommended model coefficients.

3.5.3 Fit between proposed stress-strain models and existing data

The proposed models show excellent fit between AHSS stress-strain data captured from both elevated temperature and post-fire experiments as discussed in Section 3.5.1 and 3.5.2. It is investigated whether the proposed models will accurately capture the stress-strain behavior of other steel grades with similar stress-strain behaviors.

Stress-strain curves from [78] were selected where the post-fire material properties of very high-strength steel S960 were studied. The stress-strain curves show

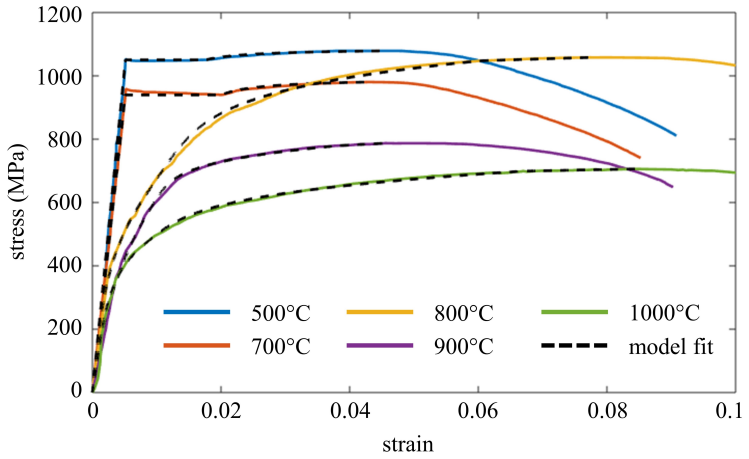

Figure 3.9: Comparison between the representative experimental stress-strain curves from [78] and the corresponding fit by the proposed models.

Mode 2 behavior between ambient (20°C) and 750°C and Mode 1 behavior from 800°C to 1000°C. Therefore, both proposed models can be verified by using a group of data from the same experiment campaign.

A few representative curves were selected for the fit following the identical procedures as described in Section 3.5.1 and 3.5.2. For Mode 1, stress-strain curves cooling down from 800°C, 900°C, and 1000°C were selected. Noticeably, the selected Mode 1 postfire curves do not show as significant strength deterioration as the AHSS elevated temperature curves at 400°C or above. Therefore, $p = 0.005$, which is recommended for very high strength steel (e.g., MS-1030 and MS-1200) at a lower temperature range, was adopted in the Mode 1 curve fit. For Mode 2, stress-strain curves cooling down from 500°C and 700°C were selected. The numerical coefficients recommended for AHSS post-fire Mode 2 curves in Section 3.5.2 were applied, where $K_1 = 0.029$, $K_2 = 4.713$, and $K_3 = 3.855$. The optimal fits between the selected experimental curves and corresponding models are shown in Fig 3.9.

The fits show excellent agreement with the test data selected from [78]. Specifically, R^2 for the 800°C, 900°C, and 1000°C postfire curve using the updated two-stage plus linear model is above 0.995 with an average of 0.997; R^2 for the 500°C and 700°C postfire curve fits using the updated bilinear plus nonlinear hardening model is above 0.96 with an average of 0.965. The excellent fit agreement illustrates the potential for the adoption of the proposed models for other grades with similar stress-strain behaviors.

3.6 Predictive equations and recommendations for model parameters

The proposed stress-strain models for steady-state tests, transient-state tests, and residual tests are discussed in Section 3.5. To define the constitutive relationships using the proposed models, accurate prediction of the required parameters is necessary.

A unified equation proposed by the authors [79], as shown in Eq. 3.30, is adopted in this study to fit the retention factors for the required material-property parameters:

$$R_{X_{T_{nor}}} = c + (1 - c)\frac{1 - T_{nor}^{b}}{1 + aT_{nor}^{b}} \tag{3.30}$$

where T_{nor} is the normalized temperature normalized by T_{max} and T_{min} as defined in Eq. 3.31, T_{max} is the maximum temperature of the test series, T_{min} is the minimum temperature of the test series. The derivative of $R_{X_{T_{nor}}}$ in Eq. 3.30 is calculated

in Eq. 3.32.

$$T_{nor} = \frac{T - T_{min}}{T_{max} - T_{min}} \tag{3.31}$$

$$\frac{\partial R_{X_{T_{nor}}}}{\partial T_{nor}} = (1 - c)\frac{-bT_{nor}^{b-1}(a + 1)}{(1 + aT_{nor}^{b})^2} \tag{3.32}$$

From Eq. 3.32, $R_{X_{T_{nor}}}$ is always monotonic regardless of the values of a, b, and c; $R_{X_{T_{nor}}}$ is monotonic decreasing when $a > -1$, b is positive, and $c < 1$. This characteristic makes Eq. 3.30 suitable for describing the deterioration of steel material properties, particularly for elastic modulus, proof stresses, and ultimate strength, with temperature increase as observed in experiments.

3.6.1 Steady-state tests

For modeling of the stress-strain curves from the steady-state tests, the proposed two-stage plus linear model (Eq. 3.23, 3.24, and 3.25) passes through the p offset point (values in Table 3.2), the equivalent ultimate point, and the ultimate point. The following parameters are required to define the model: the elastic modulus E_T, the p proof stress σ_{pT} and its strain ε_{pT}, the stress and strain of the equivalent ultimate point σ_{euT} and ε_{euT}, the ultimate strength σ_{uT}, and the ultimate strain ε_{uT}. Among these parameters, two pairs are related by definition: $\varepsilon_{pT} = \sigma_{pT}/E_T + p$ and $\sigma_{euT} = 0.99\sigma_{uT}$. In addition, two exponential coefficients n and m are also required to describe the nonlinearity of the first and the second stage model respectively.

In general, the elastic modulus is determined from the stress-strain curve as the

slope of its initial linear portion. For Mode 1 behavior (rounded curve without a distinct yield point), the linear portion is less obvious. The method from Huang and Young [10] is adopted where the slope of the linear regression for all data between 20% and 45% of nominal yield strength is regarded as the elastic modulus. An update is made to adopt this method for high-temperature tests to include the deterioration from a high-temperature environment. The update is to proportion the nominal yield strength at ambient, σ_{ny0}, by the deterioration of the experimental ultimate strength as calculated by Eq. 3.33:

$$\sigma_{nyT} = \sigma_{ny0} \times \frac{\sigma_{uT}}{\sigma_{u0}} \tag{3.33}$$

where σ_{ny} is the nominal yield strength, subscript 0 represents ambient, and subscript T represents an elevated temperature.

Parameters for the steady-state tests are shown in Table 3.3, including E_T, σ_{pT}, σ_{uT}, ε_{euT}, ε_{uT}, n and m. The test data is used as the benchmark to develop the predictive equations for the retention factor of the parameters required by the proposed model. The calibrated coefficients of the unified equation for these parameters are shown in Table 3.4. Relationships between the parameter retention factors and T are shown in Fig. 3.10 to Fig. 3.14.

Table 3.3: Properties required by the proposed two-stage plus linear model (Eq. 3.23, 3.24, and 3.25) from AHSS steady-state test results.

T (°C)	DP-340	DP-700	HSLA-700	MS-1030	MS-1200	DP-340	DP-700	HSLA-700	MS-1030	MS-1200
	E_T (GPa)									
20	202.2	203.3	208.1	216.0	207.9					
200	170.0	177.9	182.4	218.2	166.3					
300	131.1	192.5	181.9	177.1	167.5					
400	146.4	160.3	151.2	156.5	129.0					
500	110.6	103.0	89.3	62.8	68.6					
600	82.6	48.6	63.7	43.1	36.5					
700	76.0	38.0	55.4	18.5	19.7					
	σ_{pT} (MPa)					σ_{uT} (MPa)				
20	552.5	944.4	967.9	1379.3	1466.5	675.0	1025.6	1106.3	1427.6	1594.8
200	631.7	964.8	931.8	1342.4	1406.5	771.7	1099.0	1045.4	1509.3	1639.8
300	524.5	838.0	895.4	994.5	997.5	620.4	972.1	1053.0	1038.4	1073.9
400	274.0	483.1	634.8	499.9	490.5	357.2	590.8	835.1	577.7	565.9
500	171.4	260.3	365.7	219.6	217.0	194.3	306.2	425.9	270.6	277.8
600	97.1	111.7	119.5	94.3	76.5	102.9	120.7	141.3	114.5	99.5
700	41.6	41.7	30.1	26.2	28.5	45.2	49.2	42.9	43.2	42.5
	ε_{euT}					ε_{uT}				
20	0.112	0.045	0.055	0.017	0.026	0.154	0.075	0.090	0.027	0.036
200	0.094	0.060	0.035	0.035	0.036	0.123	0.087	0.056	0.056	0.051
300	0.079	0.047	0.056	0.014	0.016	0.120	0.063	0.073	0.018	0.020
400	0.048	0.017	0.034	0.010	0.012	0.067	0.026	0.045	0.017	0.015
500	0.047	0.024	0.018	0.018	0.024	0.077	0.032	0.044	0.025	0.027
600	0.007	0.010	0.015	0.035	0.035	0.024	0.010	0.030	0.055	0.044
700	0.005	0.010	0.031	0.075	0.053	0.014	0.023	0.046	0.115	0.059
	n					m				
20	7.1	8.8	6.2	15.2	15.8	4.2	2.9	3.2	1.9	4.5
200	5.8	7.0	7.4	7.8	5.8	3.0	3.3	1.8	3.4	3.7
300	6.0	6.7	6.7	6.7	5.6	3.7	3.1	3.3	2.3	2.2
400	7.2	6.3	7.0	4.6	5.3	5.1	4.3	4.4	3.9	3.2
500	7.1	6.3	10.5	5.5	4.9	11.1	8.2	4.5	3.3	7.9
600	9.0	7.6	4.9	5.1	5.0	4.0	5.7	3.2	6.4	5.4
700	5.6	7.6	4.2	7.6	7.6	4.0	3.3	3.4	3.4	3.8

Table 3.4: Proposed coefficients for the unified predictive equation (Eq. 3.30) of material property parameters required by the two-stage plus linear model for the steady-state tests.

steel	T (°C)	a	b	c	T (°C)	a	b	c
	E_T							
DP-340	[20, 700]	0.53	1.16	0.37				
DP-700	[20, 700]	3.50	4.08	0.15				
HSLA-700	[20, 700]	6.51	4.11	0.24				
MS-1030	[20, 700]	10.00	4.99	0.08				
MS-1200	[20, 700]	1.17	2.15	0.06				
	σ_{pT}				σ_{uT}			
DP-340	[20, 700]	48.00	6.64	0.12	[20, 700]	30.85	6.12	0.09
DP-700	[20, 700]	22.45	5.58	0.06	[20, 700]	25.53	6.25	0.06
HSLA-700	[20, 700]	8.22	5.07	0.02	[20, 700]	14.12	6.50	0.03
MS-1030	[20, 700]	30.26	4.94	0.03	[20, 700]	23.48	4.76	0.04
MS-1200	[20, 700]	29.91	4.73	0.02	[20, 700]	29.27	4.74	0.04
	ε_{euT}				ε_{uT}			
DP-340	[20, 700]	1.26	1.97	0.01	[20, 700]	0.91	1.76	0.07
DP-700	[20, 700]	5.72E+05	19.77	0.27	[20, 700]	215.39	7.50	0.17
HSLA-700	[20, 700]	0.00	0.72	0.25	[20, 700]	0.00	0.53	0.33
MS-1030	[20, 400]	5.08E+05	14.88	0.58	[20, 400]	3.57E+08	20.23	0.63
MS-1200	[20, 400]	1.10E+06	14.84	0.46	[20, 400]	1.96E+06	14.95	0.41

For the strain parameters, ε_{euT} and ε_{uT} for MS steels above 400°C show apparent increasing trends. Therefore, for these cases, it is difficult to predict the strains using the unified equation (Eq. 3.30) only. Instead, a combination of the unified equation and one basic function is used to build piecewise predictive equations if necessary. To lower the equation's complexity while guaranteeing the prediction accuracy, the basic functions to fit the aforementioned strain cases include exponential function (Eq. 3.34) and linear function (Eq. 3.35). The calibrated coefficients of the unified predictive equation (Eq. 3.30) for the strains are shown in Table 3.4. The calibrated coefficients of the basic functions (Eq. 3.34 and 3.35) are shown in Table 3.5. The fits of ε_{euT} and ε_{uT} between the predictive equation and experimental data are shown in Fig. 3.13 and Fig. 3.14.

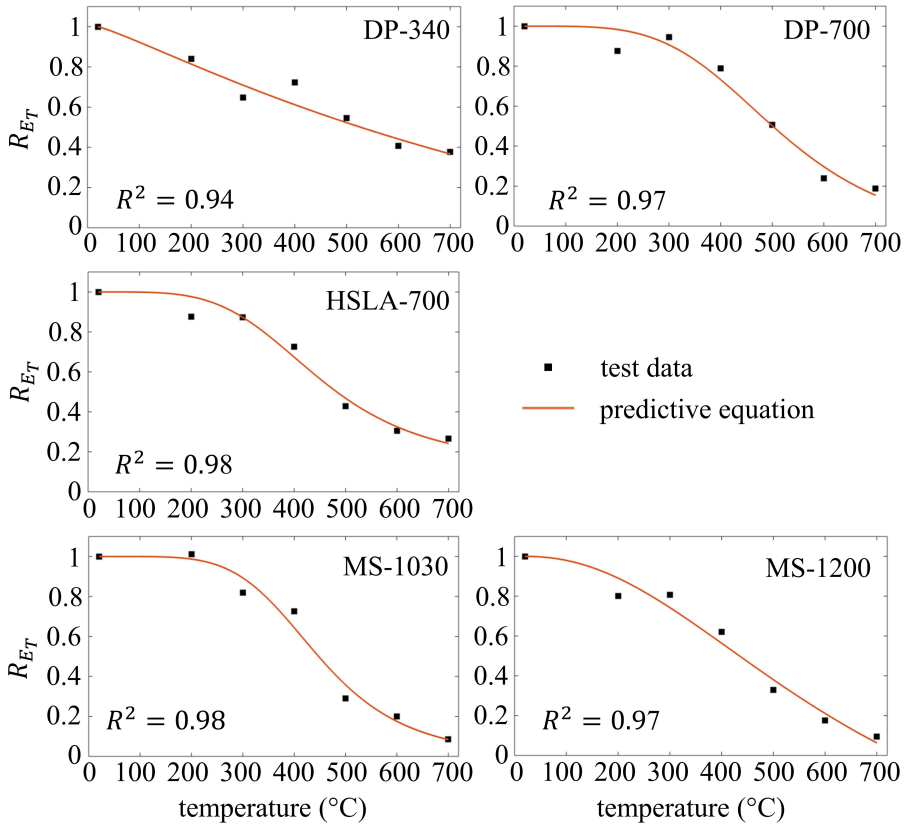

Figure 3.10: Prediction of AHSS elastic modulus for steady-state tests by Eq. 3.30 using proposed coefficients.

$$R_{X_T} = ae^{bT} \tag{3.34}$$

$$R_{X_T} = aT + b \tag{3.35}$$

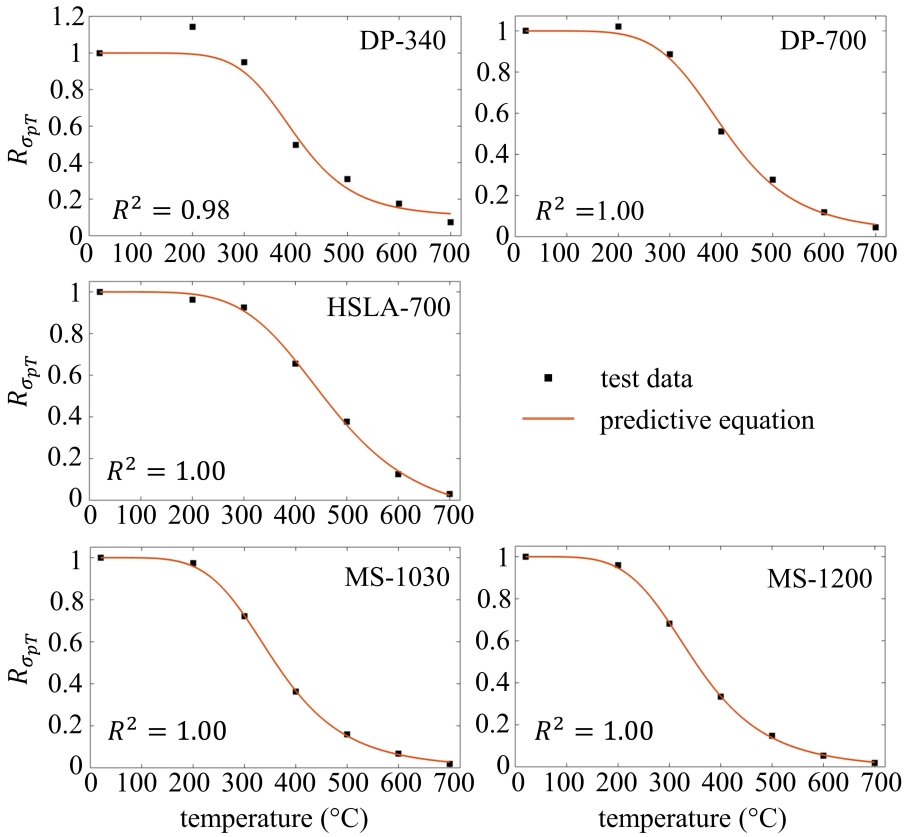

Figure 3.11: Prediction of AHSS p proof stress for steady-state tests by Eq. 3.30 using proposed coefficients.

Table 3.5: Proposed coefficients for the basic equations of required strains for AHSS steady-state tests.

	T (°C)	form	a	b
strain at equivalent ultimate point ε_{euT}				
MS-1030	(400, 700]	exp.	0.04	6.61E-03
MS-1200	(400, 700]	linear	5.05E-03	-1.56
ultimate strain ε_{uT}				
MS-1030	(400, 700]	exp.	0.05	6.34E-03
MS-1200	(400, 700]	linear	3.96E-03	-1.18

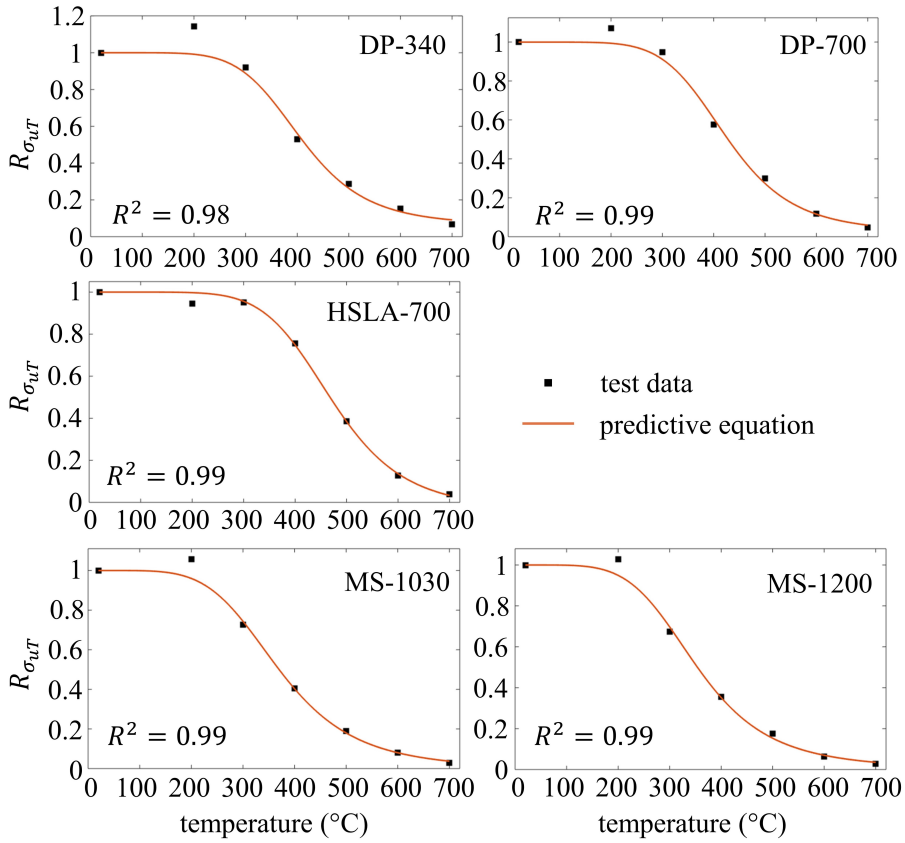

Figure 3.12: Prediction of AHSS ultimate strength for steady-state tests by Eq. 3.30 using proposed coefficients.

3.6.2 Transient-state tests

For modeling the transient-state test results, Chen and Ye's model [48] is adopted. E_T, the 0.2% proof stress $\sigma_{0.2T}$, and the exponential coefficient n at the elevated temperature T are required to define the model. As discussed in Section 3.3, for the experimental stress-strain curves generated from the AHSS transient-state tests, the curves do not approach the ultimate point. Therefore σ_{uT} is not available, and Eq. 3.33 can not be adopted to calculate σ_{nyT} and E_T. Thus, a modification is

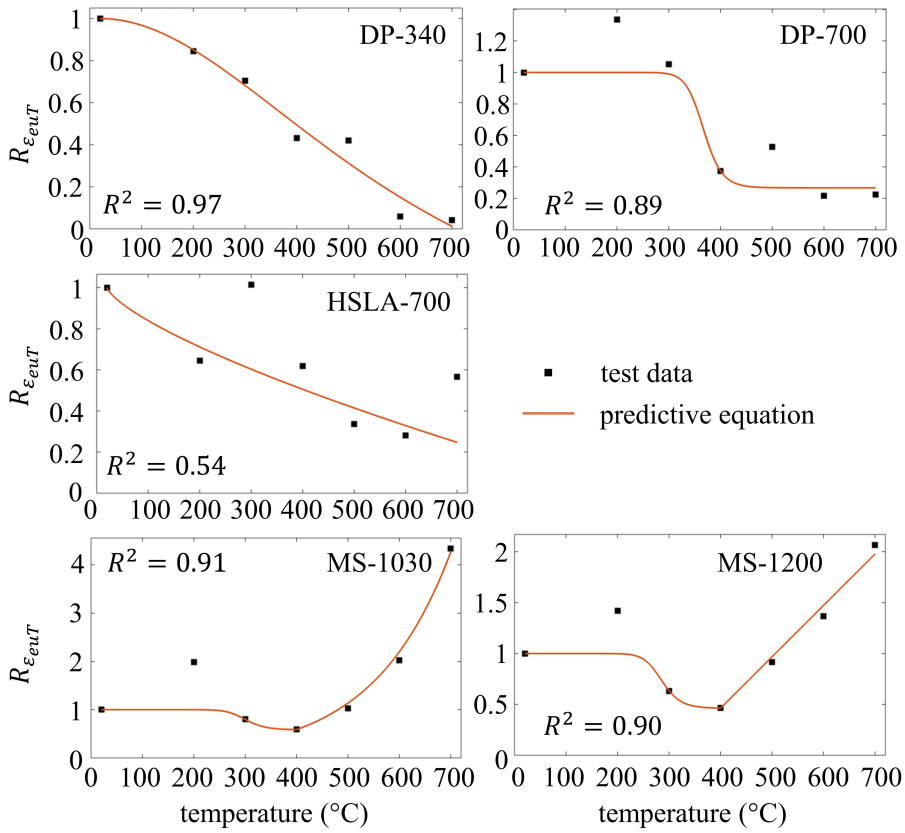

Figure 3.13: Prediction for the strain of the equivalent ultimate point for steady-state tests.

made on Eq. 3.33 for transient-state tests. The ratio between $\sigma_{t0.5T}$ (the stress at $\varepsilon_T = 0.005$ at T) and $\sigma_{t0.5,0}$ (the stress at $\varepsilon = 0.005$ at ambient) is used to account for the deterioration of the nominal yield strength at T, as shown in Eq. 3.36.

$$\sigma_{nyT} = \sigma_{ny0} \times \frac{\sigma_{t0.5T}}{\sigma_{t0.5,0}} \tag{3.36}$$

The parameters of the model for transient tests are listed in Table 3.6, including E_T, $\sigma_{0.2T}$, and n. The calibrated coefficients of the unified predictive equation (Eq. 3.30) for E_T and $\sigma_{0.2T}$ required by Chen and Ye's model [48] are shown in Table

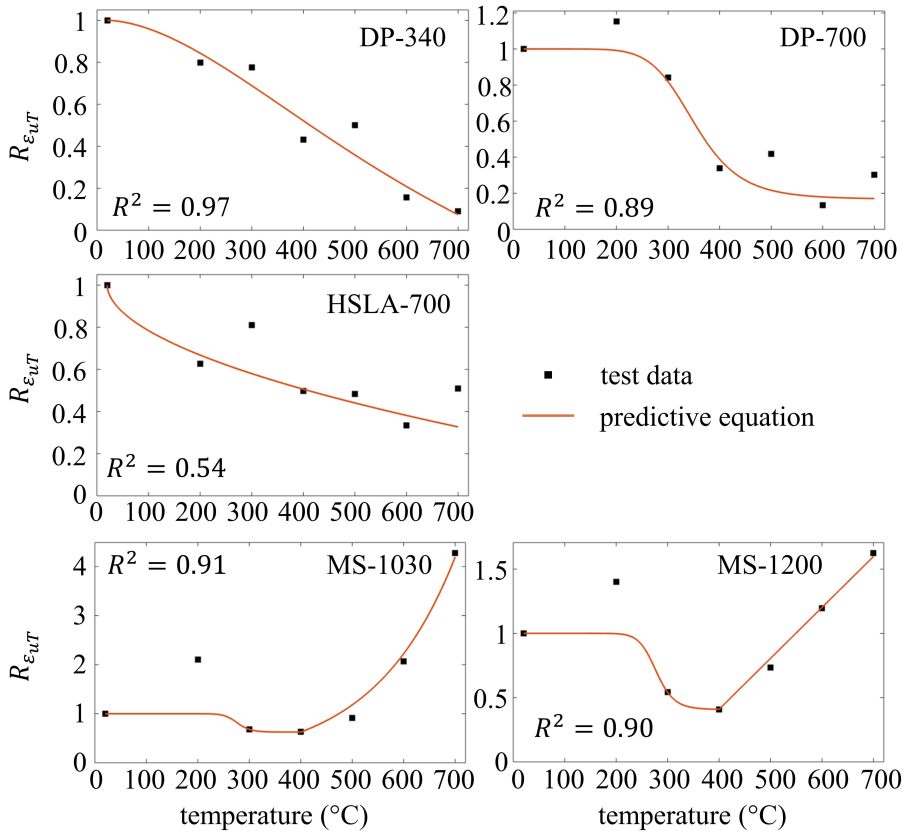

Figure 3.14: Prediction for the ultimate strain for steady-state tests.

3.7. The fits of the parameters between the proposed predictive equation and experimental values are shown in Fig 3.15 and Fig. 3.16.

3.6.3 Residual tests

For the residual test, a small number of tests show Mode 1 (i.e. gradual yielding with a nonlinear curve shape) stress-strain behavior, and they are modeled by the two-stage plus linear model (Eq. 3.23, 3.24, and 3.25). Mode 1 behavior is generally observed when the test temperature is lower than 200°C. The only exception is

Table 3.6: Properties required by the recommended one-stage model [48] from AHSS transient-state test results.

T (°C)	DP-700	MS-1200	DP-700	MS-1200	DP-700	MS-1200
	E_T (GPa)		$\sigma_{0.2T}$ (MPa)		n	
20	214.0	207.9	721.0	1327.2	4.8	9.1
100	190.4	206.9	703.8	1259.7	6.4	8.3
150	180.4	200.0	699.1	1095.2	6.8	5.1
200	164.9	185.7	700.2	1004.1	7.5	4.3
250	155.9	165.4	686.2	929.4	7.8	4.7
300	140.1	121.6	654.3	844.7	7.8	6.8
350	121.7	72.5	574.8	701.1	7.1	6.2
400	104.1	60.5	512.2	425.4	5.5	3.6
450	66.0	44.5	371.9	222.2	6.5	2.5
500	41.4	20.4	196.3	128.2	6.2	3.4
550	16.5	8.8	108.9	85.4	5.5	5.4
600	5.0	3.2	72.7	64.3	5.5	6.4

Table 3.7: Proposed coefficients for the predictive equation (Eq. 3.30) of elastic modulus and 0.2% proof stress required by the recommended one-stage R-O model [48] for transient-state test.

steel	T (°C)	a	b	c
	E_T			
DP-700	[20, 600]	0.00	1.47	0.01
MS-1200	[20, 600]	13.14	4.12	0.01
	$\sigma_{0.2T}$			
DP-700	[20, 600]	6.13	6.51	0.07
MS-1200	[20, 600]	2.31	2.46	0.00

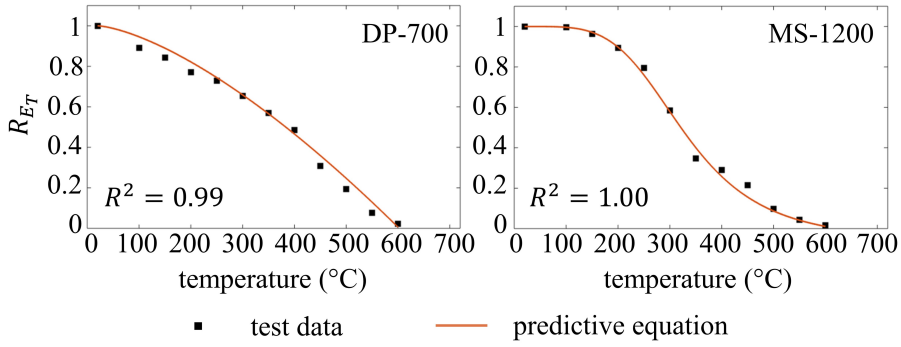

Figure 3.15: Prediction of AHSS elastic modulus for transient-state tests by Eq. 3.30 using proposed coefficients.

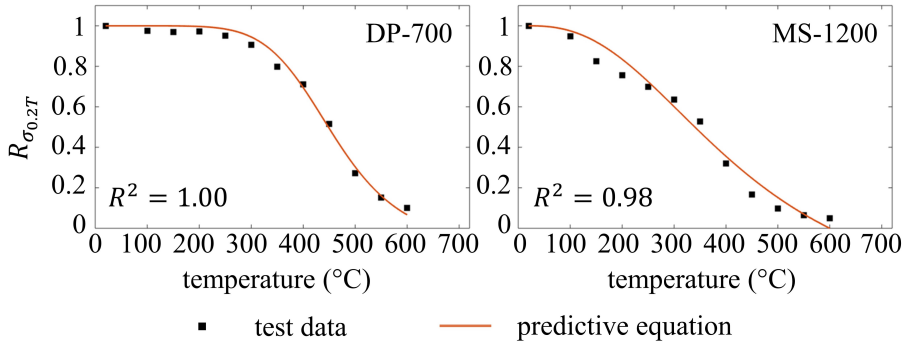

Figure 3.16: Prediction of AHSS 0.2% proof stress for transient-state tests by Eq. 3.30 using proposed coefficients.

Table 3.8: Required parameters of the proposed two-stage plus linear model from residual test with Mode 1 behavior.

T (°C)	DP-340	DP-700	MS-1030	MS-1200	DP-340	DP-700	MS-1030	MS-1200
	σ_{pT} (MPa)				ε_{euT}			
20	552.5	944.4	1379.3	1466.5	0.112	0.045	0.017	0.026
200	-	935.0	1424.7	1472.9	-	0.042	0.018	0.026
700	-	378.7	-	-	-	0.081	-	-
	n				m			
20	7.1	8.8	15.2	15.8	4.2	2.9	1.9	4.5
200	-	12.4	42.1	21.8	-	3.0	1.7	6.9
700	-	12.3	-	-	-	5.8	-	-

DP-700 from the 700°C test, which also shows Mode 1 behavior. Parameters E_T, σ_{pT}, σ_{uT}, ε_{euT}, ε_{uT}, n, and m are needed to adopt the proposed two-stage plus linear model (Eq. 3.23, 3.24, and 3.25). The values of these parameters as shown in Table 3.8 are determined by following the same procedures as the steady-state tests described in Section 3.5.1. Note that E_T, σ_{uT}, and ε_{uT} are also required by the updated bilinear plus nonlinear hardening model for the residual tests with Mode 2 behavior. Therefore, they are discussed together next and are given in Table 3.9. Due to the limited number of tests observed with Mode 1 behavior, it is difficult to conclude any credible trend for the material properties.

Most post-fire stress-strain curves show Mode 2 behavior. They are modeled by the updated bilinear plus nonlinear hardening model (Eq. 3.13, 3.14, and 3.18). The model requires elastic modulus E_T, yield strength σ_{yT}, yield strain ε_{yT}, ε_{shT} (the strain at the end of the yield plateau and the onset of the nonlinear strain hardening), ultimate strength σ_{uT}, ultimate strain ε_{uT}, and three coefficients (K1 to K3 describing the nonlinearity of the strain hardening process). Among these parameters, E_T, σ_{yT}, and ε_{yT} are related as $\varepsilon_{yT} = \sigma_{yT}/E_T$, therefore when any two of the three parameters are known, the other parameter can be calculated. Considering both simplicity and accuracy, K1 to K3 are recommended as 0.029, 4.713, and 3.855 respectively by a statistical study on the test curves using the error minimization method as discussed in Section 3.5.2.

For Mode 1 post-fire stress-strain behaviors, E_T is calculated using the same method as the steady-state tests described in Section 3.6.1. For Mode 2 post-fire stress-strain behaviors, clear linear elastic behavior is observed up to the yield point. Therefore E_T is calculated as the slope of the linear portion. E_T for the residual tests is shown in Table 3.9, and the relationship between its retention factor R_{E_T} and T is shown in Fig. 3.17.

For residual tests showing Mode 2 behavior, σ_{yT} is the stress at the yield point, where the linear elastic region ends and the yield plateau begins. σ_{yT} is shown in Table 3.9, and the relationship between its retention factor $R_{\sigma_{yT}}$ and T is shown in Fig. 3.18. σ_{yT} shows a clear gradual decreasing trend when T increases; σ_{yT} of DP-700, MS-1030, and MS-1200 have similar deterioration rates, while σ_{yT} of DP-340 deteriorates at a slower rate.

Table 3.9: Properties required by the proposed models from AHSS residual test results.

T (°C	DP-340	DP-700	MS-1030	MS-1200	DP-340	DP-700	MS-1030	MS-1200
	E_T (GPa)							
20	202.2	203.3	216.0	207.9				
200	210.4	208.1	212.9	207.4				
300	195.9	208.0	216.2	209.3				
400	218.2	213.3	211.8	204.5				
500	208.2	220.9	217.5	229.6				
600	205.3	217.7	231.8	215.0				
700	196.5	117.3	195.7	161.7				
	σ_{yT} (Mode 2) (MPa)				σ_{uT} (MPa)			
20	-	-	-	-	675.0	1025.6	1427.6	1594.8
200	528.6	-	-	-	690.6	1011.4	1455.7	1595.8
300	498.1	892.4	1371.0	1371.0	649.1	982.7	1389.8	1437.6
400	491.0	803.9	1030.0	1102.0	578.6	848.9	1041.2	1118.7
500	432.1	627.4	753.0	836.9	509.0	702.0	774.1	858.1
600	384.4	453.7	656.1	678.5	459.6	543.2	670.5	700.7
700	351.7	-	428.7	501.1	448.0	714.9	482.0	531.4
	ε_{shT} (Mode 2)				ε_{uT}			
20	-	-	-	-	0.154	0.075	0.027	0.036
200	0.018	-	-	-	0.159	0.072	0.039	0.040
300	0.015	0.014	0.013	0.014	0.129	0.048	0.044	0.036
400	0.021	0.014	0.015	0.014	0.146	0.033	0.030	0.040
500	0.030	0.018	0.039	0.036	0.146	0.098	0.059	0.055
600	0.037	0.028	0.041	0.047	0.177	0.138	0.071	0.069
700	0.038	-	0.050	0.055	0.200	0.099	0.177	0.126

The ultimate strength σ_{uT} is defined as the peak stress of the nonlinear strain hardening region. Note that σ_{uT} is not necessarily the peak stress of the curve, because the upper yield strength of several cases with Mode 2 behavior is larger than the ultimate strength (e.g., the 600°C test for MS-1200). σ_{uT} is shown in Table 3.9, and the relationship between its retention factor $R_{\sigma_{uT}}$ and T is shown in Fig. 3.19. No significant decrease is observed up to 200°C or 300°C. Above 300°C, clear decreasing trends are observed, and the MS steel shows a more rapid deterioration rate than the DP steel.

By definition, ε_{yT} can be calculated by $\varepsilon_{yT} = \sigma_{yT}/E_T$, where the predictions of

Table 3.10: Proposed coefficients for the unified predictive equation (Eq. 3.30) of material property parameters required by the updated bilinear plus nonlinear hardening model for the residual tests.

steel	T (°C)	a	b	c	T (°C)	a	b	c
	E_T							
DP-340	[20, 700]	7.47E+05	12.47	0.97				
DP-700	[20, 700]	0.00	59.53	0.58				
MS-1030	[20, 700]	0.00	7.10	0.91				
MS-1200	[20, 700]	1.30E-05	15.80	0.78				
	σ_{yT} (Mode 2)				σ_{uT}			
DP-340	[200, 700]	2.14	3.85	0.66	[20, 700]	15.18	5.46	0.66
DP-700	[300, 600]	9.91	6.97	0.42	[20, 700]	12.56	5.66	0.51
MS-1030	[300, 700]	10.74	5.47	0.35	[20, 700]	14.04	5.51	0.37
MS-1200	[300, 700]	8.37	5.49	0.38	[20, 700]	7.30	4.24	0.35
	ε_{shT} (Mode 2)				ε_{uT}			
DP-340	[200, 300]	0.00	0.00	1.00	[20, 500]	0.00	0.00	1.00
DP-700	-	-	-	-	[20, 400]	798.69	7.01	0.40
MS-1030	[300, 400]	0.00	0.00	1.00	-	-	-	-
MS-1200	[300, 400]	0.00	0.00	1.00	[20, 300]	0.00	0.00	1.00

σ_{yT} and E_T are given in this section. ε_{shT} for residual tests with Mode 2 behavior is shown in Table 3.9, and the relationship between its retention factor $R_{\varepsilon_{shT}}$ and T is shown in Fig. 3.20. ε_{shT} is stable up to 400°C and then increases rapidly when T increases. ε_{shT} of MS steel increases more rapidly than DP steel.

ε_{uT} is shown in Table 3.9, and the relationship between its retention factor $R_{\varepsilon_{uT}}$ and T is shown in Fig. 3.21.

The test data is used as the benchmark to develop the predictive equations for the retention factor of the parameters required by the proposed model. The calibrated coefficients of the unified predictive equation (Eq. 3.30) for E_T, σ_{yT} (Mode 2), and σ_{uT} are shown in Table 3.10. The fits of these properties between the experimental values and the predicted values are shown from Fig 3.17 to Fig. 3.19.

For the required strain parameters, several cases captured from the test curves show an increasing trend at a higher temperature range (e.g., above 400°C). There-

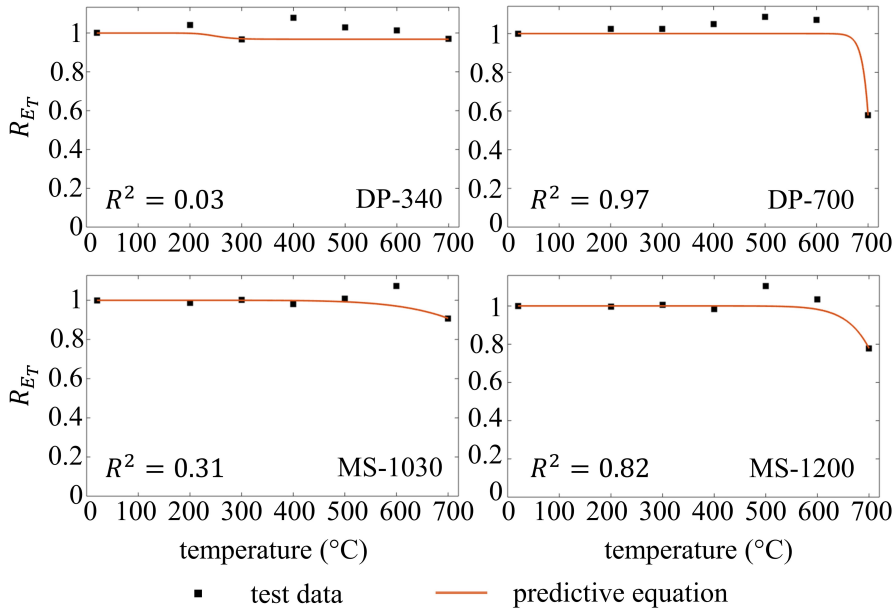

Figure 3.17: Prediction of AHSS elastic modulus for residual tests by Eq. 3.30 using proposed coefficients.

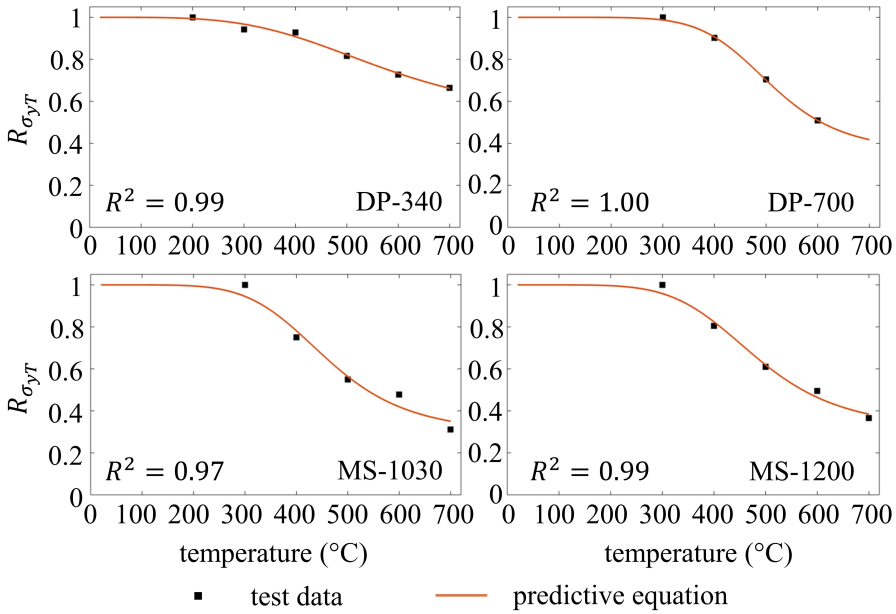

Figure 3.18: Prediction of AHSS yield strength for Mode 2 residual tests by Eq. 3.30 using proposed coefficients.

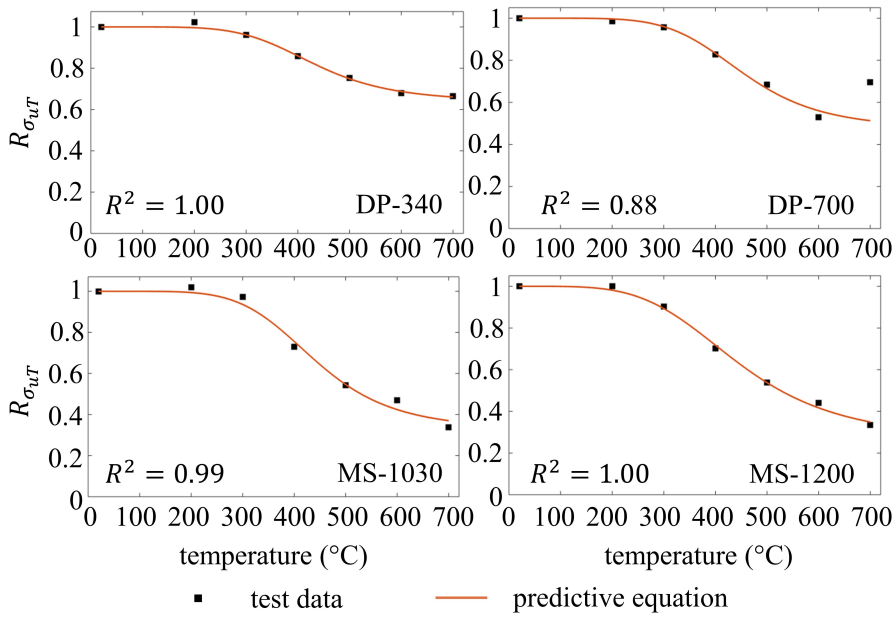

Figure 3.19: Prediction of AHSS ultimate strength for residual tests by Eq. 3.30 using proposed coefficients.

fore, it is difficult to accurately predict these strains using the unified equation (Eq. 3.30) only. A combination of the unified equation and a polynomial function up to a cubic (Eq. 3.37) is used to develop the piecewise predictive equations for strains. These equations best fit the existing experimental data. A simpler function could be proposed if less accuracy to the current data is acceptable, especially considering the variability in strain.

$$R_{X_T} = aT^3 + bT^2 + cT + d \tag{3.37}$$

The calibrated coefficients of the unified predictive equation (Eq. 3.30) for the strains are shown in Table 3.10. The calibrated coefficients of the polynomial are shown in Table 3.11, where the required strains show a clear increasing trend when

Table 3.11: Proposed coefficients for the polynomial equation of required strains from AHSS residual tests.

	T (°C)	a	b	c	d
	ε_{shT} (Mode 2)				
DP-340	(300, 700]	-5.49E-08	8.03E-05	-0.034	5.51
DP-700	[300, 600]	0.00	1.70E-05	-0.012	3.03
MS-1030	(400, 700]	4.00E-07	-6.89E-04	0.40	-72.70
MS-1200	(400, 700]	0.00	-2.67E-05	0.04	-10.29
	ε_{uT}				
DP-340	(500, 700]	0.00	0.00	1.47E-03	0.26
DP-700	(400, 700]	0.00	-3.33E-05	0.04	-10.11
MS-1030	[20, 700]	8.24E-08	-6.83E-05	1.56E-02	0.66
MS-1200	(300, 700]	0.00	1.91E-05	-1.32E-02	3.25

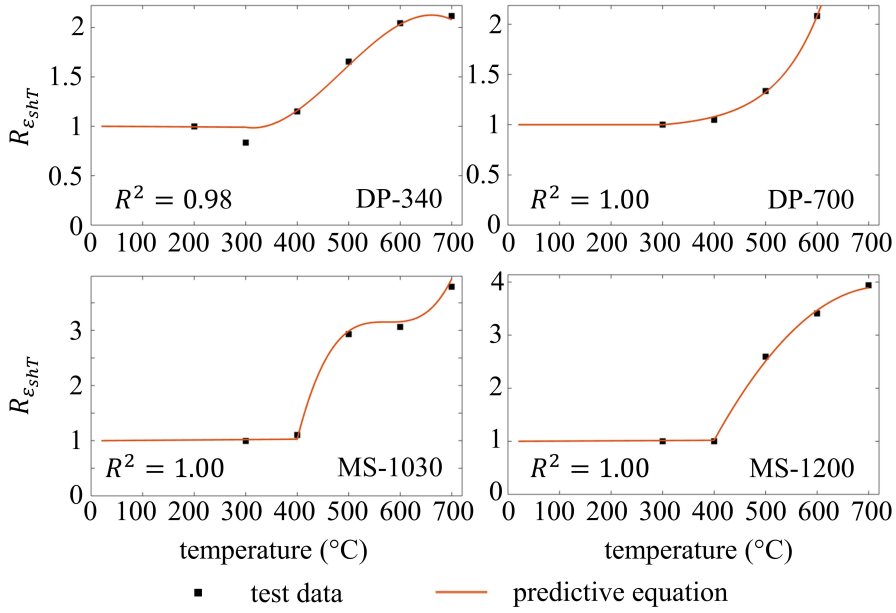

Figure 3.20: Prediction of ε_{shT} for Mode 2 residual tests.

T increases. The fits of the strains between the proposed predictive equation and experimental value are shown in Fig 3.20 and Fig. 3.21.

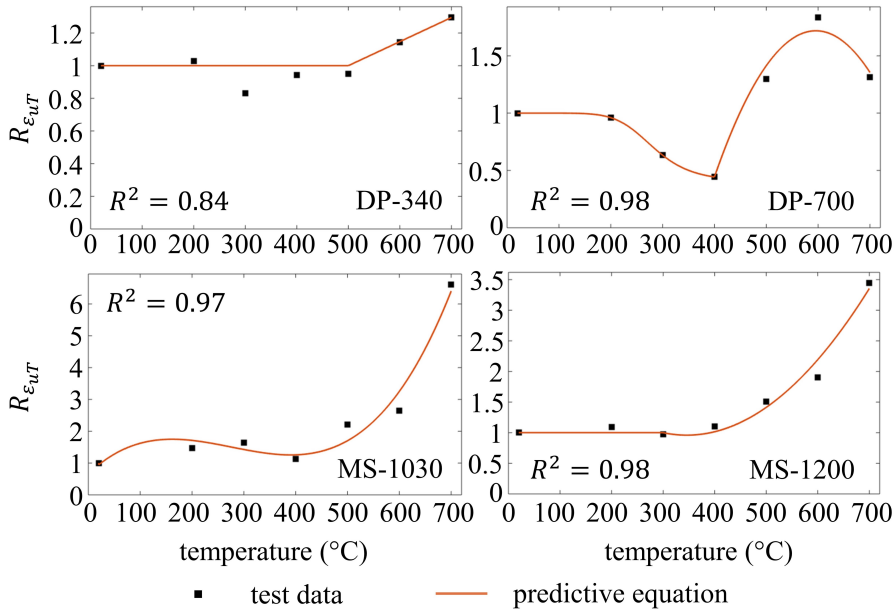

Figure 3.21: Prediction for the ultimate strain for residual tests.

3.7 Examples of AHSS stress-strain relationship modeling at elevated temperature and after cooling down

In this study, models for AHSS stress-strain relationships in steady-state test, transient-state test, and residual test protocols based on experimental data are developed. The models can be used for material property definition in a numerical simulation for AHSS in various high-temperature scenarios. In this section a stress-strain modeling example for each type of test method following the procedures discussed in Sections 3.5 and 3.6 is provided.

The proposed models and model parameter prediction for each test method are

Table 3.12: Summary of model expressions and model parameter predictive equations for each test method.

test protocol	**model expression**	**parameter prediction**		
		predictive equation	parameter at ambient	equation coefficients
steady-state test	Eq. 3.23, 3.24, 3.25	Eq. 3.30, 3.34, 3.35	Table 3.3	Table 3.4, 3.5
transient-state test	Eq. 3.22	Eq. 3.30	Table 3.6	Table 3.7
residual test	Eq. 3.28	Eq. 3.30, 3.37	Table 3.9	Table 3.10, 3.11

summarized in Table 3.12. For models designed for Mode 1 stress-strain behavior, n and m at any desired temperature are calculated by linear interpolation between its two adjacent test temperatures given in Table 3.3. For the transient-state test modeling, the expression range is up to the ultimate strength, which is unavailable from the experiment. Therefore, the ultimate strength from the steady-state test is adopted as both test protocols are designed at elevated temperatures, and the ultimate strength is only used to define the model range and has no influence on the model shape. The stress-strain modeling examples are shown in Table 3.13 and Eq. 3.38 for the steady-state test, Table 3.14 and Eq. 3.39 for the transient-state test, and Table 3.15 and Eq. 3.40 for the residual test. The numbers in Eq. 3.38, 3.39, and 3.40 are in N-mm-MPa system.

(Example 1) σ-ε modeling for MS-1200 at 450°C from the steady-state test:

$$\varepsilon_{450} = \begin{cases} \frac{\sigma_{450}}{98015} + 0.002\left(\frac{\sigma_{450}}{318.7}\right)^{5.13} & \text{for } 0 \leqslant \sigma_{450} \leqslant 318.7 \\ \frac{\sigma_{450}-318.7}{23576} + 0.011\left(\frac{\sigma_{450}-318.7}{48.6}\right)^{5.56} + 5.25\text{E-}03 & \text{for } 318.7 < \sigma_{450} \leqslant 367.3 \\ 1.01\text{E-}03(\sigma_{450} - 367.3) + 0.018 & \text{for } 367.3 < \sigma_{450} \leqslant 371.0 \end{cases} \tag{3.38}$$

(Example 2) σ-ε modeling for DP-700 at 320°C from the transient-state test:

$$\varepsilon_{320} = \frac{\sigma_{320}}{133227} + 0.002\left(\frac{\sigma_{320}}{660.3}\right)^{7.49} \text{ for } 0 \leqslant \sigma_{320} \leqslant 732.15 \tag{3.39}$$

(Example 3) σ-ε modeling for DP-340 after cooling down from 680°C from the residual test:

$$\sigma_{680} = \begin{cases} 195814\varepsilon_{680} & \text{for } 0 \leqslant \varepsilon_{680} \leqslant 1.82\text{E-}03 \\ 356.4 & \text{for } 1.82\text{E-}03 < \varepsilon_{680} \leqslant 0.039 \\ 356.4 + 92.0\left(0.029\varepsilon_{n680} + \frac{4.713\varepsilon_{n680}}{1+3.855\varepsilon_{n680}}\right) & \text{for } 0 < \varepsilon_{n680} \leqslant 1 \end{cases} \tag{3.40}$$

where $\varepsilon_{n680} = \frac{\varepsilon_{680}-0.039}{0.156}$ for $0.039 < \varepsilon_{680} \leqslant 0.195$.

Table 3.13: Calculation of the required parameters of the proposed model for the steady-state test example.

Parameter	Calculation	Required parameters	Parameter value
Determination of intermediate parameters			
p	Table 3.2	-	0.002
T_{nor}	Eq. 3.31	$T = 450°C$, $T_{max} = 700°C$, $T_{min} = 20°C$	0.632
Calculation of independent parameters			
E_{450}	Eq. 3.30, Table 3.3 and 3.4	$E_0 = 207920$ MPa, $a = 1.17$, $b = 2.15$, $c = 0.06$	98015 MPa
σ_{p450}	Eq. 3.30, Table 3.3 and 3.4	$\sigma_{p0} = 1466.5$ MPa, $a = 29.91$, $b = 4.73$, $c = 0.02$	318.7 MPa
σ_{u450}	Eq. 3.30, Table 3.3 and 3.4	$\sigma_{u0} = 1594.8$ MPa, $a = 29.27$, $b = 4.74$, $c = 0.04$	371.0 MPa
ε_{eu450}	Eq. 3.35, Table 3.3 and 3.5	$\varepsilon_{eu0} = 0.026$, $a = 5.05$E-3, $b = -1.56$	0.018
ε_{u450}	Eq. 3.35, Table 3.3 and 3.5	$\varepsilon_{u0} = 0.036$, $a = 3.96$E-3, $b = -1.18$	0.022
n_{450}	linear interpolation, Table 3.3	$n_{400} = 5.3$, $n_{500} = 4.9$	5.13
m_{450}	linear interpolation, Table 3.3	$m_{400} = 3.2$, $m_{500} = 7.9$	5.56
Calculation of dependent parameters			
ε_{p450}	$0.002 + \sigma_{p450}/E_{450}$	$\sigma_{p450} = 318.7$ MPa, $E_{450} = 98015$ MPa	5.25E-3
σ_{eu450}	$0.99\sigma_{u450}$	$\sigma_{u450} = 371.0$ MPa	367.3 MPa
E_{p450}	Eq. 3.27	$\sigma_{p450} = 318.7$ MPa, $E_{450} = 98015$ MPa, $n_{450} = 5.13$	23576 MPa

Table 3.14: Calculation of the required parameters of the recommended model for the transient-state test example.

Parameter	Calculation	Required parameters	Parameter value
Determination of intermediate parameters			
T_{nor}	Eq. 3.31	$T = 320°C$, $T_{max} = 600°C$, $T_{min} = 20°C$	0.517
Calculation of parameters			
E_{320}	Eq. 3.30, Table 3.6 and 3.7	$E_0 = 214017$ MPa, $a = 0.00$, $b = 1.47$, $c = 0.01$	133227 MPa
$\sigma_{0.2,320}$	Eq. 3.30, Table 3.6 and 3.7	$\sigma_{0.2,0} = 721.0$ MPa, $a = 6.13$, $b = 6.51$, $c = 0.07$	660.3 MPa
σ_{u320}	Eq. 3.30, Table 3.6 and 3.7	$\sigma_{u0} = 1025.6$ MPa, $a = 25.53$, $b = 6.25$, $c = 0.06$	732.15 MPa
n_{320}	linear interpolation, Table 3.6	$n_{300} = 7.8$, $n_{350} = 7.1$	7.49

Table 3.15: Calculation of the required parameters of the proposed model for the residual test example.

Parameter	Calculation	Required parameters	Parameter value
Determination of intermediate parameters			
T_{nor}	Eq. 3.31	$T = 680°C$, $T_{max} = 700°C$, $T_{min} = 20°C$	0.971
Calculation of independent parameters			
E_{680}	Eq. 3.30, Table 3.9 and 3.10	$E_0 = 202232$ MPa, $a = 7.47E{+}5$, $b = 12.47$, $c = 0.97$	195814 MPa
σ_{y680}	Eq. 3.30, Table 3.9 and 3.10	$\sigma_{y200} = 528.6$ MPa, $a = 2.14$, $b = 3.85$, $c = 0.66$	356.4 MPa
σ_{u680}	Eq. 3.30, Table 3.9 and 3.10	$\sigma_{u0} = 675.0$ MPa, $a = 15.18$, $b = 5.46$, $c = 0.66$	448.4 MPa
ε_{u680}	Eq. 3.37, Table 3.9 and 3.11	$\varepsilon_{u0} = 0.154$, $a = b = 0$, $c = 1.47E{-}3$, $d = 0.26$	0.195
ε_{sh680}	Eq. 3.37, Table 3.9 and 3.11	$\varepsilon_{sh200} = 0.018$, $a = -5.49E{-}8$, $b = 8.03E{-}5$, $c = -0.034$, $d = 5.51$	0.039
Calculation of dependent parameters			
ε_{y680}	σ_{y680}/E_{680}	$\sigma_{y680} = 356.4$ MPa, $E_{680} = 195814$ MPa	1.82E-03

3.8 Conclusions

This paper presents a detailed numerical study on the stress-strain relationships for two dual-phase (DP) and two martensitic (MS) sheets of advanced high-strength steel (AHSS) at elevated temperatures and after cooling down. Test data recently collected by the authors from a series of steady-state, transient-state, and residual tests ranging from ambient to 700°C are used as the modeling benchmarks. It was found that the stress-strain behaviors are affected by the composition of AHSS (DP or MS), the strength of the steel, the testing protocol, and the maximum temperature. Overall, two stress-strain modes were observed from steady-state and residual test protocols: a gradual strain hardening process with no well-defined yield point (Mode 1), and a sharp strain hardening process with a distinct yield point and yield plateau (Mode 2). In general, AHSS from the steady-state tests shows Mode 1 while with a few exceptions for the residual tests, Mode 1 is observed when the test temperature is at or below 200°C, and Mode 2 is observed when the test temperature is 300°C or higher. Therefore, no single material model could be defined to represent all AHSS subjected to elevated temperatures.

Existing stress-strain models were reviewed and fitted to the AHSS experimental data. It was found that existing models based on the Ramberg-Osgood equation do not accurately capture the Mode 1 stress-strain curves. Therefore, an updated two-stage plus linear model based on the Ramberg-Osgood equation is proposed to describe the stress-strain relationship of AHSS with Mode 1 behavior. An existing material model was found to fit Mode 2 stress-strain curves but is updated to improve simplicity by reducing the number of required modeling parameters. The

fit between the experimental AHSS stress-strain curves and the corresponding proposed models is excellent. Predictive temperature-dependent equations for the parameters required by the proposed models are developed using a unified equation based on the statistical analysis of the experiment data, and calibrated coefficients for the predictive equations are provided. In addition, the methodology developed in this paper could be helpful for future research on the characterization of sophisticated material stress-strain behaviors.

Addendum

This section presents some discrete information as supplements of the published journal article, which is the main body from Abstract to Conclusion for this chapter.

The setup of the loading system and the elevated temperature equipment is shown in Fig. 3.22.

Fig. 3.1 and 3.3 illustrate the effects of elevated temperatures on the AHSS for steady-state test and residual test. Besides the observations discussed in Section 3.3, the significant impact on the fracture strain is observed, particularly for the MS steel. Table shows the percentage increment at elevated temperature for the fracture strain of MS steel comparing with the ambient values.

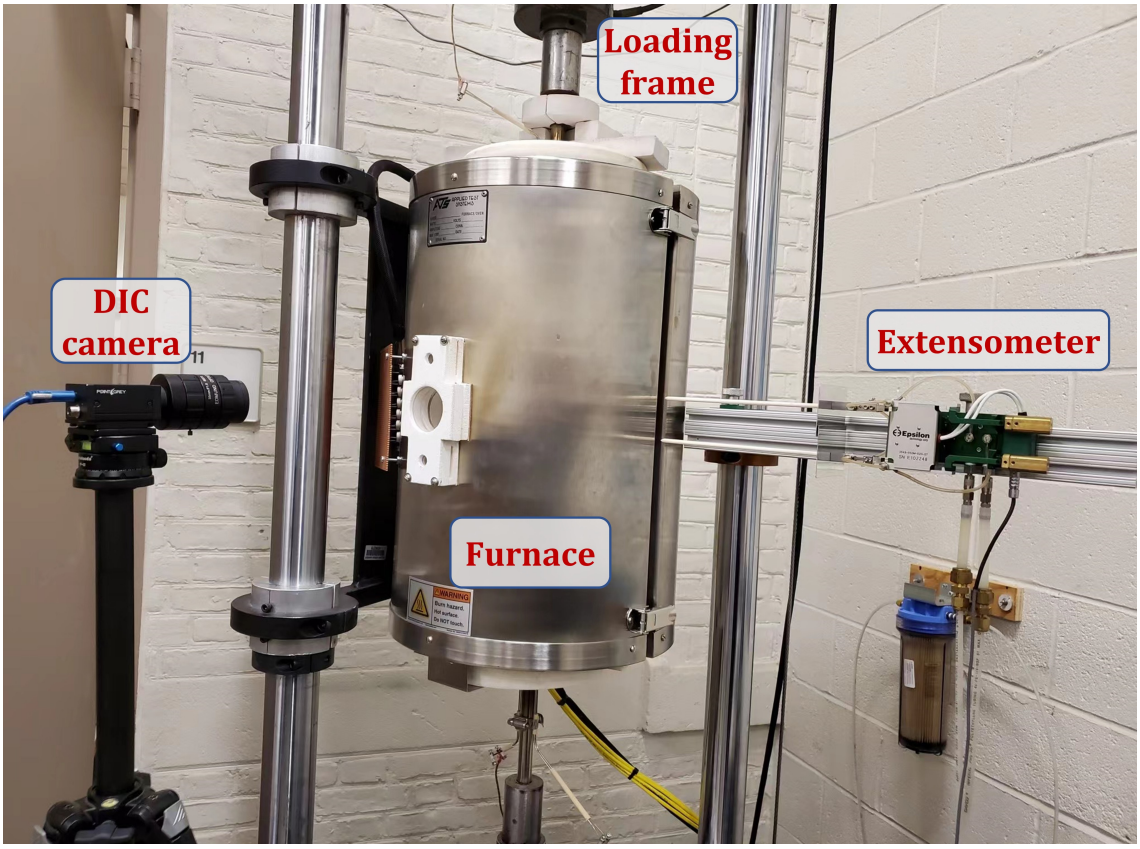

Figure 3.22: The setup of the loading system and the elevated temperature equipment for the tensile coupon test as described in [45], [46].

Table 3.16: Percentage increment of fracture strains for MS steel resulting from elevated temperatures. Fracture strains are from [45], [46].

	steady-state test				residual test			
	MS-1030		MS-1200		MS-1030		MS-1200	
T (°C)	ε_f (%)	$\Delta\varepsilon_f$	ε_f (%)	$\Delta\varepsilon_f$	ε_f (%)	$\Delta\varepsilon_f$	ε_f (%)	$\Delta\varepsilon_f$
20	2.95	0%	3.61	0%	2.95	0%	3.61	0%
200	10.83	267%	11.03	206%	5.25	78%	6.48	80%
300	9.07	207%	11.17	209%	6.28	113%	6.96	93%
400	11.78	299%	14.94	314%	7.66	160%	8.13	125%
500	24.55	732%	30.18	736%	12.86	336%	13.41	271%
600	>40	>1256%	>40	>1008%	13.58	360%	15.51	330%
700	>40	>1256%	>40	>1008%	21.48	628%	22.33	519%

Chapter 4

Material properties of advanced high-strength cold-formed steel alloys under subzero temperatures

Xia, Yu and Blum, Hannah B. "Material properties of advanced high-strength cold-formed steel alloys under subzero temperatures." Manuscript under review.

Abstract

In recent decades, the temperature in high latitude regions, including the Arctic, has been rapidly increasing for both cold and warm seasons. The warmer weather brings a substantial increase in the number of human activities, which creates a demand for infrastructure. In order to design safe infrastructure, the material properties at subzero temperature must be correctly quantified. Due to recent advances

in material science, new grades of cold-formed steel (CFS), referred to advanced high-strength steel (AHSS), have been developed, which show unprecedented strength. As cold-formed steel has a high strength-to-weight ratio among other benefits, it might be a suitable structural material in high latitude regions. However, the material properties of AHSS under subzero temperature environments have not been sufficiently quantified. In this paper, an experimental investigation following the steady-state test protocol was carried out to quantify the subzero temperature effects on the material properties of AHSS and conventional CFS sheets with yield strengths ranging from 395 MPa to 1200 MPa. Two types of AHSS (dual phase and martensitic) and two types of conventional CFS (mild and high-strength low-alloy) were investigated at temperatures down to -60°C. The stress-strain relationship, elastic modulus, and key stresses and strains were reported from the experiments. The results show that AHSS has larger yield and ultimate strengths and fracture elongation at subzero temperatures than at ambient, indicating the high potential for adopting AHSS as a construction material for structural members in the high latitude regions. Furthermore, predictive equations on critical material properties and stress-strain relationship at subzero temperatures were developed.

4.1 Introduction

As a result of rapid temperature increases in recent decades [80], the frigid high latitude regions, including north Russia, north Canada, north Scandinavia, Greenland, Alaska, and the Arctic, are open to more frequent human activities during warm

seasons, instead of people being discouraged by the gelid temperatures. Potentially linked to this shift, a rapidly increasing population has been observed in these high latitude regions for natural resource exploitation, scientific studies, and traveling [81], [82], although the permanent resident population has shown a marginal increase [83]. For example, tourism was estimated to have quadrupled in summer and increased by over 600% in winter between 2006 and 2016 in the Arctic [81]. These rapid changes lead to an increasing demand for infrastructure which is both a challenge and an opportunity [84].

Cold-formed steel (CFS), particularly thin-walled cold-formed high-strength steel, may be an ideal structural material for cold climates which are more remote due to its high strength-to-weight ratio requiring fewer transportation costs than hot-rolled structural steel and no need for formwork or skilled welders on site. Existing studies on the material properties of structural steel at subzero temperatures or even under a cryogenic environment are not rare, but most of them discuss hot-rolled steel [85]–[99], particularly hot-rolled stainless steel [100]–[110], where a large portion of the studies tested bar specimens with diameters between 4 mm and 20 mm or flat coupons with thicknesses greater than 3.0 mm. However, because interest in the performance of CFS structures at subzero temperatures is relatively new, limited data on the material performance of CFS under subzero temperatures are available. Azhari et al. [111] investigated the mechanical response of ultra-high-strength steel with a yield strength of 1200 MPa and a thickness of 3.2 mm extracted from cold-formed tubes at ambient, -40°C, and -80°C. Rokilan and Mahendran [112] investigated the mechanical properties of G300 and G550 cold-rolled steel sheets

with various thicknesses from 0.55 mm to 1.0 mm at subzero temperatures down to -70°C. Yan et al. [113] studied the behavior of concrete stub columns confined by steel tubes at subzero temperatures, where they reported the material properties of the cold-rolled steel specimens cut from steel tubes with thicknesses varying from 2.75 mm to 4.50 mm at subzero temperatures down to -80°C. Although different CFS sheets/plates showed significantly different behaviors in the existing studies, the strengths and elongations were overall affected by the decrease in temperature. Among the existing studies, few cover thin (less than 2 mm thick) high-strength CFS. Therefore, it is essential to conduct a thorough experimental study on the material properties of cold-formed high-strength steel with thin-walled geometry at subzero temperatures to better understand the low-temperature effect and to provide reliable data for future use of high-strength cold-formed steel in the high latitude regions.

Among different types of cold-formed high-strength steel (HSS), advanced high-strength steel (AHSS) is promising with significantly enhanced capabilities, owing to recent material science advances at the microstructural level over the past two decades, at a competitive cost [2]. AHSS is steel with unique microstructures utilizing complex deformation and phase transformation processes to achieve unprecedented combinations of strength and ductility. The design and manufacture of AHSS require careful selection of chemical compositions and precisely controlled heating and cooling processes. Subsequently, AHSS exhibits a multiphase microstructure containing one or more phases, including martensite, bainite, austenite, and retained austenite that is sufficient in quantities to develop unique

mechanical properties. Macroscopically, AHSS includes new steel grades with yield strength up to 1250 MPa, ultimate strength up to 1900 MPa, or tensile elongation upwards of 20% to 30%. The material properties of the steel are significantly dependent on the manufacturing technology and chemical composition. Dual-phase (DP) steel is manufactured by controlling the cooling from the two-phase ferrite plus austenite to transfer some austenite to ferrite before the rapid cooling transforms the remaining austenite to martensite. Martensitic (MS) steel is manufactured by transforming the austenite existing during the annealing to martensite in the cooling. High-strength low-alloy (HSLA) steel retains carbon content ranging from 0.5% to 2.0%, while a small amount of other alloying elements are added to its chemical composition to gain better strength, formability, and weldability than conventional mild steel [2]. Although AHSS has shown outstanding performance in the automobile industry for its excellence in stiffness, formability, and crash performance [3], its performance as a structural material is unclear because the construction industry requires different design constraints than the automobile industry. Specifically, although there is limited research on the material properties of AHSS at ambient and elevated temperatures [5], [6], [45], [46], the AHSS properties under the subzero temperature environment are unknown.

In this paper, an experimental investigation was carried out to determine the material properties of advanced high-strength CFS at subzero temperatures following a steady-state test protocol. Specimens were cut from a 1.8 mm thick dual phase (DP) steel sheet and two 1.0 mm thick martensitic (MS) steel sheets. For comparison purposes, specimens cut from a 0.6 mm thick high-strength low-alloy

(HSLA) steel sheet (a type of conventional HSS) and a 1.8 mm thick conventional CFS sheet were also investigated. The specimens were tested at various subzero temperatures from ambient down to -60°C at a 20°C intervals for each steel. Although the lowest temperature in Earth's recorded history is below -60°C [114], the lowest test temperature was selected as -60°C because the recorded lowest temperatures in the high latitude regions with frequent human activities since the twenty-first century have been above -60°C [80], [115]. From the experiments, the stress-strain (σ-ε) curves and key material properties, including elastic modulus, yield strength, ultimate strength, and elongations for AHSS, HSLA, and mild steel were collected. Furthermore, the test results were compared with existing test data and various Steel Standards requirements, particularly the elongations as some CFS sheets/plates showed the transformation from a ductile fracture at ambient to a brittle fracture at subzero temperatures [111], [112]. Additionally, predictive equations for key material properties and the constitutive model for σ-ε behaviors for AHSS at subzero temperatures were developed and verified.

4.2 Experimental study

4.2.1 Test apparatus

The experimental study was carried out in the Manufacturing and Mechanics Laboratory at the University of Wisconsin-Madison. An ADMET F-280DT environmental test chamber with the capability of active heating and cooling from -80°C to 200°C was used to obtain the target subzero temperature environment. The chamber was

connected to an Airgas liquid cylinder, which input the liquid nitrogen into the chamber for the cooling stage. The target temperature inside the chamber was controlled by an Omron E5AC digital temperature controller, which can set the target temperature and display the present temperatures and real-time cooling rate. The present temperature reading was measured by three thermocouples attached to the chamber's internal surfaces, where one thermocouple was placed on the top surface and the other two were on the two side surfaces. The cooling rate was controlled by the temperature controller. Generally, the cooling rate was approximately 5°C/min at the start of the cooling stage and it gradually decreased when the chamber temperature approached the target temperature. The chamber was mounted on a 100 kN loading capacity ADMET eXpert 1600 Series hydraulic testing frame with specially designed subzero temperature-resistant tension grips. The loading process of the tensile test was controlled by MTESTQuattro software, which can control the loading rate and stopping criterion and record and output the test data. The setup of the experiment is shown in Fig. 4.1.

The strain was measured by an MTS model 632.12B-20 extensometer, which is subzero temperature resistant. It had a gauge length of 1-inch (25.4 mm) and a maximum displacement of 0.5-inch (12.7 mm). The gauge length of the test specimen was designed as 2-inch per ASTM E8 [9] (refer to Section 4.2.2). To ensure the fracture of the specimen would occur inside the gauge of the extensometer, a 1-inch extender was manufactured and fixed to the original extensometer. As the extender could not displace, the extensometer now had a 2-inch (50.8 mm) gauge length with a 25% maximum strain measurement range.

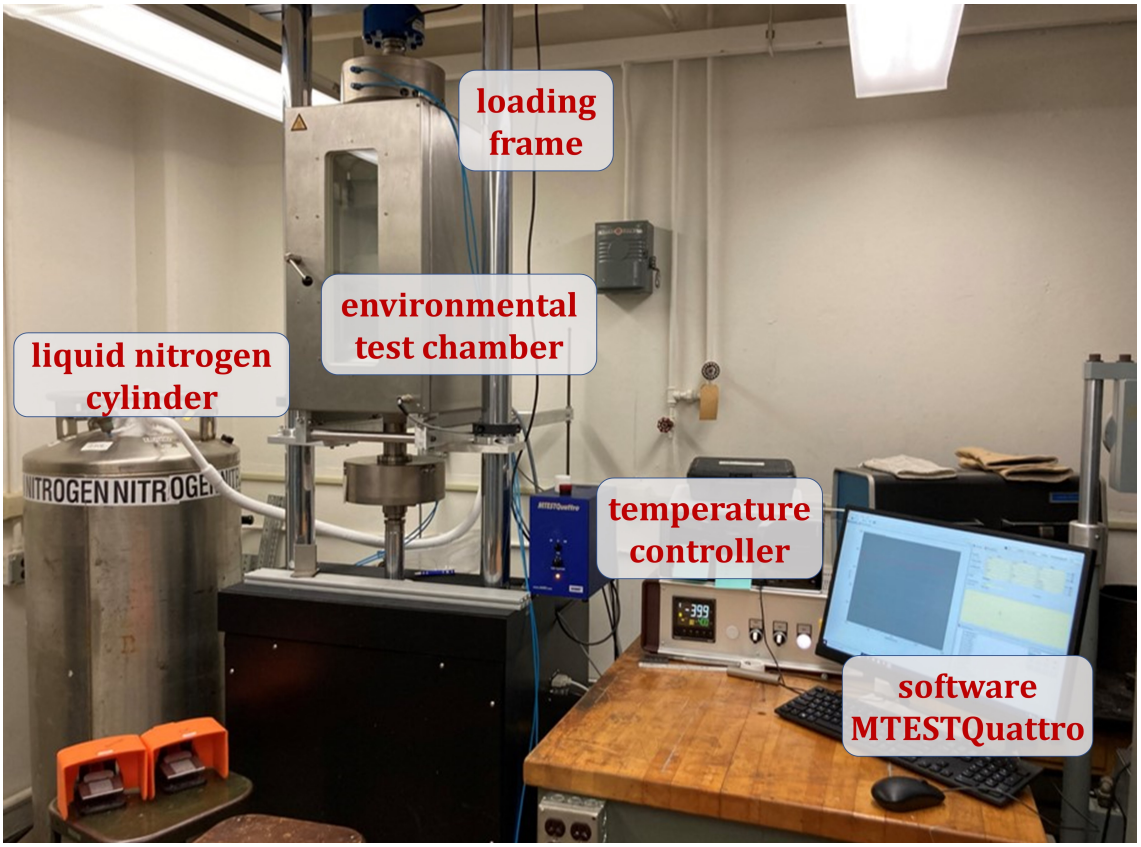

Figure 4.1: Test apparatus setup for the subzero temperature experiment.

4.2.2 Test materials and specimens

The tensile specimens were cut from various steel sheets including three AHSS steel sheets with two thicknesses and three different grades. The materials were labeled by their steel families and nominal yield strengths (in MPa), i.e., DP-580, MS-1030, and MS-1200. For comparison of AHSS to mild and high-strength steel, specimens cut from a conventional mild CFS sheet (Mild-395) and a high-strength CFS sheet (HSLA-700) were also studied. The chemical composition of the five steel sheets is listed in Table 4.1, where the values for DP-580, HSLA-700, and Mild-395 are

Table 4.1: Chemical composition of the steel sheets measured in mass percentage.

Element	DP-580	HSLA-700	MS-1030	MS-1200	Mild-395
C	0.167	0.104	0.16	0.28	0.04
Si	1.413	0.012	0.4	0.4	0.02
Mn	2.0	2.32	1.8	1.3	0.65
P	0.01	0.013	0.02	0.02	0.015
S	0.002	0.004	0.01	0.01	0.003
Al	0.047	0.031	0.015	0.015	0.025
Nb + Ti	0.006	-	0.1	0.1	0.018
Cr + Mo	0.043	0.606	1.0	1.0	0.08
V	0.005	0.001	-	-	0.002
B	0.0003	0.0001	0.005	0.01	-
Cu	0.02	0.02	0.2	0.2	0.09
Ni	0.01	0.01	-	-	0.03
Sn	0.008	0.002	-	-	0.005
N	0.004	0.005	-	-	0.008
Cb	0.003	0.002	-	-	-
Sb	-	0.001	-	-	-
Ca	-	0.001	-	-	0.002

Table 4.2: Nominal properties and coating of the steel sheets.

Steel	t_n (mm)	σ_{ny} (MPa)	σ_{nu} (MPa)	coating
Mild-395	1.8	395	450	uncoated
DP-580	1.8	580	980	uncoated
HSLA-700	0.6	700	980	coated
MS-1030	1.0	1030	1300	uncoated
MS-1200	1.0	1200	1500	uncoated

exact, while the values for MS-1030 and MS-1200 are typical because the exact data is proprietary information of the manufacturer. Nominal information of the steel sheets, including the nominal yield strength σ_{ny}, nominal ultimate strength σ_{nu}, nominal thickness t_n, and coating, is given in Table 4.2.

The specimens were cut along the rolling direction of the steel sheets by waterjet in TeamLab at UW-Madison. The dimension of the specimen was designed per ASTM E8 [9] with a length of 8 inches (203.2 mm), a width of 0.5 inches (12.7 mm), and a reduced parallel section length of 2.25 inches (57.15 mm) as shown in Fig.

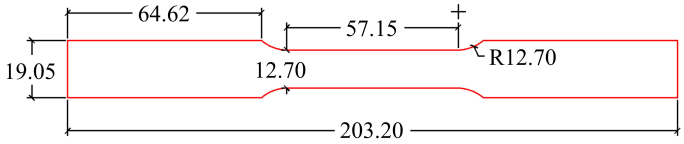

Figure 4.2: Nominal dimension of the tensile specimen (unit: mm).

4.2. For each test temperature, two specimens were tested for AHSS and HSLA steels, and one specimen was tested for mild steel. The specimen was labeled by its sheet designation(e.g., DP-580) plus its target test temperature in Celsius (e.g., +20 for ambient and -20 for -20°C) and the test number (e.g., 1 or 2). The actual width and thickness for the reduced parallel section of each specimen were measured to determine the initial cross-section area before the test. For each specimen, the width and thickness were measured at the center and two ends of the reduced parallel section, and the average of the three readings was used. The width was measured by a caliper with a precision of 0.01 mm, and the thickness was measured by a micrometer with a precision of 0.001 mm. The zinc coating of HSLA specimens was removed by immersing the specimens into one molar hydrochloric acid until complete reaction. The thicknesses before and after the removal of the zinc coating were measured. The average thickness difference was 0.04 mm and it was used as the coating thickness for HSLA specimens. The measured width (b) and uncoated thickness (t) of the reduced parallel section for each specimen are shown in Table 4.3.

4.2.3 Test procedures

The steady-state test protocol was adopted in this study where the material properties of the steels at a steady subzero temperature were measured by a uniaxial tensile test. The target test temperatures included ambient (represented by 20°C), 0°C, -20°C, -40°C, and -60°C. Each test was divided into two stages, the cooling stage and the loading stage. At the beginning of the test, the specimen was clamped vertically by the two grips of the testing frame, and the extensometer was placed at the center of the specimen. The chamber door was then closed and the cooling stage began. As a result of the cooling, thermal tensile stresses were introduced into the specimen due to thermal shrinkage. The position of the bottom grip was manually adjusted upwards using fine-tune controls during the cooling stage to maintain the thermal tensile load below 100 N. After the target temperature on the digital temperature controller was achieved and stabilized in the chamber, the specimen was conditioned for another twenty minutes to guarantee uniform distribution of the target temperature within the specimen. The position of the bottom grip was fine-tuned during the conditioning phase to maintain the tension in the specimen below 100 N as the internal temperature of the specimen equilibrated with the target temperate in the chamber.

After cooling and conditioning, the loading stage began where the tensile load was applied to the specimen until the specimen's fracture. A close shoot on the scenario of a typical specimen's fracture is shown in Fig. 4.3. The tensile load was applied in a displacement control manner with a loading rate of 0.4 mm/min. This corresponded to a strain rate of 0.007/min which met the strain rate requirement of

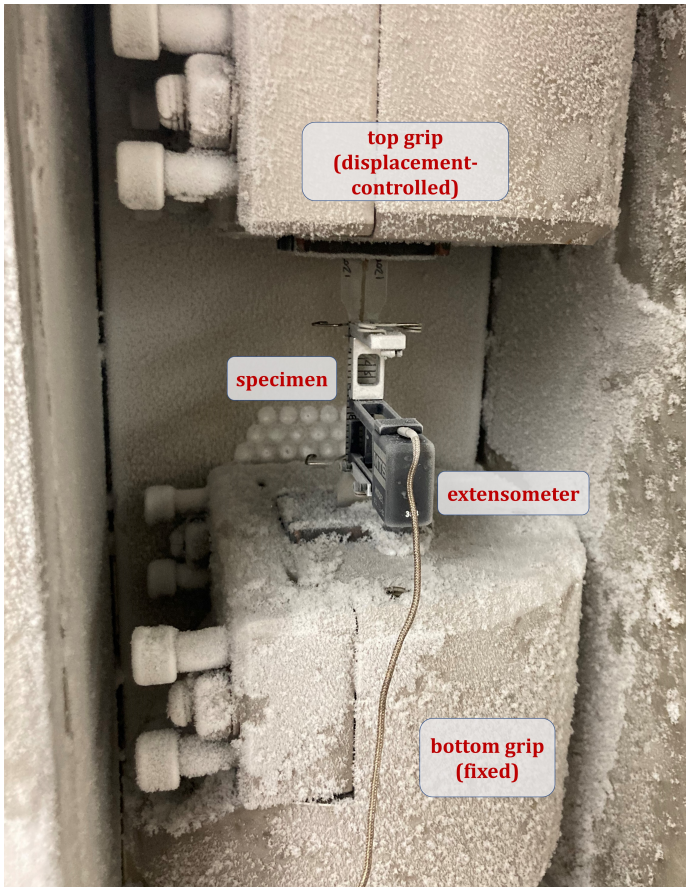

Figure 4.3: Close shoot on the fractured specimen and test equipment.

0.005±0.002 [9]. The data collection rate was set as 10 Hz. The fracture criterion for the specimen was defined as a sudden drop of more than 10% of the applied load between two successive data points in MTESTQuattro. When the fracture criterion was activated, the first point of the two successive data points was regarded as the fracture point for the test.

For elongation measurements, a grid method [116] was also adopted in addition to the extensometer. Before the test, uniformly distributed grids were drawn on the specimen center using Nalgene Cryoware markers, in which the ink was fade

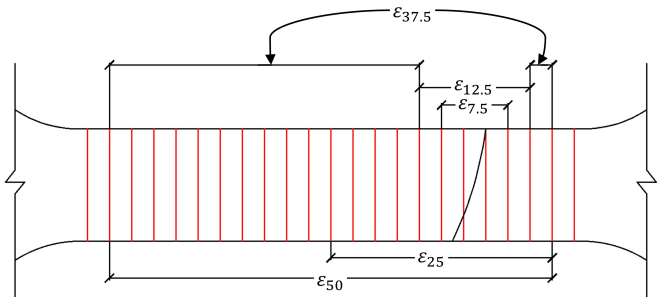

Figure 4.4: Elongations measured at various gauge lengths.

resistant at low temperatures (Fig. 4.4). The spacing between adjacent grids was 2.5 mm. When the loading was completed, the fractured specimens were removed from the chamber and returned to ambient temperature. After several hours, the spacing between various numbers of grids around the fracture position was then measured by a digital caliper. The local ($\varepsilon_{7.5}$ and $\varepsilon_{12.5}$), uniform ($\varepsilon_{37.5}$), and overall (ε_{25} and ε_{50}) elongations at various gauge lengths are illustrated in Fig. 4.4. Following the requirements of [117], the elongations were calculated using the spacing before and after the test, as shown in Eq. 4.1:

$$\varepsilon_{gl} = \frac{L_{gl} - L_{gl0}}{L_{gl0}} \tag{4.1}$$

where L_{gl} and L_{gl0} are the lengths after and before the test along specimen length between grids for ε_{gl} as notated in Fig. 4.4, and the subscript gl represents the gauge length of interest.

4.3 Experiment results

The failed specimens of the steady-state tensile tests at subzero temperatures are shown in Fig. 4.5. All specimens fractured within the reduced parallel section. Significant necking was observed for DP-580 and Mild-395 steel sheets at both ambient and subzero temperatures. However, no noticeable necking was observed for HSLA-700, MS-1030, and MS-1200 at any tested temperatures, and the specimens fractured in relatively brittle modes. The observations indicated the fracture modes of the tested AHSS, HSLA-700, and Mild-395 were not affected by exposure to subzero temperatures down to -60°C. The major results of the subzero temperature steady-state tests are the σ-ε relationship and the elongations measured at various gauge lengths.

4.3.1 Stress-strain curves

The stress was calculated as the applied load divided by the initial cross-section area of the reduced parallel section (measured b and t given in Table 4.3). The strain was measured by the extensometer. The σ-ε curves at subzero temperature for each steel are shown in Fig. 4.6.

For AHSS and HSLA-700, rounded σ-ε curves without a distinct yield point are observed for both ambient and subzero temperature tests. At ambient, the nonlinearity of the σ-ε curve around yield is the greatest for DP-580 and is reduced for HSLA-700, MS-1030, and MS-1200 (in decreasing order). As the test temperature T decreases, the steel strength tends to increase and the nonlinearity of the σ-ε curve

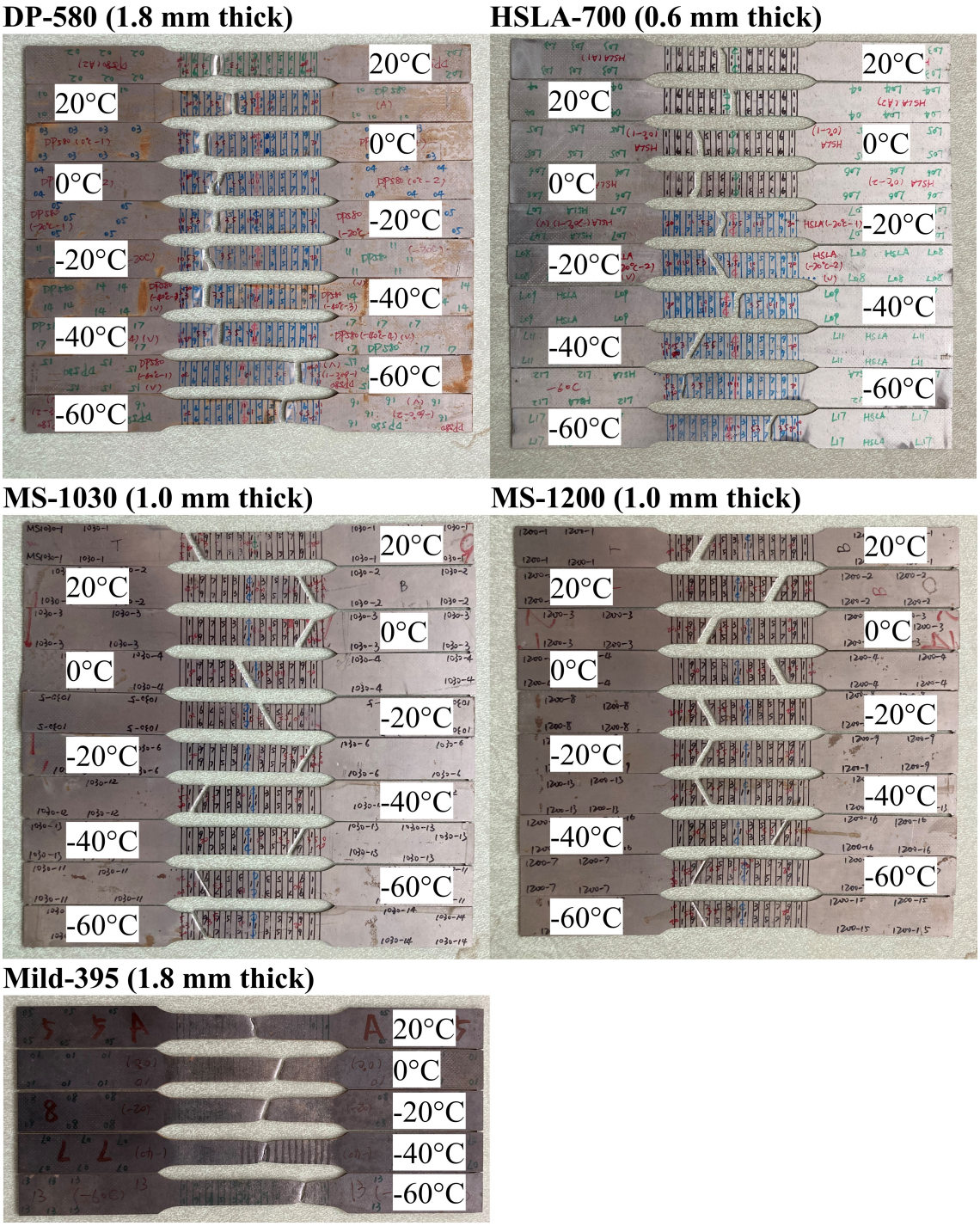

Figure 4.5: The failure modes of the specimens at fracture. Necking is observed in DP-580 and Mild-395 specimens.

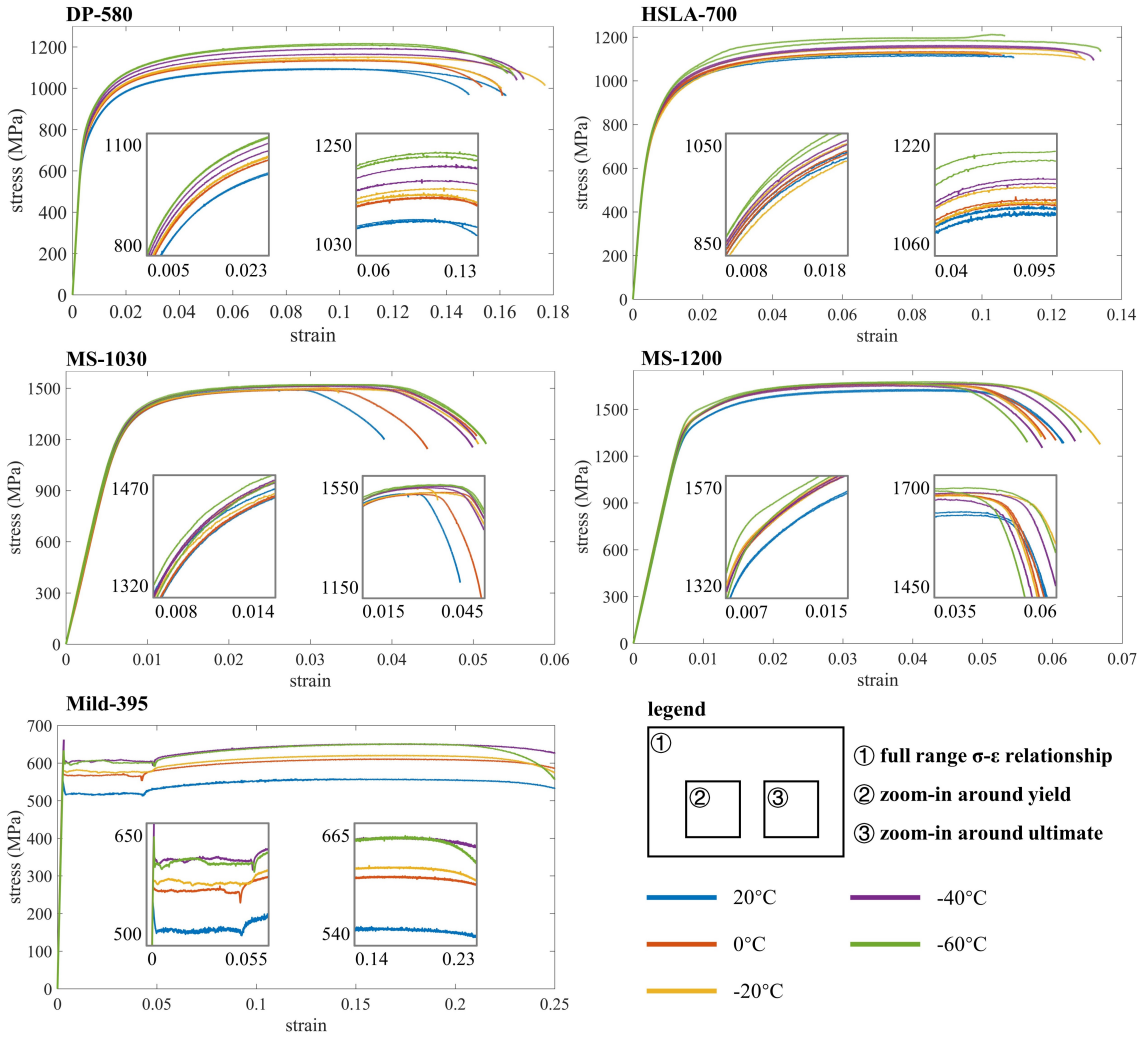

Figure 4.6: Experimental σ-ε curves from the steady-state subzero temperature tests.

tends to decrease. This trend is more significant for DP-580 and HSLA-700 than for MS-1030 and MS-1200. The fracture of HSLA specimens occurred closely after reaching the ultimate point, while for DP-580, MS-1030, and MS-1200, noticeable strain-softening processes occurred after reaching the ultimate point. For all steels, no noticeable effect on the strain-softening portion of the σ-ε curve resulted from the decrease of temperature T.

For Mild-395, σ-ε curves with distinct upper yield point, yield point, and yield plateau are observed for all test temperatures. The steel strength increased when the test temperature decreased. This trend was significant when the temperature decreased from ambient to 0°C and from -20°C to -40°C. For all tests, no fracture was observed when the strain reached the extensometer measurement limit of 25%. Thus, no fracture elongation was measured from the extensometer. Instead, ε_{50} calculated using the grid method is reported as the fracture elongation for Mild-395. In addition, to prevent damage to the extensometer, the test was paused once the extensometer reached its maximum limit and the extensometer was quickly detached. Afterward, the cooling and conditioning stages were repeated and the loading process was then resumed until specimen fracture. Therefore, the σ-ε curves up to 25% strain and the elongations at fracture measured by the grid method are reported, while the σ-ε curve after reaching 25% strain is not reported. Although the fracture point is not observed from the σ-ε curve, the ultimate point was captured for all tests (i.e., the ultimate strains are less than 25%).

4.3.2 Material properties

Important material properties extracted from the σ-ε curves are shown in Table 4.3, which includes elastic modulus E_T, 0.2% proof stress $\sigma_{0.2T}$ and its strain $\varepsilon_{0.2T} = 0.002 + \sigma_{0.2T}/E_T$, stress at 2% total strain $\sigma_{2.0T}$, ultimate strength σ_{uT} and ultimate strain ε_{uT}, fracture strength σ_{fT}, and elongation strain ε_{fT}. The subscript T represents the material property at test temperature T.

4.3.2.1 Elastic modulus

E_T is defined as the slope of the initial linear elastic portion of the σ-ε curve. However, for those showing rounded σ-ε behaviors (e.g., AHSS and HSLA-700), defining the linear elastic portion is challenging. Huang and Young [10] recommended defining the linear portion for the rounded σ-ε curve based on the metal grade and type (e.g., carbon steel, lean duplex stainless steel, and aluminum) where the slope of the linear regression on all σ-ε data between 20% and 45% of the nominal yield strength is calculated as E for the ambient condition. For the subzero temperature cases, the nominal yield strength at ambient might not provide accurate results following this recommendation because of the strength increase with decreasing temperature observed from the experiments. The authors previously developed a method [6] to approximate the nominal yield strength at elevated temperature and this methodology is adopted in this study, where the ratio between the nominal yield strengths at T (σ_{nyT}) and ambient (σ_{ny20}) is proportioned to the ratio between the ultimate strength at T (σ_{uT}) and ambient (σ_{u20}), as calculated in Eq. 4.2. By adopting this method, the resulting coefficient of determination R^2 between the

Table 4.3: Experimental properties of AHSS, HSLA, and mild CFS specimens.

specimen	b	t	E_T	$\sigma_{0.2T}$	$\varepsilon_{0.2T}$	$\sigma_{2.0T}$	σ_{uT}	ε_{uT}	σ_{fT}	ε_{fT}
	mm	mm	GPa	MPa	%	MPa	MPa	%	MPa	%
Mild-395+20-1	12.92	1.905	226.7	514.4	0.427	516.2	559.1	11.97	-	31.04
Mild-395-0-1	12.86	1.912	218.1	566.8	0.460	567.4	611.1	17.71	-	26.90
Mild-395-20-1	12.83	1.905	231.9	575.7	0.449	576.0	621.8	15.05	-	27.22
Mild-395-40-1	12.86	1.908	220.9	601.7	0.472	605.9	651.2	16.45	-	30.26
Mild-395-60-1	12.89	1.910	211.7	600.0	0.483	606.3	652.7	17.73	-	26.98
DP-580+20-1	12.94	1.804	213.2	750.5	0.552	985.6	1095.5	9.84	967.5	14.84
DP-580+20-2	12.91	1.822	216.6	752.5	0.548	982.3	1097.0	10.53	964.0	16.22
DP-580-0-1	12.95	1.820	212.9	785.2	0.569	1019.6	1137.2	10.92	1005.3	15.32
DP-580-0-2	12.96	1.806	215.5	788.6	0.566	1016.6	1136.3	9.72	963.6	16.10
DP-580-20-1	12.94	1.810	218.0	789.4	0.562	1023.2	1143.7	9.89	998.3	16.05
DP-580-20-2	12.93	1.833	207.4	798.8	0.585	1027.6	1153.0	11.05	1013.3	17.69
DP-580-40-1	12.91	1.832	212.0	826.5	0.590	1056.9	1195.5	11.77	1042.8	16.89
DP-580-40-2	12.97	1.815	214.0	808.2	0.577	1039.8	1167.9	9.77	1039.0	16.64
DP-580-60-1	12.94	1.830	210.0	846.5	0.603	1074.1	1218.4	11.97	1071.5	16.29
DP-580-60-2	12.95	1.816	214.7	840.4	0.592	1070.9	1212.9	11.22	1061.0	16.51
HSLA-700+20-1	12.70	0.590	203.6	767.0	0.577	1033.2	1127.7	8.91	1112.1	10.17
HSLA-700+20-2	12.70	0.591	202.4	758.2	0.575	1023.9	1119.9	10.62	1103.7	10.91
HSLA-700-0-1	12.73	0.589	199.8	772.6	0.587	1037.2	1137.9	7.65	1127.5	10.23
HSLA-700-0-2	12.75	0.584	197.6	764.5	0.587	1031.0	1130.6	6.98	1117.3	10.57
HSLA-700-20-1	12.80	0.581	199.7	760.4	0.581	1021.7	1132.4	8.00	1096.0	12.96
HSLA-700-20-2	12.76	0.591	203.2	779.3	0.583	1049.3	1152.0	8.54	1103.7	12.86
HSLA-700-40-1	12.71	0.593	202.4	782.0	0.586	1055.5	1162.5	8.68	1123.9	12.73
HSLA-700-40-2	12.76	0.585	202.2	779.6	0.585	1048.0	1155.7	8.50	1093.9	13.21
HSLA-700-60-1	12.73	0.597	198.9	798.6	0.601	1070.9	1187.0	9.85	1134.2	13.40
HSLA-700-60-2	12.79	0.598	194.2	798.6	0.611	1083.8	1212.7	10.26	1205.9	10.66
MS-1030+20-1	12.63	0.991	215.9	1333.0	0.817	1484.1	1493.3	2.49	1196.2	2.48
MS-1030+20-2	12.62	0.992	208.0	1317.1	0.833	1477.9	1492.7	2.77	1199.6	3.91
MS-1030-0-1	12.63	0.990	201.6	1332.3	0.861	1479.6	1498.1	3.47	1220.0	5.04
MS-1030-0-2	12.62	0.991	202.4	1329.6	0.857	1477.4	1491.9	2.95	1143.9	4.44
MS-1030-20-1	12.58	0.993	216.4	1323.0	0.811	1479.9	1497.8	3.25	1172.6	5.06
MS-1030-20-2	12.65	0.990	205.9	1347.4	0.854	1496.4	1511.4	2.90	1182.5	3.22
MS-1030-40-1	12.56	0.985	209.9	1343.1	0.840	1499.2	1517.9	3.22	1199.4	5.03
MS-1030-40-2	12.54	0.986	208.4	1341.9	0.844	1496.5	1513.1	3.21	1153.2	4.99
MS-1030-60-1	12.54	0.985	215.0	1348.4	0.827	1505.5	1524.1	3.40	1177.2	5.15
MS-1030-60-2	12.63	0.988	206.4	1335.4	0.847	1501.0	1521.7	3.32	1173.5	5.16
MS-1200+20-1	12.53	1.010	204.6	1401.6	0.885	1578.4	1620.3	4.15	1282.3	6.16
MS-1200+20-2	12.57	1.003	199.6	1412.5	0.908	1584.1	1626.4	4.03	1282.5	6.15
MS-1200-0-1	12.58	1.006	208.6	1442.4	0.892	1620.0	1660.7	4.02	1301.2	6.05
MS-1200-0-2	12.60	0.996	208.5	1452.1	0.896	1622.7	1661.5	3.97	1307.4	5.90
MS-1200-20-1	12.63	1.000	203.2	1452.5	0.915	1619.5	1660.0	4.05	1322.9	5.84
MS-1200-20-2	12.60	1.007	206.5	1457.6	0.905	1625.4	1664.7	3.92	1275.4	6.68
MS-1200-40-1	12.63	1.011	205.7	1450.1	0.905	1615.0	1652.8	3.71	1253.1	5.86
MS-1200-40-2	12.47	1.008	204.8	1451.6	0.909	1623.9	1665.6	4.11	1295.3	6.33
MS-1200-60-1	12.56	0.992	207.9	1495.8	0.919	1637.0	1669.4	3.45	1288.8	5.64
MS-1200-60-2	12.58	1.011	198.6	1464.1	0.937	1633.5	1675.5	4.19	1350.9	6.41

linear regression and the test data of the selected data range (between 20% and 45% of the adjusted nominal yield strength σ_{nyT}) for all steels at all test temperatures is larger than 0.99, which indicates the strong linearity of the selected data ranges and thus demonstrates the method validity. The elastic moduli for AHSS and HSLA steel slightly fluctuate without a clear trend with decreasing temperature. The differences between the average E_T and E_{20} for all AHSS and HSLA steels are within $\pm$4%. For Mild-395, however, a decreasing trend for E_T is observed with decreasing temperature with an exception at -20°C. The most significant decrease is observed at -60°C where E_{-60} is 93% of E_{20}.

$$\sigma_{nyT} = \sigma_{ny20} \times \frac{\sigma_{uT}}{\sigma_{u20}} \tag{4.2}$$

4.3.2.2 Key stresses

Yield strength (σ_{yT}) for AHSS and HSLA cannot be easily defined, for no distinct yield point was observed from the experiments. The 0.2% proof stress ($\sigma_{0.2T}$, the stress with a plastic strain of 0.002) is commonly used as the yield strength for metals with a rounded σ-ε curve but without a distinct yield point, and therefore is reported to represent the yield strength. In addition, the stress at 2.0% total strain ($\sigma_{2.0T}$) is also reported, which depicts the steel strain hardening process. As temperature decreases, $\sigma_{0.2T}$ and $\sigma_{2.0T}$ increase for all steels, although for varying amounts. Mild-395 shows the largest increase of over 16% between ambient and -60°C (although minimal change between -40°C and -60°C), followed by DP-580, MS-1200, HSLA-700, and lastly MS-1030 which shows the smallest increase of 2%

Table 4.4: Yield strength and upper yield strength of Mild-395 at subzero temperatures.

T	20°C	0°C	-20°C	-40°C	-60°C
σ_{yT} (MPa)	517.0	566.8	576.5	604.2	601.2
σ_{uyT} (MPa)	555.9	591.2	625.6	662.3	633.7
ε_{yT} (%)	0.228	0.260	0.249	0.274	0.284
ε_{shT} (%)	4.36	4.32	4.70	4.87	4.95

from ambient to -60°C.

Uniquely for Mild-395, an overshoot was observed at the end of the linear portion followed by a small stress drop before the yield plateau. The peak stress of the overshoot is the upper yield strength σ_{uyT}, and the stress at the yield plateau is reported as the yield strength σ_{yT}, as shown in Table 4.4. Table 4.3 and 4.4 show that the differences among σ_{yT}, $\sigma_{0.2T}$, and $\sigma_{2.0T}$ at any tested temperature are within 0.8%, which indicates a relatively constant yield plateau stress. Similar to $\sigma_{0.2T}$ and $\sigma_{2.0T}$ for Mild-395, σ_{yT} and σ_{uyT} increase with decreasing T down to -40°C, with minimal change between -40°C and -60°C.

The ultimate stress, σ_{uT}, is defined as the peak stress of the nonlinear strain hardening and softening portion. As temperature decreases, the ultimate stress tends to increase. This trend is significant for Mild-395 and DP-580, moderate for HSLA-700, and insignificant for MS-1030 and MS-1200. The stress at specimen fracture, σ_{fT}, occurs when the specimen fractures which is depicted on the σ-ε curve as a significant stress drop between two consecutive data points. As T decreases, only σ_{fT} for DP-580 shows a clear increasing trend, while for HSLA-700, MS-1030, and MS-1200, the effect of the low temperature on σ_{fT} is not apparent.

4.3.2.3 Key strains and elongations

Yield strain ε_{yT} and ultimate strain ε_{uT} are essential to depict the steel strain hardening process and develop an ideal constitutive model, where $\varepsilon_{yT} = \varepsilon_{0.2T} = 0.002 + \sigma_{0.2T}/E_T$ for AHSS and HSLA (Table 4.3) and $\varepsilon_{yT} = \sigma_{yT}/E_T$ for Mild-395 (Table 4.4). The yield strain ε_{yT} is dependent on the yield strength and elastic modulus. As the elastic modulus E_T is overall unaffected by the test temperature, the relationship between the yield strain ε_{yT} and T is similar to the relationship between the yield stress σ_{yT} and T. Specifically, the yield strain ε_{yT} tends to increase when T decreases for each steel, while the increase is more significant for Mild-395 and DP-580. The ultimate strain ε_{uT} varies for each test and there is no obvious trend with decreasing temperature.

The strain at the end of the yield plateau (ε_{shT}) is also important for steel with a distinct yield point and yield plateau (e.g., Mild-395). As shown in Table 4.4, there is a clear increasing trend of ε_{shT} with decreasing temperature T for Mild-395.

Elongation at fracture, ε_{fT}, is one of the most critical material properties that depicts steel ductility. The strains at fracture measured by the extensometer are reported in Table 4.3. In addition, the average elongations for different gauge lengths measured by the grid method for each steel are defined and shown in Fig. 4.7. Generally, $\varepsilon_{7.5T} > \varepsilon_{12.5T} > \varepsilon_{25.0T} > \varepsilon_{50.0T} > \varepsilon_{37.5T}$ for each steel at each test temperature. Recall that $\varepsilon_{7.5}$ and $\varepsilon_{12.5}$ are considered local elongations, $\varepsilon_{37.5}$ is a uniform elongation, and $\varepsilon_{25.0}$ and $\varepsilon_{50.0}$ are considered overall elongations.

Overall trends in elongation versus temperature are more obvious when viewing the normalized elongations. For MS-1030, increasing trends are observed for all

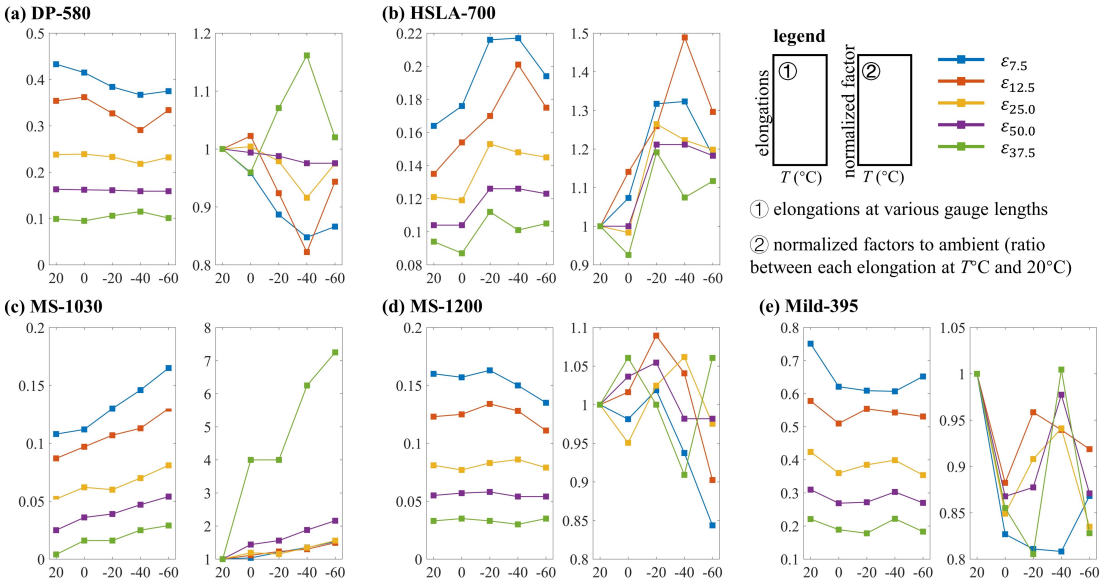

Figure 4.7: Elongations of various gauge lengths measured by grid method and corresponding normalized factors.

elongations when T decreases, and the uniform elongation is the most affected by subzero temperatures. For DP-580, HSLA-700, and Mild-395, there are anomalies in the elongation trends at -40°C. There are no clear trends for MS-1200 with decreasing temperature.

4.4 Discussion on experimental results

This section compares the effect of subzero temperatures on AHSS material properties with other types of steel. This comparison includes conventional and high-strength CFS sheets/plates [111]–[113], as introduced in Section 4.1, hot-rolled steel (HRS) specimens including HRS bar/strand/headed studs [86], [87], [93]–[96], [118] and HRS sheets/plates [89], [92], [97], [98], [108], [110]. The trends of the

material properties variations associated with temperature decrease for different steels are reported and then compared with AHSS, HSLA, and mild steel in this study.

The normalized factor for each material property, which is the ratio of the material property at the subzero temperature T to ambient, is calculated to depict the effects of subzero temperature on different steels. The existing data is divided into three categories: CFS sheets/plates, HRS bar/strand/headed studs, and HRS sheets/plates. The comparisons among AHSS, HSLA, and mild steel and the existing test data for elastic modulus, yield strength, ultimate strength, yield strain, ultimate strain, and overall elongation are shown in Fig. 4.8 to 4.13.

For the elastic modulus as shown in Fig. 4.8, most data, including AHSS and HSLA steel, does not show significant change with temperature decrease, the majority being within 95% to 120% of the ambient value. The largest decrease is for a 3 mm thick S316 stainless steel plate which shows a 9% decrease at -30°C [110]. In contrast, a few HRS specimens (12 mm thick mild steel plate [89], 6 mm thick Q690 HSS plate [97], S30408 steel plate [108] and S316 stainless steel plate [110] with various thicknesses) show increases over 20% at subzero temperatures, as emphasized with red fill in Fig. 4.8.

For the yield strength, as shown in Fig. 4.9, most data exhibits an increasing trend with decreasing temperature, with the increase typically within 30% of the ambient values. Some of this data shows minimal increases within 5% at low temperatures compared with the ambient values, including HSLA-700 and MS-1030. The S355 sheet [119] is the only case that shows a decrease at subzero temperatures, with a

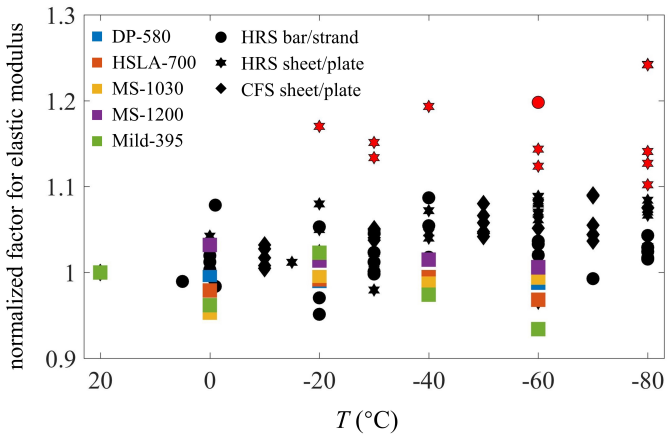

Figure 4.8: Normalized factors of elastic modulus for AHSS, Mild-395, and data from published experiments (scatter with red fill represents an increase over 20% compared with ambient).

decrease of only 2%. The data with an increase greater than 30%, as emphasized with red fill in Fig. 4.9, are G300 CFS sheets with thicknesses varying from 0.55 mm to 1.00 mm [112], which have 33% to 75% greater yield strengths at -50°C and -70°C than at ambient, as well as S30408 and S316 stainless steel plates with thicknesses varying from 3 mm to 6 mm [108], [110], which have 32% to 42% greater yield strengths at -60°C and -80°C than at ambient.

For the ultimate strength, as shown in Fig. 4.10, the effect of decreasing temperature is similar to the effect on yield strength. Increased ultimate strengths are observed in most studies where most steels possess an increase within 30% of the ambient values. The increase is more pronounced for G300 CFS sheets [112], which show approximately a 50% increase at -70°C compared to the ambient values, and S30408 and S316 stainless steel plates [108], [110], which show 34% to 98% increase at subzero temperatures compared to the ambient values. This data is emphasized with red fill in Fig. 4.10.

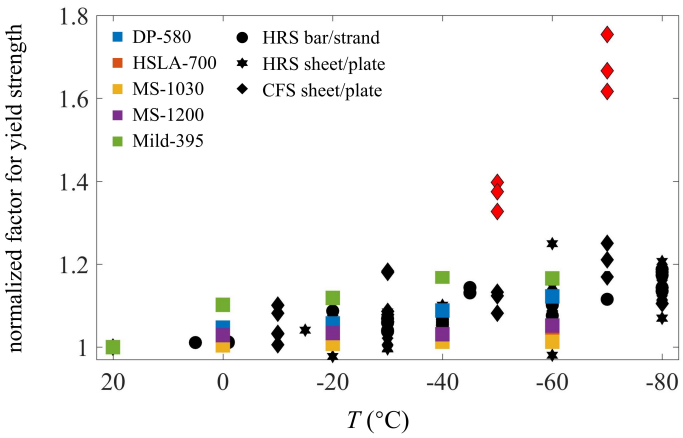

Figure 4.9: Normalized factors of yield strength for AHSS, Mild-395, and data from published experiments (scatter with red fill represents an increase over 30% compared with ambient).

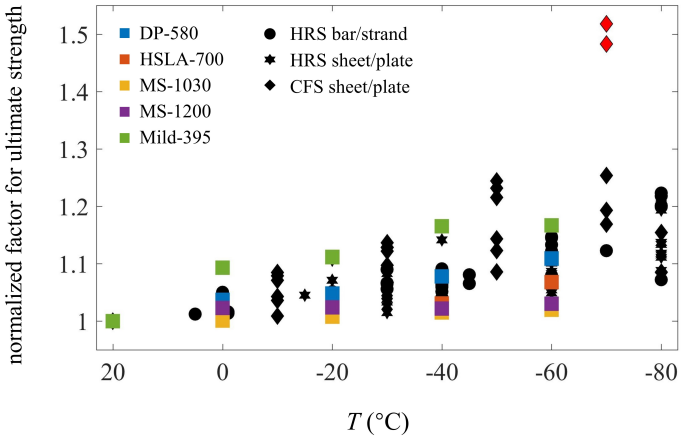

Figure 4.10: Normalized factors of ultimate strength for AHSS, Mild-395, and data from published experiments (scatter with red fill represents an increase over 30% compared with ambient).

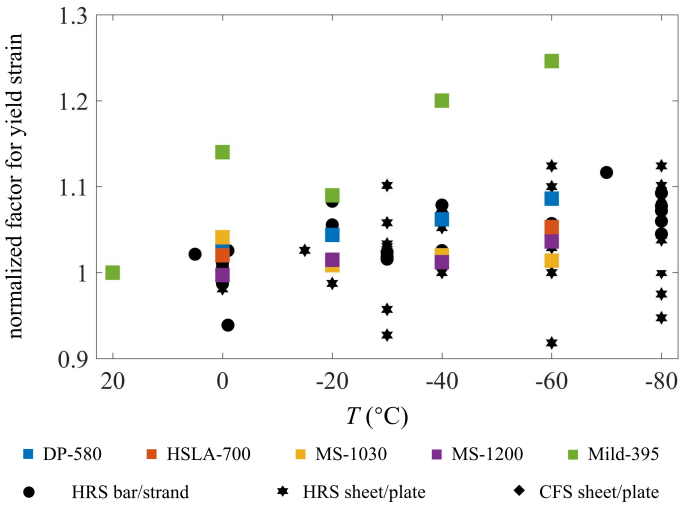

Figure 4.11: Normalized factors of yield strain for AHSS, Mild-395, and data from published experiments.

For the yield strain, as shown in Fig. 4.11, the majority of the data is not significantly affected by subzero temperatures where most data is within ±10% of the ambient values. Most HRS bar/strand specimens and CFS sheet/plate specimens, including AHSS and HSLA-700 in this study, show minor increases compared with ambient values and a clear increasing trend with decreasing temperature. Mild-395 shows a greater increase than any other steel, where the maximum yield strain observed at -60°C is 125% of its ambient value. Some HRS sheet/plate specimens show decreased yield strains at certain subzero temperatures.

For the ultimate strain, several trends are observed with decreasing temperature as shown in Fig. 4.12. In general, increasing trends are found for most steels, however, various fluctuations are observed. Most data from existing literature show similar behaviors with AHSS, HSLA-700, and Mild-395, while two groups of steel illustrate substantially different behaviors. The first group (filled in red) includes

ϕ13 headed stud [93], 0.70 and 0.95 mm thick G550 CFS sheets [112], and 4 mm thick Q690 and Q960 HRS plates [97]. These specimens exhibit significant increases in ultimate strain with decreasing temperature, where the maximum increases are larger than 30% as emphasized with red fill in Fig. 4.12. A special case, 0.75 mm thick G550 CFS sheet [112], has ultimate strain increases more than four times the ambient value at -10, -30, and -50°C, but suddenly decreases to less than half of the ambient value at -70°C due to the ductility loss and change of the yielding mode. The second group (filled in brown) includes G300 CFS sheets [112], 3 mm thick Q960 HRS plate [97], and 2.8 mm and 4.5 mm thick S316 stainless steel plate [110], where the ultimate strains show significant decreases at specific subzero temperatures due to the shape change of the stress-strain curves.

The changing trends for the fracture strain or the total elongation over the full specimen gauge length are compared in Fig. 4.13. The fracture strains for most HRS specimens are close to or higher than their ambient values. The exceptions are the G20Mn5QT cast steel bar [95] and 3 mm thick Q690 HRS plate [97], which show clear decreasing trends with decreasing temperature where maximum decreases of 18% and 12% are observed, respectively. For CFS specimens, AHSS, HSLA-700, and 0.95 and 0.75 mm thick G550 CFS sheets [112] show increased fracture strains with decreasing temperature, while other data shows either gradual or sudden ductility loss when exposed to subzero temperatures (as labeled with brown fill). Mild-395 shows a gradually decreasing trend with a maximum decrease of 13% at -60°C. For the UHSS 1200 [111], 0.55 mm thick G550 CFS sheet [112], and G300 CFS sheet [112], large ductility losses are observed at certain subzero temperatures.

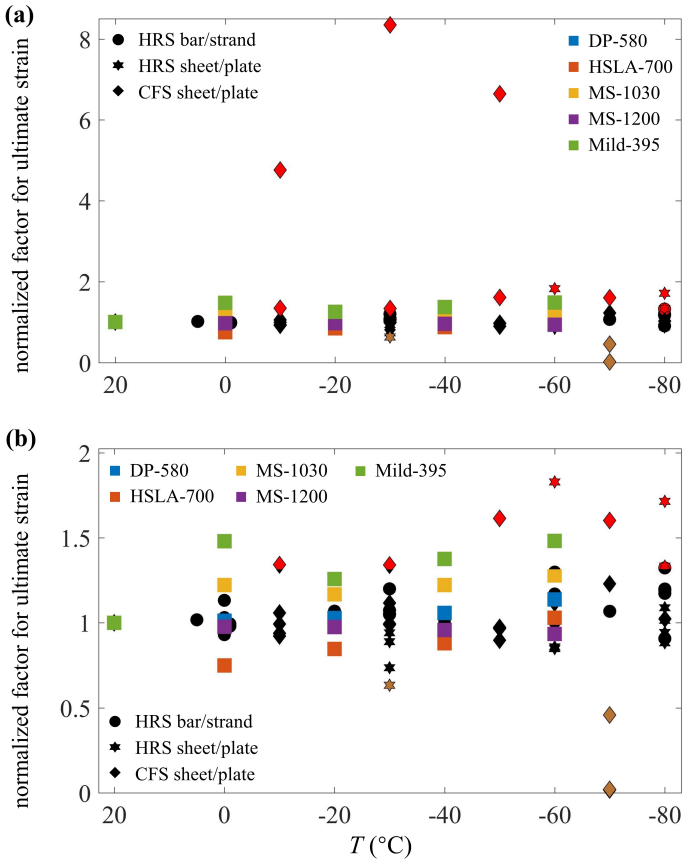

Figure 4.12: (a) Normalized factors of ultimate strain for AHSS, Mild-395, and data from published experiments; (b) magnification of plot (a) at a normalized factor of 1. The scatter with red/brown fill represents an increase/decrease over 30% compared with ambient.

A ductility loss of 32% is observed at -40°C and continues decreasing to 36% of ambient at -80°C for the UHSS 1200 [111]. Ductility losses between 30% to 34% of ambient are observed for S30408 stainless steel sheet at -60°C or -80°C [108]. For the G300 CFS sheet and 0.55 mm thick G550 CFS sheet [112], the fracture strain is increased to higher than the ambient value at -30°C or -50°C, followed by decreases of up to 78% of the ambient value at -70°C.

Unlike other CFS which shows a transition from relatively ductile to brittle

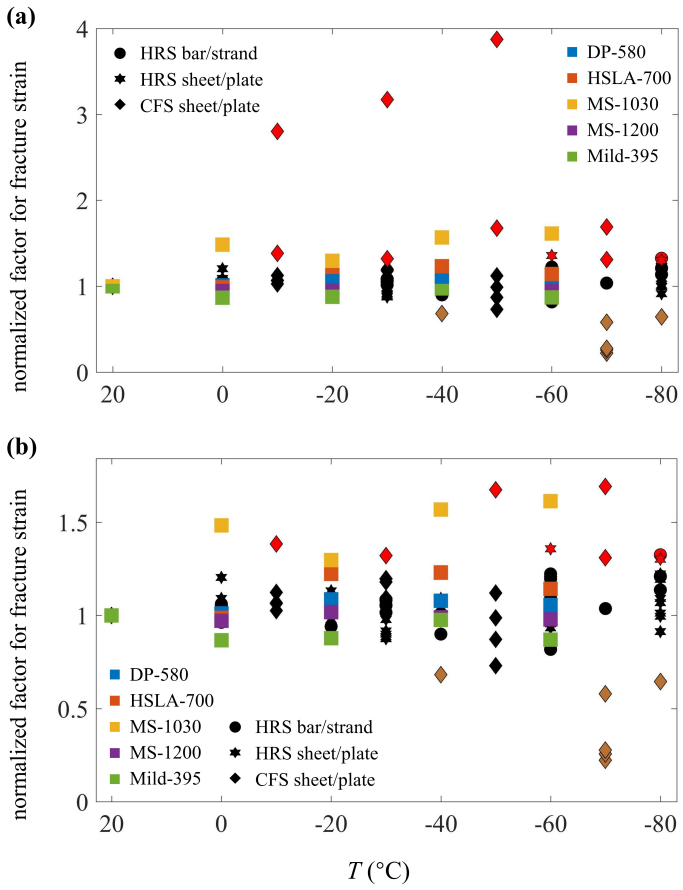

Figure 4.13: (a) Normalized factors of fracture strain for AHSS, Mild-395, and data from published experiments; (b) magnification of plot (a) at normalized factor of 1. The scatter with red/brown fill represents an increase/decrease over 30% compared with ambient.

fracture modes at specific low temperatures, the fracture strains of AHSS and HSLA-700 are not noticeably affected by subzero temperatures. In addition to studying the trend of fracture strain with decreasing temperature, it is also critical to compare the ductility of AHSS, HSLA-700, and Mild-395 with current CFS standards, which include the elongation, the ratio between ultimate strength and yield strength, and the ratio between ultimate strain and yield strain.

Eurocode 3 Part 1.3 [120], which cites Eurocode 3 Part 1.1 [71], requires an elon-

gation at failure no less than 15% for cold-formed structural steel, while Eurocode 3 Part 1.12 [121] reduces this limit to 10% for HSS with a nominal yield strength between 460 MPa and 700 MPa. The minimum elongation with a 50-mm gauge length required by the Australian and New Zealand standard [122] is dependent on the steel grade. For example, for the highest listed grade, G550, the minimum elongation is 2%. No requirement in the current standard is available for steel with a grade higher than 700 MPa, including MS-1030 and MS-1200. The overall elongation for existing test data and standard limits are plotted in Fig. 4.14. Although steel elongation is significantly dependent on steel grade and cross-section geometry, most available data below the 15% (red dashed line) [120] and/or the 10% (blue dashed line) [121] limits are CFS specimens, including HSLA-700, MS-1030, and MS-1200. Even worse, a few cases of cold-formed HSS specimens, including UHSS 1200 [111] and 0.55 mm thick G550 CFS sheet [112], also fail to meet the 2% elongation requirement [122]. Besides the overall elongation, the local and uniform elongation requirements for structural steels [116], [123] are also checked for AHSS, HSLA-700, and Mild-395 (Fig. 4.7). The lower limit is 20% for the local elongations ($\varepsilon_{7.5T}$ and $\varepsilon_{12.5T}$) and 3% for the uniform elongation ($\varepsilon_{37.5T}$). DP-580 and Mild-395 pass all elongation checks at all test temperatures. HSLA-700 does not meet the local elongation requirement at ambient and 0°C, while it passes the uniform elongation check at all temperatures. MS-1200 meets the uniform elongation requirement while it does not pass the local elongation requirements at any temperature. MS-1030 does not meet any of the local or uniform elongation requirements.

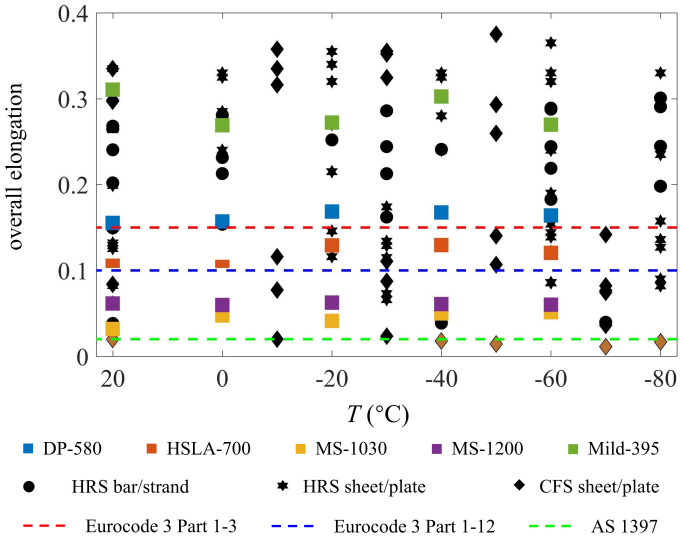

Figure 4.14: Overall elongations for AHSS, Mild-395, and data from published experiments compared with current standard requirements [120]–[122] (scatter with brown fill represents an overall elongation less than 2%).

The ratio between ultimate strength and the yield strength is also a steel ductility indicator required by Eurocode 3 Part 1.3 [120] and Part 1.12 [121], where the minimum ratio is 1.10 and 1.05, respectively. As shown in Fig. 4.15, most data are far above the limit, including DP-580, HSLA-700, and many HRS specimens, which indicates a significant strain hardening process after reaching the yield point. MS-1030 and MS-1200 also possess adequate ductility to pass these requirements. Nevertheless, a few specimens cannot pass the limit, particularly some CFS specimens at subzero temperatures, including Mild-395, most G550 and G300 CFS sheets [112], and most Q960 HRS plates [97], [98].

In addition, Eurocode 3 Part 1.3 [120] and Eurocode 3 Part 1.12 [121] require $\varepsilon_u \geqslant 15\sigma_y/E$ as an additional ductility requirement. DP-580, HSLA-700, and Mild-395 possess sufficient ductility to meet this requirement at all test temperatures.

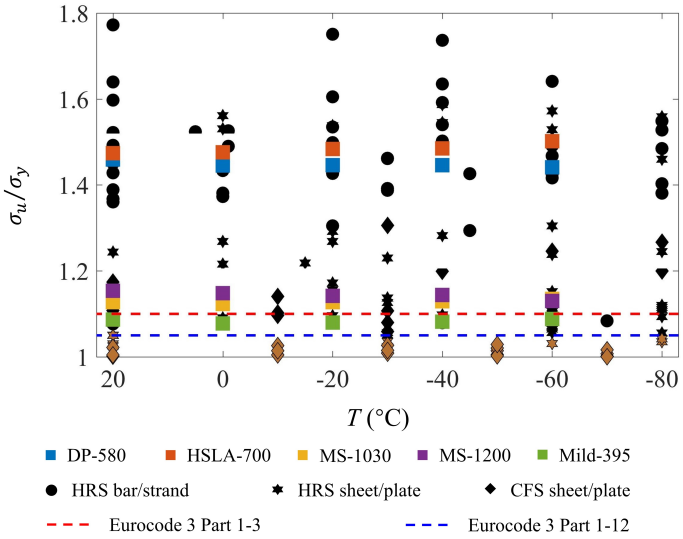

Figure 4.15: (a) The ratio between ultimate strength and yield strength for AHSS, Mild-395, and data from published experiments compared with current standard requirements [120], [121]; (b) magnification of plot (a) at normalized factor of 1.3. The scatter with brown fill represents σ_u/σ_y less than 1.05.

MS-1030 and MS-1200 are not able to pass the requirement at any test temperature, while the ratio at subzero temperatures is larger than the ratio at ambient.

4.5 Material properties characterization

4.5.1 Key material properties

Key material properties are necessary for determining steel material behaviors in both engineering practice and scientific research. This experimental study provides test data from ambient (20°C) down to -60°C with an interval of 20°C. A series of predictive equations as functions of temperature for various key material properties, including E_T, σ_{yT}, σ_{uT}, σ_{fT}, and ε_{50T}, are developed using the tested data as

benchmark.

The predictive equations are developed to produce the average normalized factor N_{X_T} for each steel at each test temperature, which is the ratio between material property X at T and ambient. From the statistical study result, a quadratic equation with a general form of Eq. 4.3 can provide accurate agreement with most of the critical material properties, excluding ε_{50T}.

$$N_{X_T} = a_2 \left(\frac{T}{100}\right)^2 + a_1 \cdot \frac{T}{100} + (1 - 0.04a_2 - 0.2a_1) \tag{4.3}$$

The coefficients of the equation are calibrated using error minimization. The general form of the quadratic equation (Eq. 4.3) only has two coefficients because it is forced to pass through 1 when $T = 20°C$, which assumes the predicted value equals to the test data at ambient. When the relationship between N_{X_T} and T is generally linear, $a_2 = 0$ is adopted, which is preferred when applicable to develop a simpler form of the predictive equation. Additionally, the effects resulting from the subzero temperatures are minor for a few cases, for example, the elastic modulus of DP-580. The ambient value is therefore recommended to be adopted as the values at the subzero temperatures to simplify the predictions (i.e., $a_2 = a_1 = 0$). $\pm 5\%$ tolerance lines from $N_{X_T} = 1$ are added to depict these cases as shown in Fig. 4.16. If the material property at all test temperatures is between these two lines, the ambient values are recommended. The normalized factors, including E_T, σ_{yT}, σ_{uT}, and σ_{fT}, and T are shown in Fig. 4.16, where the solid squares are the average normalized factor and the crosses are the normalized factor from each test. The calibrated coefficients for the predictive equations are shown in Table 4.5.

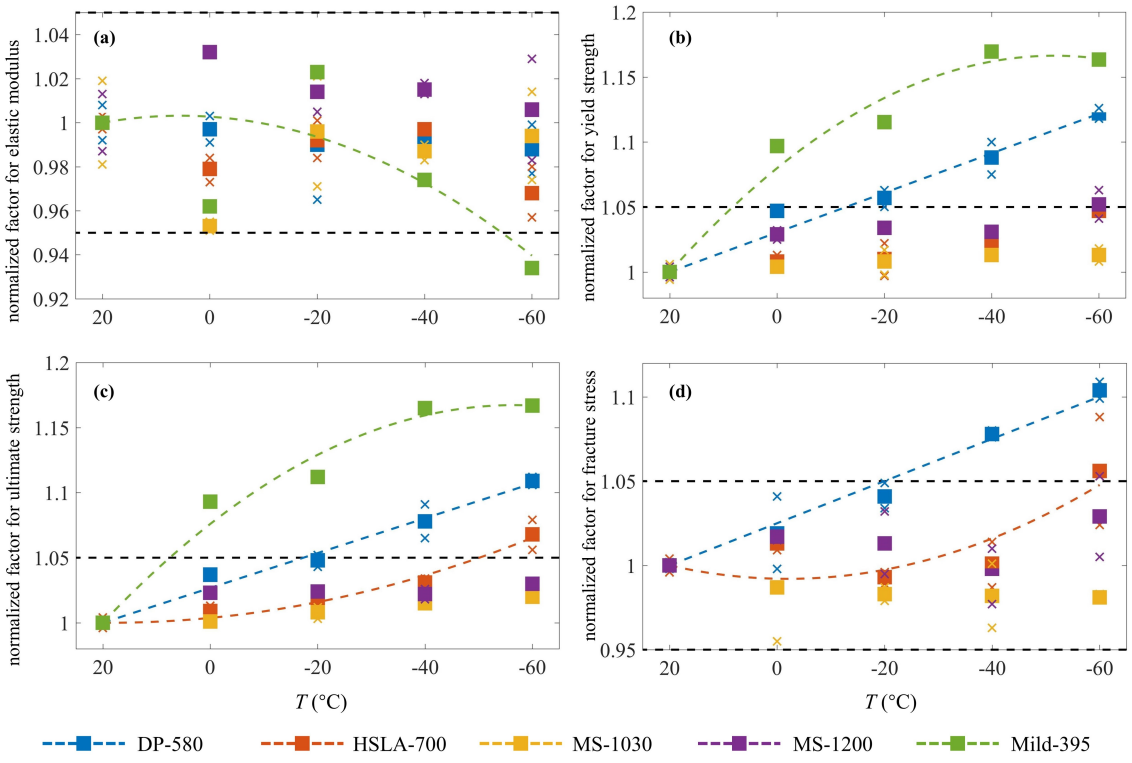

Figure 4.16: Comparison between test data and predictive equation for (a) elastic modulus, (b) yield strength, (c) ultimate strength, and (d) fracture stress (cross is data from single test and square is the average of all data for each steel at each temperature).

Table 4.5: Calibrated coefficients for the predictive equations for the normalized factors of E_T, σ_{yT}, σ_{uT}, and σ_{fT}.

property	steel	a_2	a_1	property	steel	a_2	a_1
E_T	Mild-395	-0.148	0.016	σ_{uT}	Mild-395	-0.285	-0.323
	DP-580	0	0		DP-580	0	-0.134
	HSLA-700	0	0		HSLA-700	0.105	-0.040
	MS-1030	0	0		MS-1030	0	0
	MS-1200	0	0		MS-1200	0	0
σ_{yT}	Mild-395	-0.324	-0.335	σ_{fT}	Mild-395	0	0
	DP-580	0	-0.152		DP-580	0	-0.125
	HSLA-700	0	0		HSLA-700	0.165	0.006
	MS-1030	0	0		MS-1030	0	0
	MS-1200	0	0		MS-1200	0	0

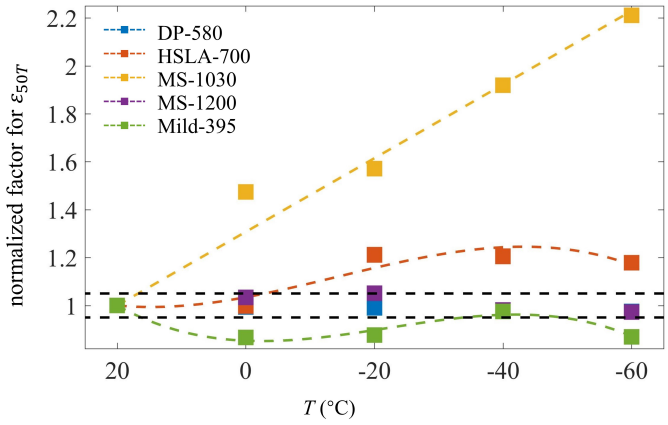

Figure 4.17: Comparison between test data and predictive equation for overall elongation ε_{50T}.

The subzero temperature effects on the overall elongation ε_{50T} vary for different steels and are too complex to be depicted by a single quadratic pattern. Instead, a cubic pattern with a general form of Eq. 4.4 is able to fit ε_{50T} accurately and is thus utilized to describe the relationship between $N_{\varepsilon_{50T}}$ and T.

$$N_{\varepsilon_{50T}} = a_3\left(\frac{T}{100}\right)^3 + a_2\left(\frac{T}{100}\right)^2 + a_1\cdot\frac{T}{100} + (1 - 0.008a_3 - 0.04a_2 - 0.2a_1) \quad (4.4)$$

$N_{\varepsilon_{50T}}$ for DP-580 and MS-1200 is recommended as 1.0 because its variation between -60°C and 20°C is within the 1±0.05 tolerance lines. The trends and predictive equations of $N_{\varepsilon_{50T}}$ for other four steel sheets are shown in Fig. 4.17. The calibrated coefficients for Eq. 4.4 are shown in Table 4.6.

Fig. 4.18(a) and (b) shows the experimental values of E_T and key strengths (σ_{yT}, σ_{uT}, and σ_{fT}) against the predicted values, respectively. The predictions for most elastic moduli, except the MS-1030 at 0°C, are within ±5% errors from the test

Table 4.6: Calibrated coefficients for the predictive equations for the normalized factors of ε_{50T}.

property	steel	a_3	a_2	a_1
ε_{50T}	Mild-395	3.582	2.393	0.113
	DP-580	0	0	0
	HSLA-700	2.580	1.099	-0.495
	MS-1030	0	0	-1.536
	MS-1200	0	0	0

Table 4.7: The average and coefficient of variance of the test-to-prediction ratio for key parameters.

	E_T	σ_{yT}	σ_{uT}	σ_f	ε_{50T}
mean	0.99	1.00	1.01	1.00	1.00
COV	0.023	0.009	0.012	0.020	0.059

data. The error of the predicted elastic modulus for MS-1030 at 0°C is 6% higher than the test values. The average and coefficient of variance (COV) for the ratio between the test data and the prediction for each parameter are shown in Table 4.7.

The accuracy of the fit of ε_{50T} between the test data and the predicted values is evaluated in Fig. 4.19. The predicted ε_{50T} are generally within $\pm$10% from the test data for AHSS and HSLA-700 and within $\pm$5% for Mild-395. The average and COV for the ratio between the test data and the prediction for ε_{50T} are shown in Table 4.7.

Fig. 4.16 to 4.19 and Table 4.7 demonstrate that the proposed quadratic and cubic equations (Eq. 4.3 and 4.4) with the calibrated coefficients (Table 4.5 and 4.6) have good agreements with the test data. However, there are several limitations to this accuracy. First, the presented data represents two samples per steel per temperature. While this number of samples is sufficient to show general trends, more samples are needed to refine the coefficients and more accurate trend relationships. Second, the test specimens were extracted from CFS sheets, which only experienced coiling and uncoiling. Specimens subjected to additional amounts of cold-working, such

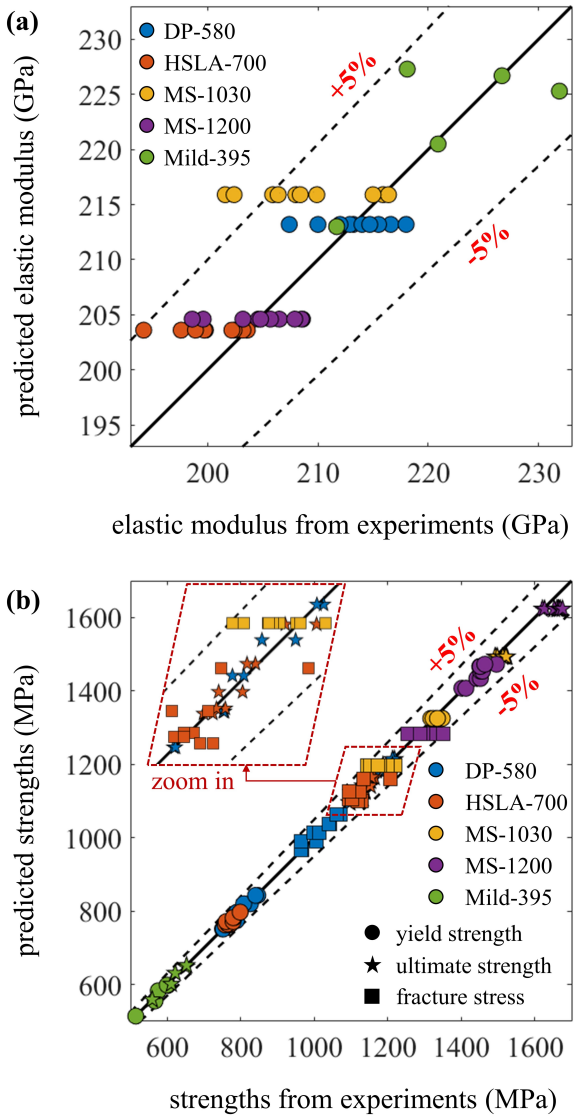

Figure 4.18: The evaluation of fits between test data and predicted data for (a) elastic modulus and (b) key strengths (including yield strength, ultimate strength, and fracture stress).

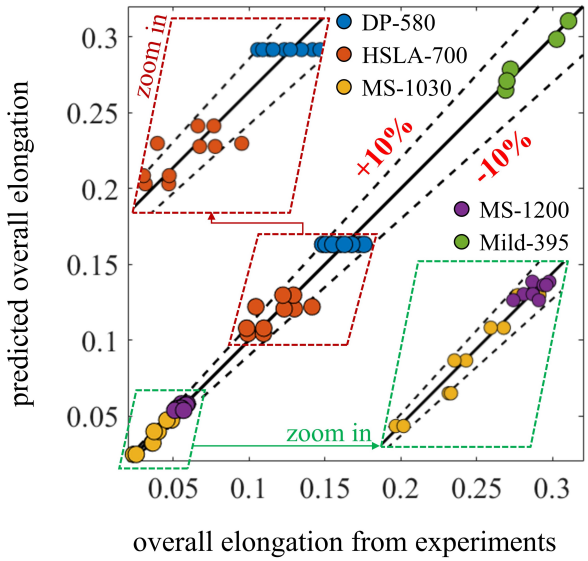

Figure 4.19: The evaluation of fits between test data and predicted data for overall elongation.

as press-braking, roll-forming, etc., might show different coefficient values. Third, the elongation of steel at subzero temperatures is strongly dependent on the sheet thickness (e.g., cases in [97], [108], [112]). Therefore, thinner sheets may result in different coefficients than what is presented herein.

For simplicity, the ambient values could be used to represent the strength and elongations at subzero temperatures, as most steels in this study show increased strengths and elongations at low temperatures. The only exceptions are E_T and ε_{50T} for Mild-395, which show decreasing values with decreasing temperature, and therefore the ambient values are unconservative and the proposed equations are recommended for those subzero temperature properties.

4.5.2 Stress-strain relationships

An accurate description of the steel σ-ε relationship is necessary for advanced numerical analysis, which plays an increasingly important role in engineering design and a dominant role in scientific research. The most commonly-used models adopted in current design standards are multi-stage linear models (e.g., elastic-perfectly-plastic model). However, as discussed in Section 4.3.1, AHSS and HSLA steel show significant nonlinearity during their yielding process and lack a distinct yield plateau, and Mild-395 shows nonlinear behavior after the end of its yield plateau. Therefore their σ-ε behaviors are not accurately captured using simple bilinear or trilinear models.

Previous research [5] investigated the accuracy of using existing constitutive models (e.g., [13]) to portray the stress-strain relationship of AHSS and HSLA at ambient. Due to the unique behavior of AHSS, it was found that standard material models using either parameters determined directly from experiments or parameters from recommended predictive equations ([25]), did not provide an accurate representation of the stress-strain curve, in particular for DP and HSLA, especially around the nonlinear transition region. Therefore, a two-stage plus linear model based on the Ramberg-Osgood equation [11] was created and validated with the tested specimens [5]. Since the shape of the stress-strain curves for AHSS and HSLA at subzero temperatures are similar to those at ambient, it was determined to modify the model in [5] for subzero temperatures. The updated stress-strain model considering subzero temperature effects is shown in Eq. 4.5:

$$\varepsilon_T = \begin{cases} \frac{\sigma_T}{E_T} + p\left(\frac{\sigma_T}{\sigma_{pT}}\right)^n & \text{for } 0 \leqslant \sigma_T \leqslant \sigma_{pT} \\ \frac{\sigma_T - \sigma_{pT}}{E_{pT}} + \left(\varepsilon_{euT} - \varepsilon_{pT} - \frac{\sigma_{euT} - \sigma_{pT}}{E_{pT}}\right)\left(\frac{\sigma_T - \sigma_{pT}}{\sigma_{euT} - \sigma_{pT}}\right)^m + \varepsilon_{pT} & \text{for } \sigma_{pT} < \sigma_T \leqslant \sigma_{euT} \\ \frac{\varepsilon_{uT} - \varepsilon_{euT}}{\sigma_{uT} - \sigma_{euT}} \cdot (\sigma_T - \sigma_{euT}) + \varepsilon_{euT} & \text{for } \sigma_{euT} < \sigma_T \leqslant \sigma_{uT} \end{cases} \tag{4.5}$$

where the parameters were defined at ambient in [5] but have been replaced by the corresponding parameters at subzero temperature T.

The comparison between the test σ-ε curves for AHSS and HSLA steel and the two-stage plus linear model from the origin to the ultimate point are shown in Fig. 4.20. From the regression analysis, R^2 of the fit for any single test curve is larger than 99.5%, which indicates an excellent fit accuracy between the model and the test curve.

To model the stress-strain behavior of Mild-395, the bilinear plus nonlinear model for HRS proposed by Yun and Gardner [73] is updated with fewer coefficients by the authors [6], for accurately describing the postfire σ-ε relationships for AHSS, as shown in Eq. 4.6.

$$\sigma_T = \begin{cases} E_T \varepsilon_T & \text{for } 0 \leqslant \varepsilon_T \leqslant \varepsilon_{yT} \\ \sigma_{yT} & \text{for } \varepsilon_{yT} < \varepsilon_T \leqslant \varepsilon_{shT} \\ \sigma_{yT} + (\sigma_{uT} - \sigma_{yT})\left[K_1 \varepsilon_{nT} + \frac{K_2 \varepsilon_{nT}}{(1 + K_3 \varepsilon_{nT})}\right] & \text{for } 0 < \varepsilon_{nT} \leqslant 1 \end{cases} \tag{4.6}$$

where ε_{nT} is the normalized strain calculated by Eq. 4.7 and other parameters are clearly defined in [73] and [6].

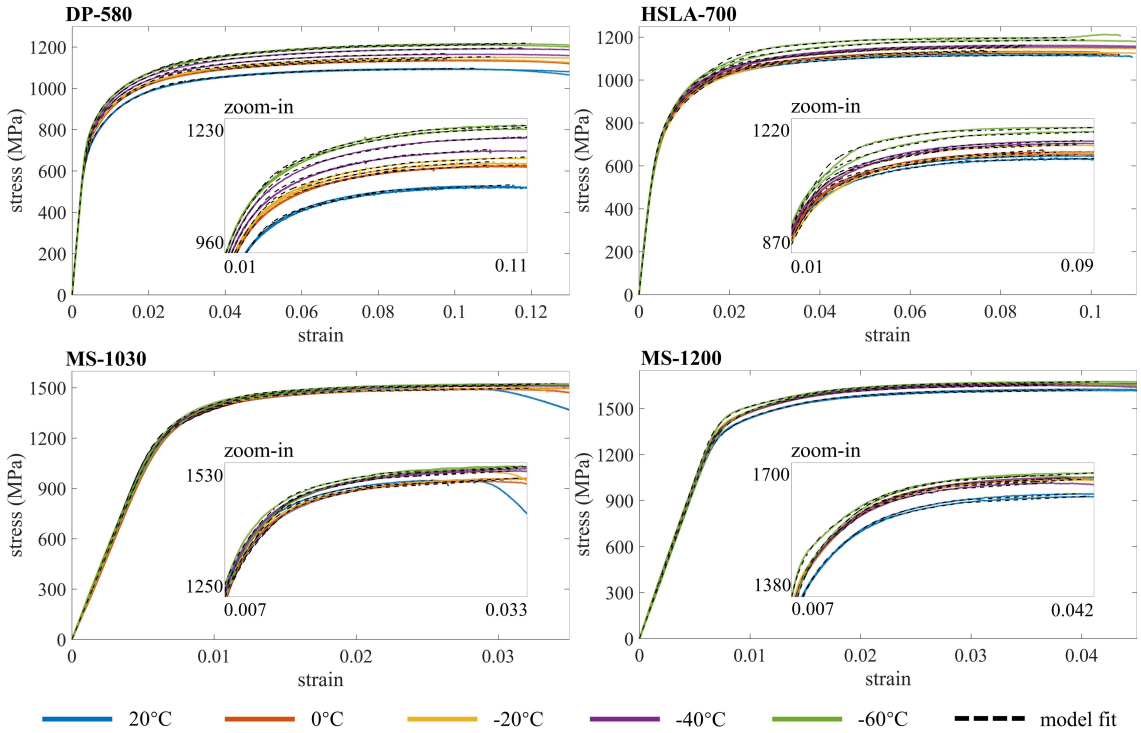

Figure 4.20: Fit between the test curves and the two-stage plus linear model for AHSS and HSLA steel at ambient and subzero temperatures.

$$\varepsilon_{nT} = \frac{\varepsilon_T - \varepsilon_{shT}}{\varepsilon_{uT} - \varepsilon_{shT}} \quad \text{for } \varepsilon_{shT} < \varepsilon_T \leqslant \varepsilon_{uT} \tag{4.7}$$

The model coefficients are recalibrated as $K_1 = 0.103$, $K_2 = 5.360$, and $K_3 = 4.974$, and the updated bilinear and nonlinear model is able to accurately fit the σ-ε curves at subzero temperatures for Mild-395. The model fit from the origin to the ultimate point is shown in Fig. 4.6, and the average R_2 between the test curves and the model fit is 98.7%, which shows satisfactory agreement between the test curves and the recalibrated model.

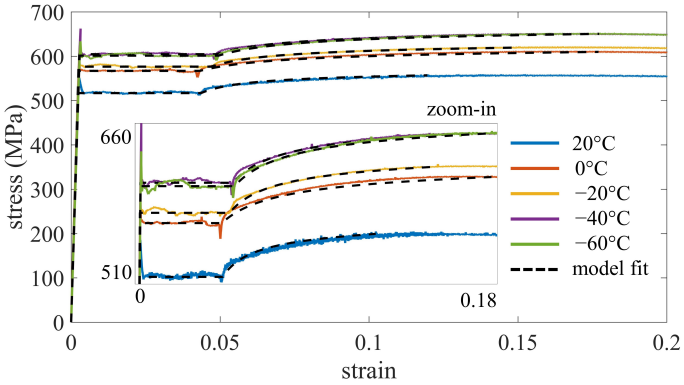

Figure 4.21: Fit between the test curves and the updated bilinear plus nonlinear model with recalibrated coefficients for Mild-395 at ambient and subzero temperatures.

4.6 Conclusion

In this paper, a test series consisting of 45 tensile tests were carried out to investigate the material properties of advanced high-strength cold-formed steel (AHSS) at subzero temperatures. Specimens were cut from three different AHSS sheets, dual-phase (DP-580) and martensitic (MS-1030 and MS-1200), one cold-formed HSS sheet, high-strength low-alloy (HSLA-700), and one conventional CFS sheet (Mild-395). All steels were investigated at ambient, 0°C, -20°C, -40°C, and -60°C following the steady-state test protocol. The stress-strain relationships and key material properties, including elastic modulus, yield strength and strain, ultimate strength and strain, and elongation at subzero temperatures were reported. Additionally, local, overall, and uniform elongations at fracture were measured using the grid method. The changes in the key material properties with decreasing temperature for AHSS, HSLA-700, and Mild-395 were compared with the existing data and the requirements in several Steel Standards. The test results showed a minimal decrease in the elastic modulus, and varying degrees of increases in key strengths and strains

for AHSS and HSLA steel with decreasing temperature. The results indicated that the material performance of AHSS and HSLA steel did not deteriorate under subzero temperatures, but were even strengthened in various amounts. Therefore, the tested AHSS and HSLA steel could be ideal construction materials in subzero temperature environments including high latitude regions. Additionally, predictive equations for the stress-strain relationships and key material properties for the steels as functions of temperature were proposed and shown to have high accuracy, thus enabling accurate material properties of AHSS at subzero temperatures for advanced numerical analyses.

Chapter 5

Experimental and numerical investigation on residual stresses of dual phase high-strength cold-formed steel angles

Xia, Yu, Koh, Hyeyoung, Li, Zhanjie, and Blum, Hannah B. "Experimental and numerical investigation on residual stresses of dual phase high-strength cold-formed steel angles." Manuscript in preparation and to be submitted Fall 2022.

Abstract

The rapid advance in advanced high-strength cold-formed steel makes this material promising for the construction industry to use as structural framing, but necessitates

an accurate understanding of mechanical properties, including residual stresses. An experimental and numerical study was conducted to measure the residual stress which is generated during the member manufacturing process of press-braked lipped angle members composed of advanced high-strength cold-formed sheet steel. The magnitude and distribution of membrane and flexural residual stresses on both surfaces around the member cross-section are presented and the magnitude of residual stresses relative to the yield strength for the test specimen and other previous studies are compared. Additionally, the residual stress distribution through member thickness is investigated by using a validated finite element model.

5.1 Introduction

Cold-formed steel (CFS) is widely used in structural framing for its beneficial high strength-to-weight ratio, recyclability, and convenient transportation and construction. Due to the rapid advancement of material science during the past two decades, new grades of steel, known as advanced high-strength steel (AHSS), have been developed and applied in the automobile industry. To bring AHSS to the construction industry, the material properties and behavior of the structural sections composed of this material must be quantified. This includes the residual stresses induced in the structural members as a result of the cold-forming process. The distribution and magnitude of residual stresses affect the strength and stability behavior of the CFS members.

Previous experimental studies quantified the residual stress of conventional CFS

members. Ingvarsson [124] measured the residual stresses in a channel member by the sectioning method. The channel was formed by press-braking a 7.5-mm thick CFS plate with a yield strength of 800 MPa. Strain gauges were attached to both inner and outer surfaces. The result shows the distribution for strain readings is symmetric to the symmetrical axis of the member. For the inner surface, the strain reading is positive and has the largest magnitude (around 300 MPa) at the free end of the flanges. All other stresses are negative, and the largest stress is found at the corner region (around 300 MPa). The readings for the flat part of the web are close to 0. For the outer surface, the stresses for the central regions of the flanges are negative while for all other regions are positive. The largest magnitude is found at the corner region and the free end of the flanges (both around 400 MPa). Weng [125] measured the residual stresses of a series of lipped CFS channel members. The thickness of the steel sheets ranged from 1.63 to 3.07 mm. The yield strengths for the steels ranged from 221 MPa to 385 MPa. A total of nine members were measured, six were rolled-formed and three were press-braked. The residual stresses in the members were released by the sectioning method using electrical discharge machining (EDM). The residual stress distribution was assumed to be symmetrical to the member geometric symmetrical axis. From the results, for the outer surface distribution, the stresses are negative; the maxi-mum stresses are found at the corner regions, and they are approximately three times of those at flat regions of web and flanges. For the inner surface distribution, the stresses are positive; stresses at the corner regions are the largest while generally smaller than their corresponding stresses at the outer surface. The stresses at the flat regions of

the web and flanges generally have the same magnitude and inverse stress direction compared to their outer surface counterparts. No clear relationship of the residual stress magnitude between roll forming and press braking is found. Batista [126] measured the residual stress distribution for two lipped channel members by the sectioning method. The channels were made from a 1.52 mm thick steel sheet. From the results, the residual stresses for the rolled-formed member are negative at the internal surface and positive at the external surface; the residual stresses are stable along the flat region of the web, and they range from 100 MPa to around 200 MPa. No obvious increment is observed for the measurement locations adjacent to the corners. The residual stress measurements on the internal and external surfaces at the same location on the web are similar, so the average of the two stresses, known as membrane residual stress resulting from the Poisson's stretching due to the cold-forming process, is low. A similar distribution is found for the flanges, but their stress magnitude (generally ranging from 50 to 100 MPa) is smaller than those of the web. Different observations are noted for the press-braked member. The magnitude of the stress is much lower than its rolled-formed counterpart. Generally, it ranges from 0 to 50 MPa. For the flat part of the web and the flanges, the stresses for internal and external surfaces do not have a uniform direction. However, the residual stress magnitudes of the internal and external surfaces at the same measurement point are close, so a small membrane residual stress is observed. Young [127] measured the longitudinal residual stress distribution for two cold-formed lipped channels by sectioning. The members were formed from a 1.5-mm thick CFS sheet with a yield strength of 450 MPa. The result shows

the residual stresses tend to be small for inelastic straining occurs mainly in the transverse direction. The membrane residual stresses range from 0 to 14.0 MPa and the flexural residual stress (defined as half of the difference between the inner and outer surface residual stresses at the same measurement location) range from 3.2 MPa to 37.2 MPa. Both the membrane residual stresses and the flexural residual stress were concluded by the authors as negligible, compared to the nominal yield strength of 450 MPa. Abdel-Rahman [36] performed the residual stress tests on two groups of cold-formed lipped channel members by the sectioning method. One group of channels was made from a 1.91-mm thick steel sheet with a yield strength of 379 MPa and the other group of channels was made from a 1.22-mm thick steel sheet with a yield strength of 313 MPa. Linear strain gauges were used to measure the longitudinal residual strains and a rosette strain gauge was used to measure the residual strains along longitudinal, transverse, and 45° directions. From the result, the location of the highest magnitudes of residual stresses for all the test specimens is found to be at the web area adjacent to the curved corner; The lip area and the flange-lip corner also show relatively high magnitudes of residual stresses; the web-flange corner shows lower magnitudes of residual stresses. It is concluded, in terms of residual stresses for different directions, the principal residual stress direction is the longitudinal direction, and the magnitudes of transverse residual strains are not significant compared to their longitudinal counterparts. Schafer [128] provided a flexural residual stress distribution model for both rolled-formed and press-braked cold-formed lipped channel steel members based on average values of previous experimental studies as shown in Fig. 5.1. For the flexural residual stresses in rolled-

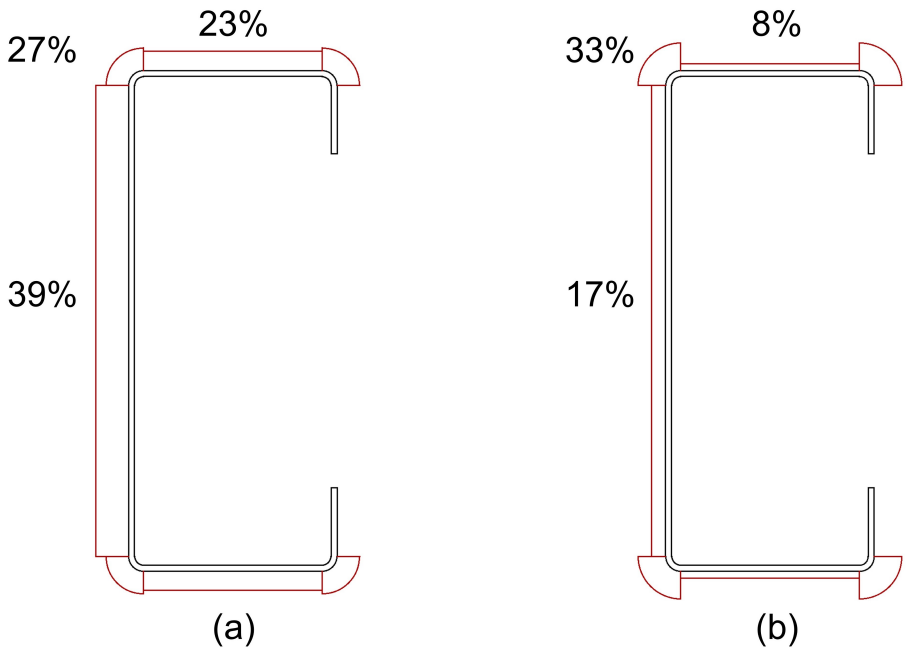

Figure 5.1: Flexural residual stresses distribution as percentage of steel yield strength for (a) roll-formed channel and (b) press-braked channel proposed by Schafer [128].

formed members, in terms of percentage of yield strength, the web average is 39%, which is the highest region; the corner average is 27% and the flange average is 23%. For the flexural residual stresses in press-braked members, in terms of percentage of yield strength, the corner average has the largest magnitude, and it is 33%; the web average is 17% and the flange average is 8%. A more conservative recommendation based on statistical analysis (CDF development with the increasing of the ratio between flexural residual stress and yield strength) of the previous experimental data is also given. From the literature review, although previous researchers studied the residual stress distribution of conventional CFS members, the studies of residual stresses in high-strength CFS are highly limited.

Additionally, a noteworthy operation from most previous experimental studies

is, for CFS members, a relatively long length from the two edges is cut off and discarded; only the center section is reserved for the residual stress measurement. In Ingvarsson's study [124], the total length of the member was 2050 mm and a distance of 800 mm was cut up from each end. From Dat's experiment [129], only the center 76.2 mm section was kept for the residual stress measurement and at least 152.4 mm from the edge was cut for each side. In Batista's study [126], the total length for different members was at least 1000 mm long, while only the central 60 mm for each member was reserved for the test. In Young's study [127], the total length for different specimens was at least 1000 mm, while all of them were cut to 500 mm before the residual stress measurement. In another study [36], the test specimens were cut from long CFS members to 300 mm and 600 mm respectively to preclude any damaged ends of the long columns. Although this operation was commonly practiced by several researchers, few of them provided any persuasive rationale behind it beyond concern for end effects.

Based on the preceding discussion, this study mainly focused on two objectives. First, an experimental study on lipped angle members with different corner radii manufactured from a 1.8-mm thick AHSS sheet was carried out to study the distribution of residual stress along member length on its cross-section by using the sectioning method. Two 533.4 mm (21 inches) long lipped angle member was cut into seven sections respectively with equal length along the perpendicular direction to the member length as shown in Fig. 5.2(a). For each member, the longitudinal residual stress distributions of an edge section and a center section were studied and a discussion on the longitudinal residual stress distributions on the inner and

outer surfaces for both sections was presented. Additionally, as the major forms of the residual stresses that lead to deterioration of material strength, a discussion on the distribution of the membrane residual stresses, which result in internal membrane forces, and flexural residual stresses, which result in internal flexural moments, on member cross-section of both sections was presented. Second, a numerical study on the residual stresses resulting from the practical press-braking manufacturing process was conducted by using step-wise finite element modeling. The comparison of residual stresses on specimen surfaces between the experimental measurement and the simulation was presented. The residual stress distribution through member cross-section thickness was given and discussed by using the validated finite element model.

5.2 Experimental study

5.2.1 Material properties

A dual-phase (DP) steel sheet was used for this program. Its nominal thickness was 1.8 mm, and it was uncoated. Its nominal yield strength was 580 MPa and its nominal ultimate strength was 980 MPa. Its nominal minimum elongation was 12%. Detailed chemical composition of the steel sheet is shown in the DP-580 column of Table 2.1.

A series of tensile coupon tests [5] were carried out to study the material properties of this DP steel. The tensile coupon dimension was designed per ASTM standard [9] and coupons were cut along both parallel and perpendicular to the

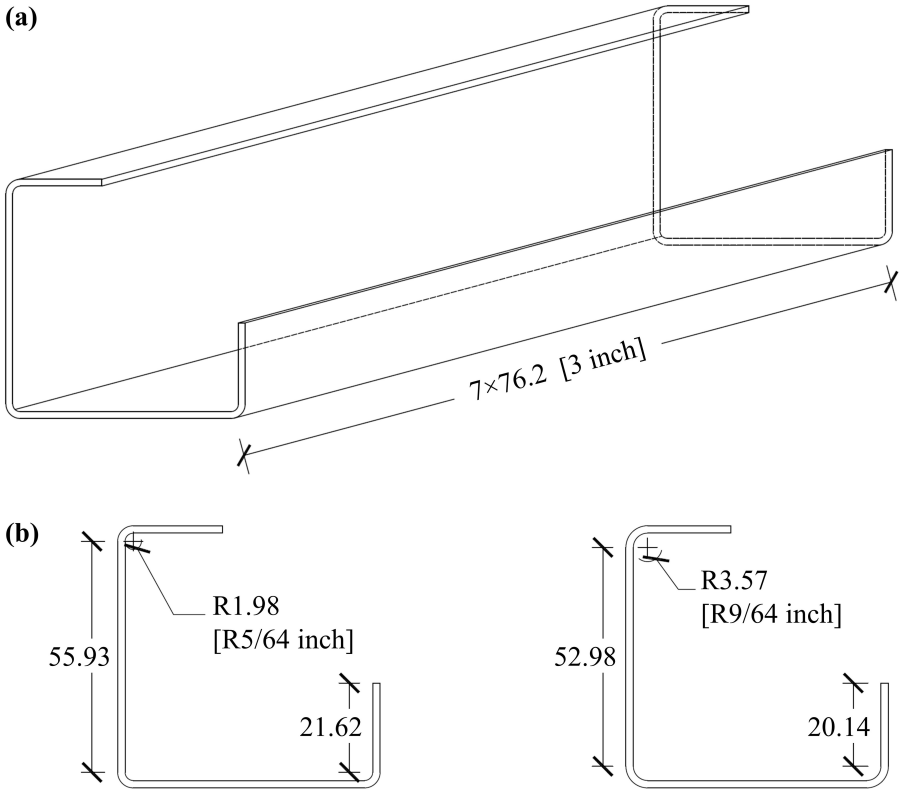

Figure 5.2: Design dimension of the angle section (in mm if not specified).

steel sheet coiling direction. The typical stress-strain relationship of DP-580 from the tensile coupon test is shown in Fig. 2.5. A summary including modulus of elasticity E, 0.2% proof stress $\sigma_{0.2}$ used as yield strength, ultimate strength σ_u, and elongation ε_f is shown in Table 5.1. It shows for E, $\sigma_{0.2}$, and σ_u, the variation for either longitudinal or transverse coupons is small (COV is less than 3%); the difference between average values of the longitudinal and transverse coupons is small (ΔAVG is less than 2%) except for E; the difference is intermediate for E (ΔAVG is 6.35%). The elongation was measured by an extensometer with a gauge length of 25.4 mm (1 inch) positioned at the center of the tensile coupons. The elongation

Table 5.1: Tensile coupon test results.

Direction		E GPa	$\sigma_{0.2}$ MPa	σ_u MPa	ε_f %
Long.	AVG	193.3	629.2	954.3	18.4
	COV	1.55%	1.39%	1.29%	20.97%
Trans.	AVG	205.1	640.5	959.1	11.6
	COV	2.18%	0.68%	1.22%	4.90%
ΔAVG		6.35%	1.75%	0.63%	-36.96%

varies significantly for the longitudinal coupons (COV is 20.97%) and it ranges from 12.97% to 22.92%; the variation for the transverse coupons is intermediate (COV is 4.90%) and ranges from 11.20% to 12.4%. The difference in the average elongation between longitudinal and transverse specimens is 36.96%. The potential reason for the large difference is the fracture positions of the specimens are different. Three out of five of the longitudinal specimens fractured within the gauge length of the extensometer, while all the four transverse specimens fractured outside the gauge length of the extensometer. For these three longitudinal specimens which fractured within the gauge length of the extensometer, the average elongation is 20.9% and the COV is 8.27%.

5.2.2 Specimen design and manufacture

Two lipped angle members were designed for this study. The members' longitudinal direction was along the sheet rolling direction and the member length was 533.4 mm (21 inches). For the nominal cross-section dimension, the outer length of both legs was 63.5 mm. The inner radius at the corner referred to Eq. 5.1 per [130] (the original equation is in inch) and selected as 1.98 mm (5/64 inch) and 3.57 mm (9/64 inch), which were both larger than $2.38 - 0.5t = 1.48$ mm. The nominal

bending radii at the corner were thus 2.88 and 4.47 mm respectively. The nominal design dimensions of the equal leg angle member are shown in Fig. 5.2(b). The members were manufactured by a CNC hydraulic press brake metal bender in the Sheetmetal Shop at UW-Madison. After forming, the true inner surface radii at the corner were measured by a radius gauge with a precision of 1/64 inch (0.40 mm) and the readings were the same as the designed values.

$$r_{in} = \max\{2.38 \text{ mm} - 0.5t, 1.5t\} = 2.7 \text{ mm} \tag{5.1}$$

To study the effect of longitudinal location on the cross-section residual stress distribution, various locations along the member longitudinal direction were studied. The members were cut into seven equal sections with a length of 76.2 mm (3 inches). The sections were labeled from 1 to 7 based on the position of the original member before cutting. For example, 1 was the left edge section and 4 was the center section. For each member, two sections, located at or next to the center and the left edge, were used for the test and comparison. The member with the larger corner radius was labeled as RL and that with the smaller corner radius was labeled as RS. The cutting was performed by a vertical band saw specifically designed for steel cutting with a low range of revolutions per minute (rpm) setting in the TEAMLab at UW-Madison. The specimens were labeled as member-location. For example, RS-4 is the center section cut from the lipped angle member with the smaller corner radius. By the nomenclature, two sections from each member were included in this study, which were RS-1, RS-5, RL-1, and RL-4.

The longitudinal residual strains within each section of the members were

measured by linear strain gauges FLA-5 produced by Texas Measurements. The sensing element of the strain gauge has a length of 5 mm and a width of 1.5 mm. The total width of the strain gauge including the backing was as small as 3.0 mm, which made it feasible to attach them directly onto both the inside and outside surface at the member corner region without large bending. A few trial tests for sectioning cut by using the vertical band saw were conducted and the readings of the strain gauges were poor as the vibrations caused by the band saw cutting adversely affected the strain gauges. Therefore, strong protections were added to make the strain gauge more resilient. M-Coat A Polyurethane protective coating produced by Micro Measurements was used to protect the strain gauge sensing element, and Kapton polyimide tape was used to protect the strain gauge lead wires. The strain gauges were attached on both inside and outside surfaces of the member section at certain designed positions. The strain gauge positions for each section are shown in Fig. 5.3(a) and labeled by dark blue numbers in parentheses. The dashed lines indicate the designed sectioning positions and the red numbers in parentheses are the sectioning order. Fig. 5.4 shows photos of two sides of the representative section ready for sectioning with installed strain gauges.

5.2.3 Test procedure

The lead wires for each strain gauge were connected to an NI SCXI-1001 Chassis produced by National Instruments for recording strain. A total of 18 strain gauges were connected to the chassis for each section. The chassis was connected to a desktop for operation and control. At the beginning of any test, the strain gauge

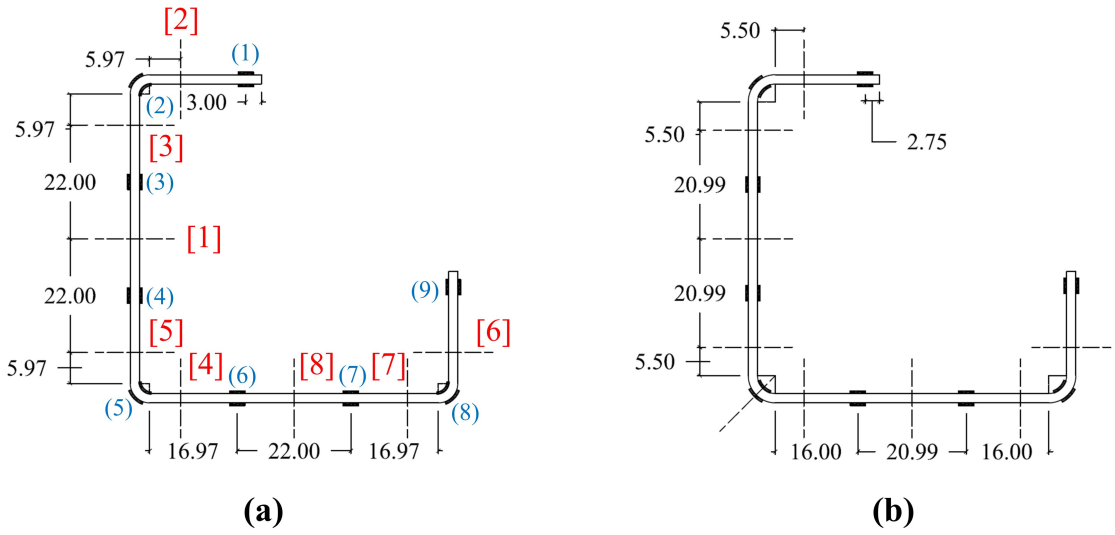

Figure 5.3: Design cross-section geometry and strain gauge distribution on cross-section for (a) RS-1 and RS-5 and (b) RL-1, and RL-4.

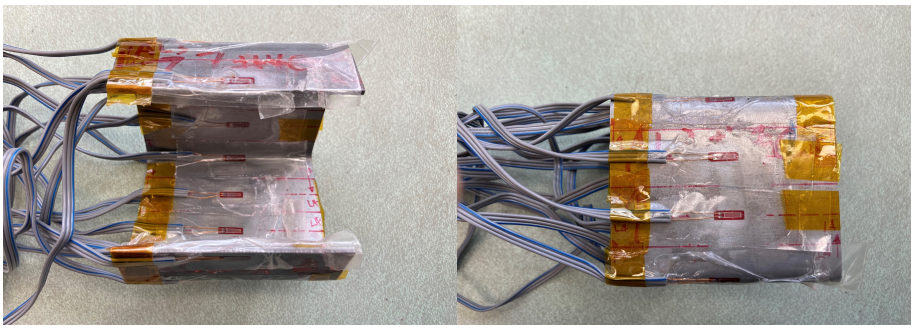

Figure 5.4: Photos for a representative section with strain gauges installed.

reading represented by the channel output was calibrated by NI Measurement & Automation Explorer and zeroed. The strain readings for all channels were recorded over time through a custom program made in LabView. The steel section was cut along its length by the vertical band saw. Fig. 5.5 shows a photo of the actual sectioning scenario during the test. For most sectioning operations, the leg was placed on the table horizontally and a vise was used to clamp the other leg or

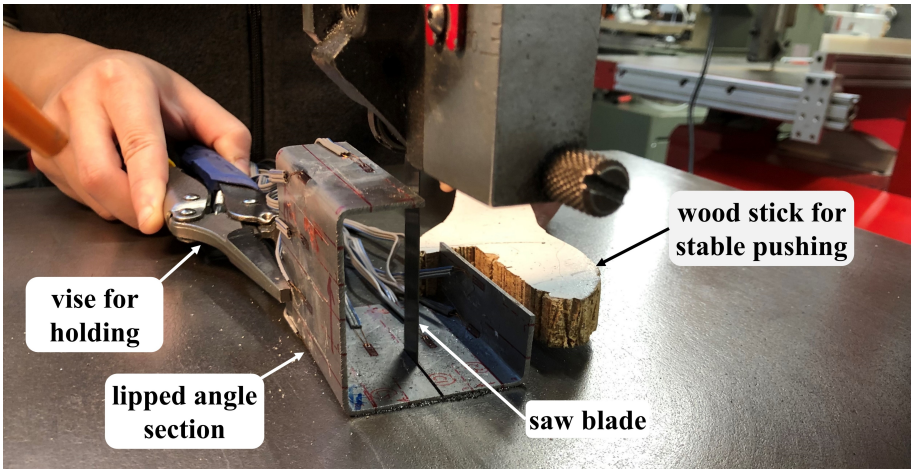

Figure 5.5: A photo showing the sectioning process.

near lip for stable sectioning while a wood push stick was used to push the steel section slowly and steadily into the blade. For the second and the sixth sectioning, the section was pushed by two wood push sticks to ensure stable movement.

After each sectioning operation, the real-time readings from the LabView monitor were observed to determine when the strain gauges adjacent to the sectioning position stabilized. This process usually took around three minutes for each sectioning operation, after which the next sectioning was conducted. Following this procedure, all eight sectioning operations for each section were finished.

5.2.4 Test results

The relationship between test time and strain reading for each measurement location as indicated by the blue numbers in parentheses in Fig. 5.3(a) was extracted. Using RS-5 as an example, the strain-time relationship at measurement location (5) as an example for the corner region is shown in Fig. 5.6(a), the relationship at

measurement location (6) as an example for the flat portion of the angle leg is shown in Fig. 5.6(b), and the relationship at measurement location (1) as an example for the angle lip is shown in Fig. 5.6(c). The beginning and the end time of the adjacent sectioning positions for the corresponding measurement locations are indicated by vertical black lines. The solid vertical lines indicate the beginning time and the dashed vertical lines the end time of the sectioning operation. Indicated times do not include the time waiting for the readings to stabilize. For measurement locations 2 to 8 of each section, two sectioning positions were adjacent to the measurement location (e.g., sectioning positions 4 and 5 were adjacent to measurement location 5 as shown in Fig. 5.6(a); sectioning positions 4 and 8 were adjacent to measurement location 6 as shown in Fig. 5.6(b)). For measurement locations 1 and 9 of each section, one sectioning position was adjacent to the measurement location (e.g., sectioning position 2 was adjacent to measurement location 1 as shown in Fig. 5.6(c)). After completing the adjacent sectioning, a short time was allowed for the specimen to cool before proceeding with the next cut. From Fig. 5.6, a clear strain plateau is observed, and the strain of the plateau is regarded as the stabilized reading for the strain gauge.

The measured strain level is as low as 10^{-4}, which is strictly within the elastic range. Therefore, the residual stress for each measurement location was calculated as the corresponding residual strain multiplied by the average modulus of elasticity of the longitudinal specimens in the tensile coupon test, which was determined as 193291 MPa. It should be noted that a measured positive residual strain after the sectioning process corresponds to compressive residual stress resulting from

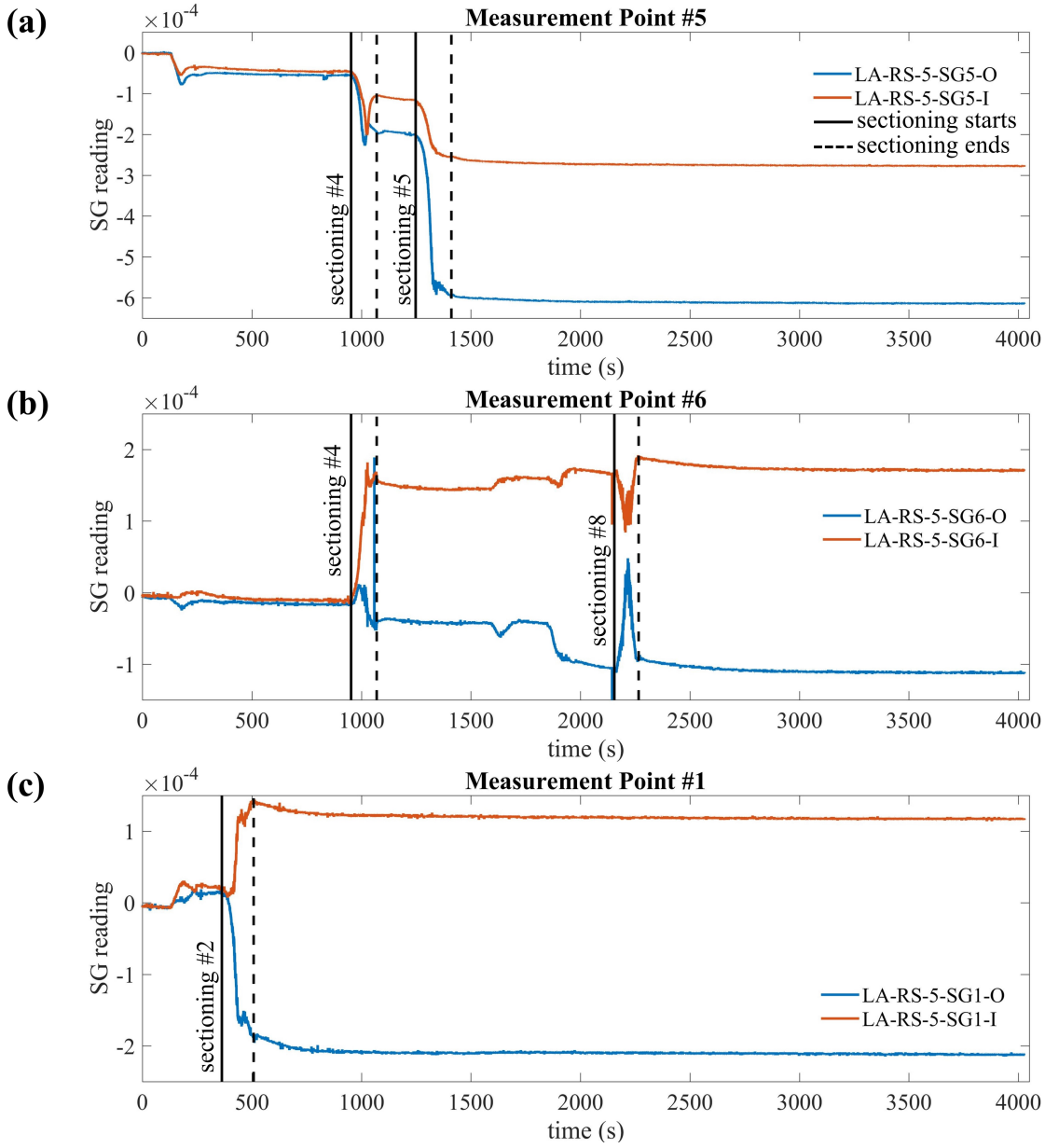

Figure 5.6: Examples of the relationship between strain readings and time for (a) corner region, (b) flat portion of the angle leg, and (c) lip region.

the forming process, and a measured negative residual strain after the sectioning process corresponds to tensile residual stress from the forming process. Therefore, the inner surfaces have compressive residual stresses, and the outer surfaces have tensile residual stresses. The relationship between the residual stress and the measured strain is shown in Eq. 5.2.

$$\sigma = -E\varepsilon \tag{5.2}$$

A summary of the measured residual strains and calculated residual stresses of all measurement locations for all sections is shown in Table 5.2 and 5.3. For both center and edge sections with different corner radii, the readings of the strain gauges attached to the outer surfaces are negative, which indicates that the outer surface contracted after the residual stresses were released. The inner surface strain readings are more complex. The strain readings are positive for the corners, negative for the flat regions of the legs, and relatively small with both positive and negative values for the lips. The largest measured strains for each section are observed at corners. The strains for RS specimens measured at outer surface corners are generally larger than those for RL specimens; while for most strains measured at the flat region on both outer and inner surfaces, those for RL specimens are larger than the RS specimen counterparts. The strain readings on the lip for both outer and inner surfaces vary significantly. For the comparison between sections cut from different locations of the same steel member (e.g., RS-1 and RS-5; RL-1 and RL-4), the percentage differences for residual stresses at corners and flat regions of legs are relatively low and most of them are within 10%. The percentage differences for the

Table 5.2: Measured residual strains at each measurement locations.

Location		RS-1		RS-5		RL-1		RL-4	
		Outer $\times 10^{-4}$	Inner $\times 10^{-4}$	Outer $\times 10^{-4}$	Inner $\times 10^{-4}$	Outer $\times 10^{-4}$	Inner $\times 10^{-4}$	Outer $\times 10^{-4}$	Inner $\times 10^{-4}$
1	lip	-2.380	1.375	-2.070	1.225	-2.595	1.230	-1.935	1.185
2	corner	-6.705	-0.460	-5.685	-2.080	-4.455	-2.395	-3.700	-1.830
3	flat leg	-0.920	1.805	-1.010	1.785	-1.290	2.510	-1.340	2.235
4	flat leg	-0.925	1.590	-1.115	1.510	-0.965	2.095	-1.195	2.205
5	corner	-6.025	-2.745	-6.130	-2.740	-4.925	-2.720	-5.325	-2.905
6	flat leg	-0.745	1.470	-1.040	1.750	-1.115	2.335	-0.700	2.295
7	flat leg	-0.835	1.360	-0.410	1.070	-1.175	2.560	-1.175	2.455
8	corner	-5.035	-1.845	-4.280	-1.370	-3.175	-2.150	-3.640	-1.930
9	lip	-0.700	-0.750	0.005	-0.275	-1.280	-0.270	-0.545	0.155

lips are relatively high and the differences are around 40%, which is still within a reasonable range considering the large force and high energy dissipated during the sectioning process. Additionally, no clear tendency in the distribution of the stress difference related to the measurement location within cross-section or along the member length was found. Therefore, based on the test data, it is suggested that the comparison between the center section and the edge section of the member does not show a significant difference in terms of residual stress distribution. Hence the procedure inherited from hot-rolled steel research to remove a significant portion of the member end and only keep the center section for residual stress measurement may not be required if the steel is not flame cut.

The major forms of residual stress which reduce the strength capacity of CFS members are internal membrane forces and flexural moments. Their corresponding stresses are referred to as membrane stress σ_m, flexural stress on outer surface σ_{fo}, and flexural stress on inner surface σ_{fi} as calculated in Eq. 5.3, 5.4, and 5.5, where ε_i and ε_o are the residual strain readings of the inside and outside surface at a

Table 5.3: Calculated residual stresses at each measurement locations.

Location		RS-1		RS-5		RL-1		RL-4	
		Outer	Inner	Outer	Inner	Outer	Inner	Outer	Inner
		MPa	MPa	MPa	MPa	MPa	MPa	MPa	MPa
1	lip	46.0	-26.6	40.0	-23.7	50.2	-23.8	37.4	-22.9
2	corner	129.6	8.9	109.9	40.2	86.1	46.3	71.5	35.4
3	flat leg	17.8	-34.9	19.5	-34.5	24.9	-48.5	25.9	-43.2
4	flat leg	17.9	-30.7	21.6	-29.2	18.7	-40.5	23.1	-42.6
5	corner	116.5	53.1	118.5	53.0	95.2	52.6	102.9	56.2
6	flat leg	14.4	-28.4	20.1	-33.8	21.6	-45.1	13.5	-44.4
7	flat leg	16.1	-26.3	7.9	-20.7	22.7	-49.5	22.7	-47.5
8	corner	97.3	35.7	82.7	26.5	61.4	41.6	70.4	37.3
9	lip	13.5	14.5	-0.1	5.3	24.7	5.2	10.5	-3.0
	corner	114.5	32.6	103.7	39.9	80.9	46.8	81.6	43.0
AVG	flat leg	16.6	-30.1	17.3	-29.6	22.0	-45.9	21.3	-44.4
	lip	29.8	-6.1	20.0	-9.2	37.5	-9.3	24.0	-13.0
	corner	14.2%	68.4%	18.0%	33.2%	21.6%	11.8%	22.6%	26.8%
COV	flat leg	10.0%	-12.3%	36.5%	-21.5%	11.7%	-8.9%	25.3%	-4.9%
	lip	77.2%	-480.4%	142.1%	-222.9%	48.1%	-220.5%	79.4%	-108.7%

measurement location.

$$\sigma_m = -E\frac{\varepsilon_o + \varepsilon_i}{2} \tag{5.3}$$

$$\sigma_{fo} = -E\frac{\varepsilon_o - \varepsilon_i}{2} \tag{5.4}$$

$$\sigma_{fi} = +E\frac{\varepsilon_o - \varepsilon_i}{2} \tag{5.5}$$

A summary of the membrane residual stresses and outer surface flexural residual stresses for all steel sections at all measurement locations is shown in Table 5.4; the inner surface flexural residual stress equals to the opposite of its outer surface counterpart. The sign on the membrane stresses indicates tension (positive) and

Table 5.4: Membrane and flexural residual stresses at measurement locations for every sections.

Location		membrane residual stress (MPa)				flexural residual stress (outer) (MPa)			
		RS-1	RS-5	RL-1	RL-4	RS-1	RS-5	RL-1	RL-4
1	lip	9.7	8.2	13.2	7.3	36.3	31.9	37.0	30.2
2	corner	69.3	75.1	66.2	53.5	60.4	34.9	19.9	18.1
3	flat leg	-8.6	-7.5	-11.8	-8.7	26.4	27.0	36.7	34.6
4	flat leg	-6.4	-3.8	-10.9	-9.8	24.3	25.4	29.6	32.9
5	corner	84.8	85.8	73.9	79.6	31.7	32.8	21.3	23.4
6	flat leg	-7.0	-6.9	-11.8	-15.5	21.4	27.0	33.4	29.0
7	flat leg	-5.1	-6.4	-13.4	-12.4	21.2	14.3	36.1	35.1
8	corner	66.5	54.6	51.5	53.9	30.8	28.1	9.9	16.6
9	lip	14.0	2.6	15.0	3.8	-0.5	-2.7	9.8	6.8
	corner	73.5	71.8	63.9	62.3	41.0	31.9	17.0	19.3
AVG	flat leg	-6.8	-6.1	-12.0	-11.6	23.3	23.4	33.9	32.9
	lip	11.9	5.4	14.1	5.5	17.9	14.6	23.4	18.5
	corner	13.4%	22.0%	17.8%	24.0%	41.0%	10.8%	36.5%	18.5%
COV	flat leg	-21.2%	-26.4%	-8.7%	-26.2%	10.6%	26.1%	9.5%	8.5%
	lip	25.7%	73.0%	8.8%	45.0%	145.4%	167.6%	82.4%	89.7%

compression (negative). For most cases except the lips on location 9 for small radius sections, the flexural residual stresses are considered to be in compression on the inner surface and in tension on the outer surface and vary linearly through the thickness [128]. The flexural residual stresses of the lips on location 9 for small radius sections have opposite direction from the majority while their magnitudes are relatively small and close to zero. The membrane and flexural residual stress distribution on member cross-section, as well as the percentage ratio between the residual stress and the yield strength for the smaller corner radius sections, are shown in Fig. 5.7(a) and those for the larger corner radius sections are shown in Fig. 5.7(b).

The following observations are made from the residual stress distribution of the four test sections. First, the direction of the stresses (i.e., tension or compression) at each measurement location is the same between the edge and center section. Second,

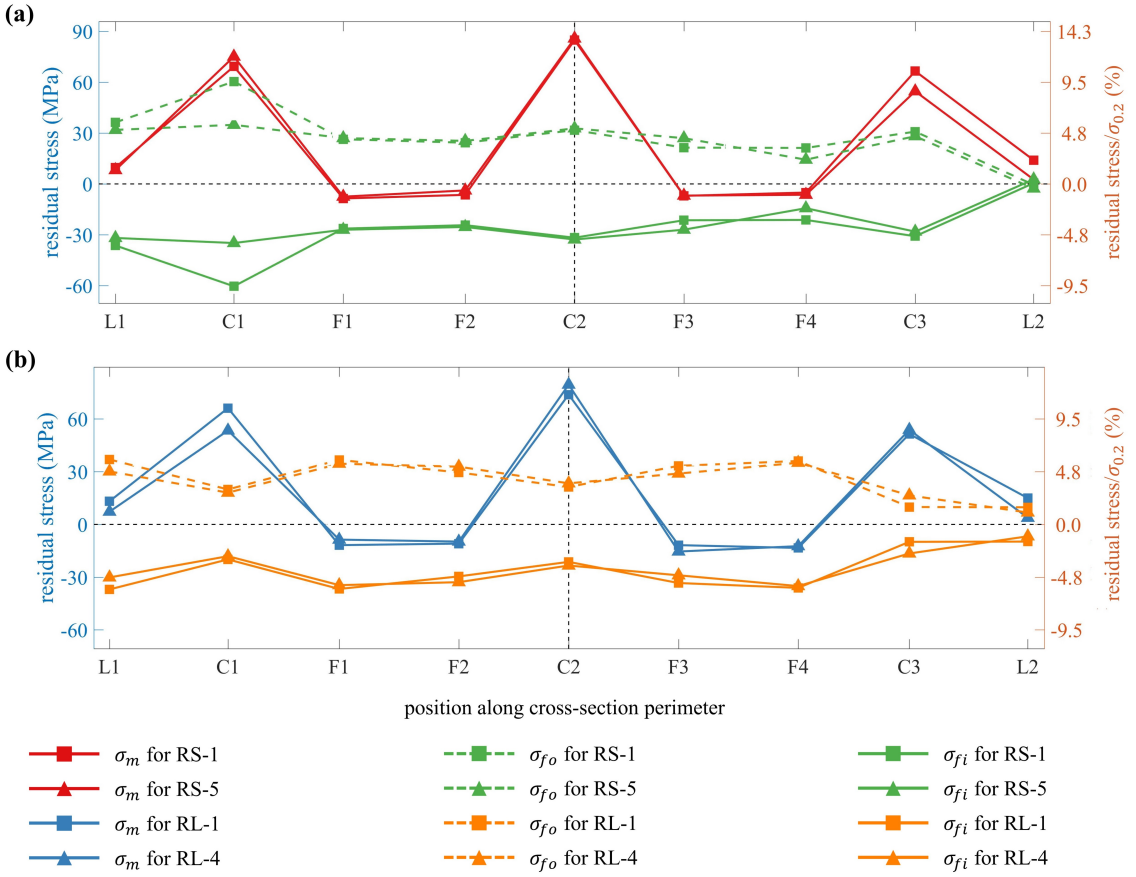

Figure 5.7: The distribution of membrane and flexural residual stresses along the cross-section perimeter for DP-580 lipped angle sections with (a) 5/64 inch inner corner radius and (b) 9/64 inch inner corner radius.

for the flexural residual stress, at different measurement locations on both corners and flat regions of legs, the percentage difference between the edge and center section ranges from 0.4% to 24.8% for the RS sections and from 3.2% to 12.6% for the RL sections. For the lip, the percentage difference of the flexural residual stress is large, while the influence is negligible considering the residual stress magnitude on the lip is small, where the flexural stress difference between the center and edge sections is 3.3 MPa for RS sections and 4.9 MPa for RL sections. For all four sections,

the flexural residual stress is relatively stable along the cross-section perimeter and the stress magnitude is around 30 MPa. Additionally, the flexural residual stresses at the corners are generally larger than those at its adjacent flat regions for RS sections; the situations are opposite for the RL sections. Relative to the yield strength (0.2% proof stress, which equals 629.2 MPa), the flexural residual stress ranges from 0.1% to 9.6% for RS sections and ranges from 1.1% to 5.9% RL sections. Thirdly, for the membrane residual stress, the magnitude and direction at different locations of the section cross-section vary. The largest membrane residual stresses are observed at corners, where the average magnitude is 72.7 MPa for the RS sections and 63.1 MPa for the RL sections and they are all in tension. While at the flat regions, including both legs and lips, the membrane residual stress magnitudes are much smaller and range from 2.6 MPa to 14.0 MPa for the RS section and range from 3.8 MPa to 15.5 MPa for the RL sections. For the direction, those at the lips are in tension and those at the flat regions of the legs are in compression. In summary, the flexural residual stresses are relatively stable and moderate along the cross-section perimeter. The membrane residual stresses at the corners are more significant and those at the flat regions have less influence.

To compare the residual stress distribution of press-braked members made of AHSS material used in this study with press-braked members made of conventional CFS from previous studies, a summary of the flexural and membrane residual stresses is shown in Table 5.5. Some literature does not include all information and is therefore labeled as N/A (not applicable). Some literature used figures only, rather than specific values, to illustrate the results, so the values for these

cases are estimated. The value or value range in this table is the absolute value of the residual stresses (i.e., the directions of the residual stresses are not included). Each specimen label from the original paper is shown in the second column of the table. For each specimen, two rows of data are listed. The first row is the residual stress in MPa, and the second row is the ratio between the residual stress and mate-rial yield strength. From Ingvarsson's study [124], much larger membrane residual stresses are observed at the corner and flange compared to other studies. Note, the thickness of the plate (7.5 mm) in Ingvarsson's work [124] is much larger than the thicknesses of sheets (from 1.22 mm to 3.07 mm) in other studies. For Weng's tests [125], the flexural residual stresses on the corner, flange, and web are larger compared to others' work and some of the maximum values are larger than the nominal yield strength. The membrane residual stresses for Weng's work [125] are low. For Batista's work [126], the flexural residual stresses in the flat part are much larger than the flexural residual stresses from the results of this study (e.g., the maximum stress on the web of Batista's work is around 3.5 times of the maximum stress on the leg of this study), while the membrane residual stresses of the flat parts are similar to their counterpart of this study. For Young's study [127], both the flexural and membrane residual stresses at the flat parts are similar to their counterpart in this study. Compared to the model based on experimental statistics proposed by Schafer [128], the ratio between flexural residual stresses and yield strength at the corner in this study is only around one-fourth of the model recommendation. The ratio for the flat part is slightly smaller than the flange value and much smaller than the web value of the model recommendation.

Table 5.5: Flextural and membrane residual stresses as well as the percentage ratio between residual stresses and material yield strength for press-braked cold-formed steel from previous studies.

Source	Member label	σ_y (MPa)	σ_f (MPa) / σ_f/σ_y			σ_m (MPa) / σ_m/σ_y		
			Curved Corner	Flat Flange	Flat Web	Curved Corner	Flat Flange	Flat Web
Ingvarsson [124]	member	802		N/A		100	0 to 300	20
				N/A		12%	0% to 37%	2.5%
Weng [125]	P11	232	270	170	170	5	5	5 to 10
			116%	73%	73%	2%	2%	2% to 4%
	P16	221	240	160	160	10	0	0 to 10
			109%	72%	72%	4%	0%	0% to 4%
	PBC14	250	250	100 to 120	130	15	0	5
			100%	40% to 48%	52%	6%	0%	2%
Batista [126]	CP3	not given	N/A	15 to 100	25 to 130	N/A	0 to 10	0 to 15
Young [127]	Specimen I	450	N/A	3.9 to 34.1	9.9 to 31.7	N/A	0.0 to 9.7	1.4 to 9.7
			N/A	0.9% to 7.6%	2.2% to 7.0%	N/A	0.0% to 2.1%	0.3% to 2.2%
	Specimen II	450	N/A	2.1 to 37.0	32.6 to 37.2	N/A	4.3 to 8.6	3.0 to 3.8
			N/A	0.5% to 8.2%	7.2% to 8.3%	N/A	1.0% to 1.9%	0.7% to 0.8%
Schafer [128]	Press-braked		33%	8%	17%	ignored (counteract with σ_y elevation)		
This study	RS-1	629.2	41.0	0.5 to 36.3		73.5	5.1 to 14.0	
			7%	0.1% to 5.8%		12%	0.8% to 2.2%	
	RS-5	629.2	31.9	2.7 to 31.9		71.8	2.6 to 8.2	
			5%	0.4% to 5.1%		11%	0.4% to 1.3%	
	RL-1	629.2	17.0	9.8 to 37.0		63.9	10.9 to 15.0	
			3%	1.5% to 5.9%		10%	1.7% to 2.4%	
	RL-4	629.2	19.3	0.5 to 36.3		62.3	3.8 to 15.5	
			3%	1.1% to 5.6%		10%	0.6% to 2.5%	

5.3 Numerical study

5.3.1 Scope

Although using the sectioning method to measure the residual stress is straightforward and the results are relatively reliable, the method is a destructive method with non-negligible time, labor, and equipment costs. Therefore, conducting a large number of sectioning tests is difficult and costly. Additionally, for the sections with thin-walled geometry, only the residual stresses at section surfaces can be measured, while those through section thickness can not be measured because of the difficulty of strain gauge installation. However, in many existing studies [131]–[136], the maximum residual stresses are commonly observed through the thickness based on the steel section material, shape, forming method, and thickness. Therefore, in this section, a finite element model is designed to simulate the press-braking process for the DP-580 lipped angle section. The model is validated by comparing the results between the experimental study and the simulation. The through-thickness residual stresses are extracted from the validated finite element model.

5.3.2 Simulation setup

The finite element software Abaqus [137] was used to simulate the press-braking process for the DP-580 lipped angle sections. The punch and die were designed as 2D discrete rigid parts and therefore meshed using discrete rigid elements since the deformation is negligible. The geometry of the punch and die were designed to perfectly fit the desired steel corner deformation, where the radius of the punch

equaled the inner corner radius of the section and the radius of the die equaled the outer corner radius of the section. The steel sheet was designed as a 2D deformable part and meshed using CPE4R (four-node plane strain element), which is suitable for sheets with thin-walled geometry subjected to large strains. The width of the steel sheet equaled the perimeter of the cross-section, which was 172.7 mm for RL sections and 171.9 mm for RS sections. The element size was 0.09 mm, which corresponded to 20 elements for the 1.8-mm thickness. For the material definition, an engineering stress-strain relationship was generated using the two-stage plus linear model proposed in [5], where the model parameters were from the averages of experimental stress-strain data for DP-580 specimens cut along sheet longitudinal direction. The generated engineering stress-strain curve was converted to true stress-strain curve by Eq. 5.6 and 5.7, where σ_t and ε_t are the true stress and strain, σ_e and ε_e are the engineering stress and strain. The relationship between post-yield stress and plastic strain generated using the true stress-strain curve was used as the material input for the steel sheet.

$$\sigma_t = \sigma_e \times (1 + \varepsilon_e) \tag{5.6}$$

$$\varepsilon_t = \ln(1 + \varepsilon_e) \tag{5.7}$$

Step-wise dynamic implicit analysis was adopted in the simulation. Each step represented the press-braking and spring back for each section corner. Therefore, three steps were needed for each lipped angle section because of its three corners.

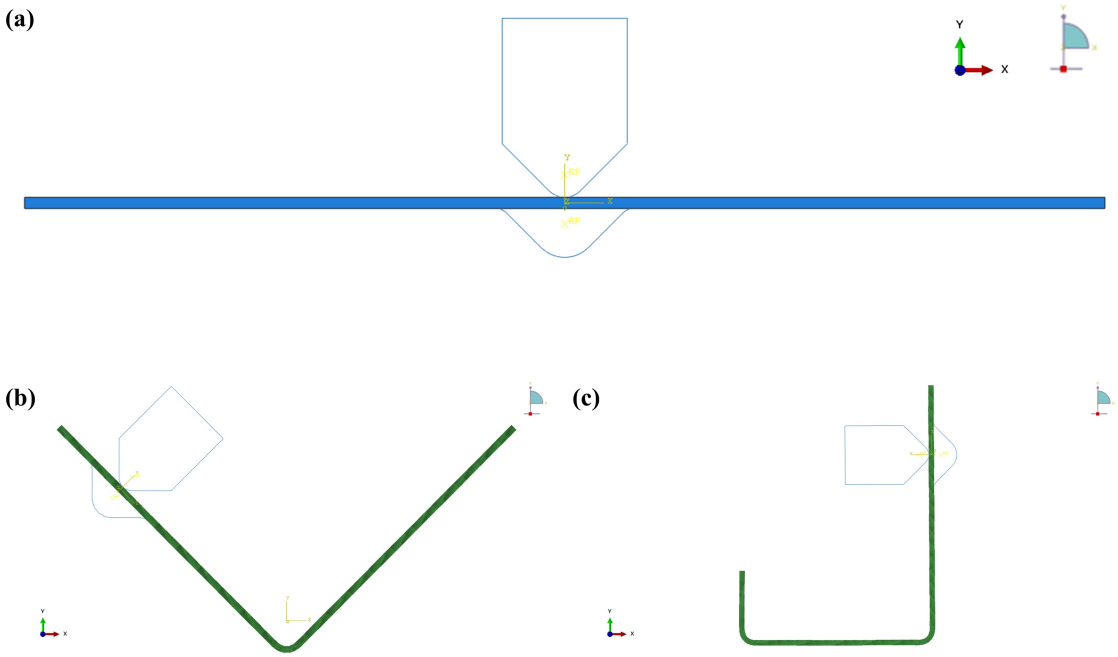

Figure 5.8: The placement of the steel section, punch, and the die for (a) the first step, (b) the second step, and (c) the third step.

For each step, the punch head was placed perpendicular to the inner surface of the desired corner location and the horizontal support of the die was placed at the outer surface of the same desired corner location. The placement of the steel sheet, the punch, and the die for each step is shown in Fig. 5.8. A contact was defined between the punch head and the cross-section inner surface for the press-braking process while it was removed during the spring back process. Another contact was defined between the horizontal support of the die and the outer surface of the steel sheet for both press-braking and spring back processes.

The residual stresses for the press-braked sections result from the press-braking and spring back processes, plus the coiling, uncoiling, and flattening processes during the forming of the CFS sheet. For the first step to form the corner at the

sheet center, the residual stresses resulting from the sheet forming process were included by using the model proposed by Moen and Schafer [138]. The direction of the residual stress in the model could be tension for the inner side and compression for the outer side, or the opposite situations based on the coiling direction of the sheet. It was reasonable to assume that the residual stress direction in the model was consistent with that of the test result at the flat region of the legs, where the stresses on the inner surface were negative and on the outer surfaces were positive. The loading was always applied along a local direction which was perpendicular to the sheet at the desired corner. In terms of the local direction, the die was fully fixed during both the press brake and spring back processes, and the punch was fixed in all directions except the loading direction. A displacement control loading was applied on the punch during the press brake process and the displacement was set from the circle center of the punch head to the circle center of the die. Then that exact displacement was set back to zero during the following process to simulate the spring back. For the second and the third step, the deformed cross-section and the stresses and strains within each element of the deformed section were necessary to proceed. therefore, the deformed section geometry was imported as a new part and the stress state was imported as a predefined initial state from the output database of the previous step.

Additionally, it was found that the residual stress distribution and magnitudes were significantly affected by the die shape. When the die shape perfectly fit the design dimension and the die radius for this situation was labeled as R_0, the outer surface of the steel sheet experienced intense direct contact with the die because

of the sheet deformation along the sheet thickness direction. When a sharp die (i.e., die radius equals zero) was adopted, this contact could be avoided. The longitudinal residual stress distributions for members press-braked with a fully rounded die and a sharp die are shown in Fig. 5.9. Considering the inevitable errors during steel section manufacturing and the sectioning processes, plus the unknown dimension for the die being used, the residual stress magnitude and distribution by using different die shapes with different radii between 0 and R_0 were investigated. Besides the die radii, all other procedures and setups for the simulation were identical.

5.3.3 Simulation results

The stresses along the direction perpendicular to the plane (i.e., S33 of the output database) were extracted. The width of the strain gauge used in the experimental study was 1.5 mm, which corresponds to around 17 elements. The average stresses of S33 for the center 17 elements at each corner position for both outer and inner surfaces were calculated and used for comparison with test data. By varying the die radius between 0 and R_0, certain radii were selected exhibiting reasonable differences between test and simulation data. The selected die radii were 3.634 mm for RS sections and 4.72 mm for RL sections respectively. The comparison between the test data and the simulation results using three different base radii ($r = R_0$, $r = 0$, and the selected radius) are shown in Fig. 5.10 and 5.11 for RS and RL sections respectively. For the locations in the figures, 0.9 mm represents the inner surface and -0.9 mm represents the outer surface. The comparison shows the selected radius

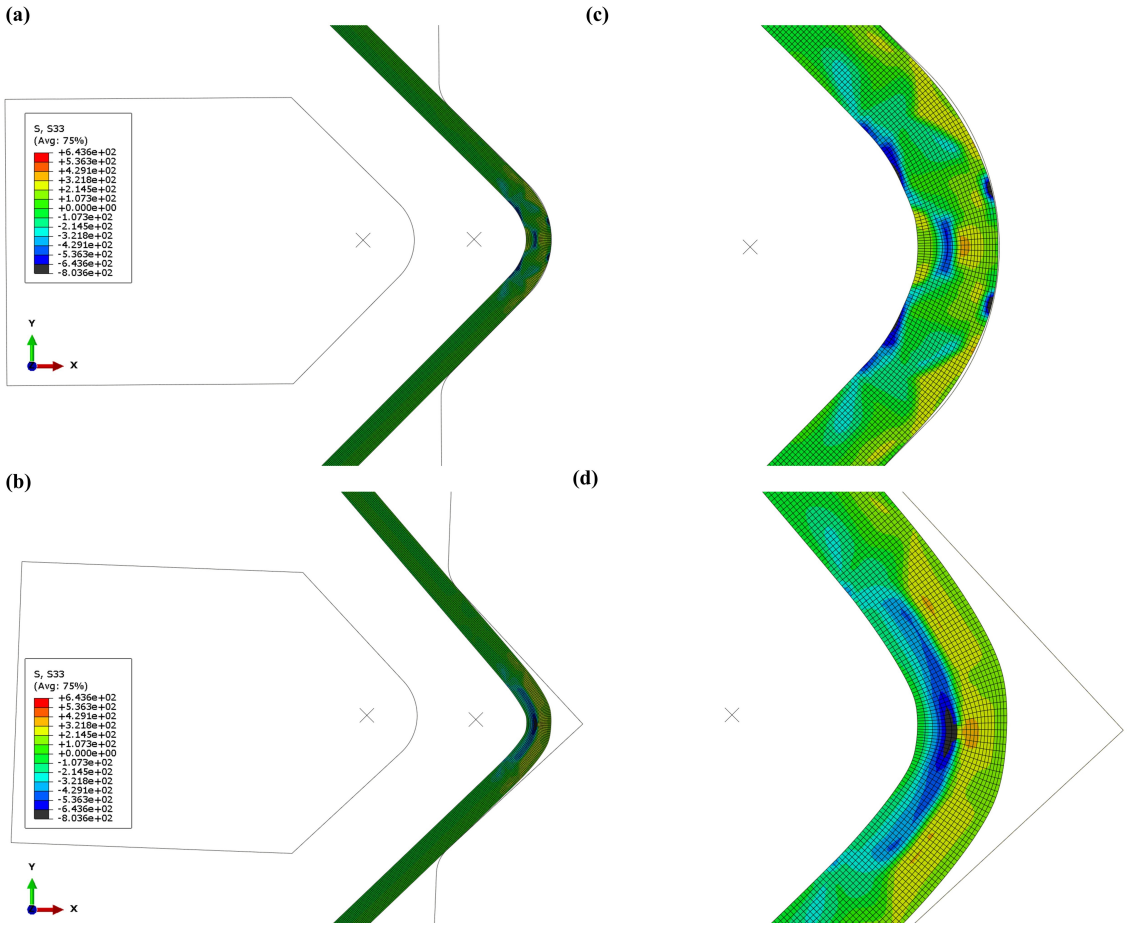

Figure 5.9: (a) and (b): deformation of the angle member after press-braking and spring-back processes using rounded and shape die respectively. (c) and (d): a close look of (a) and (b) illustrating the longitudinal residual stress distribution through member thickness at angle corners.

simulation cases have minimal differences from the corresponding experiment data at the corners, where the stresses are more pronounced. The stresses at the flat region could have large percentage differences, while the absolute differences are small, which lead to negligible influence on steel member strength. Fig. 5.10 and 5.11 also illustrate the through-thickness residual stresses captured from the simulation. For both RS and RL sections at corners, the maximum stresses are observed at around a quarter of the thickness from the inner surface and the maximum stresses are in compression as high as 700 MPa in compression. Additionally, the stresses are observed to vary drastically between the inner surface and the centerline of the sheet.

5.4 Conclusions

Four sections with two different corner radii cut from two 21-inch long advanced high-strength cold-formed steel pressed-braked angle members were used to measure the cross-section residual stress distribution. Two sections were cut from the member edge, and the other two were cut from the member center along member length. The results show the residual stresses on the corners are in tensions on both surfaces and are more pronounced than the residual stresses on the flat regions. For the residual stresses on the flat regions, those on the outer surfaces are generally in tension while those on the inner surfaces are in compression, which is considered as a direct result of the cold-forming process and shows good consistency with the results from existing studies. The membrane and flexural residual stresses on the

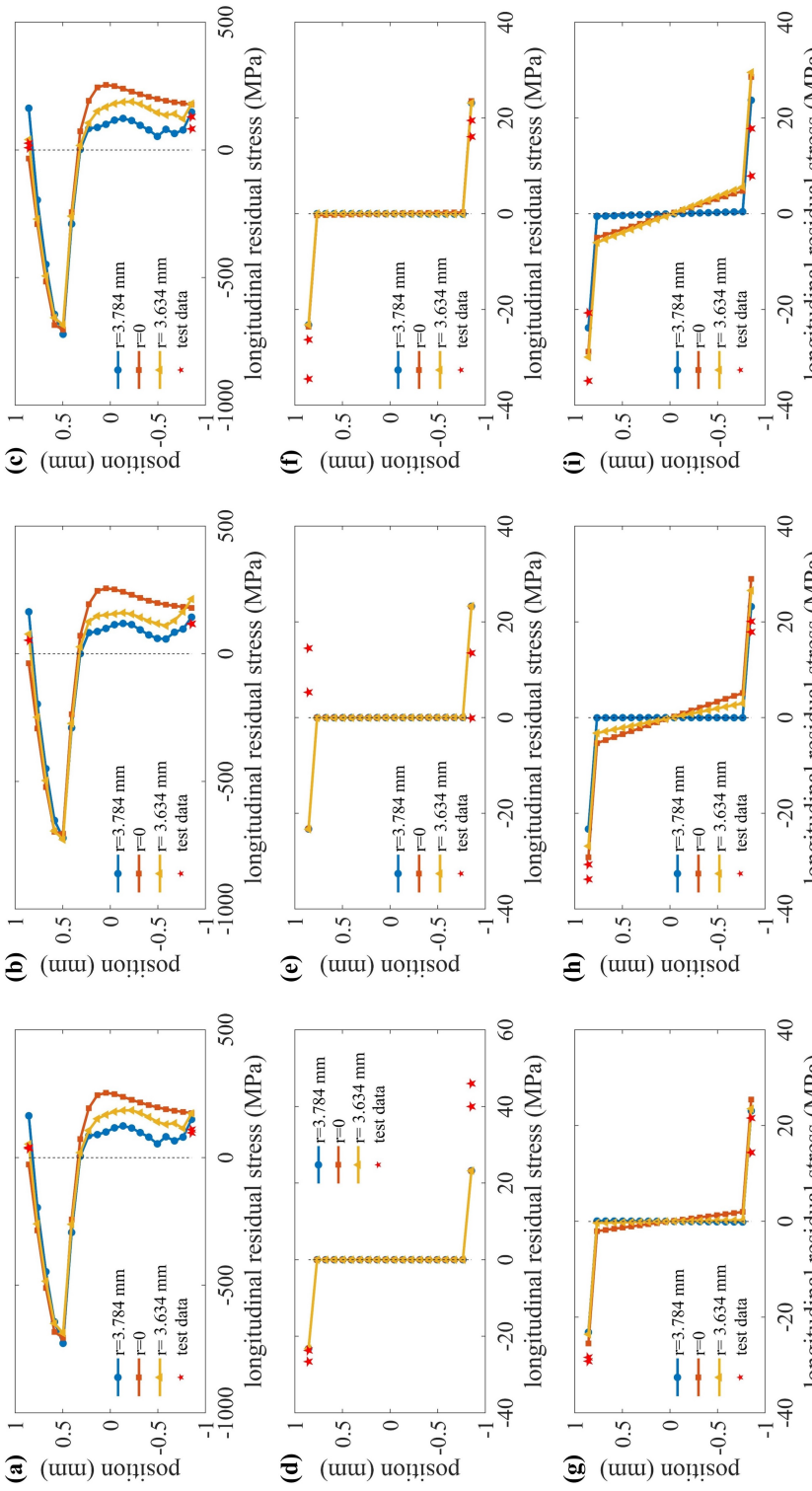

Figure 5.10: Comparison between the test results and the simulation results with three different die shapes for RS sections at (a) left corner (#2), (b) center corner (#5), (c) right corner (#8), (d) left lip(#1), (e) right lip (#9), (f) flat region (#3), (g) flat region (#4), (h) flat region (#6), and (i) flat region (#7).

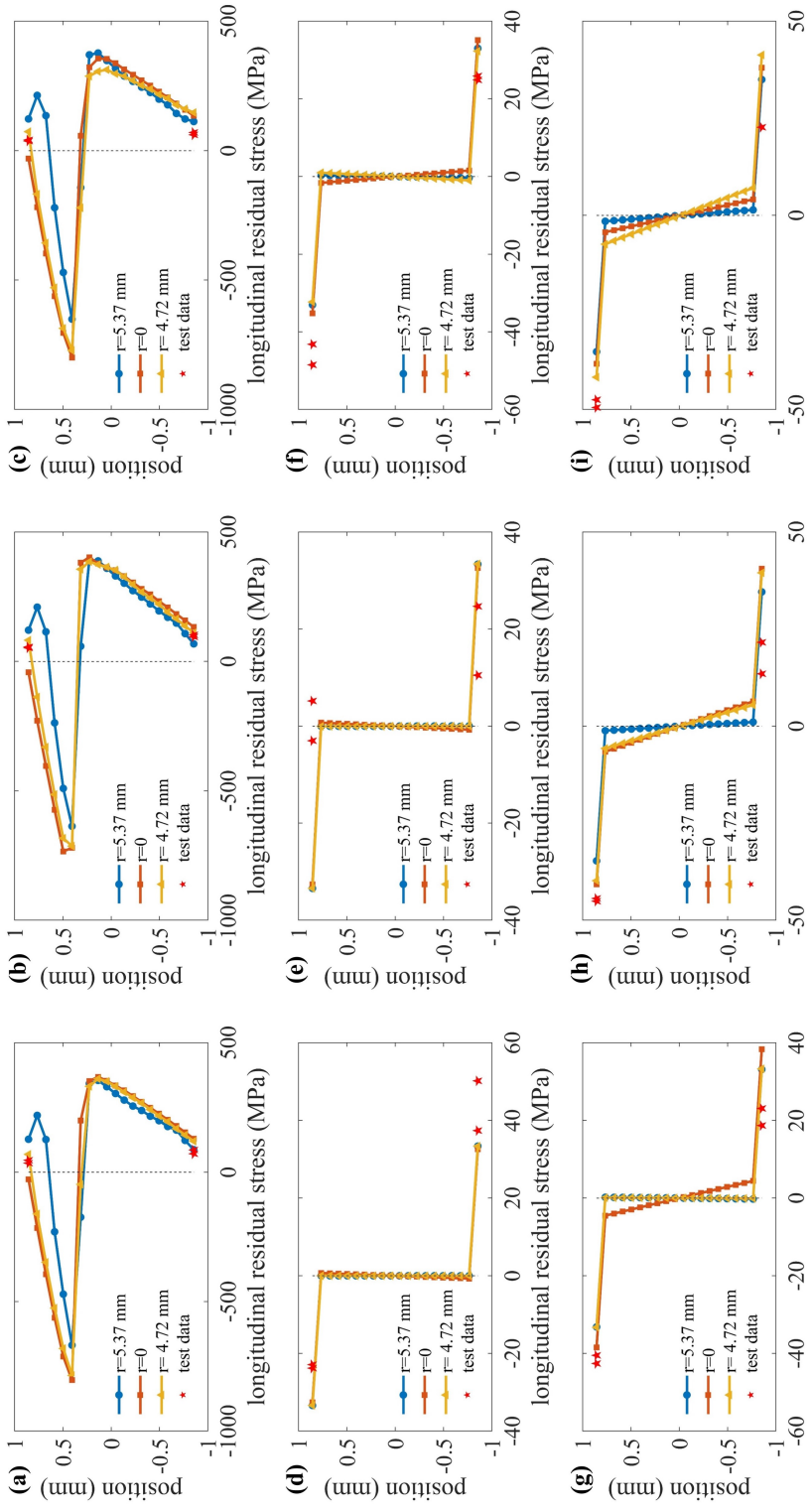

Figure 5.11: Comparison between the test results and the simulation results with three different die shapes for RL sections at (a) left corner (#2), (b) center corner (#5), (c) right corner (#8), (d) left lip (#1), (e) right lip (#9), (f) flat region (#3), (g) flat region (#4), (h) flat region (#6), and (i) flat region (#7).

surfaces are calculated based on the measured residual stresses. For the membrane residual stress, corners and lips show compression stresses and flat regions of legs show tension stresses. The highest value of membrane residual stress is found at corners, while the lips and flat regions of the legs have a relatively low magnitude of membrane residual stress. The flexural residual stresses generally have a larger and more stable magnitude than the membrane residual stress, except at the corner region where membrane residual stresses are highest. Relative to yield strength measured from tensile coupon tests, the membrane residual stresses are 0.4% to 12%, and the flexural residual stresses are 0.1% to 7% of yield strength. Based on the test data, no significant difference is found between the residual stresses of the edge section and the center section. A finite element model is developed and validated. By adopting the validated model, more data of the residual stress distribution are provided, including the through-thickness residual stresses, where a maximum residual stress of around 700 MPa is observed.

Chapter 6

Cold-formed steel strength predictions for combined bending and torsion

Xia, Yu, Glauz, Robert S., Schafer, Benjamin W., Seek, Michael, and Blum, Hannah B. "Cold-formed steel strength predictions for combined bending and torsion." Manuscript in preparation and to be submitted Fall 2022.

Abstract

Locally slender open cross-section members are susceptible to significant twisting and high warping torsion stresses. Torsion considerations are complicated by whether it is derived as a first-order effect from loading or a second-order effect from instability. Previous direct torsion experiments on lipped channels have shown sig-

nificant inelastic reserve in limited cases. The current design for combined bending and torsion interaction has some limitations, including only considering the first yield in torsion and ignoring the cross-section slenderness in torsion. A parametric study is conducted to predict the torsion capacity in locally slender cross-sections. Shell finite element models of lipped Cee and Zee section members are validated with existing experiments on combined bending and torsion. The validated models are utilized for a parametric study with applied torsion on a range of cross-sections, steel grades, and member lengths to cover the range of practically expected torsional slenderness. A set of bimoment parameters, including yield bimoment, buckling bimoment, and plastic bimoment, are calculated and the ultimate bimoment is determined by performing shell finite element collapse analyses. A simple uniform equation is adopted to predict the bimoment capacity and two bimoment strength curves under torsion only are proposed for local and distortional buckling controlled cases respectively. The validated models are updated and utilized for another parametric study with applied bending-torsion on a range of cross-section geometries, member lengths, bracing conditions, and loading eccentricities. The interaction equations for different loading cases between bending moments and bimoments are developed.

6.1 Introduction

Cold-formed steel (CFS) is a common construction material in which steel sheets are shaped into structural members by the cold-working processes and are widely used

in many structural and non-structural applications. Among different types of CFS shapes, the thin-walled open sections (e.g., Cee and Zee) are the most common for structural framing. The thin-walled geometries are beneficial to reducing the self-weight, hence lower transportation, material costs, and labor costs. However, due to the open thin-walled geometries, CFS sections have low torsional stiffness and can be vulnerable to even a small amount of torsional load. Therefore, understanding the internal torsional forces for CFS members is important to correctly conduct the member and structure design [139].

A member subjected to torsional loads may develop both shear stresses and longitudinal stresses. For typical open cross-sections, the most critical internal force is the bimoment (B) caused by the longitudinal stresses. However, limited literature shows the method to calculate the bimoment strength, while a few design standards provide indirect methods to consider the effect resulting from torsional stresses. Section H4 of AISI S100 [30] states that for members under combined bending and torsion, the flexural strength should be reduced by a reduction factor R, which is given as Eq. 6.1:

$$R = \frac{f_{bending,max}}{f_{bending} + f_{torsion}} \tag{6.1}$$

where $f_{bending,max}$ is the bending stress at extreme fiber, $f_{bending}$ is the bending stress at location in cross-section where combined bending and torsion stress is maximum, and $f_{torsion}$ is the torsional warping stress at location in cross-section where combined bending and torsion stress is maximum.

Section 6.1.6 of Eurocode 3 Part 1-3 [120] stipulates the upper bound of the total

longitudinal stress and the total shear stress for members under combined bending and torsion as shown in Eq. 6.2:

$$\sqrt{\sigma_{tot,Ed}^2 + 3\tau_{tot,Ed}^2} \leqslant 1.1\frac{f_{ya}}{\gamma_{MO}} \tag{6.2}$$

where $\sigma_{tot,Ed}$ is the design total direct stress, calculated on the relevant effective cross-section, $\tau_{tot,Ed}$ is the design total shear stress, calculated on the gross cross-section, f_{ya} is the steel average yield strength, and γ_{MO} is a safety factor.

Section 5.3.2 of GB 50018 [140] stipulates the upper bound of the sum of normalized bending moment and bimoment as shown in Eq. 6.3, which is transformed into Eq. 6.4 by Wan et al. [4]:

$$\sigma = \frac{M}{W_{enx}} + \frac{B}{W_{\omega}} \leqslant f \tag{6.3}$$

$$\frac{M}{M_b} + \frac{B}{B_y} \leqslant 1 \tag{6.4}$$

where M_b is the bending capacity under bending moment only and B_y is the bimoment capacity under torsion only.

These standards consider the reduction for yield moment and bimoment, while member inelastic behaviors are not considered.

Wan et al. [4] carried out an experimental campaign to investigate the torsional strength of a pair of Cee and Zee sections under combined bending and torsion caused by vertical loads at different eccentricities. The experimental results were compared with Eq. 6.4 and the comparison showed the design equation is very

conservative, particularly for Zee sections. Bian et al. [141] investigated the member behavior of a set of Cee section short beams under torsion only by both experimental and numerical study. Based on the experimental results and the simulation results with expanded torsional slenderness and strengths, two groups of piecewise equations predicting the torsion capacity were provided as shown in Eq. 6.5 with parabolic inelastic reserve and Eq. 6.6 with linear inelastic reserve:

$$\frac{T_n}{T_y} = \begin{cases} 2 - \lambda_T^2 & \text{for } \lambda_T \leqslant 1 \\ 1/\lambda_T^2 & \text{for } \lambda_T > 1 \end{cases} \tag{6.5}$$

$$\frac{T_n}{T_y} = \begin{cases} 2.5 - 1.5\lambda_T & \text{for } \lambda_T \leqslant 1 \\ 1/\lambda_T^2 & \text{for } \lambda_T > 1 \end{cases} \tag{6.6}$$

where T_n is the torsional strength, T_y is the torque at first yield, $\lambda_T = \sqrt{T_y/T_{cr}}$ is the torsional slenderness, and T_{cr} is the critical elastic torsional buckling moment.

However, the data used in the numerical study only included one Cee section (400S162-54). Other Cee section geometries and Zee sections should also be investigated. Furthermore, it is desirable to determine if the torsional strength can be predicted by a simpler and uniform equation in lieu of piecewise equations.

In this paper, a numerical study is carried out to predict the bimoment capacity of thin-walled CFS Cee and Zee sections under torsional load. Firstly, a finite element model is developed and validated by the benchmark data reported previously [4] which considered combined torsion and bending loading. Then the validated model is modified for applied torsional loads only and the model is used in a parametric

study. Various Cee and Zee sections from design manuals, various steel grades, and various member lengths were investigated. Bimoment parameters, including yield bimoment, buckling bimoment, and plastic bimoment, are calculated based on the member cross-section geometry and yield strength. The ultimate bimoment for each case is also calculated from the longitudinal stresses obtained from finite element analyses. Based on the relationship between the ultimate bimoment and other bimoment parameters, a single continuous equation with only two numerical coefficients is adopted for the bimoment strength calculation. In addition, for local buckling (LB) and distortional buckling (DB) controlled cases, two groups of equation coefficients are provided. Additionally, a parametric study to understand the interaction between bending and torsion is conducted for the combined bending-torsion case and a series of interaction equations between bending moment and bimoment are proposed.

6.2 Development and validation of torsion finite element model

A finite element model was designed and developed based on a combined torsion and bending experimental study [4]. Firstly, to guarantee the reliability of the model, the model was developed to simulate the experiment from all aspects and the simulation results were compared directly with the experiment results. Then, upon completion of model validation, the model was adjusted to support a parametric study of members under torsion only by adopting different cross-section

geometries and different material definitions.

The experimental study [4] investigated the member behaviors of press-braked CFS Cee and Zee sections under combined bending and torsion. The study included two cross-section geometries ($180\times70\times20\times2.5$ and $185\times70\times20\times1.8$ in the form of $D \times B \times d \times t$ in mm, where D, B, and d are the outer-to-outer web depth, flange width, and lip length, t is the thickness) for Cee and Zee respectively, where the yield strength for the 2.5 mm thick steel is 345 MPa and for the 1.8 mm thick steel is 318 MPa. For each cross-section geometry, two different member lengths (1200 mm and 1500 mm) were included. The members were simply-supported and loaded under an eccentric vertical load at mid-span, where the vertical load introduced the bending and the eccentricity of the load introduced the torsion. For each case, three different eccentricities on the side away from the top flange (30, 40, and 50 for Cee, and 40, 50, and 60 for Zee, in mm) were investigated. A schematic diagram from the literature [4] is shown in Fig. 6.1 to help readers better visualize the test setup.

The finite element model was developed using FEA software Abaqus [137]. The member was modeled by S4R shell elements, and each element had an aspect ratio between 0.5 and 2 except those at the corners. The material was modeled as elastic-perfectly-plastic (EPP) using the yield strengths from the experiments and $E = 203$ GPa recommended by AISI S100 [30]. By adopting the principle of force transmissibility as illustrated in Fig. 6.2, the eccentric vertical load was transformed into a vertical load P directly acting on the juncture of web and top flange, and a pair of lateral loads Q with opposite directions acting on the juncture of web and

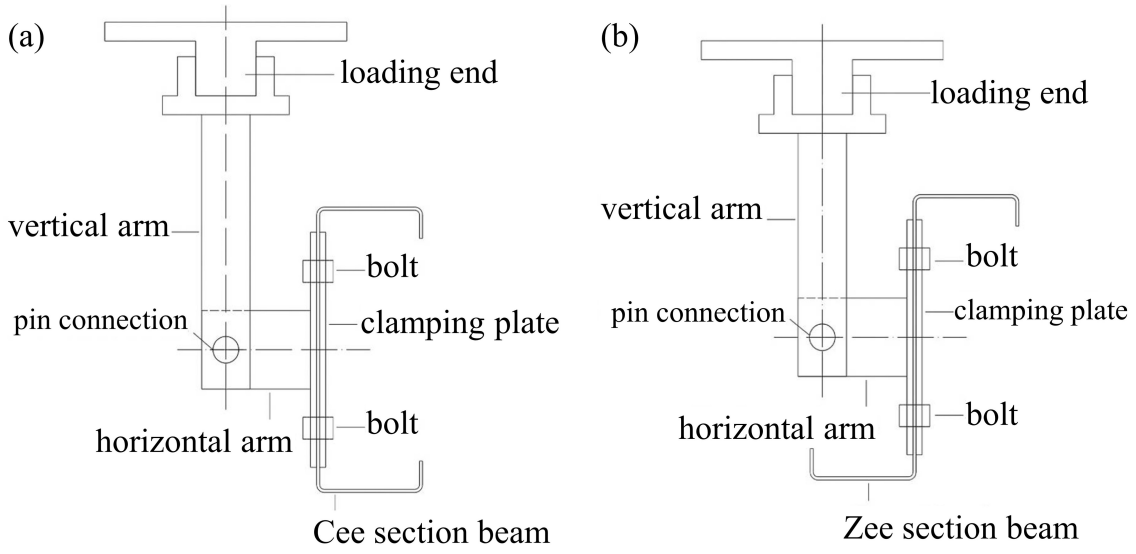

Figure 6.1: Loading method for (a) Cee section beam and (b) Zee section beam (Fig. 5 from [4]).

top flange as well as the juncture of web and bottom flange respectively. Different eccentricities reflected the relationship between P and $Q = P(ds+e)/D$, where ds is the horizontal distance between the web center and shear center. For the boundary conditions at the two Cee or Zee ends, the nodes were restrained in the cross-section plane, thus the rotation about the member longitudinal direction was automatically restrained. The nodes at two ends were free to move in the longitudinal direction based on a longitudinal warping-free assumption. At midspan, all nodes along one cross-section were restrained in the longitudinal direction to prevent rigid body motion. Both scenarios without and with initial geometric imperfection (GI) were studied. The buckled shapes corresponding to the local and distortional minima of signature curves due to bending generated in CUFSM's [142] finite strip analyses were selected as the shapes of initial GI. Both inward and outward GI shapes were considered, where *inward* and *outward* describe the deformation direction of top

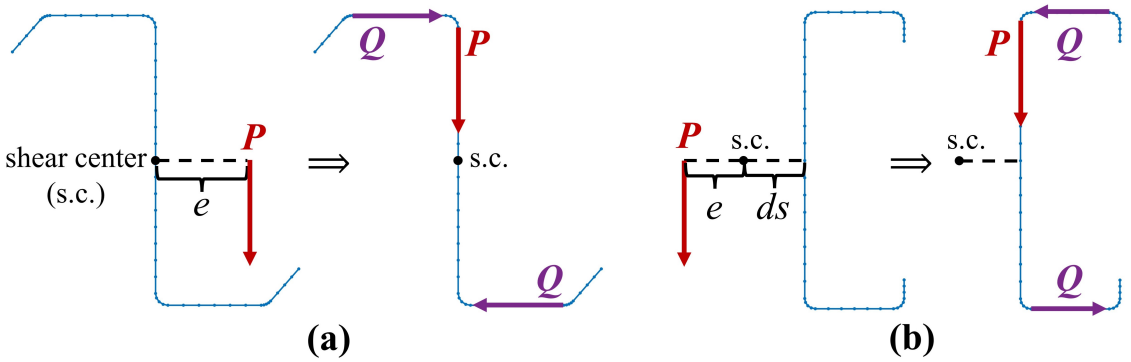

Figure 6.2: Transformation of eccentrically load for (a) Zee section and (b) Cee section.

flange for local buckling (LB) and lip-flange juncture for distortional buckling (DB) as illustrated in Fig. 6.3. Either the inward or outward GI shape was generated from CUFSM analyses, and the other GI shape was determined by switching the sign of the displaced nodes (ΔY and ΔZ as shown in Fig 6.10) of the cross-section. The average magnitudes of GI summarized in [143] (0.47t for LB and 1.03t for DB) were selected as the maximum magnitudes of the GI shapes. The residual stress was not included. The simulations were conducted using Abaqus' Riks solver to obtain a post-peak response. Typical simulation setup for Cee and Zee section is shown in shown in Fig. 6.4.

The longitudinal stress distribution and deformed shape for representative members at peak applied load is shown in Fig. 6.5. The magnitude of the peak applied vertical load P was extracted from the simulations as the major result.

The comparison of peak vertical load P between the experiment [4] and the simulations is shown in Fig. 6.6 and Table 6.1. There are two results with geometric imperfections for each case – one considering inward imperfections (Fig. 6.3(b) and (d)) and the other considering outward imperfections (Fig. 6.3(a) and (c)).

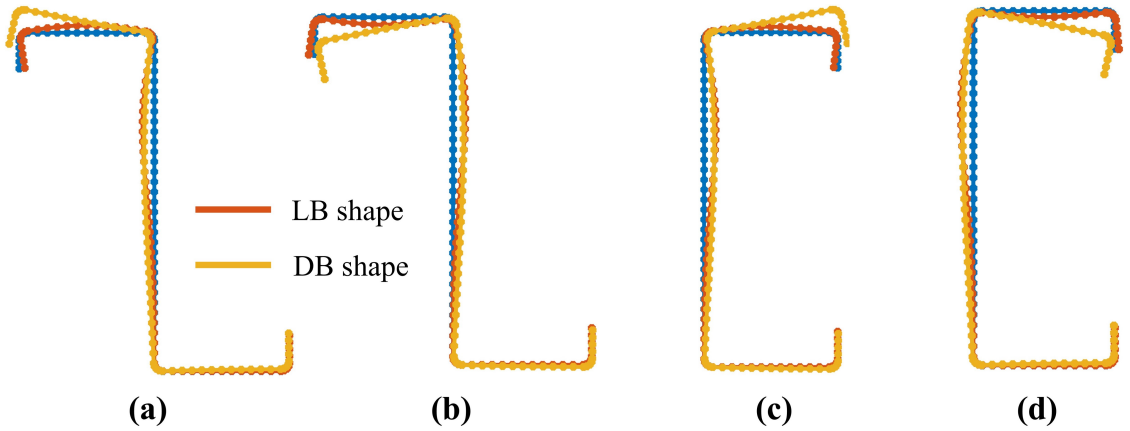

Figure 6.3: Typical buckled shapes under bending generated in CUFSM [142] as initial GI for (a) Zee section outward shape, (b) Zee section inward shape, (c) Cee section outward shape, and (d) Cee section inward shape.

For most cases, the experimental data is between the corresponding simulation data with and without GI. The average ratio between the experimental peak P and the peak P from simulation without GI is 99.4%. The average ratio between the experimental peak P and the average peak P from simulation with GI is 101.7%. The average ratio between the experimental peak P and the average peak P from all simulations with and without GI is 100.8%. The excellent agreement indicates the experimental setup can be well represented by the developed finite element model.

6.3 Data from simulation for parametric study

The validated FEA model was adjusted to accommodate the scenario under torsional loads only for the thin-walled CFS members. Firstly, the vertical load P introducing bending was removed. The couple created by lateral forces Q was used to represent applied torsional loads and vertical load P was removed from

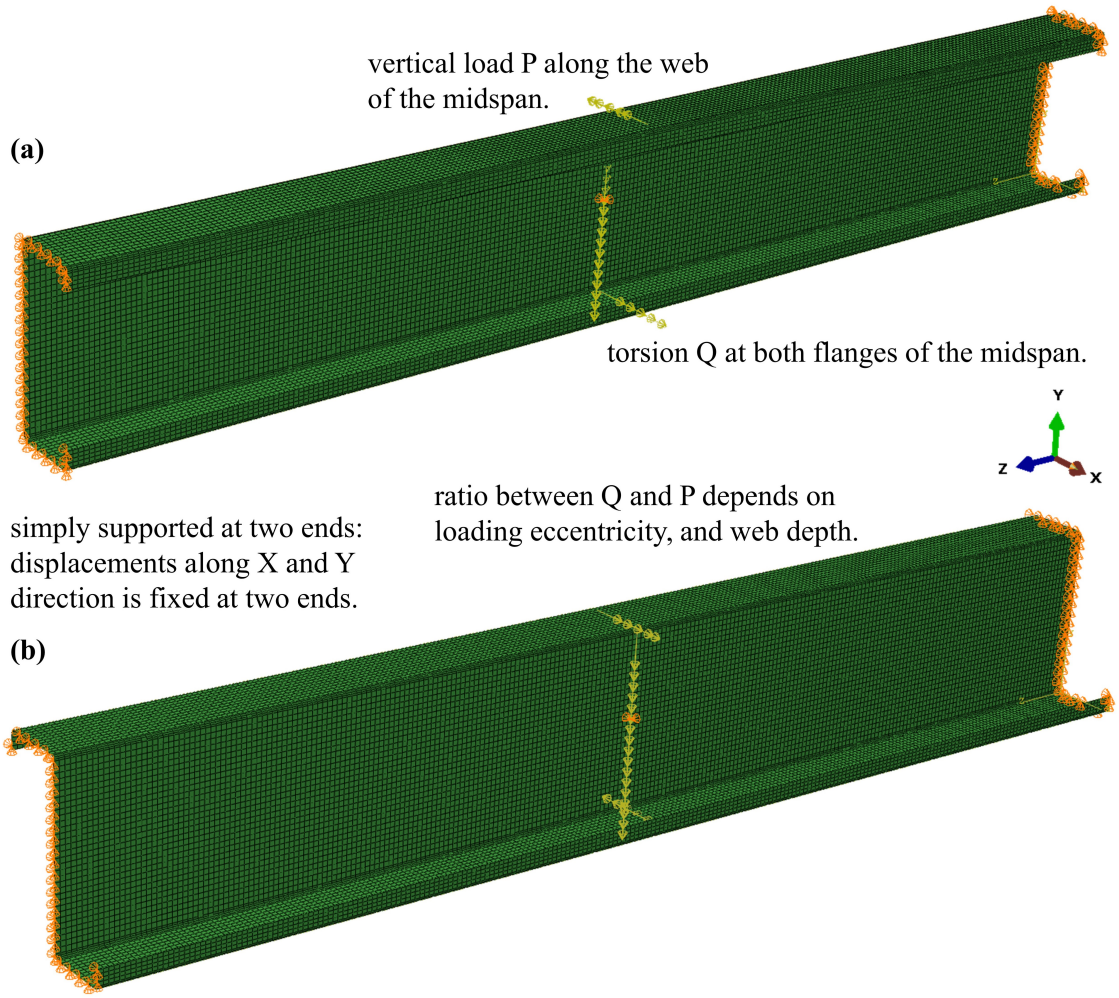

Figure 6.4: Typical setup of the finite element model aiming for simulating the experiment [4] for (a) Cee section and (b) Zee section.

Table 6.1: Peak applied load from experiments [4] and numerical simulation considering different geometric imperfection.

(1) section	(2) $h \times b \times d \times t$ mm^4	(3) L mm	(4) e mm	(5)	(6)	(7) P_{max} (kN)	(8)
				test	GI0	GI1	GI2
Cee	$180 \times 70 \times 20 \times 2.5$	1200	30	24.30	25.54	22.30	27.72
		1200	40	19.59	21.08	18.54	23.80
		1200	50	19.37	18.00	15.90	20.91
		1500	30	20.68	19.54	17.64	22.55
		1500	40	17.84	16.21	14.74	19.17
		1500	50	16.10	13.87	12.72	16.59
	$185 \times 70 \times 20 \times 1.8$	1200	30	14.18	18.55	14.60	17.84
		1200	40	12.19	14.78	11.96	15.63
		1200	50	11.08	12.42	10.17	13.81
		1500	30	11.42	13.21	10.95	14.52
		1500	40	10.16	10.82	9.00	12.55
		1500	50	9.27	9.04	7.66	10.93
Zee	$180 \times 70 \times 20 \times 2.5$	1200	40	29.64	30.81	30.66	29.16
		1200	50	26.52	25.53	25.44	24.95
		1200	60	22.73	21.67	21.70	21.49
		1500	40	25.67	25.20	26.34	22.32
		1500	50	22.81	21.06	20.28	19.19
		1500	60	18.58	17.95	16.63	16.78
	$185 \times 70 \times 20 \times 1.8$	1200	40	17.45	17.85	18.21	17.62
		1200	50	15.07	14.87	15.13	14.67
		1200	60	12.78	12.75	12.96	12.57
		1500	40	14.34	14.42	14.67	14.24
		1500	50	12.49	11.76	11.92	11.62
		1500	60	10.27	9.93	10.05	9.82

[1] h is the web depth, b is the flange width, d is the lip length, t is the member thickness.

[2] L is the member length, e is the loading eccentricity from the cross-section shear center.

[3] P_{max} is the peak applied load.

[4] Columns (6)-(8) are P_{max} from numerical simulation, GI0 represents no geometric imperfection, GI1 and GI2 represent outward and inward buckling shapes (shown in Fig. 6.3) as geometric imperfection.

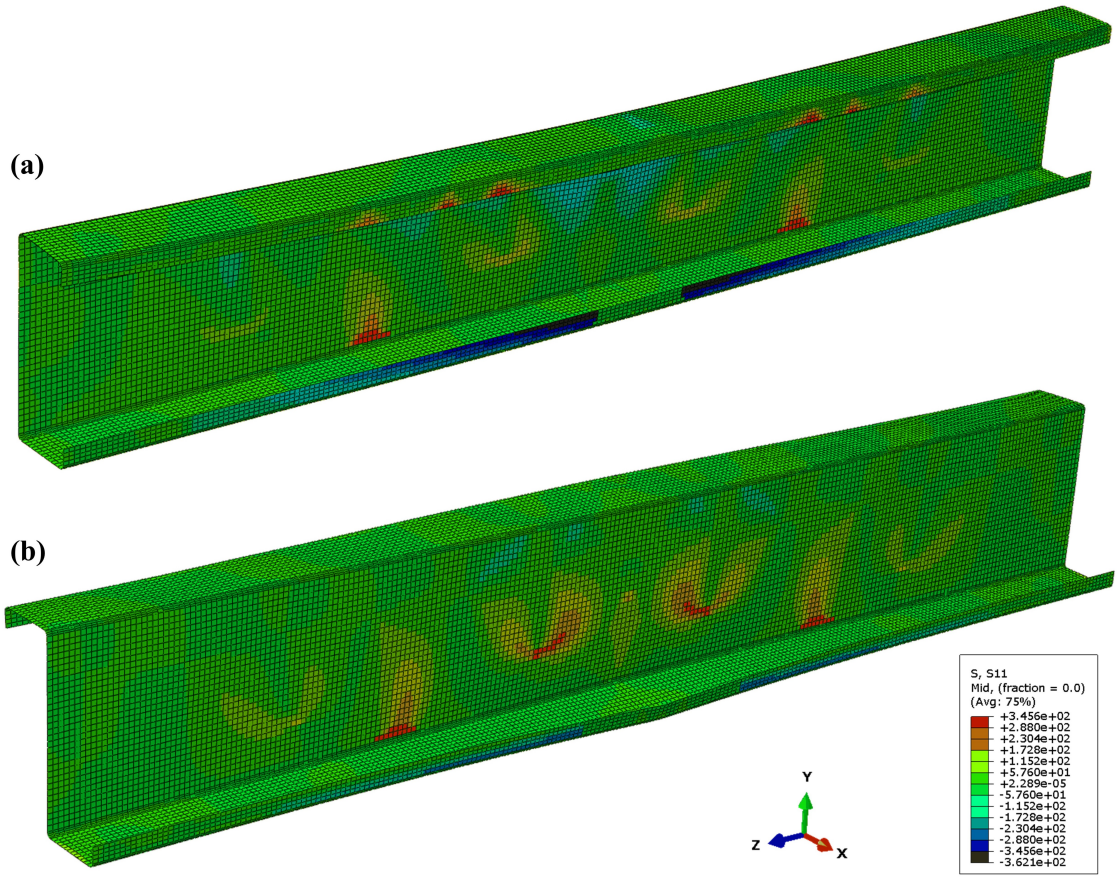

Figure 6.5: Deformed member shape and longitudinal stress distribution for representative (a) Cee and (b) Zee members at the ultimate applied load.

the model. In addition, to develop a case with bimoment only at midspan, the applied load was transformed from concentrated torsion to uniformly distributed torsion along member longitudinal direction, where the magnitude of the uniformly distributed torsion $q = Q/L$ and L is the member length.

Secondly, steel with various grades and stress-strain behaviors was included. The primary cases included mild steel (Mild-1x) with a yield strength of 50 ksi (345 MPa) for Cee [130] and 55 ksi (379 MPa) for Zee [144] and the stress-strain behavior

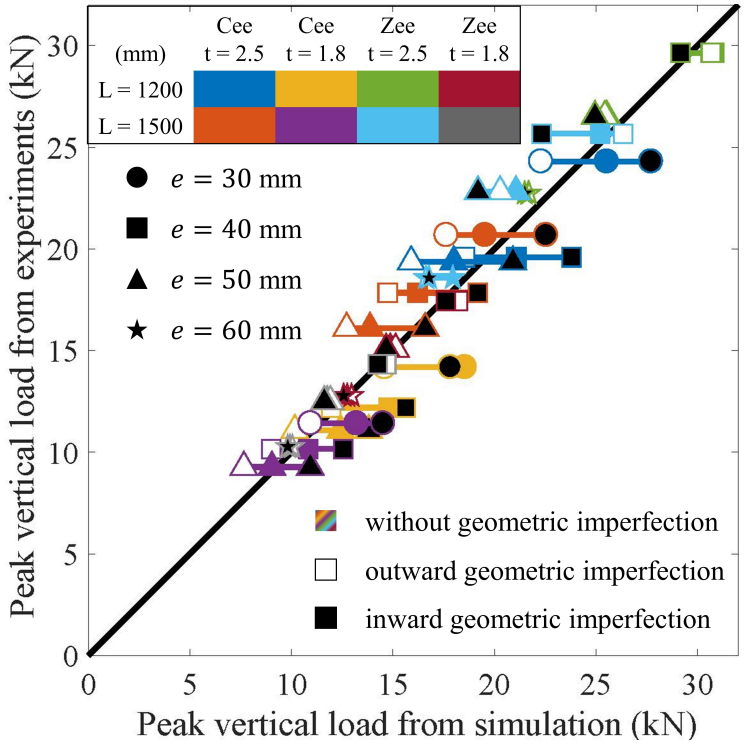

Figure 6.6: Comparison between the results of the experimental study [4] and the developed Abaqus model.

of the mild steel was described by the EPP model. In addition, higher steel grades were included to investigate the cases with higher torsional slenderness. A few cases of mild steel with doubled (Mild-2x) and quadruple (Mild-4x) yield strength were modeled using the EPP model. The elastic moduli for all mild steel were 203 GPa. In addition, a few supplementary cases using Martensitic steel (MS-1200) with a nominal yield strength of 1200 MPa were included, which showed a rounded stress-strain relationship and was modeled by the two-stage plus linear model [5]. The average of the tensile coupon test experimental data was adopted for MS-1200, where the elastic modulus was 215,684 MPa [5] and the yield strength ($\sigma_{0.2}$) was 1307 MPa. The material definitions of MS-1200 for Zee and Cee cross-sections were

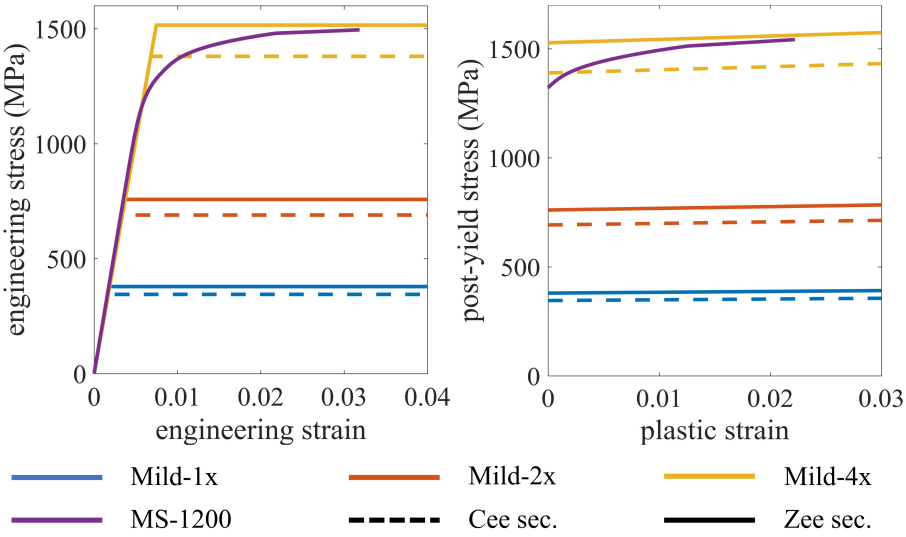

Figure 6.7: Constitutive relationships for steel adopted in finite element models. Mild-1x has a yield strength of 345 MPa (50 ksi) for Cee section and 379 MPa (55 ksi) for Zee section.

identical. The engineering stress-strain relationship and the relationship between plastic strain and post-yield stress for each steel are shown in Fig. 6.7.

Thirdly, the member geometry was expanded and the initial imperfections were adjusted. Typical cross-section sizes from AISI D100 [144] and SSMA product technical guide [130] were selected as shown in Table 6.2. The initial GI shapes for local and distortional buckling were determined through a finite strip analysis in CUFSM [142] where the member was subjected to bimoment only. The applicable local and distortional minima provided the buckled shapes. Zee sections under counterclockwise torsion (web in compression) only have a local buckling minimum, therefore only the local buckling shape was adopted as the initial GI shape for this case. A typical example of initial imperfection shapes for torsion is shown in Figure 6.8. The maximum magnitudes of the imperfections are the same as discussed in Section 6.2 (0.47t for LB and 1.03t for DB). The member length (L)

Table 6.2: Selected cross-sections for the parametric study.

Cee cross-section			
1200S300x97	1000S300x97	800S250x97	600S200x97
1200S300x68	1000S300x68	800S250x68	600S200x68
1200S300x54	1000S300x54	800S250x54	600S200x54
Zee cross-section			
12Z325x105	10Z325x105	8Z275x105	6Z225x105
12Z325x070	10Z325x070	8Z275x070	6Z225x070
12Z325x059	10Z325x059	8Z275x059	6Z225x059

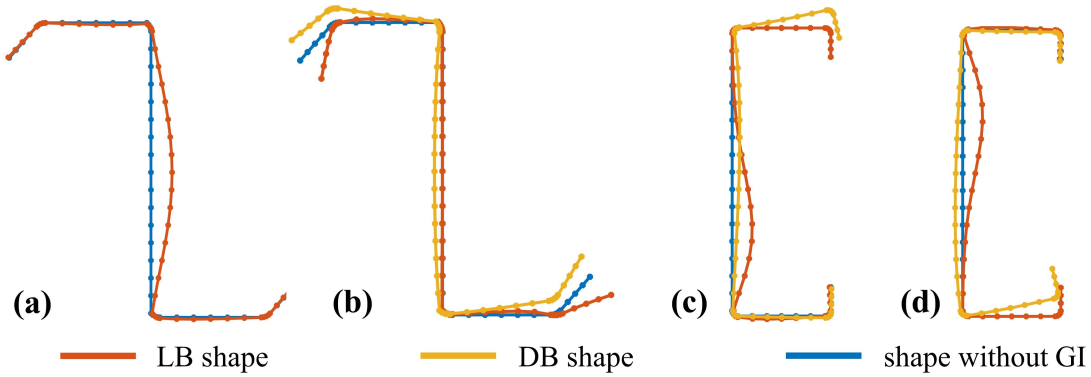

Figure 6.8: Typical buckled shapes generated in CUFSM [142] as initial GI for (a) Zee section under counterclockwise torsion, (b) Zee section under clockwise torsion, (c) Cee section under counterclockwise torsion, and (d) Cee section under clockwise torsion.

was also adjusted so that it was dependent on the web depth D of the cross-section. For Mild-1x, Mild-4x, and MS-1200, L = 10D. In addition, a few cases with shorter span lengths were investigated to compare the effect of different spans on member behavior, which included L = 6D for Mild-2x and L = 3D for Mild-4x. Also, to compare the influence of the lip length on buckling behavior, a group of Cee sections, with 10D member length and Mild-1x material, had the lip length increased from 0.625 inches (15.875 mm) to 1 inch (25.4 mm).

For each cross-section, simulations for both torsion directions, clockwise (CW) and counterclockwise (CCW) about the member longitudinal axis, were run for

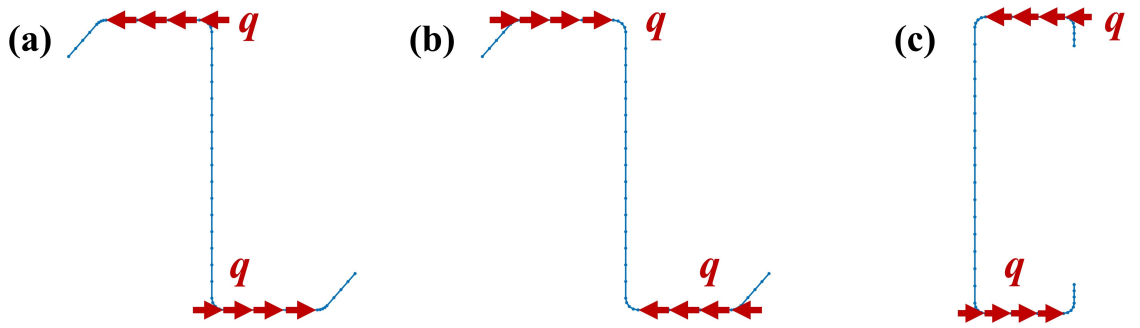

Figure 6.9: Torsion loading cases: (a) CCW torsion for Zee section; (b) CW torsion for Zee section; (c) CCW torsion for Cee section

Mild-1x with L = 10D, and the internal bimoment B at midspan was calculated by using the nodal longitudinal stresses at midspan when peak q was achieved. The results showed that the bimoments of Zee sections for the opposite torsion cases were substantially different, while the bimoments for Cee sections under the opposite torsions were almost the same in magnitude (within 0.3% difference). Therefore, for the other steel grades, member lengths, or lip lengths, cases of both directions of torsions were investigated for Zee sections, while only one direction of torsion was studied for Cee sections, as illustrated in Fig. 6.9. In addition, from the initial simulations, the difference of the internal bimoment B calculated at midspan between cases with and without GI was minor, where the average difference was within 1%. Therefore, only the cases with GI were investigated for the parametric study to mimic the more realistic scenario.

By comparing the deformed shapes at peak applied torsion with the local and distortional deformed shapes under torsion generated by CUFSM [142], each case was categorized as local buckling (LB) or distortional buckling (DB) controlled case. The results and the post-processed data of the simulation are shown in Table 6.3 for

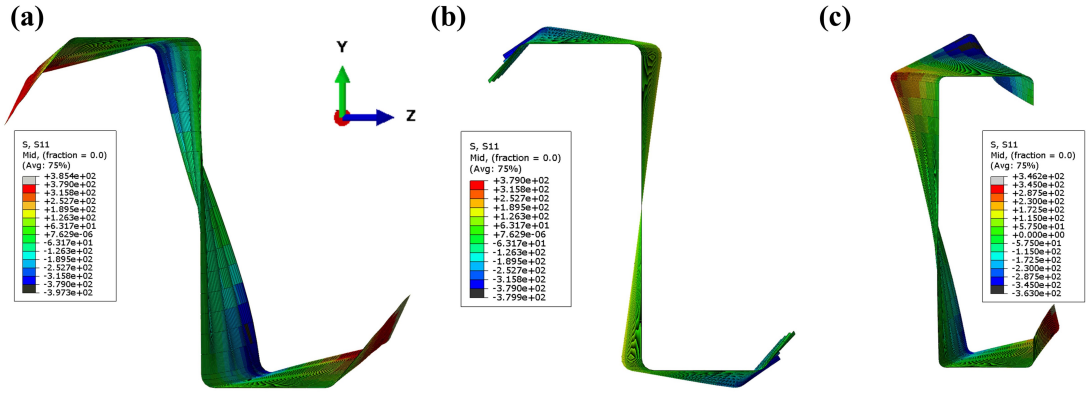

Figure 6.10: Representative deformed shapes at peak applied torsion (scale factor=1). Examples (a) CCW torsion case showing LB behavior (6Z225x070, Mild-1x-10D); (b) CW torsion case showing DB behavior (6Z225x070, Mild-1x-10D); (c) CCW torsion case showing DB behavior (600S200x68, Mild-1x-10D). Colors represent the magnitudes of longitudinal stresses. Mild-1x has a yield strength of 379 MPa (55 ksi) for Zee section and 345 MPa (50 ksi) for Cee section.

LB controlled cases and Table 6.4 for DB controlled cases. Fig. 6.10 shows typical examples of the side view (YZ plane) of the deformed shapes at peak applied load under CCW and CW torsion. The steel grade, member length, and loading direction were combined and given as *Type* in Table 6.3 and 6.4. For example, Mild-1x-10D-CCW for section 1200S300x97 represents the case for a member 1200S300x97 under CCW torsion (Fig. 6.9), where the member is made of Mild-1x and member length is 10D. The only exception is type LargeLip-10D-CCW, where the member for this type is made of Mild-1x and its lip length is 1 inch.

Furthermore, the yield bimoment B_y, the plastic bimoment B_p, and the buckling bimoment B_{cr} are given for each case. B_y and B_p are calculated based on the yield strength and cross-section geometry. B_{cr} is calculated by CUFSM [142]. In addition, by using Eq. 6.7, the internal ultimate bimoment $B_{n\sigma}$ for each case at midspan is calculated by the longitudinal nodal stresses when the peak applied distributed

torsion $m_t = q \times D$ is achieved:

$$B_{n\sigma} = \int \sigma w_n dA = \sum_{i=1}^{N-1} t_i l_i \sigma_i \left(w_{ni} + \frac{1}{2} R_{oi} l_i \right) + \frac{1}{2} t_i l_i (\sigma_{i+1} - \sigma_i) \left(w_{ni} + \frac{2}{3} R_{oi} l_i \right) \tag{6.7}$$

where element i is defined from node i to node $i+1$, N is the number of nodes on the cross-section, l_i is the length of element i, t_i is the thickness of element i, σ_i is the longitudinal stress at node i, w_{ni} is the normalized unit warping at node i, R_{oi} is perpendicular distance between the shear center and element i.

The results show the calculated internal bimoment $B_{n\sigma}$ is larger than B_y and B_{crl} for most LB controlled cases, while $B_{n\sigma}$ is between B_y and B_{crd} for most DB controlled cases. Also, $B_{n\sigma}$ is smaller than B_p for almost all cases.

Table 6.3: Results for cases showing controlling LB behaviors.

Section	Type	B_p kN-m^2	B_y kN-m^2	B_{crl} kN-m^2	$B_{n\sigma}$ kN-m^2	λ_B	B_{npred} kN-m^2	$\frac{B_{n\sigma}}{B_p}$	$\frac{B_{n\sigma}}{B_{npred}}$
12Z325x105	Mild-1x-10D-CCW	1.681	0.878	0.751	1.564	1.08	1.471	0.93	1.06
12Z325x070	Mild-1x-10D-CCW	1.110	0.580	0.222	0.879	1.62	0.864	0.79	1.02
12Z325x059	Mild-1x-10D-CCW	0.932	0.488	0.133	0.703	1.91	0.681	0.75	1.03
10Z325x105	Mild-1x-10D-CCW	1.404	0.778	0.850	1.302	0.96	1.260	0.93	1.03
10Z325x070	Mild-1x-10D-CCW	0.928	0.514	0.251	0.729	1.43	0.752	0.79	0.97
10Z325x059	Mild-1x-10D-CCW	0.779	0.432	0.150	0.588	1.70	0.596	0.76	0.99
8Z275x105	Mild-1x-10D-CCW	0.868	0.472	0.764	0.814	0.79	0.804	0.94	1.01
8Z275x070	Mild-1x-10D-CCW	0.573	0.312	0.225	0.488	1.18	0.491	0.85	0.99
8Z275x059	Mild-1x-10D-CCW	0.481	0.262	0.135	0.375	1.40	0.393	0.78	0.95
6Z225x105	Mild-1x-10D-CCW	0.482	0.257	0.688	0.487	0.61	0.460	1.01	1.06
6Z225x070	Mild-1x-10D-CCW	0.318	0.170	0.202	0.283	0.92	0.288	0.89	0.98
6Z225x059	Mild-1x-10D-CCW	0.267	0.142	0.121	0.225	1.09	0.234	0.84	0.96
12Z325x105	Mild-4x-10D-CCW	6.725	3.511	0.751	4.663	2.16	4.667	0.69	1.00
12Z325x070	Mild-4x-10D-CCW	4.442	2.321	0.222	2.660	3.23	2.590	0.60	1.03
12Z325x105	MS-1200-10D-CCW	6.725	3.511	0.751	4.548	2.16	4.667	0.68	0.97
6Z225x059	MS-1200-10D-CCW	1.070	0.569	0.121	0.635	2.17	0.741	0.59	0.86
12Z325x105	Mild-2x-6D-CCW	3.362	1.756	0.751	2.839	1.53	2.668	0.84	1.06
12Z325x070	Mild-2x-6D-CCW	2.221	1.161	0.222	1.593	2.28	1.505	0.72	1.06

Table 6.3 continued from previous page

Section	Type	B_p kN-m^2	B_y kN-m^2	B_{crl} kN-m^2	$B_{n\sigma}$ kN-m^2	λ_B	B_{npred} kN-m^2	$\frac{B_{n\sigma}}{B_p}$	$\frac{B_{n\sigma}}{B_{npred}}$
12Z325x059	Mild-2x-6D-CCW	1.865	0.975	0.133	1.226	2.71	1.174	0.66	1.04
10Z325x105	Mild-2x-6D-CCW	2.808	1.555	0.850	2.353	1.35	2.317	0.84	1.02
10Z325x070	Mild-2x-6D-CCW	1.855	1.029	0.251	1.331	2.03	1.323	0.72	1.01
10Z325x059	Mild-2x-6D-CCW	1.558	0.865	0.150	1.029	2.40	1.034	0.66	1.00
8Z275x105	Mild-2x-6D-CCW	1.736	0.945	0.764	1.496	1.11	1.509	0.86	0.99
8Z275x070	Mild-2x-6D-CCW	1.146	0.624	0.225	0.862	1.67	0.882	0.75	0.98
8Z275x059	Mild-2x-6D-CCW	0.962	0.524	0.135	0.674	1.97	0.694	0.70	0.97
6Z225x105	Mild-2x-6D-CCW	0.965	0.514	0.688	0.866	0.86	0.881	0.90	0.98
6Z225x070	Mild-2x-6D-CCW	0.637	0.339	0.202	0.506	1.29	0.532	0.79	0.95
6Z225x059	Mild-2x-6D-CCW	0.535	0.285	0.121	0.402	1.54	0.424	0.75	0.95
12Z325x070	Mild-4x-3D-CCW	4.442	2.321	0.222	2.696	3.23	2.590	0.61	1.04
12Z325x059	Mild-4x-3D-CCW	3.730	1.950	0.133	2.009	3.83	2.031	0.54	0.99
10Z325x070	Mild-4x-3D-CCW	3.710	2.058	0.251	2.260	2.86	2.278	0.61	0.99
10Z325x059	Mild-4x-3D-CCW	3.116	1.729	0.150	1.687	3.40	1.780	0.54	0.95
8Z275x105	Mild-4x-3D-CCW	3.473	1.889	0.764	2.732	1.57	2.729	0.79	1.00
8Z275x070	Mild-4x-3D-CCW	2.292	1.249	0.225	1.514	2.36	1.532	0.66	0.99
8Z275x059	Mild-4x-3D-CCW	1.924	1.049	0.135	1.147	2.79	1.195	0.60	0.96
6Z225x105	Mild-4x-3D-CCW	1.930	1.027	0.688	1.562	1.22	1.639	0.81	0.95

Table 6.3 continued from previous page

Section	Type	B_p kN-m^2	B_y kN-m^2	B_{crl} kN-m^2	$B_{n\sigma}$ kN-m^2	λ_B	B_{npred} kN-m^2	$\frac{B_{n\sigma}}{B_p}$	$\frac{B_{n\sigma}}{B_{npred}}$
6Z225x070	Mild-4x-3D-CCW	1.274	0.678	0.202	0.916	1.83	0.946	0.72	0.97
6Z225x059	Mild-4x-3D-CCW	1.070	0.569	0.121	0.700	2.17	0.741	0.65	0.94

Table 6.4: Results for cases showing controlling DB behaviors.

Section	Type	B_p kN-m^2	B_y kN-m^2	B_{crd} kN-m^2	$B_{n\sigma}$ kN-m^2	λ_B	B_{npred} kN-m^2	$\frac{B_{n\sigma}}{B_p}$	$\frac{B_{n\sigma}}{B_{npred}}$
1200S300x97	Mild1x-10D-CCW	0.975	0.523	1.113	0.645	0.69	0.641	0.66	1.01
1200S300x68	Mild1x-10D-CCW	0.713	0.384	0.523	0.386	0.86	0.393	0.54	0.98
1200S300x54	Mild1x-10D-CCW	0.578	0.312	0.321	0.282	0.99	0.278	0.49	1.02
1000S300x97	Mild1x-10D-CCW	0.788	0.412	0.919	0.600	0.67	0.526	0.76	1.14
1000S300x68	Mild1x-10D-CCW	0.577	0.303	0.433	0.327	0.84	0.325	0.57	1.01
1000S300x54	Mild1x-10D-CCW	0.467	0.246	0.268	0.216	0.96	0.231	0.46	0.93
800S250x97	Mild1x-10D-CCW	0.449	0.234	0.764	0.342	0.55	0.335	0.76	1.02
800S250x68	Mild1x-10D-CCW	0.331	0.174	0.363	0.232	0.69	0.216	0.70	1.07
800S250x54	Mild1x-10D-CCW	0.269	0.141	0.225	0.150	0.79	0.158	0.56	0.94
600S200x97	Mild1x-10D-CCW	0.223	0.116	0.600	0.222	0.44	0.183	1.00	1.21
600S200x68	Mild1x-10D-CCW	0.166	0.087	0.287	0.140	0.55	0.125	0.84	1.13
600S200x54	Mild1x-10D-CCW	0.136	0.071	0.179	0.095	0.63	0.094	0.70	1.01
12Z325x105	Mild1x-10D-CW	1.681	0.878	1.334	1.081	0.81	0.972	0.64	1.11
12Z325x059	Mild1x-10D-CW	0.932	0.488	0.361	0.448	1.16	0.373	0.48	1.20
10Z325x105	Mild1x-10D-CW	1.404	0.778	1.190	0.896	0.81	0.814	0.64	1.10
10Z325x070	Mild1x-10D-CW	0.928	0.514	0.473	0.489	1.04	0.420	0.53	1.16
10Z325x059	Mild1x-10D-CW	0.779	0.432	0.320	0.362	1.16	0.312	0.46	1.16
8Z275x105	Mild1x-10D-CW	0.868	0.472	0.945	0.555	0.71	0.558	0.64	0.99

Table 6.4 continued from previous page

Section	Type	B_p kN-m^2	B_y kN-m^2	B_{crd} kN-m^2	$B_{n\sigma}$ kN-m^2	λ_B	B_{npred} kN-m^2	$\frac{B_{n\sigma}}{B_p}$	$\frac{B_{n\sigma}}{B_{npred}}$
8Z275x070	Mild1x-10D-CW	0.573	0.312	0.375	0.321	0.91	0.298	0.56	1.08
8Z275x059	Mild1x-10D-CW	0.481	0.262	0.254	0.241	1.02	0.224	0.50	1.07
6Z225x105	Mild1x-10D-CW	0.482	0.257	0.686	0.335	0.61	0.341	0.69	0.98
6Z225x070	Mild1x-10D-CW	0.318	0.170	0.275	0.192	0.79	0.189	0.60	1.02
6Z225x059	Mild1x-10D-CW	0.267	0.142	0.188	0.145	0.87	0.145	0.54	1.00
1200S300x97	Mild1x-10D-CW	0.975	0.523	1.113	0.645	0.69	0.641	0.66	1.01
1200S300x68	Mild1x-10D-CW	0.713	0.384	0.523	0.386	0.86	0.393	0.54	0.98
1200S300x54	Mild1x-10D-CW	0.578	0.312	0.321	0.282	0.99	0.278	0.49	1.01
1000S300x97	Mild1x-10D-CW	0.788	0.412	0.919	0.600	0.67	0.526	0.76	1.14
1000S300x68	Mild1x-10D-CW	0.577	0.303	0.433	0.327	0.84	0.325	0.57	1.01
1000S300x54	Mild1x-10D-CW	0.467	0.246	0.268	0.217	0.96	0.231	0.46	0.94
800S250x97	Mild1x-10D-CW	0.449	0.234	0.764	0.341	0.55	0.335	0.76	1.02
800S250x68	Mild1x-10D-CW	0.331	0.174	0.363	0.232	0.69	0.216	0.70	1.07
800S250x54	Mild1x-10D-CW	0.269	0.141	0.225	0.150	0.79	0.158	0.56	0.94
600S200x97	Mild1x-10D-CW	0.223	0.116	0.600	0.222	0.44	0.183	1.00	1.21
600S200x68	Mild1x-10D-CW	0.166	0.087	0.287	0.140	0.55	0.125	0.84	1.13
600S200x54	Mild1x-10D-CW	0.136	0.071	0.179	0.095	0.63	0.094	0.70	1.01
1200S300x97	Mild4x-10D-CCW	3.899	2.091	1.113	1.168	1.37	1.264	0.30	0.92

Table 6.4 continued from previous page

Section	Type	B_p kN-m^2	B_y kN-m^2	B_{crd} kN-m^2	$B_{n\sigma}$ kN-m^2	λ_B	B_{npred} kN-m^2	$\frac{B_{n\sigma}}{B_p}$	$\frac{B_{n\sigma}}{B_{npred}}$
1200S300x68	Mild4x-10D-CCW	2.853	1.537	0.523	0.569	1.71	0.669	0.20	0.85
1200S300x54	Mild4x-10D-CCW	2.311	1.248	0.321	0.462	1.97	0.435	0.20	1.06
1000S300x68	Mild4x-10D-CCW	2.306	1.212	0.433	0.558	1.67	0.562	0.24	0.99
1000S300x54	Mild4x-10D-CCW	1.868	0.984	0.268	0.370	1.92	0.368	0.20	1.01
800S250x68	Mild4x-10D-CCW	1.324	0.695	0.363	0.423	1.38	0.424	0.32	1.00
800S250x54	Mild4x-10D-CCW	1.076	0.566	0.225	0.278	1.59	0.284	0.26	0.98
600S200x97	Mild4x-10D-CCW	0.891	0.464	0.600	0.482	0.88	0.480	0.54	1.01
600S200x68	Mild4x-10D-CCW	0.665	0.347	0.287	0.274	1.10	0.284	0.41	0.96
600S200x54	Mild4x-10D-CCW	0.544	0.284	0.179	0.187	1.26	0.197	0.34	0.95
12Z325x070	Mild4x-10D-CW	4.442	2.321	0.528	0.706	2.10	0.756	0.16	0.93
12Z325x059	Mild4x-10D-CW	3.730	1.950	0.361	0.484	2.32	0.533	0.13	0.91
6Z225x059	Mild4x-10D-CW	1.070	0.569	0.188	0.214	1.74	0.245	0.20	0.87
1200S300x97	MS1200-10D-CCW	3.899	2.091	1.113	1.276	1.37	1.264	0.33	1.01
1200S300x54	MS1200-10D-CCW	2.311	1.248	0.321	0.477	1.97	0.435	0.21	1.10
1000S300x68	MS1200-10D-CCW	2.306	1.212	0.433	0.582	1.67	0.562	0.25	1.04
1000S300x54	MS1200-10D-CCW	1.868	0.984	0.268	0.389	1.92	0.368	0.21	1.06
800S250x68	MS1200-10D-CCW	1.324	0.695	0.363	0.438	1.38	0.424	0.33	1.03
800S250x54	MS1200-10D-CCW	1.076	0.566	0.225	0.289	1.59	0.284	0.27	1.02

Table 6.4 continued from previous page

Section	Type	B_p kN-m^2	B_y kN-m^2	B_{crd} kN-m^2	$B_{n\sigma}$ kN-m^2	λ_B	B_{npred} kN-m^2	$\frac{B_{n\sigma}}{B_p}$	$\frac{B_{n\sigma}}{B_{npred}}$
600S200x97	MS1200-10D-CCW	0.891	0.464	0.600	0.527	0.88	0.480	0.59	1.10
600S200x68	MS1200-10D-CCW	0.665	0.347	0.287	0.288	1.10	0.284	0.43	1.01
600S200x54	MS1200-10D-CCW	0.544	0.284	0.179	0.192	1.26	0.197	0.35	0.98
12Z325x070	MS1200-10D-CW	4.442	2.321	0.528	0.752	2.10	0.756	0.17	1.00
12Z325x059	MS1200-10D-CW	3.730	1.950	0.361	0.511	2.32	0.533	0.14	0.96
8Z275x059	MS1200-10D-CW	1.924	1.049	0.254	0.328	2.03	0.345	0.17	0.95
6Z225x070	MS1200-10D-CW	1.274	0.678	0.275	0.330	1.57	0.341	0.26	0.97
6Z225x059	MS1200-10D-CW	1.070	0.569	0.188	0.226	1.74	0.245	0.21	0.92
1200S300x97	LargeLip-10D-CCW	1.169	0.636	1.871	0.912	0.58	0.849	0.78	1.07
1200S300x68	LargeLip-10D-CCW	0.851	0.464	0.895	0.492	0.72	0.541	0.58	0.91
1200S300x54	LargeLip-10D-CCW	0.688	0.375	0.555	0.354	0.82	0.393	0.52	0.90
1000S300x97	LargeLip-10D-CCW	0.943	0.500	1.559	0.744	0.57	0.695	0.79	1.07
1000S300x68	LargeLip-10D-CCW	0.687	0.365	0.751	0.395	0.70	0.446	0.57	0.88
1000S300x54	LargeLip-10D-CCW	0.555	0.295	0.469	0.287	0.79	0.327	0.52	0.88
800S250x97	LargeLip-10D-CCW	0.553	0.292	1.286	0.486	0.48	0.442	0.88	1.10
800S250x68	LargeLip-10D-CCW	0.405	0.214	0.622	0.259	0.59	0.293	0.64	0.88
800S250x54	LargeLip-10D-CCW	0.329	0.174	0.388	0.190	0.67	0.219	0.58	0.87
600S200x97	LargeLip-10D-CCW	0.287	0.151	0.979	0.260	0.39	0.245	0.91	1.06

Table 6.4 continued from previous page

Section	Type	B_p kN-m^2	B_y kN-m^2	B_{crd} kN-m^2	$B_{n\sigma}$ kN-m^2	λ_B	B_{npred} kN-m^2	$\frac{B_{n\sigma}}{B_p}$	$\frac{B_{n\sigma}}{B_{npred}}$
600S200x68	LargeLip-10D-CCW	0.212	0.111	0.477	0.135	0.48	0.169	0.64	0.80
600S200x54	LargeLip-10D-CCW	0.173	0.091	0.299	0.098	0.55	0.129	0.57	0.76
1200S300x97	Mild2x-6D-CCW	1.950	1.045	1.113	0.963	0.97	0.955	0.49	1.01
1200S300x68	Mild2x-6D-CCW	1.427	0.769	0.523	0.514	1.21	0.542	0.36	0.95
1200S300x54	Mild2x-6D-CCW	1.155	0.624	0.321	0.352	1.39	0.366	0.30	0.96
1000S300x97	Mild2x-6D-CCW	1.575	0.824	0.919	0.792	0.95	0.790	0.50	1.00
1000S300x68	Mild2x-6D-CCW	1.153	0.606	0.433	0.426	1.18	0.452	0.37	0.94
1000S300x54	Mild2x-6D-CCW	0.934	0.492	0.268	0.301	1.35	0.308	0.32	0.98
800S250x97	Mild2x-6D-CCW	0.898	0.469	0.764	0.565	0.78	0.534	0.63	1.06
800S250x68	Mild2x-6D-CCW	0.662	0.347	0.363	0.297	0.98	0.321	0.45	0.93
800S250x54	Mild2x-6D-CCW	0.538	0.283	0.225	0.219	1.12	0.225	0.41	0.97
600S200x97	Mild2x-6D-CCW	0.446	0.232	0.600	0.348	0.62	0.312	0.78	1.12
600S200x68	Mild2x-6D-CCW	0.333	0.174	0.287	0.192	0.78	0.199	0.58	0.97
600S200x54	Mild2x-6D-CCW	0.272	0.142	0.179	0.137	0.89	0.145	0.50	0.95
8Z275x105	Mild2x-6D-CW	1.736	0.945	0.945	0.866	1.00	0.823	0.50	1.05
8Z275x070	Mild2x-6D-CW	1.146	0.624	0.375	0.452	1.29	0.402	0.39	1.12
6Z225x105	Mild2x-6D-CW	0.965	0.514	0.686	0.516	0.87	0.527	0.54	0.98

6.4 Prediction of bimoment strength for torsion alone

A standardized direct strength prediction equation for bimoment strength B_n incorporating plastic bimoment B_p, buckling bimoment B_{cr}, and yield bimoment B_y was adopted to fit the data described in Section 6.3 The equation form proposed by the second and the third authors [145] is shown in Eq. 6.8. The numerical coefficients a and b were iterated and determined in the regression analysis by finding the optimal fit between the simulation data and the predicted data, where R^2 was used as the fit error indicator.

$$B_n = B_p \cdot \frac{B_{cr} + aB_y}{B_{cr} + bB_y} \tag{6.8}$$

For cases showing controlling LB or DB, different buckling bimoment (B_{crl} or B_{crd}) was adopted in Eq. 6.8. Therefore, the regression analyses for cases showing different buckling behaviors were carried out respectively. For LB controlled cases, a and b were determined as 0.094 and 0.230 respectively, which led to a $R^2 = 0.997$. The comparison between the predicted bimoment strength B_{npred} and the calculated bimoment $B_{n\sigma}$ at midspan is shown in Fig. 6.11. The average $B_{n\sigma}/B_{npred}$ is 0.992 and the COV is 4.2%. For DB-controlled cases, a and b were determined as $a = 0$ and $b = 1.110$. The R^2 for the DB-controlled case is 0.979. The relationship between B_{npred} and $B_{n\sigma}$ is shown in Fig. 6.12. The average $B_{n\sigma}/B_{npred}$ for the DB controlled cases is 1.006, and the COV is 8.6%.

In addition, Eq. 6.8 can be transformed into the relationship between B_n/B_p and the slenderness for bimoment $\lambda_B = \sqrt{B_y/B_{cr}}$ as shown in Eq. 6.9. The curves

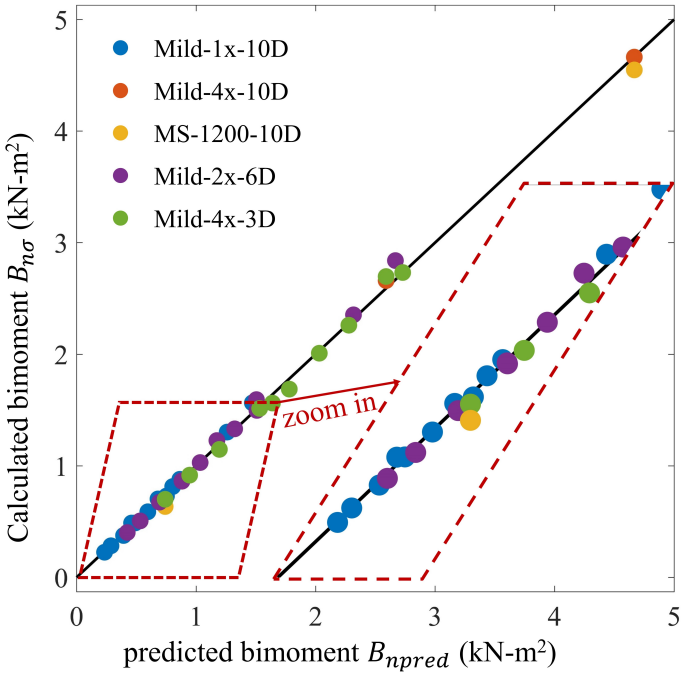

Figure 6.11: Comparison between predicted bimoment and calculated bimoment for cases showing LB behaviors.

built by Eq. 6.9 using the calibrated coefficients a and b for LB and DB controlled cases are shown in Fig. 6.13 and 6.14 respectively. For LB-controlled cases (Fig. 6.13), λ_{LB} varies from 0.5 to 4 for different member geometries and steel grades, and B_n/B_p varies from 0.5 to 1. For DB-controlled cases (Fig. 6.14), λ_{DB} various from 0.4 to 2.5, and B_n/B_p various from 0.13 to 1. For both curves, λ_B tends to increase for cases using higher strength material, and this tendency is more significant for the LB-controlled cases. Additionally, B_n/B_p shows an obvious decreasing trend when λ_B increases and the trend is more prominent for the DB-controlled cases.

$$\frac{B_n}{B_p} = \frac{B_{cr} + aB_y}{B_{cr} + bB_y} = \frac{1 + a{\lambda_B}^2}{1 + b{\lambda_B}^2} \tag{6.9}$$

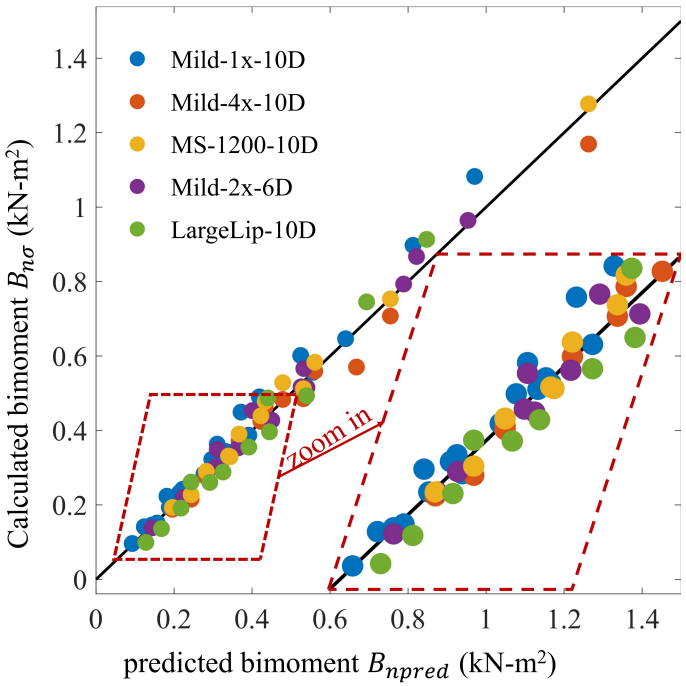

Figure 6.12: Comparison between predicted bimoment and calculated bimoment for cases showing DB behaviors.

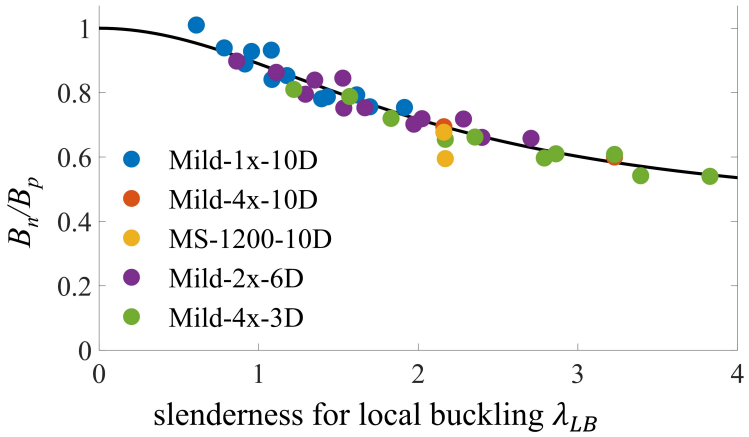

Figure 6.13: Proposed bimoment strength curve considering local slenderness compared with FEA simulation data.

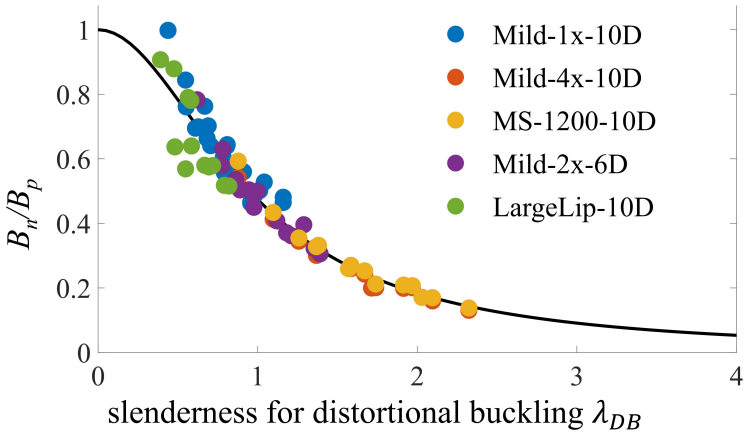

Figure 6.14: Proposed bimoment strength curve considering distortional slenderness compared with FEA simulation data.

The comparisons shown in Fig. 6.11 to 6.14 indicate the adopted equation (Eq. 6.8) with calibrated coefficients show excellent agreement between the prediction and the whole set of simulation data from a wide range of different materials and member geometries. In other words, the chosen bimoment strength equation and the calibrated coefficients might work well for other CFS members.

6.5 Interactions for combined bending torsion behaviors

From Section 6.4, a uniform equation is proposed for accurate bimoment capacity prediction based on the member buckling mode (i.e., LB or DB). In this section, the interaction for combined bending-torsion behaviors for CFS is studied adopting the bimoment prediction from the previous section. The model developed in Section 6.2 was updated and adapted to investigate the combined bending-torsion behaviors by

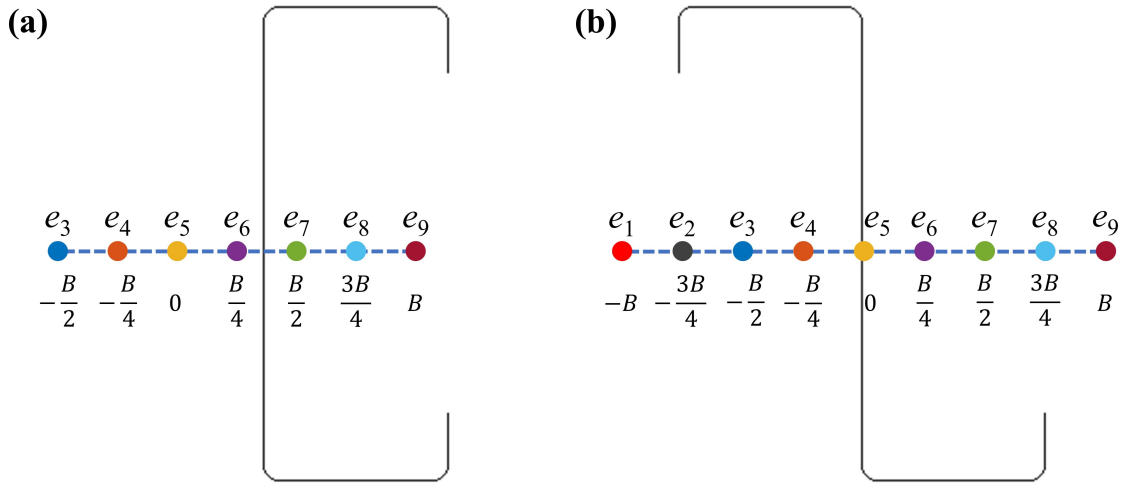

Figure 6.15: Selected eccentricities from shear center (location 5, e_5) for (a) Cee and (b) Zee sections for the combined bending-torsion analysis.B is the flange width.

adding the vertical distributed load p at the top flange while keeping the horizontal distributed loads q at the top and bottom flanges. The material properties of the conventional mild steel in Section 6.2 were adopted. Additionally, both braced and unbraced midspan cases were studied respectively. The member length was selected as $10D_0$ for the unbraced case and $20D_0$ for the braced case, where D_0 is the out-to-out web depth. The relationship between q and p is determined by the loading eccentricity from the shear center. For both braced and unbraced conditions, up to nine different eccentricities considering engineering practice were selected and a sketch diagram is shown in Fig. 6.15, where B is the length of the flange flat region. Fig. 6.16 and 6.17 provide typical simulation setup for unbraced and braced cases respectively.

The vertical load on each node $p = P/n_f$, where P is the total vertical load and n_f is the number of nodes for either flange. The horizontal load on each node

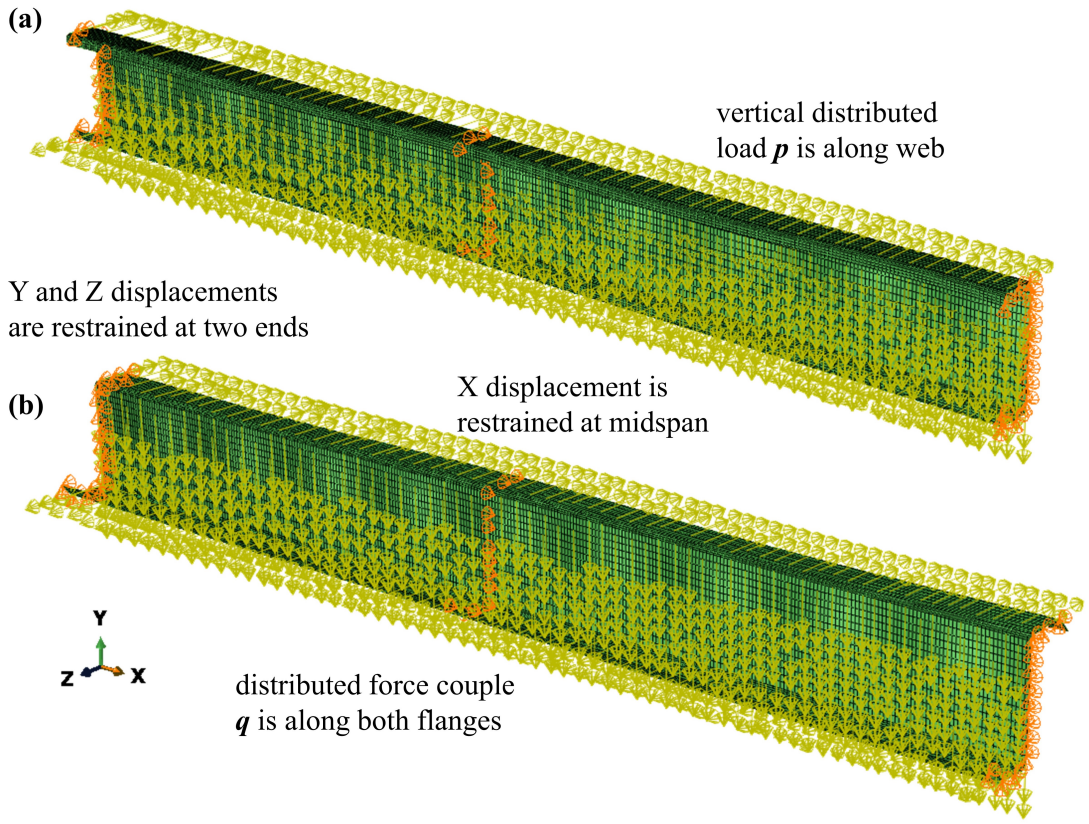

Figure 6.16: Typical simulation setup with unbraced midspan for (a) Cee and (b) Zee sections under combined bending-torsion loading condition.

$q = P(e + ds)/D_0$, where e is the eccentricity and ds is the distance between the web center and the shear center, where ds is negative for Cee sections and zero for Zee sections. For both unbraced and braced cases, the member ends were simply supported, where the displacements along both directions on the cross-section plane were restrained. For the midspan of the unbraced case, only the displacement along member length was restrained. While for the midspan of the braced case, only the vertical direction of all three displacement directions was unrestrained and the rotation along the member length was restrained. The theoretical moment

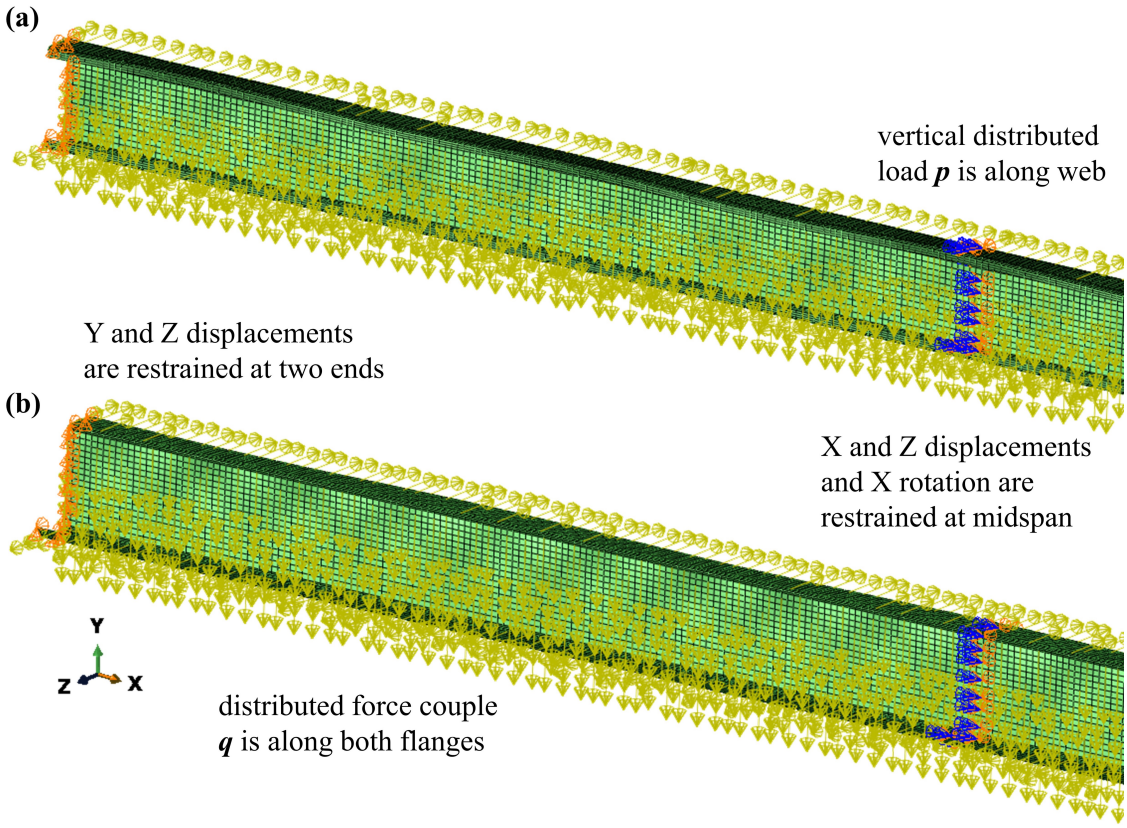

Figure 6.17: Typical simulation setup with braced midspan for (a) Cee and (b) Zee sections under combined bending-torsion loading condition. The right half not shown is symmetric with the left half about the midspan.

and bimoment distribution along member span for the different bracing condition is shown in Fig. 6.18. The mesh size adopted the identical ones as described in Section 6.2, where the mesh was denser at corners than at the flat regions.

The longitudinal stresses (S11) caused by the combined bending-torsion are needed to calculate the ultimate moment and bimoment. From the simulation results, significantly different stress distributions with different directions of eccentricities (i.e., sign of eccentricity in Fig. 6.15) were observed for both unbraced

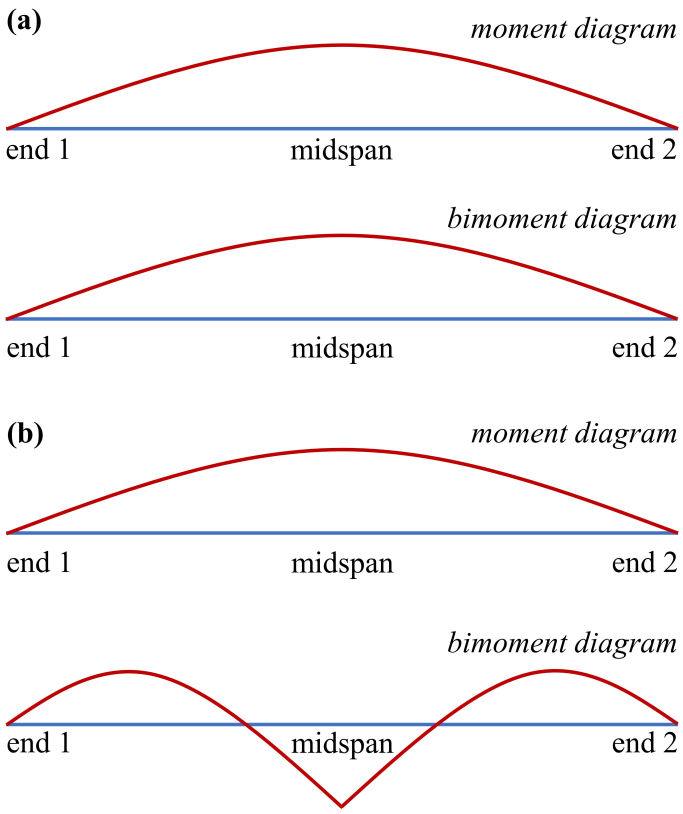

Figure 6.18: Theoretical moment and bimoment distribution along member length for (a) the unbraced condition and (b) the braced condition.

Zee and Cee sections. Representative S11 distributions for unbraced Cee and Zee sections with different eccentricity directions are shown in Fig. 6.19 and 6.20. For all unbraced cases, the most significant stress concentration was observed at the midspan. Specifically, for unbraced Cee section considering negative eccentricity, high tension on the bottom lip and high compression at the top lip were observed. For unbraced Cee section with positive eccentricity, high tension at the top lip, web, and bottom flange, particularly the web-bottom flange conjunction, were observed; high compression at the top flange and the upper web were observed. For unbraced

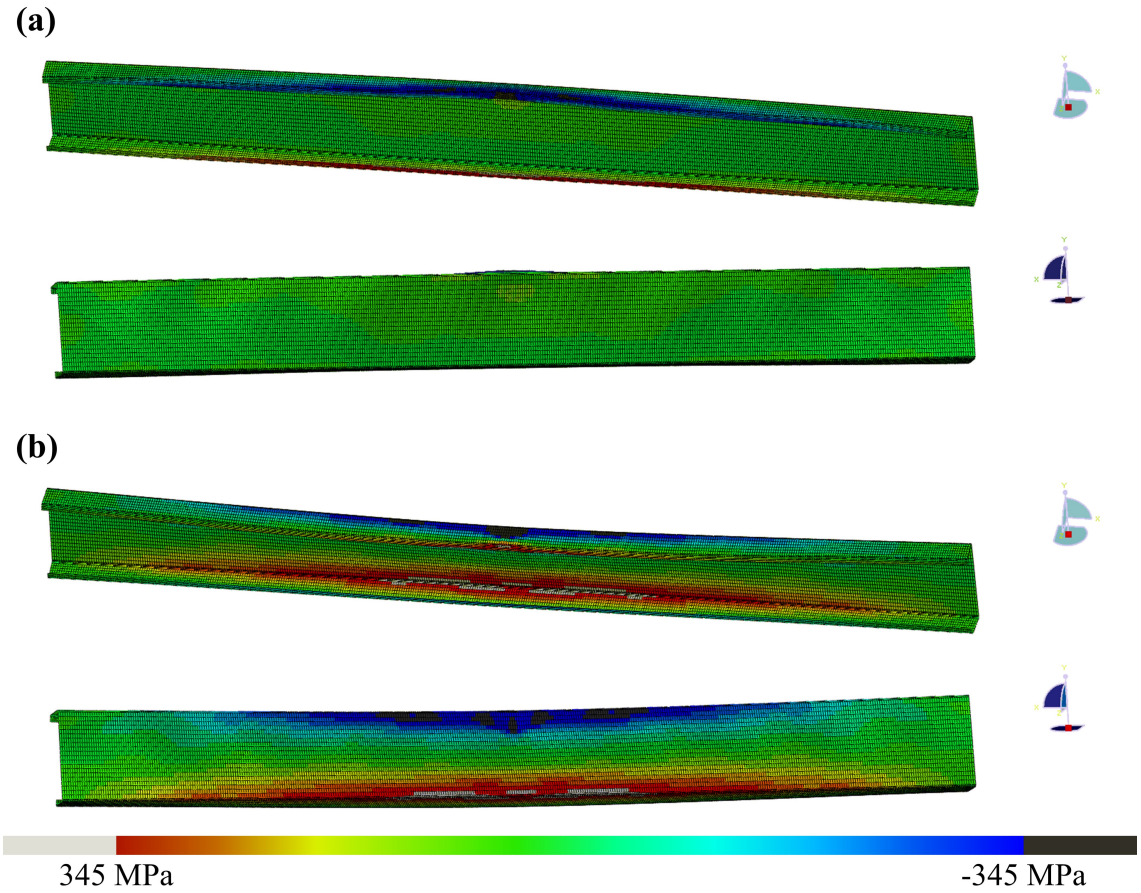

Figure 6.19: Representative S11 distribution of unbraced Cee section (800S250x97) with (a) $e_3 = -B/2$ and (b) $e_7 = +B/2$ at ultimate load.

Zee section with negative eccentricity, significant compression was observed at the upper web and web-top flange conjunction; high tension was observed at the top lip. For the Zee section with positive eccentricity, significant tension was observed at the web-bottom flange conjunction and the lower web, while significant compression was found at the bottom lip and top flange-top lip conjunction.

For the braced Cee and Zee sections with both negative and positive eccentricities, the general distribution of S11 was similar, where the upper half of the

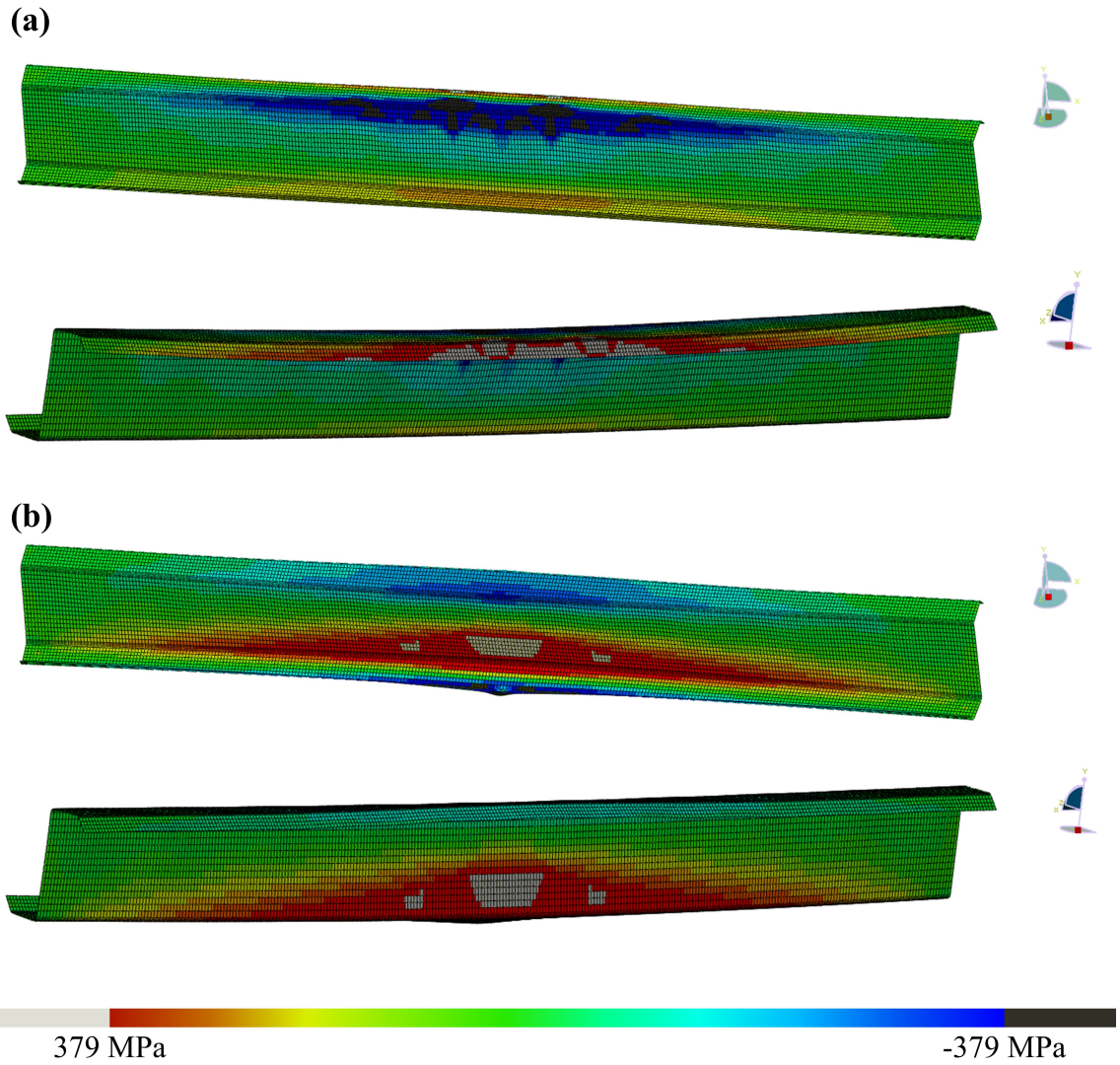

Figure 6.20: Representative S11 distribution of unbraced Zee section (6Z225x105) with (a) $e_1 = -B$ and (b) $e_9 = +B$ at ultimate load.

cross-section was general in compression and the lower half was general in tension. While for different cases, the detailed S11 distribution and magnitudes were different. Specifically, as the two examples shown in Fig. 6.21 and 6.22, the largest compression was found at web-top flange conjunction and the largest tension was found at web-bottom flange conjunction for Cee sections with negative eccentricities; while for Cee sections with positive eccentricities, the largest compression was found at top lip and the largest tension was found at bottom lip. For the braced Zee section, the compression at the top lip was most significant and no tension yielded when the loading was applied at $e_1 = -B$. When the eccentricity tended to increase, the compression at the upper half of the section decreased and the tension at the lower half section increased. At $e_9 = B$, significant tension was observed at the bottom lip, while no compression beyond yield was observed at the upper half section.

Two methods were adopted to calculate the corresponding ultimate moment M_u and bimoment and B_u from the combined bending-torsion simulation. The first method directly calculated the ultimate parameters based on elastic equations using the applied ultimate loads. The M_u for unbraced Cee sections is calculated by Eq. 6.10, where ω is the distributed load along member length and $\omega = P/L$. For unbraced Zee sections, the vertical load causes unsymmetric bending stresses at midspan, therefore the bending stresses were resolved into moments about major and minor principal axes, M_1 and M_2. The ultimate moments M_{1u} and M_{2u} thus were calculated by Eq. 6.11 and 6.12 respectively, where θ is the acute angle between the major principal axis and the x-x geometric axis.

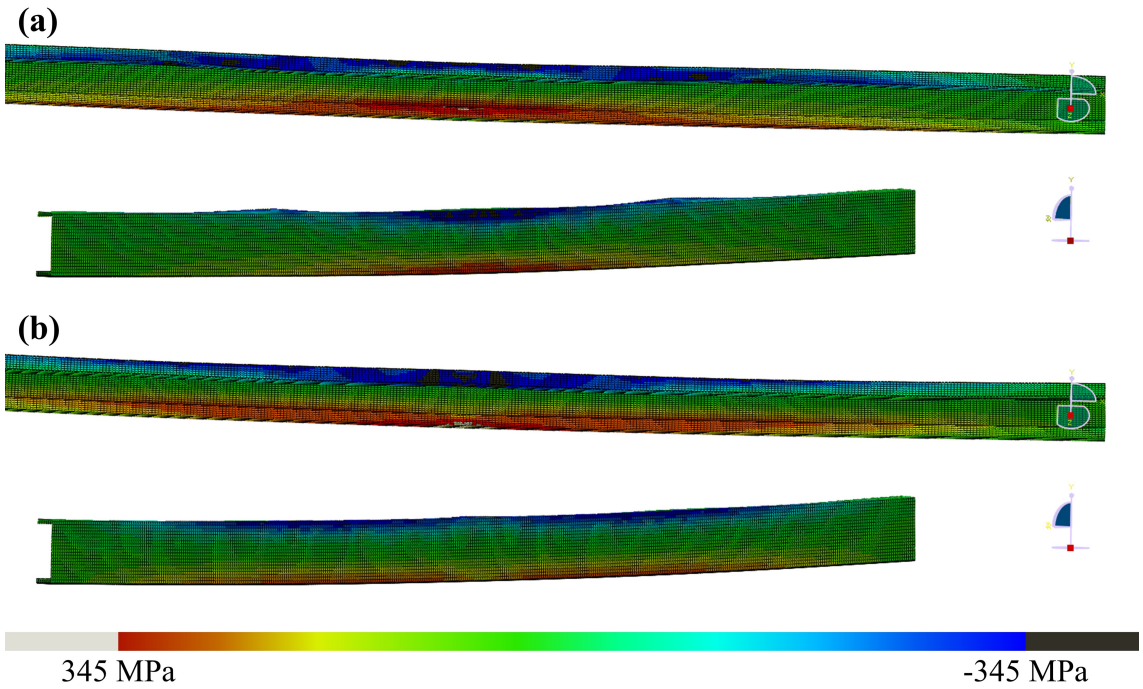

Figure 6.21: Representative S11 distribution of braced Cee section (800S250x68) with (a) $e_3 = -B/2$ and (b) $e_7 = +B/2$ at ultimate load.

$$M_u = \frac{\omega L^2}{8} \tag{6.10}$$

$$M_{1u} = \frac{\omega L^2 \cos\theta}{8} \tag{6.11}$$

$$M_{1u} = \frac{\omega L^2 \sin\theta}{8} \tag{6.12}$$

The ultimate bimoment B_u was calculated by Eq. 6.13 for both unbraced Cee and Zee sections, where L is the unbraced length and equals the total member length. α is a constant calculated by Eq. 6.14, where C_w is torsional warping constant of

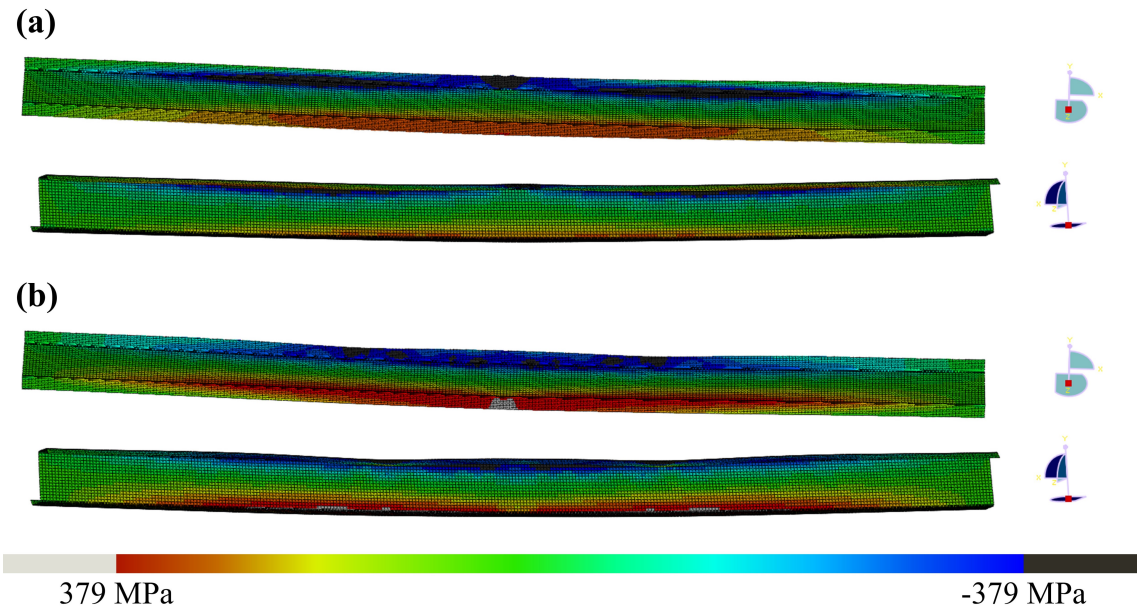

Figure 6.22: Representative S11 distribution of braced Zee section (6Z225x070) with (a) $e_1 = -B$ and (b) $e_9 = +B$ at ultimate load.

cross-section, G is the shear modulus and $G = E/(2+2\upsilon)$, and J is the Saint-Venant torsion constant.

$$B_u = \frac{Pa^2}{L} \cdot \left[\sinh\left(\frac{L}{2a}\right) \cdot \tanh\left(\frac{L}{2a}\right) + 1 - \cosh\left(\frac{L}{2a}\right) \right] \tag{6.13}$$

$$a = \sqrt{\frac{EC_w}{GJ}} \tag{6.14}$$

For the braced case of both Cee and Zee sections, the ultimate moment M_u was calculated by Eq. 6.10 and the ultimate bimoment B_u was calculated by Eq. 6.15, where L is the unbraced length and equals to half of the total member length. a is calculated by Eq. 6.14.

$$B_u = -\frac{Pea^2}{L} \cdot \left[\cosh\left(\frac{L}{a}\right) - 1 + \left(\frac{\cosh\left(\frac{L}{a}\right) - 1 + \frac{L^2}{2a^2} - \frac{L}{a} \cdot \sinh\left(\frac{L}{a}\right)}{\frac{L}{a} \cdot \cosh\left(\frac{L}{a}\right) - \sinh\left(\frac{L}{a}\right)} \right) \cdot \sinh\left(\frac{L}{a}\right) \right] \tag{6.15}$$

The second method is stress-based and it calculated the ultimate moment and bimoment by directly using the longitudinal stresses S11 following Eq. 6.16, 6.17, and 6.18, where the subscript x and y represent x-x and y-y geometric axes. For the unbraced Cee section, $M_u = M_{xu}$ and for the unbraced Zee section the ultimate moment M_{1u} and M_{2u} are calculated by Eq. 6.19 and 6.20. For both braced Cee and Zee sections, $M_u = M_{xu}$.

$$M_{xu} = \int \sigma y \, dA \tag{6.16}$$

$$M_{yu} = \int \sigma x \, dA \tag{6.17}$$

$$B_u = \int \sigma w_n \, dA \tag{6.18}$$

$$M_{1u} = +M_{xu} \cos\theta + M_{yu} \sin\theta \tag{6.19}$$

$$M_{2u} = -M_{xu} \sin\theta + M_{yu} \cos\theta \tag{6.20}$$

The nominal flexural strengths M_n (or M_{1n} and M_{2n} for unbraced Zee sections)

was calculated following Ch. F of AISI S100 [30]. The bimoment capacity B_n was calculated by Eq. 6.8 with proposed coefficients in Section 6.4 for LB controlled and DB controlled cases respectively. The relationship between B_u/B_n versus M_u/M_n for unbraced Cee sections is shown Fig. 6.23. The plot shows that the interaction is dependent on the direction of the eccentricity. For the negative eccentricities, the bimoments are positive following the CUFSM [142] sign convention (the same hereinafter) and are general above $M_u/M_n + B_u/B_n = 0.8$. For the positive eccentricities, the bimoments are negative and are general above $M_u/M_n - B_u/B_n = 1.3$. The relationship between B_u/B_n versus M_{1u}/M_{1n} versus M_{2u}/M_{2n} for unbraced Zee sections is shown Fig. 6.24. Unbraced Zee sections with both positive and negative eccentricities show conservative interaction behaviors, where the data are general above $M_{1u}/M_{1n} + M_{2u}/M_{2n} + B_u/B_n = 1.3$ for the cases with negative eccentricities and are above $M_{1u}/M_{1n} + M_{2u}/M_{2n} - B_u/B_n = 1.3$ for the cases with positive eccentricities. The positive eccentricity cases are even more conservative than the negative eccentricity cases.

For the braced cases, the Cee and Zee sections show similar interaction behaviors between B_u/B_n versus M_u/M_n as shown in Fig. 6.25. Significantly different behaviors are observed in positive and negative eccentricity cases. The negative eccentricity cases show negative bimoments and the data is general above $M_u/M_n - B_u/B_n = 1$. In contrast, the positive eccentricity cases show positive bimoments and the data is more conservative and general above $M_u/M_n + B_u/B_n = 1.2$.

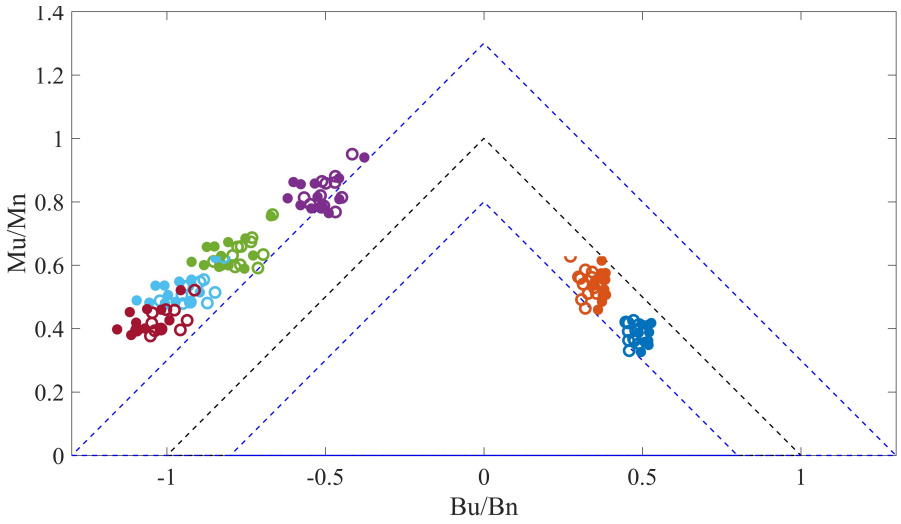

Figure 6.23: Interaction between B_u/B_n and M_u/M_n for unbraced Cee sections. Different colors represent different eccentricities as shown in Fig. 6.15(a). Solid scatters represent stress-based method and hollow ones represent equation-based method.

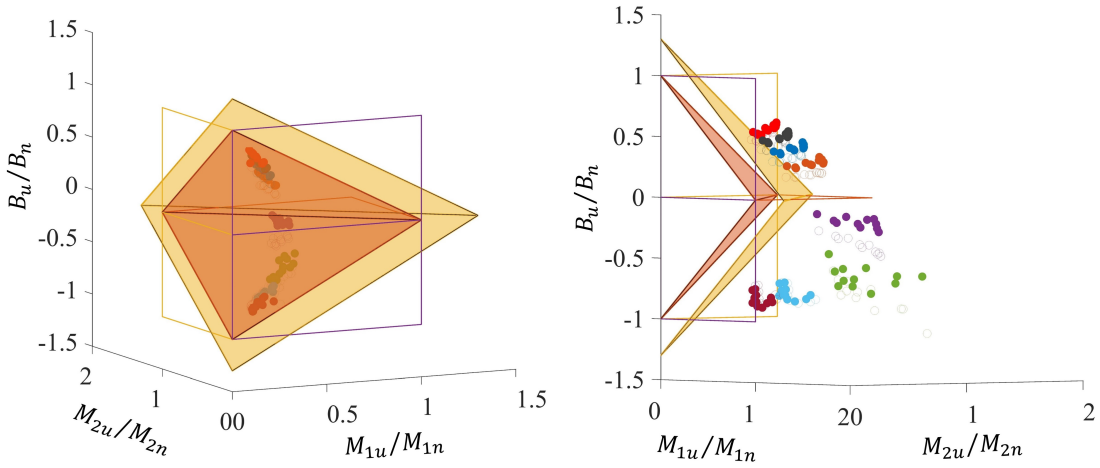

Figure 6.24: Interaction among B_u/B_n versus M_{1u}/M_{1n} versus M_{2u}/M_{2n} for unbraced Zee sections from two perspectives. Different colors represent different eccentricities as shown in Fig. 6.15(b). Solid scatters represent stress-based method and hollow ones represent equation-based method.

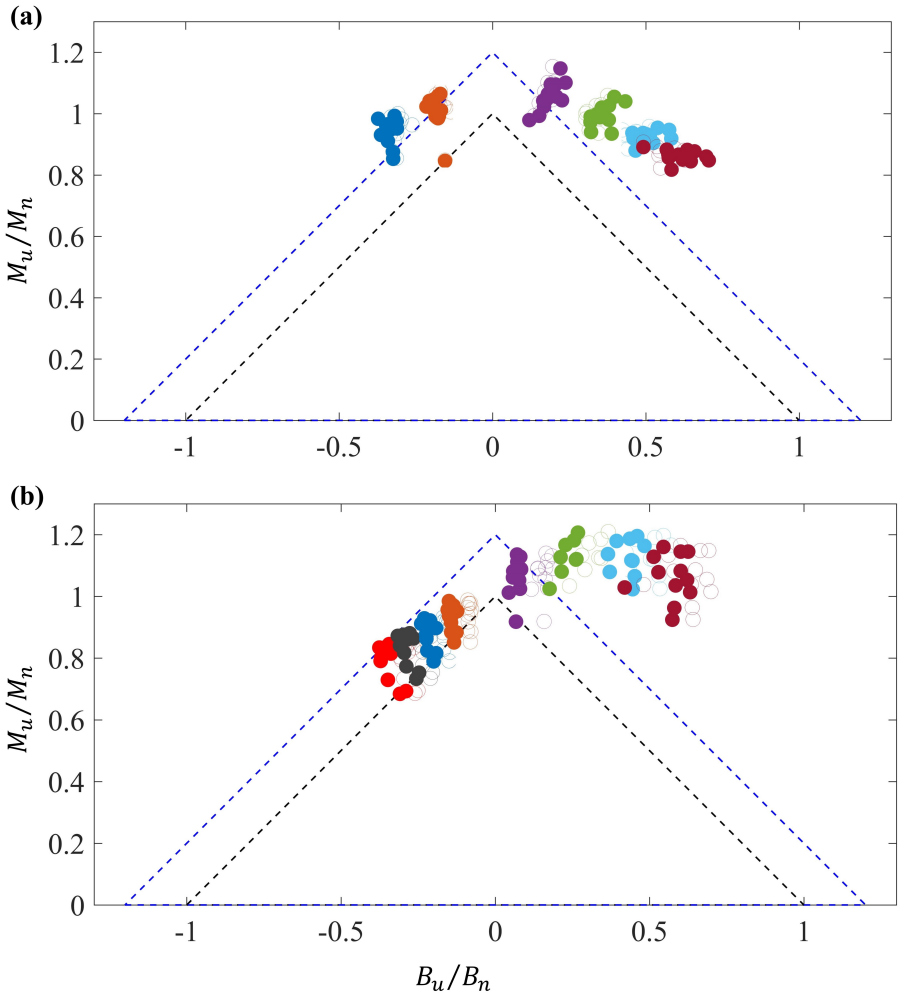

Figure 6.25: Interaction between B_u/B_n and M_u/M_n for braced (a) Cee and (b) Zee sections. Different colors represent different eccentricities as shown in Fig. 6.15. Solid scatters represent stress-based method and hollow ones represent equation-based method.

6.6 Conclusion

A simple method to predict thin-walled CFS member bimoment capacity has been developed. A set of bimoment parameters, including yield bimoment B_y, plastic bimoment B_p, buckling bimoment B_{cr}, and bimoment strength B_n, are calculated and determined using a validated finite element model considering buckling and/or inelastic behaviors. A wide range of steel grades with yield strengths from conventional mild steel to ultra-high-strength steel and different typical Cee and Zee sections are investigated. A simple and uniform equation is adopted to predict the bimoment strength B_n of CFS member incorporating B_y, B_p, and B_{cr}. The calibrated coefficients of the equation for local buckling and distortional buckling are proposed respectively based on the regression analyses. Excellent agreements between the adopted equation with calibrated coefficients and simulation data show the validity of the equation. Furthermore, the wide range of cross-section geometries and steel grades being considered indicate the equation and calibrated coefficients might apply to other common geometries and steel grades in the CFS market. Additionally, a series of interaction equations for both braced and unbraced Cee and Zee sections under combined bending-torsion are developed using data from the simulation.

Chapter 7

Conclusions

7.1 Summary and Conclusions

Advanced high-strength cold-formed steel faces multiple challenges before its adoption as the material to form structural members in the construction industry, because its material properties are significantly different from conventional steel. Therefore, its structural performance is unclear and needs to be understood. This dissertation conducts a thorough study focusing on the material properties of thin AHSS alloys and the structural behaviors of thin-walled AHSS members.

The chapters of the AHSS material properties include various temperature scenarios including ambient, elevated temperature, and subzero temperature scenarios. For each temperature scenario, detailed stress-strain data and key material properties from tensile coupon tests covering a wide range of steel strengths are presented. Additionally, modeling of the experimental stress-strain database is pro-

vided accompanied by predictive equations for the required model parameters. By adopting the proposed predictive equations for the constitutive relationships and key material properties, simple and accurate description of AHSS can be developed in future advanced numerical simulation studies considering different temperature scenarios.

The chapter of the residual stress provides detailed results on the magnitudes and distribution of the residual stress for the thin-walled press-braked AHSS lipped angle sections from an experimental and numerical investigation. A comparison of the residual stress distribution between the experiment and existing studies for thin-walled CFS open sections shows the uniqueness of the residual stress distribution for AHSS members. A numerical model is designed and validated with the experimental data to simulate the member press-braking processes, and it provides extra residual stress data through the member thickness. The measured experimental residual stress distribution and proposed numerical model can be adopted for defining and determining the residual stress in numerical analyses on thin-walled cold-formed high-strength steel members.

The chapter of the torsional behavior of CFS members provides detailed development and recommendation for the bimoment strength prediction for members under torsional loads and the moment-bimoment interaction equations for the members under combined bending-torsion. The study considers thin-walled open sections (e.g., Cee and Zee sections) with different bracing conditions, cross-section dimensions, and loading eccentricities, which covers the common situations in engineering practices. The results from this chapter can be adopted to calculate

the bimoment strength and moment-bimoment interaction for CFS members with different loading and bracing conditions in a simple and accurate manner.

7.2 Future Work

This dissertation has provided detailed data and information from a few perspectives including the material properties and the member structural performance of AHSS to help the industry better understand the potential and limitations of AHSS as future construction material. Meanwhile, the following work that could be finished in the future might further help to understand AHSS structural behaviors:

In Ch. 3 and 4, the predictive equations for AHSS constitutive relationship and key material properties under extreme temperature conditions were developed. Predictive equations for some model parameters were fit using simple equation form (e.g., polynomial and exponential) considering the simplicity. In the future, it is possible to adopt machine learning technique to explore different equation forms to find more accurate prediction, particularly for those with relatively large variation (e.g., some key strains).

In Ch. 5, the numerical study was designed to simulate the press-braking processes for the members used in the experimental studies. It is practicable to change the material properties and/or thicknesses by using the database from Ch. 2. It will be helpful to consider investigating the mesh size effects on the residual stress distribution and to obtain a reasonable balance between efficiency and accuracy. Additionally, it is possible to adopt the measured test data and developed simulation

to determine the residual stress in numerical studies for members under different loading conditions, and the effect of developed residual stresses on the member structural performance can be investigated.

In Ch. 6, a series of numerical studies were conducted to develop the predictions on bimoment strength and moment-bimoment interaction for CFS members under different loading conditions. Different material properties were considered in the torsion only scenario. It will be helpful to also include different material properties in the combined bending-torsion scenario. For the braced sections under the combined bending-torsion scenario, it might be helpful to include moment parameters about both principal axes in the interaction equations. Additionally, considering the significantly different behaviors for CFS members with different cross-section shapes, loading positions, and bracing conditions under combined bending-torsion, it will be helpful to define different resistance factors for the cases with different structural behaviors. It is also possible to conclude the final design equations for the industry by using the interaction data provided in this study.

Appendix A

Determination of purlin bracing stiffness

The appendix introduces a numerical method to determine the stiffness of purlin bracing for metal building system by using AHSS material properties in material definition.

Metal building system is an important constitute of modern metal buildings. Its main application includes warehouses, office buildings, garages, supermarkets, and retail stores. Compared with other building forms, its advantages include the ability to span long distances, faster occupancy, cost efficiency, expansion flexibility, lower maintenance cost, etc [146]. A detailed sketch of a typical metal building system from Fig. 1.2 of [146] is shown in Fig. A.1.

Among different components of the metal building system, this appendix focuses on the bracing for the purlins. Purlin is a secondary framing member. It

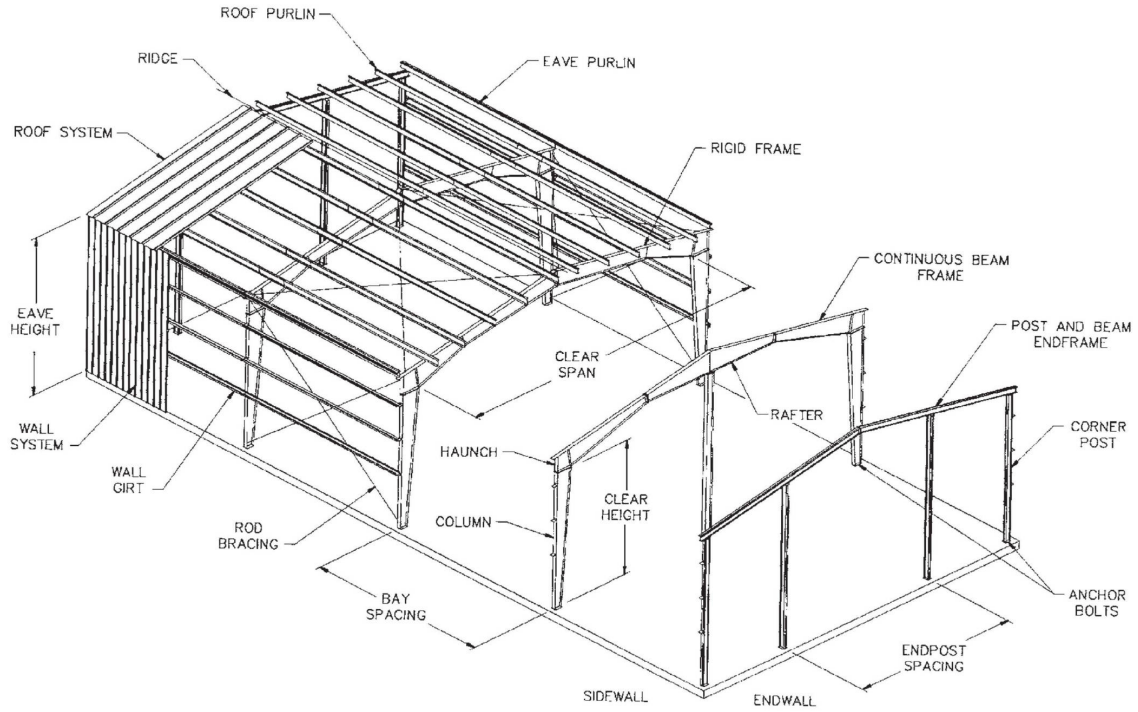

Figure A.1: Typical components of a metal building system from Fig. 1.2 of [146].

supports roof covering and carrying exterior loads to main frames. It also provides flange bracing for primary framing. Additionally, it functions as a part of the building's lateral load-resisting system [146].

Purlins have relatively lower loading demand and thus have smaller dimension compared with primary framing members. Therefore, CFS open sections are suitable and popular for manufacturing purlins. Meanwhile, considering the thin-walled geometry of the purlins, sufficient bracing for purlins is essential for providing lateral flange bracing, restraining the purlin from rotation and to relieve torsion, and restraining the whole assembly of purlins and roofing from lateral translation [146].

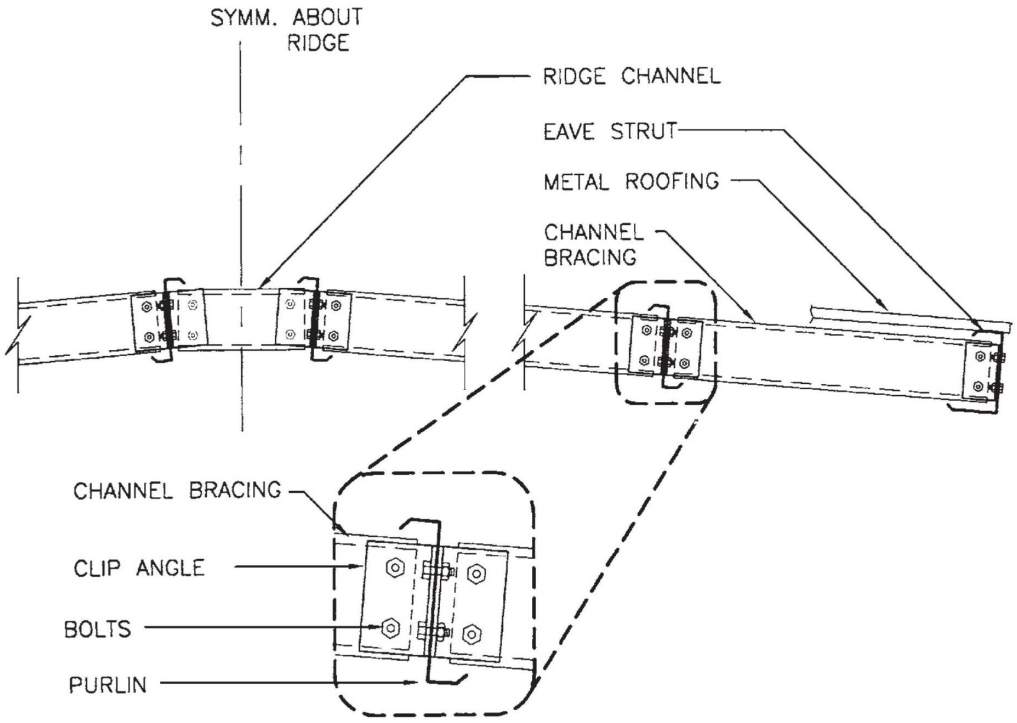

Figure A.2: Perhaps the most effective system of purlin bracing is provided by closely spaced bolted channels from Fig. 5.17 of [146].

Among various purlin bracing forms, the purlin bracing running parallel to the roof slope from eave to eave is the most popular. Fig. A.2 (Fig. 5.17 of [146]) shows the typical constitutes for this purlin bracing system.

For the numerical work on simulating the purlin and its bracing system, directly modeling each part in the real engineering practice is difficult, which could demand a massive calculation and cause convergence issues. Instead, using springs with predefined stiffnesses along different degrees of freedoms (DOFs) can decently simplify the model and overcome the aforementioned issues. Therefore, it is essential to accurately determine the stiffnesses of the purlin bracing along each DOF.

A numerical model is developed and its setup is based on Fig. A.2 to simulate

Table A.1

purlin section	brace section	clip angle		bolts	
		section	D_{ca} (in.)	number	d_b (in.)
6ZS2.25x105	400S250-97	2LU2x135	4.0	4	0.19
8ZS2.75x105	550S250-97	2LU2x135	5.5	4	0.19
10ZS3.25x105	600S250-97	2LU2x135	6.0	4	0.19

[1] D_{ca} is the depth of the clip angle and d_b is the bolt diameter.

the real bracing situation and to determine the bracing stiffnesses. DP-700 was used as the material for all steel members. Different dimensions of purlin cross-section are investigated as shown in Table A.1.

A typical simulation setup is shown in Fig. A.3 and A.4 using 6ZS2.25x105 purlin case as an example. Two different bolting modes were investigated. The case that the clip angle was bolted to the inner web of purlin bracing is called mode 1, and the case that the clip angle was bolted to the outer web of purlin bracing is called mode 2. A small truncation of the Zee purlin was used to represent the purlin. A few reasons were considered to make this simplification. Firstly, it decreased the number of elements on the purlin and thus reduced the calculation demand. Secondly, since the objective of this section was to determine the stiffness for a single purlin brace, there was no need to simulate more than one purlin brace location. For the two ends of the purlin truncation, only the rotations along Y and Z directions were restrained and all other DOFs were free.

A half-span channel bracing on each side of purlin web were connected to the purlin by being bolted to the clip angles. The full length of the channel bracing was selected as 60 inch, so the half span length of the channel bracing was 30 inch (762 mm). For each side of the purlin web, only a half-span channel bracing was

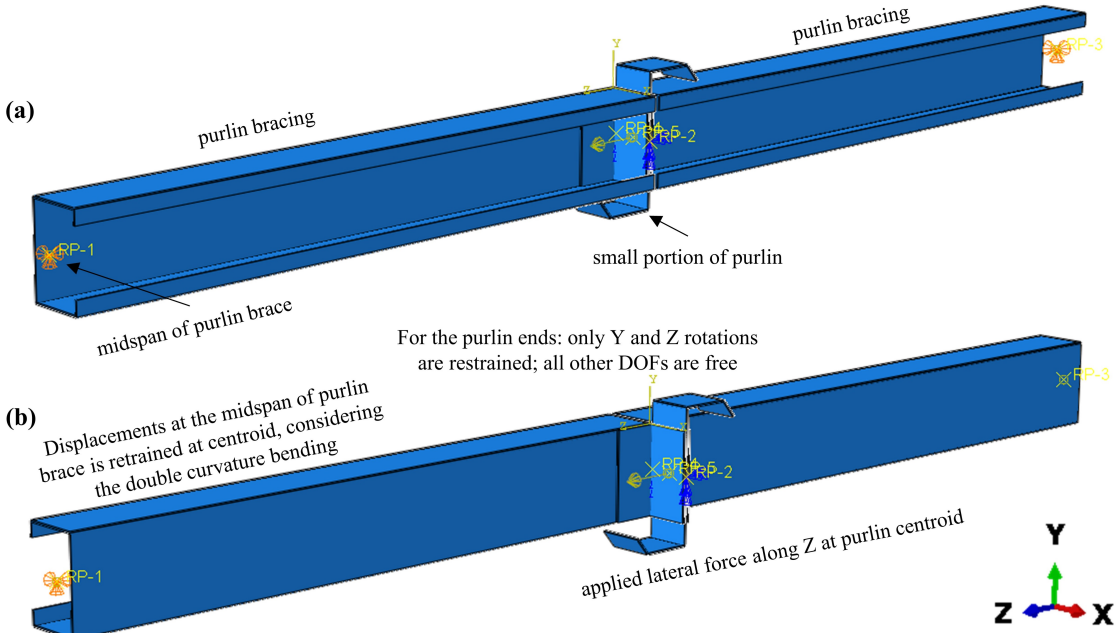

Figure A.3: Simulation setup of 6ZS2.25x105 purlin for (a) mode 1 and (b) mode 2.

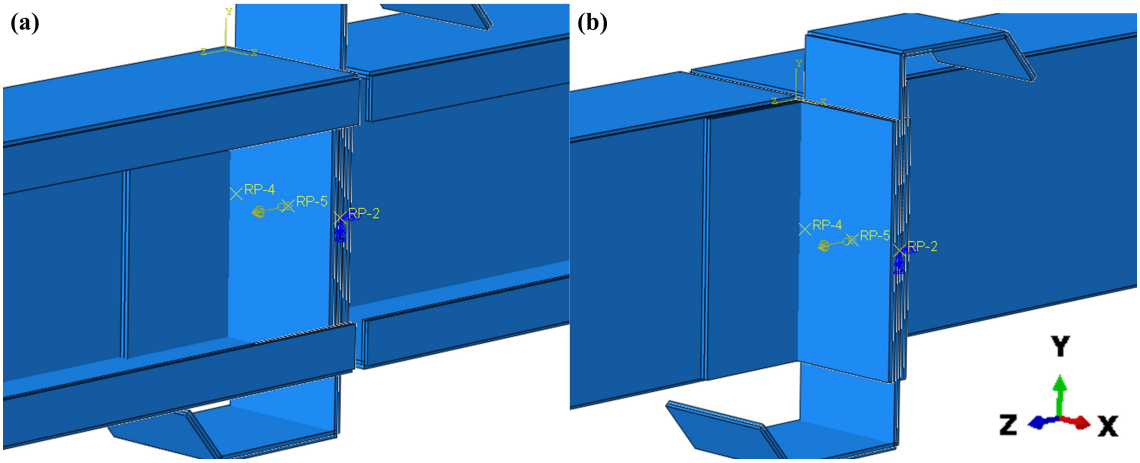

Figure A.4: Magnification at the purlin part for Fig. A.3. (a) represents mode 1 and (b) represents mode 2.

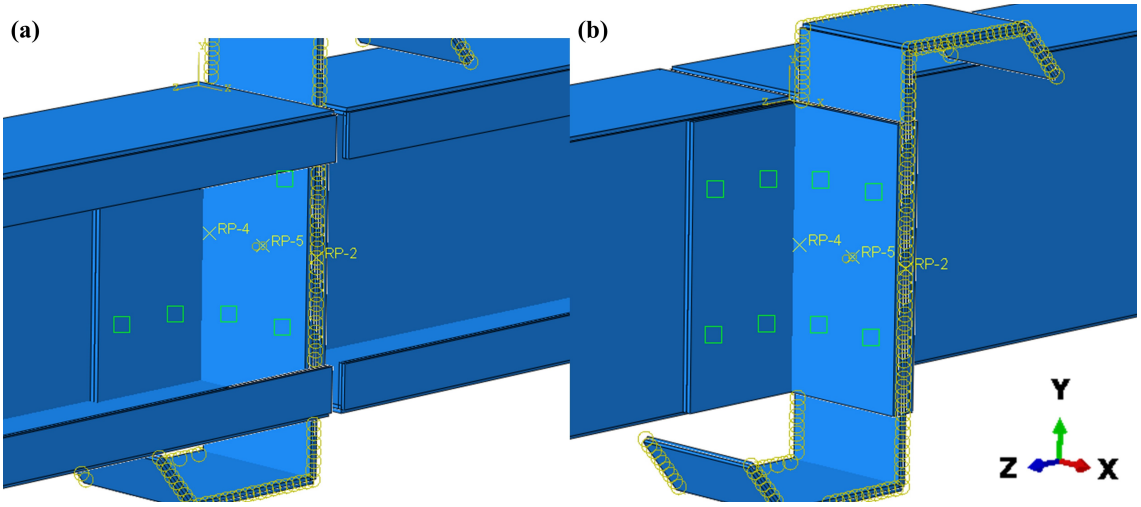

Figure A.5: Fasteners and interaction detailing for (a) mode 1 and (b) mode 2.

considered based on the assumption that the displacements at the midspan of the channel bracing were zero considering the double curvature bending. In other words, the displacements along all three directions for the end of the half-span channel bracing (i.e., the midspan of the full-span channel bracing) were restrained. The restraints were defined at the cross-section centroid of the channel bracing. Point-based fasteners were used to simulate the bolts going through the clip angles, channel bracing, and purlin respectively, as shown in Fig. A.5. Four fasteners were designed to penetrate each leg of the clip angle respectively. The physics radius of the fastener was set per the design dimension of the bolt as listed in Table A.1. Contacts were defined between the clip angle and the channel bracing and between the Zee purlin and the clip angle.

The major effects from the purlin bracing are restraining the lateral displacement and longitudinal rotation (i.e., rotation along X direction). Therefore, the stiffnesses for these two DOFs were determined respectively. A unit lateral load was applied

Table A.2: Lateral linear stiffness K_Z and purlin longitudinal direction rotational stiffness $K_{\phi X}$ calculated by the developed model

purlin section	bolting mode	K_Z kN/mm	$K_{\phi X}$ kN-m/rad
6ZS2.25x105	mode 1	11.60	45.17
	mode 2	11.86	47.47
8ZS2.75x105	mode 1	18.00	78.83
	mode 2	18.64	82.38
10ZS3.25x105	mode 1	20.14	76.30
	mode 2	21.26	80.28

at the purlin centroid, and the lateral (Z direction) displacement Δ_Z was then calculated. By adopting $K\Delta = F$, the lateral linear stiffness for the purlin brace was calculated as $K_Z = 1/\Delta_Z$. Similarly, a unit moment along X direction was applied at the purlin centroid, and the rotation along X direction θ_X was then calculated. The X direction rotational stiffness for the purlin brace was therefore calculated as $K_{\phi X} = 1/\theta_X$. By adopting the same method, a summary of the lateral linear stiffness K_Z and the X direction rotational stiffness $K_{\phi X}$ for the different purlin sections is calculated and shown in Table A.2.

Bibliography

[1] W. Yu, R. A. LaBoube, and H. Chen, *Cold-formed steel design*, 5th. John Wiley & Sons, Inc., 2019, pp. 1–528, ISBN: 9781119487418.

[2] S. Keeler, M. Kimchi, and P. Mooney, *Advanced High-Strength Steels Application Guidelines*, 6.0. Brussels, Belgium: WorldAutoSteel, 2017.

[3] R. Kuziak, R. Kawalla, and S. Waengler, "Advanced high strength steels for automotive industry," *Archives of Civil and Mechanical Engineering*, vol. 8, no. 2, pp. 103–117, 2008, ISSN: 1644-9665. DOI: 10.1016/S1644-9665(12)60197-6.

[4] H. X. Wan, B. Huang, and M. Mahendran, "Experiments and numerical modelling of cold-formed steel beams under bending and torsion," *Thin-Walled Structures*, vol. 161, p. 107 424, 2021, ISSN: 02638231. DOI: 10.1016/j.tws.2020.107424.

[5] Y. Xia, C. Ding, Z. Li, B. W. Schafer, and H. B. Blum, "Numerical modeling of stress-strain relationships for advanced high strength steels," *Journal of Constructional Steel Research*, vol. 182, p. 106 687, Jul. 2021, ISSN: 0143974X. DOI: 10.1016/j.jcsr.2021.106687.

[6] Y. Xia, X. Yan, T. Gernay, and H. B. Blum, "Elevated temperature and post-fire stress-strain modeling of advanced high-strength cold-formed steel alloys," *Journal of Constructional Steel Research*, vol. 190, p. 107 116, 2022.

[7] Y. Xia, Z. Li, B. W. Schafer, and H. Blum, "Experimental study on residual stresses of dual phase high-strength cold-formed steel angles," *ce/papers*, vol. 4, no. 2-4, pp. 387–392, 2021. DOI: 10.1002/cepa.1307.

[8] Y. Xia, R. S. Glauz, B. W. Schafer, M. Seek, and H. B. Blum, "Cold-formed steel strength predictions for torsion," in *Proceedings of Annual Stability Conference, Structural Stability Research Council*, 2022. [Online]. Available: https://cloud.aisc.org/SSRC/2022/Xia_et_al_SSRC_2022.pdf.

[9] ASTM E8, *Standard Test Methods for Tension Testing of Metallic Materials*, 2016.

[10] Y. Huang and B. Young, "The art of coupon tests," *Journal of Constructional Steel Research*, vol. 96, pp. 159–175, 2014, ISSN: 0143974X. DOI: 10.1016/j.jcsr.2014.01.010.

[11] W. Ramberg and W. R. Osgood, "Description of stress-strain curves by three parameters," *National Advisory Committee For Aeronautics*, no. l, Technical Note No. 902, 1943.

[12] H. N. Hill, "Determination of stress-strain relations from the offset yield strength values, Technical Note No. 927," National Advisory Committee for Aeronautics, Washington, D.C., USA, Tech. Rep. No. 927, 1944.

[13] E. Mirambell and E. Real, "On the calculation of deflections in structural stainless steel beams: An experimental and numerical investigation," *Journal of Constructional Steel Research*, vol. 54, no. 1, pp. 109–133, 2000, ISSN: 0143-974X. DOI: 10.1016/S0143-974X(99)00051-6.

[14] K. J. Rasmussen, "Full-range stress–strain curves for stainless steel alloys," *Journal of constructional steel research*, vol. 59, no. 1, pp. 47–61, 2003.

[15] L. Gardner and D. A. Nethercot, "Experiments on stainless steel hollow sections-Part 1: Material and cross-sectional behaviour," *Journal of Constructional Steel Research*, vol. 60, no. 9, pp. 1291–1318, Sep. 2004, ISSN: 0143974X. DOI: 10.1016/j.jcsr.2003.11.006.

[16] H.-T. Li and B. Young, "Cold-formed high strength steel shs and rhs beams at elevated temperatures," *Journal of Constructional Steel Research*, vol. 158, pp. 475–485, 2019.

[17] P. Hradil, A. Talja, E. Real, E. Mirambell, and B. Rossi, "Generalized multistage mechanical model for nonlinear metallic materials," *Thin-Walled Structures*, vol. 63, pp. 63–69, Feb. 2013, ISSN: 02638231. DOI: 10.1016/j.tws.2012.10.006.

[18] W. M. Quach, J. G. Teng, and K. F. Chung, "Three-Stage Full-Range Stress-Strain Model for Stainless Steels," *Journal of Structural Engineering*, vol. 134, no. 9, pp. 1518–1527, 2008, ISSN: 0733-9445. DOI: 10.1061/(asce)0733-9445(2008)134:9(1518).

[19] A. Olsson, "Stainless steel plasticity: Material modelling and structural applications," Ph.D. dissertation, Luleå tekniska universitet, 2001.

[20] L. Gardner and M. Ashraf, "Structural design for non-linear metallic materials," *Engineering Structures*, vol. 28, no. 6, pp. 926–934, May 2006, ISSN: 01410296. DOI: 10.1016/j.engstruct.2005.11.001.

[21] W. M. Quach, "Residual stresses in cold-formed steel sections and their effect on column behaviour," Ph.D. dissertation, Hong Kong Polytechnic University, 2005.

[22] M. MacDonald, J. Rhodes, and G. T. Taylor, "Mechanical properties of stainless steel lipped channels," in *International Specialty Conference on Cold-Formed Steel Structures: Recent Research and Developments in Cold-Formed Steel Design and Construction*, 2000, pp. 673–686.

[23] K. Abdella, "Inversion of a full-range stress-strain relation for stainless steel alloys," *International Journal of Non-Linear Mechanics*, vol. 41, no. 3, pp. 456–463, Apr. 2006, ISSN: 00207462. DOI: 10.1016/j.ijnonlinmec.2005.10.002.

[24] J. L. Ma, T. M. Chan, and B. Young, "Material properties and residual stresses of cold-formed high strength steel hollow sections," *Journal of Constructional Steel Research*, vol. 109, pp. 152–165, Jun. 2015, ISSN: 0143974X. DOI: 10.1016/j.jcsr.2015.02.006.

[25] L. Gardner and X. Yun, "Description of stress-strain curves for cold-formed steels," *Construction and Building Materials*, vol. 189, pp. 527–538, Nov. 2018, ISSN: 09500618. DOI: 10.1016/j.conbuildmat.2018.08.195.

[26] Y. Huang and B. Young, "Material properties of cold-formed lean duplex stainless steel sections," *Thin-Walled Structures*, vol. 54, pp. 72–81, 2012, ISSN: 02638231. DOI: 10.1016/j.tws.2012.02.003.

[27] A. J. Sadowski, J. M. Rotter, T. Reinke, and T. Ummenhofer, "Statistical analysis of the material properties of selected structural carbon steels," *Structural Safety*, vol. 53, pp. 26 –35, 2015, ISSN: 0167-4730. DOI: 10.1016/j.strusafe.2014.12.002.

[28] C. Ding, Z. Li, H. Blum, Y. Xia, and B. W. Schafer, "Ductility Demands on CFS Structural Connections of Advanced High Strength Steel," in *Proceedings of the Cold-Formed Steel Research Consortium Colloquium*, Oct. 2020. [Online]. Available: http://jhir.library.jhu.edu/handle/1774.2/63168.

[29] H. B. Blum and K. J. Rasmussen, "Experimental investigation of long-span cold-formed steel double channel portal frames," *Journal of Constructional Steel Research*, vol. 155, pp. 316–330, Apr. 2019, ISSN: 0143974X. DOI: 10.1016/j.jcsr.2018.11.020.

[30] AISI S100-16, *North American Specification for the Design of Cold-Formed Steel Structural Members*. Washington, DC, U.S.A.: AISI, 2016.

[31] Y. Fukumoto, "New constructional steels and structural stability," *Engineering structures*, vol. 18, no. 10, pp. 786–791, 1996.

[32] P Langenberg, "Relation between design safety and y/t ratio in application of welded high strength structural steels," in *Proceedings of International Symposium on Applications of High Strength Steels in Modern Constructions and Bridge-Relationship of Design specifications, Safety and Y/T ratio. Beijing*, 2008, pp. 28–46.

[33] W. M. Quach and J. F. Huang, "Stress-strain models for light gauge steels," *Procedia Engineering*, vol. 14, pp. 288–296, 2011, ISSN: 18777058. DOI: 10.1016/j.proeng.2011.07.035.

[34] C. Salmon, J. Johnson, and F. Malhas, *Steel Structures: Design and Behavior*, 5th ed. Pearson, 2009, ISBN: 978-0131885561.

[35] C. A. Rogers and G. J. Hancock, "Ductility of G550 Sheet Steels in Tension - Elongation Measurements and Perforated Tests," The University of Sydney, Sydney, Tech. Rep. December 1996, 1996.

[36] N. Abdel-Rahman and K. Sivakumaran, "Material properties models for analysis of cold-formed steel members," *Journal of Structural Engineering*, vol. 123, no. 9, pp. 1135–1143, 1997.

[37] R. Kanno, "Advances in steel structures and steel materials in Japan," *ce/papers*, vol. 1, no. 4, pp. 394–404, 2017.

[38] G. Shi and X. Chen, "Research advances in HSS structures at Tsinghua University and codification of the design specification," *Steel Construction*, vol. 11, no. 4, pp. 286–293, 2018.

[39] Steel Construction Institute, "High Strength Steel design and Execution Guide," Steel Construction Institute, Berkshire, U.K., Tech. Rep., 2019, pp. 1–163. [Online]. Available: https://steel-sci.com/high-strength-steel-design-and-execution-guide-(p432).html.

[40] AISC Committee on Specifications Task Group on High Strength Steel, "Ad Hoc Task Group Report on High Strength Steel," American Institute of Steel Construction, Chicago, IL, U.S.A., Tech. Rep., 2019, pp. 1–89. [Online]. Available: https://www.aisc.org/technical-resources/research/researchlibrary/ad-hoc-task-group-report-on-high-strength-steel/.

[41] American Institute of Steel Construction (AISC), *ANSI/AISC 360-16: Specification for Structural Steel Buildings*. Chicago, IL, U.S.A., 2016.

[42] European Committee for Standardization (CEN), *Eurocode 3: Design of steel structures, Part 1-2: General rules - Structural fire design*. Brussels, Belgium, 2005, pp. 1–81.

[43] Standards Australia, *AS 4100-1998 (R2016) Steel structures*. Sydney, Australia, 2016, pp. 1–238.

[44] T. Ranawaka and M. Mahendran, "Experimental study of the mechanical properties of light gauge cold-formed steels at elevated temperatures," *Fire Safety Journal*, vol. 44, no. 2, pp. 219–229, 2009, ISSN: 03797112. DOI: 10.1016/j.firesaf.2008.06.006.

[45] X. Yan, Y. Xia, H. B. Blum, and T. Gernay, "Elevated temperature material properties of advanced high strength steel alloys," *Journal of Constructional Steel Research*, vol. 174, p. 106 299, Nov. 2020, ISSN: 0143974X. DOI: 10.1016/j.jcsr.2020.106299.

[46] X. Yan, Y. Xia, H. B. Blum, and T. Gernay, "Post-fire mechanical properties of advanced high-strength cold-formed steel alloys," *Thin-Walled Structures*, vol. 159, p. 107 293, 2021.

[47] J. H. Lee, M. Mahendran, and P. Makelainen, "Prediction of mechanical properties of light gauge steels at elevated temperatures," *Journal of Constructional Steel Research*, vol. 59, no. 12, pp. 1517–1532, Dec. 2003, ISSN: 0143974X. DOI: 10.1016/S0143-974X(03)00087-7.

[48] W. Chen and J. Ye, "Mechanical properties of G550 cold-formed steel under transient and steady state conditions," *Journal of Constructional Steel Research*, vol. 73, pp. 1–11, 2012, ISSN: 0143974X. DOI: 10.1016/j.jcsr.2011.12.010.

[49] Y. Huang and B. Young, "Stress-strain relationship of cold-formed lean duplex stainless steel at elevated temperatures," *Journal of Constructional Steel Research*, vol. 92, pp. 103–113, 2014, ISSN: 0143974X. DOI: 10.1016/j.jcsr.2013.09.007.

[50] J. Chen and B. Young, "Stress-strain curves for stainless steel at elevated temperatures," *Engineering Structures*, vol. 28, no. 2, pp. 229–239, 2006, ISSN: 01410296. DOI: 10.1016/j.engstruct.2005.07.005.

[51] J. Outinen and P. Mäkeläinen, "Mechanical properties of structural steel at elevated temperatures and after cooling down," *Fire and Materials*, vol. 28, no. 2-4, pp. 237–251, Mar. 2004, ISSN: 03080501. DOI: 10.1002/fam.849.

[52] J. Chen and B. Young, "Experimental investigation of cold-formed steel material at elevated temperatures," *Thin-Walled Structures*, vol. 45, no. 1, pp. 96–110, 2007, ISSN: 02638231. DOI: 10.1016/j.tws.2006.11.003.

[53] L. Gardner, A. Insausti, K. T. Ng, and M. Ashraf, "Elevated temperature material properties of stainless steel alloys," *Journal of Constructional Steel Research*, vol. 66, no. 5, pp. 634–647, May 2010, ISSN: 0143974X. DOI: 10.1016/j.jcsr.2009.12.016.

[54] N. D. Kankanamge and M. Mahendran, "Mechanical properties of cold-formed steels at elevated temperatures," *Thin-Walled Structures*, vol. 49, no. 1, pp. 26–44, 2011, ISSN: 02638231. DOI: 10.1016/j.tws.2010.08.004.

[55] J. Ye and W. Chen, "Elevated temperature material degradation of cold-formed steels under steady- and transient-state conditions," *Journal of Materials in Civil Engineering*, vol. 25, no. 8, pp. 947–957, 2013, ISSN: 08991561. DOI: 10.1061/(ASCE)MT.1943-5533.0000640.

[56] A. Landesmann, F. C. M. Da Silva, and E. De Miranda Batista, "Experimental investigation of the mechanical properties of ZAR-345 cold-formed steel at elevated temperatures," *Materials Research*, vol. 17, no. 4, pp. 1082–1091, 2014, ISSN: 15161439. DOI: 10.1590/1516-1439.297014.

[57] M. Imran, M. Mahendran, and P. Keerthan, "Mechanical properties of cold-formed steel tubular sections at elevated temperatures," *Journal of Constructional Steel Research*, vol. 143, pp. 131–147, 2018, ISSN: 0143974X. DOI: 10.1016/j.jcsr.2017.12.003.

[58] T. G. Singh and K. D. Singh, "Mechanical properties of YSt-310 cold-formed steel hollow sections at elevated temperatures," *Journal of Constructional Steel Research*, vol. 158, pp. 53–70, 2019, ISSN: 0143974X. DOI: 10.1016/j.jcsr.2019.03.004.

[59] J. Outinen and P Mäkeläinen, "Mechanical properties of structural steel at elevated temperatures," in *Advances in Steel Structures* (*ICASS'02*), Elsevier, 2002, pp. 1103–1110.

[60] S. Gunalan and M. Mahendran, "Experimental investigation of post-fire mechanical properties of cold-formed steels," *Thin-Walled Structures*, vol. 84, pp. 241–254, 2014, ISSN: 02638231. DOI: 10.1016/j.tws.2014.06.010.

[61] F. Azhari, A. Heidarpour, X. Zhao, and C. R. Hutchinson, "Mechanical properties of ultra-high strength (Grade 1200) steel tubes under cooling phase of a fire: an experimental investigation," *Construction and Building Materials*, vol. 93, pp. 841–850, 2015.

[62] J. Lu, H. Liu, Z. Chen, and X. Liao, "Experimental investigation into the post-fire mechanical properties of hot-rolled and cold-formed steels," *Journal of Constructional Steel Research*, vol. 121, pp. 291–310, 2016.

[63] Y. Huang and B. Young, "Post-fire behaviour of ferritic stainless steel material," *Construction and Building Materials*, vol. 157, pp. 654–667, 2017, ISSN: 09500618. DOI: 10.1016/j.conbuildmat.2017.09.082.

[64] C. Maraveas, Z. C. Fasoulakis, and K. D. Tsavdaridis, "Mechanical properties of high and very high steel at elevated temperatures and after cooling down," *Fire Science Reviews*, vol. 6, no. 1, 2017, ISSN: 2193-0414. DOI: 10.1186/s40038-017-0017-6.

[65] S. Kesawan and M. Mahendran, "Post-fire mechanical properties of cold-formed steel hollow sections," *Construction and Building Materials*, vol. 161, pp. 26–36, 2018.

[66] H. T. Li and B. Young, "Residual mechanical properties of high strength steels after exposure to fire," *Journal of Constructional Steel Research*, vol. 148, pp. 562–571, 2018, ISSN: 0143974X. DOI: 10.1016/j.jcsr.2018.05.028.

[67] T. G. Singh and K. D. Singh, "Post-fire mechanical properties of YSt-310 cold-formed steel tubular sections," *Journal of Constructional Steel Research*, vol. 153, pp. 654–666, 2019.

[68] A. O. Olawale and R. J. Plank, "The collapse analysis of steel columns in fire using a finite strip method," *International Journal for Numerical Methods in Engineering*, vol. 26, no. 12, pp. 2755–2764, Dec. 1988, ISSN: 0029-5981. DOI: 10.1002/nme.1620261212.

[69] Z. Tao, X. Wang, and B. Uy, "Stress-strain curves of structural and reinforcing steels after exposure to elevated temperatures," *Journal of Materials in Civil Engineering*, vol. 25, no. 9, pp. 1306–1316, 2013.

[70] J. B. Mander, "Seismic design of bridge piers," Ph.D. dissertation, University of Canterbury, 1983.

[71] European Committee for Standardization (CEN), *Eurocode 3: Design of steel structures, Part 1-1: General rules and rules for buildings*. Brussels, Belgium, 2016.

[72] European Committee for Standardization (CEN), *Eurocode 3: Design of steel structures, Part 1-5: Plated structural elements*. Brussels, Belgium, 2006, pp. 1–53.

[73] X. Yun and L. Gardner, "Stress-strain curves for hot-rolled steels," *Journal of Constructional Steel Research*, vol. 133, pp. 36–46, Jun. 2017, ISSN: 0143974X. DOI: 10.1016/j.jcsr.2017.01.024.

[74] S. Afshan, B. Rossi, and L. Gardner, "Strength enhancements in cold-formed structural sections - Part I: Material testing," *Journal of Constructional Steel Research*, vol. 83, pp. 177–188, 2013.

[75] L Gardner and D. Nethercot, "Numerical modeling of stainless steel structural somponents - a consistent approach," *Journal of Structural Engineering*, vol. 130, no. 10, pp. 1586–1601, 2004.

[76] A. J. Sadowski, J. M. Rotter, T. Reinke, and T. Ummenhofer, "Statistical analysis of the material properties of selected structural carbon steels," *Structural Safety*, vol. 53, pp. 26–35, 2015.

[77] M. Mišović, N. Tadić, and D. Lučić, "Deformation characteristics of aluminium alloys," *Gradjevinar*, vol. 68, no. 3, pp. 179–190, Apr. 2016, ISSN: 13339095. DOI: 10.14256/JCE.1457.2015.

[78] X. Qiang, F. S. Bijlaard, and H. Kolstein, "Post-fire performance of very high strength steel S960," *Journal of Constructional Steel Research*, vol. 80, pp. 235–242, 2013.

[79] X. Yan, J. C. Batista Abreu, R. S. Glauz, B. W. Schafer, and T. Gernay, "Simple three-coefficient equation for temperature dependent mechanical properties of cold-formed steels," *Journal of Structural Engineering*, vol. 147, no. 4, p. 04 021 035, Apr. 2021, ISSN: 0733-9445. DOI: 10.1061/(ASCE)ST.1943-541X.0002990.

[80] J. E. Box, W. T. Colgan, T. R. Christensen, N. M. Schmidt, M. Lund, F.-J. W. Parmentier, R. Brown, U. S. Bhatt, E. S. Euskirchen, V. E. Romanovsky, J. E. Walsh, J. E. Overland, M. Wang, R. W. Corell, W. N. Meier, B. Wouters, S. Mernild, J. Mård, J. Pawlak, and M. S. Olsen, "Key indicators of Arctic climate change: 1971–2017," *Environmental Research Letters*, vol. 14, no. 4, p. 045 010, Apr. 2019, ISSN: 1748-9326. DOI: 10.1088/1748-9326/AAFC1B.

[81] C. A. Runge, R. M. Daigle, and V. H. Hausner, "Quantifying tourism booms and the increasing footprint in the arctic with social media data," *PLOS ONE*, vol. 15, no. 1, pp. 1–14, Jan. 2020. DOI: 10.1371/journal.pone.0227189.

[82] S. A. Agarkov, A. V. Kozlov, S. V. Fedoseev, and A. B. Teslya, "Major trends in efficiency upgrading of the economic activity in the arctic zone of Russian Federation," *Journal of Mining Institute*, vol. 230, pp. 209–216, 2018. DOI: 10.25515/PMI.2018.2.209.

[83] A. V. Smirnov, "The arctic population: Dynamics and centers of the settlement system," *Arctic and North*, no. 40, pp. 270–290, 2020.

[84] G. K. Hovelsrud, B. Poppel, B. Van Oort, and J. D. Reist, "Arctic societies, cultures, and peoples in a changing cryosphere," *Ambio*, vol. 40, no. 1, pp. 100–110, 2011.

[85] H.-S. Shin, H.-M. Lee, and M.-S. Kim, "Impact tensile behaviors of 9% nickel steel at low temperature," *International journal of impact engineering*, vol. 24, no. 6-7, pp. 571–581, 2000.

[86] A. Filiatrault and M. Holleran, "Stress-strain behavior of reinforcing steel and concrete under seismic strain rates and low temperatures," *Materials and Structures/Materiaux et Constructions*, vol. 34, pp. 235–239, Apr. 2001, ISSN: 13595997. DOI: 10.1007/bf02480594.

[87] J. Levings and S. Sritharan, "Effects of Cold Temperature and Strain Rate on the Stress-Strain Behavior of ASTM A706 Grade 420(60) Steel Reinforcement," *Journal of Materials in Civil Engineering*, vol. 24, pp. 1441–1449, Dec. 2012, ISSN: 0899-1561. DOI: 10.1061/(asce)mt.1943-5533.0000523.

[88] Y. Wang, X. Liu, Z. Hu, and Y. Shi, "Experimental study on mechanical properties and fracture toughness of structural thick plate and its butt weld along thickness and at low temperatures," *Fatigue & fracture of engineering materials & structures*, vol. 36, no. 12, pp. 1258–1273, 2013.

[89] J. B. Yan, J. Y. Liew, M. H. Zhang, and J. Y. Wang, "Mechanical properties of normal strength mild steel and high strength steel S690 in low temperature relevant to Arctic environment," *Materials and Design*, vol. 61, pp. 150–159, Sep. 2014, ISSN: 18734197. DOI: 10.1016/j.matdes.2014.04.057.

[90] H. Furuya, T. Tagawa, and T. Ishikawa, "Effect of tempering temperature on tensile straining behavior in ni bearing cryogenic steel," *TETSU TO HAGANE-JOURNAL OF THE IRON AND STEEL INSTITUTE OF JAPAN*, vol. 100, no. 5, pp. 104–111, 2014.

[91] Y.-j. Li, R.-d. Fu, Y. Li, Y. Peng, and H.-j. Liu, "Tensile properties and fracture behavior of friction stir welded joints of fe-32mn-7cr-1mo-0.3 n steel at cryogenic temperature," *Journal of Materials Science & Technology*, vol. 34, no. 1, pp. 157–162, 2018.

[92] Z. Li, D. Zhang, H. Wu, F. Huang, W. Hong, and X. Zang, "Fatigue properties of welded Q420 high strength steel at room and low temperatures," *Construction and Building Materials*, vol. 189, pp. 955–966, Nov. 2018, ISSN: 09500618. DOI: 10.1016/j.conbuildmat.2018.07.231.

[93] J. Xie, X. Zhao, and J. B. Yan, "Mechanical properties of high strength steel strand at low temperatures: Tests and analysis," *Construction and Building Materials*, vol. 189, pp. 1076–1092, Nov. 2018, ISSN: 09500618. DOI: 10.1016/j.conbuildmat.2018.09.053.

[94] J. Xie, G. R. Zhu, and J. B. Yan, "Mechanical properties of headed studs at low temperatures in Arctic infrastructure," *Journal of Constructional Steel Research*, vol. 149, pp. 130–140, Oct. 2018, ISSN: 0143974X. DOI: 10.1016/j.jcsr.2018.07.028.

[95] Y. Yin, S. Li, Q. Han, and M. Li, "Material parameters in void growth model for G20Mn5QT cast steel at low temperatures," *Construction and Building Materials*, vol. 243, p. 118 123, May 2020, ISSN: 09500618. DOI: 10.1016/j.conbuildmat.2020.118123.

[96] L. An, W. Jiang, H. Zhang, and J. Wu, "Experimental research on bolted joint strength and dispersion in steel lattice transmission tower legs under low temperatures," *Fatigue and Fracture of Engineering Materials and Structures*, vol. 43, pp. 919–931, May 2020, ISSN: 14602695. DOI: 10.1111/ffe.13165.

[97] J. B. Yan, Y. L. Luo, X. C. Lin, Y. B. Luo, and L. X. Zhang, "Effects of the Arctic low temperature on mechanical properties of Q690 and Q960 high-strength steels," *Construction and Building Materials*, vol. 300, p. 124 022, 2021, ISSN: 0950-0618. DOI: 10.1016/j.conbuildmat.2021.124022.

[98] J. B. Yan, Y. L. Luo, L. Su, X. Lin, Y. B. Luo, and L. Zhang, "Low-temperature compression behaviour of square CFST columns using Q960 ultra-high strength steel," *Journal of Constructional Steel Research*, vol. 183, p. 106 727, Aug. 2021, ISSN: 0143974X. DOI: 10.1016/j.jcsr.2021.106727.

[99] C. Li, K. Li, J. Dong, J. Wang, and Z. Shao, "Mechanical behaviour and microstructure of fe-20/27mn–4al-0.3 c low magnetic steel at room and cryogenic temperatures," *Materials Science and Engineering: A*, vol. 809, p. 140 998, 2021.

[100] Y Fujimura and H Ishii, "Tensile behaviors of high cr-low ni two-phase stainless steels at room and low temperatures," *Japan Institute of Metals, Journal*, vol. 37, pp. 33–39, 1973.

[101] R. Miura, K. Ohnishi, H. Nakajima, and S. Shimamoto, "Effects of carbon and nitrogen on the tensile deformation behavior of sus304 and 316 stainless steels at cryogenic temperatures," *Tetsu-to-Hagané*, vol. 73, no. 6, pp. 715–722, 1987.

[102] J He, G Han, S Fukuyama, and K Yokogawa, "Tensile behaviour of duplex stainless steel at low temperatures," *Materials science and technology*, vol. 15, no. 8, pp. 909–920, 1999.

[103] D Sun, G Han, S Vaodee, S Fukuyama, and K Yokogawa, "Tensile behaviour of type 304 austenitic stainless steels in hydrogen atmosphere at low temperatures," *Materials science and technology*, vol. 17, no. 3, pp. 302–308, 2001.

[104] W. S. Park, S. W. Yoo, M. H. Kim, and J. M. Lee, "Strain-rate effects on the mechanical behavior of the aisi 300 series of austenitic stainless steel under cryogenic environments," *Materials & Design*, vol. 31, no. 8, pp. 3630–3640, 2010.

[105] S.-W. Yoo, C.-S. Lee, W.-S. Park, M.-H. Kim, and J.-M. Lee, "Temperature and strain rate dependent constitutive model of trip steels for low-temperature applications," *Computational Materials Science*, vol. 50, no. 7, pp. 2014–2027, 2011.

[106] C. Zheng and W. Yu, "Effect of low-temperature on mechanical behavior for an aisi 304 austenitic stainless steel," *Materials Science and Engineering: A*, vol. 710, pp. 359–365, 2018.

[107] H. Ding, Y. Wu, Q. Lu, P. Xu, J. Zheng, and L. Wei, "Tensile properties and impact toughness of s30408 stainless steel and its welded joints at cryogenic temperatures," *Cryogenics*, vol. 92, pp. 50–59, 2018.

[108] J.-B. Yan, Z. Lin, P. Xie, Y.-B. Luo, and Y. Li, "Tensile behavior of stainless steel s30408 at the arctic low temperature," *Steel and Composite Structures*, vol. 40, no. 5, pp. 633–648, 2021.

[109] N. Koga, T. Nameki, O. Umezawa, V. Tschan, and K.-P. Weiss, "Tensile properties and deformation behavior of ferrite and austenite duplex stainless steel at cryogenic temperatures," *Materials Science and Engineering: A*, vol. 801, p. 140 442, 2021.

[110] J.-B. Yan, Y. Geng, P. Xie, and J. Xie, "Low-temperature mechanical properties of stainless steel 316l: Tests and constitutive models," *Construction and Building Materials*, vol. 343, p. 128 122, 2022.

[111] F. Azhari, A. A. Hossain Apon, A. Heidarpour, X. L. Zhao, and C. R. Hutchinson, "Mechanical response of ultra-high strength (Grade 1200) steel under extreme cooling conditions," *Construction and Building Materials*, vol. 175, pp. 790–803, Jun. 2018, ISSN: 09500618. DOI: 10.1016/j.conbuildmat.2018.04.191.

[112] M. Rokilan and M. Mahendran, "Sub-zero temperature mechanical properties of cold-rolled steel sheets," *Thin-Walled Structures*, vol. 154, p. 106 842, Sep. 2020, ISSN: 02638231. DOI: 10.1016/j.tws.2020.106842.

[113] J. B. Yan, W. J. Xie, Y. Luo, and T. Wang, "Behaviours of concrete stub columns confined by steel tubes at cold-region low temperatures," *Journal of Constructional Steel Research*, vol. 170, p. 106 124, Jul. 2020, ISSN: 0143974X. DOI: 10.1016/j.jcsr.2020.106124.

[114] M. C. Serreze and R. G. Barry, *The Arctic climate system*. Cambridge University Press, 2014.

[115] S. J. Vavrus, M. M. Holland, A. Jahn, D. A. Bailey, and B. A. Blazey, "Twenty-First-Century Arctic Climate Change in CCSM4," *Journal of Climate*, vol. 25, no. 8, pp. 2696–2710, Apr. 2012, ISSN: 0894-8755. DOI: 10.1175/JCLI-D-11-00220.1.

[116] C. A. Rogers and G. J. Hancock, "Ductility of G550 Sheet Steels in Tension," *Journal of Structural Engineering*, vol. 123, no. 12, pp. 1586–1594, Dec. 1997, ISSN: 0733-9445. DOI: 10.1061/(asce)0733-9445(1997)123:12(1586).

[117] American Iron and Steel Institute (AISI), *S903-17: Test Standard for Determining the Uniform and Local Ductility of Carbon and Low-Alloy Steels*. Washington, DC, U.S.A., 2017.

[118] J. B. Yan and J. Xie, "Experimental studies on mechanical properties of steel reinforcements under cryogenic temperatures," *Construction and Building Materials*, vol. 151, pp. 661–672, Oct. 2017, ISSN: 09500618. DOI: 10.1016/j.conbuildmat.2017.06.123.

[119] K. Valtonen, V. Ratia, K. R. Ramakrishnan, M. Apostol, J. Terva, and V. T. Kuokkala, "Impact wear and mechanical behavior of steels at subzero temperatures," *Tribology International*, vol. 129, pp. 476–493, Jan. 2019, ISSN: 0301679X. DOI: 10.1016/j.triboint.2018.08.016.

[120] European Committee for Standardization (CEN), *Eurocode 3: Design of steel structures, Part 1-2: General rules - Structural fire design*. Brussels, Belgium, 2005, pp. 1–81.

[121] European Committee for Standardization (CEN), *Eurocode 3: Design of steel structures, Part 1-12: Additional rules for the extension of EN 1993 up to steel grades S700*. Brussels, Belgium, 2007, pp. 1–9.

[122] Standards Australia, *AS/NZS 1397:2021 Continuous hot-dip metallic coated steel sheet and strip - Coatings of zinc and zinc alloyed with aluminium and magnesium*. Sydney, Australia, 2021, pp. 1–29.

[123] A. K. Dhalla and G. Winter, "Suggested steel ductility requirements," *Journal of the Structural Division*, vol. 100, no. 2, pp. 445–462, 1974.

[124] L. Ingvarsson, "Cold-forming residual stresses effect on buckling," 1975, pp. 85–119.

[125] C. C. Weng and T. Peköz, "Residual-stresses in cold-formed steel members," *Journal of Structural Engineering-ASCE*, vol. 116, no. 6, pp. 1611–1625, 1990.

[126] E. de M. Batista and F. Rodrigues, "Residual stress measurements on cold-formed profiles," *Experimental Techniques*, vol. 16, pp. 25–29, 5 1992. DOI: 10.1111/j.1747-1567.1992.tb00702.x.

[127] B. Young and K. Rasmussen, *Compression tests of fixed-ended and pin-ended cold-formed lipped channels*, Sep. 1995.

[128] B. W. Schafer and T. Peköz, "Computational modeling of cold-formed steel: Characterizing geometric imperfections and residual stresses," *Journal of Constructional Steel Research*, vol. 47, pp. 193–210, 3 1998, ISSN: 0143974X. DOI: 10.1016/S0143-974X(98)00007-8.

[129] D. T. Dat and T. Peköz, "The strength of cold-formed steel columns," Cornell University, 1980. [Online]. Available: https://scholarsmine.mst.edu/ccfss-library/110.

[130] SSMA, "Steel Stud Manufacturers Association Product Technical Guide," Steel Stud Manufacturers Association, Boise, ID, USA, Tech. Rep., 2022, pp. 1–70.

[131] C. Weng, R. White, *et al.*, "Residual stresses in cold-bent thick steel plates," *Journal of Structural Engineering-ASCE*, vol. 116, no. 1, pp. 24–39, 1990.

[132] W. Quach, J. Teng, and K. F. Chung, "Finite element predictions of residual stresses in press-braked thin-walled steel sections," *Engineering structures*, vol. 28, no. 11, pp. 1609–1619, 2006.

[133] W. Quach, J. Teng, and K. F. Chung, "Residual stresses in press-braked stainless steel sections, ii: Press-braking operations," *Journal of Constructional Steel Research*, vol. 65, no. 8-9, pp. 1816–1826, 2009.

[134] H. Amouzegar, B. Schafer, and M. Tootkaboni, "An incremental numerical method for calculation of residual stresses and strains in cold-formed steel members," *Thin-Walled Structures*, vol. 106, pp. 61–74, 2016.

[135] Y. Sun, V. Luzin, S. Khan, N. Vajragupta, P. Meehan, B. Daniel, J. Yanagimoto, Z. Xiong, and S. Ding, "Understanding of residual stresses in chain-die-formed dual-phase (dp) metallic components: Predictive modelling and experimental validation," *The International Journal of Advanced Manufacturing Technology*, vol. 103, no. 9, pp. 3337–3360, 2019.

[136] A. Mutafi, N Yidris, J Loughlan, R Zahari, and M. Ishak, "Investigation into the distribution of residual stresses in pressed-braked thin-walled steel lipped channel sections using the 3d-fem technique," *Thin-Walled Structures*, vol. 135, pp. 437–445, 2019.

[137] Abaqus, *version 6.16*. Dassault Systèmes Simulia Corp, 2016.

[138] C. D. Moen, T. Igusa, and B. W. Schafer, "Prediction of residual stresses and strains in cold-formed steel members," *Thin-walled structures*, vol. 46, no. 11, pp. 1274–1289, 2008.

[139] R. S. Glauz, "Torsion Analysis for Cold-Formed Steel Members Using Flexural Analogies," in *Proceedings of the Cold-Formed Steel Research Consortium Colloquium*, 2020. [Online]. Available: `http://jhir.library.jhu.edu/handle/1774.2/63139`.

[140] Ministry of Construction of the People's Republic of China and General Administration of Quality Supervision, Inspection and Quarantine of the People's Republic of China, *Technical code of cold-formed thin-wall steel structures*. Beijing, China, 2002, pp. 1–93.

[141] G. Bian, K. D. Peterman, S. Torabian, and B. W. Schafer, "Torsion of cold-formed steel lipped channels dominated by warping response," *Thin-Walled Structures*, vol. 98, pp. 565–577, 2016.

[142] Z. Li and B. W. Schafer, "Buckling Analysis of Cold-formed Steel Members with General Boundary Conditions Using CUFSM Conventional and Constrained Finite Strip Methods," in *CCFSS Proceedings of International Specialty Conference on Cold-Formed Steel Structures (1971 - 2018)*, St. Louis, Missouri, U.S.A., 2010.

[143] V. Zeinoddini-Meimand, "Geometric imperfections in cold-formed steel members," English, Ph.D. dissertation, 2011, p. 280, ISBN: 978-1-267-15044-8.

[144] American Iron and Steel Institute (AISI), *D100-17: AISI Manual Cold-Formed Steel Design*. Washington, DC, U.S.A., 2017.

[145] R. S. Glauz and B. W. Schafer, "Modifications to the direct strength method of cold-formed steel design for members unsymmetric about the axis of bending," *Thin-Walled Structures*, vol. 173, p. 109 025, Apr. 2022, ISSN: 0263-8231. DOI: 10.1016/J.TWS.2022.109025.

[146] A. Newman, *Metal Building Systems: Design and Specifications*, 2nd. McGraw-Hill Education, 2004, pp. 1–465, ISBN: 9780071402019.